Université Libanaise
Ecole Doctorale
Sciences et Technologie

Université
de Lille

THESE de doctorat en Cotutelle

Pour obtenir le grade de Docteur délivré par

L'Université Libanaise
L'Ecole Doctorale des Sciences et Technologie

Et

L'Université de Lille - Sciences et Technologies

Spécialité : Chimie des matériaux

Présentée et soutenue publiquement par

Ibrahim Maya

Le 1er décembre 2020

Optimization of catalysts based on copper and manganese oxides supported on hydroxyapatite for the total oxidation of toluene

Optimisation de catalyseurs à base d'oxydes de cuivre et de manganèse supportés sur hydroxyapatite pour l'oxydation totale du toluène

Membres du Jury

Mme Jane ESTEPHANE, University of Balamand, Professeur Associé	Rapporteur
Mme Florence EPRON, Université de Poitiers, Directeur de Recherche CNRS	Rapporteur
M. Houssam RASSY, American University of Beirut, Professeur Associé	Examinateur
M. Charbel AFIF, Université Saint-Joseph, Professeur	Président du Jury
Mme Antonella GERVASINI, University of Milan, Professeur	Examinateur
M. Michel NAKHL, Université Libanaise, Professeur	Invité
Mme Anne PONCHEL, Université d'Artois, Professeur	Invité
Mme Madona LABAKI, Université Libanaise, Professeur	Co-directeur
M. Jean-François LAMONIER, Université de Lille, Professeur	Directeur
M. Jean-Marc GIRAUDON, Université de Lille, Maître de Conférences	Co-encadrant

Acknowledgments

I would like to thank Pr Fawaz El OMAR and Pr Joël CUGUEN for having accepted me as a doctoral student in joint supervision between the Doctoral School of Science and Technology (DSST) of the Lebanese University and the Doctoral School of Material, Radiation and Environment Sciences of the University of Science and Technology (USTL) - Lille.

This thesis work took place between the *Laboratory of Physical Chemistry of Materials- Plateforme De Recherche Et Nanotechnologie* (LCPM / PR2N) in Fanar and *Unité de Catalyse et Chimie du Solide* (UCCS UMR 8181 CNRS) in Lille. In this regard, I would like to express my appreciation to Professors Mirvat ZAKHOUR and Franck DUMEIGNIL, directors of laboratory in Lebanon and France, respectively, for providing me with the working facilities required to pursue my doctoral studies.

I would particularly like to thank my supervisors in Lille, Pr Jean-François LAMONIER and Dr Jean-Marc-GIRAUDON for generously dispensing their time, scientific expertise and wisdom. Our discussions over the years have helped me to widen the scope of my knowledge and hone my interpretation skills. Furthermore, the counsel they offered when faced with a problem constituted a great source of guidance. But most importantly, their patience and kindness in a most difficult period is a service I'll always appreciate.

A deep feeling of recognition goes as well to my supervisor in Lebanon, Pr Madona LABAKI, in whom I have found both an amazing mentor and a sympathizing ear. Her boundless passion for work is a quality I had already witnessed through the courses she gave me during my Bachelor and Master degrees. Still, my admiration continues to grow and I hope to, one day, acquire such a commendable skill set of amiability, helpfulness and scientific proficiency.

I also owe a great deal of gratitude to Pr Michel NAKHL who has actively fought for me at various stages of my PhD. I'll be forever indebted to him for the invaluable favor he gratuitously did me. A big thank you goes as well to my hometown neighbor and university teacher, Dr Charbel AMINE, who also strived to assist me in a moment of need. Moreover, I would like to express my sincerest appreciation to Christine LANCELOT who is not only an exceptional associate professor at the University of Lille but one of the most kind hearted and solicitous people I had the pleasure of knowing.

I am much obliged to Professors Anne PONCHEL and Eric MONFLIER for meeting with my supervisors and me to discuss the possibility of working with the β-cyclodextrin oligosaccharide and subsequently providing me with the β-cyclodextrin batch required for my research studies.

I would like to thank the jury members of my thesis, CNRS research director Florence EPRON (IC2MP, University of Poitiers, reviewer), Pr Jane ESTEPHANE (University of Balamand, Professor, reviewer), Pr Antonella GERVASINI (University of Milan, examiner), Pr Houssam RASSY (American University of Beirut, examiner), Pr Charbel AFIF (Saint Joseph University, examiner), Pr Anne PONCHEL (Artois University, invited member) and Pr Michel NAKHL (Lebanese University, invited member), for graciously accepting to read and evaluate my work.

Furthermore, I am filled with gratitude towards the entire UCCS team, especially Nicolas NUNS, Olivier GARDOLL, Martine TRENTESAUX, Jean-Charles MORIN, Asma TOUGERTI, Pardis SIMON, Pascal BLANCHARD, Jean-Philippe DACQUIN, Nora DJELAL and Laurence BURYLO, for their precious technical help, generously offered explanations and inspiring dedication to the research field. I am also thankful for the wonderful friendships I made in Lille and the amazing colleagues I got to share precious memories with, namely Guillaume ROCHARD, Tanushree KANE, Noura HAIDAR, Balsam HAMIEH, Grêce ABDALLAH, Rim BITAR, Bertrand HEIDINGER, Hermann Wilfried SIAKA, Shilpa SONAR, Juliana APARICIO, Sara HOUDA, Jérémy DHAINAUT, Guillaume POMALAZA, Carmen CIOTONEA, Yash BOYJOO, Francesco MAZZANTI, and Hattie CHISNALL. The same goes to the incredible people I met and worked with at Fanar, namely Dayan CHLALA, Amanda SFEIR, Rana BCHARA and Serena KHAIRALLAH.

I am deeply grateful as well to my two cousins Dominique and Antoinette. Domi, my stay in France would not have been half as pleasant without the assistance you provided on a constant basis, whether with my luggage, room accommodation, travelling documents … or by simply being welcoming and hospitable whenever I came to Paris. Nounette, there are some comments in life that mark you profoundly and such was the case of the words you said to me on a very special day in which I sought your advice, feeling a bit lost and unsure. You told me “There’s no shame but only courage in admitting one’s mistake”. That piece of wisdom helped carry me through to the finish line of this particular journey.

I would like to thank my parents from the bottom of my heart for their constant love and support, as well as their unwavering faith in me. To my sisters, Maria and Sandra, no words will be able to express my gratitude for your unconditional love, which remained my strongest anchor through the various hardships I encountered. You have always been and will always remain my strongest allies, my biggest comfort and my best friends.

Last but not least, I offer my most humble praise to God who’s been with me every step of the way, guiding me and steering me towards the right path. I also thank HIM for keeping my loved ones and me in good health during the COVID-19 pandemic.

Abstract

The use of catalytic processes in air pollution abatement is widespread and regarded as one of the most promising methods for atmospheric pollutants removal. Heterogeneous catalysts are efficiently used to reduce toxic emissions, such as Volatile Organic Compounds (VOC), among which toluene was selected as model molecule to be used in this study. Hydroxyapatite ($Ca_{10}(PO_4)_6(OH)_2$), which was shown, through previous investigations, to be extremely useful in the field of environmental management, owing to its particular structure and attractive properties, was chosen to be the active phase support in the current work. Copper and manganese oxides, transition metal oxides which had proven to be highly active in the total oxidation of toluene in the past, were designated for the role of active phases in the presently prepared hydroxyaptite (Hap) -supported catalysts. Firstly, a close examination into the use of Hap supported binary Cu-Mn oxides with different atomic Cu/Mn composition (2; 1; 0.5) was conducted. This study showed binary oxide catalysts to be more efficient than the single transition metal oxide catalysts, and determined an optimal Cu/Mn molar ratio value equal to 2. Secondly, β-cyclodextrin (β-CD), an organic complexing agent, was employed to adjust poor copper species dispersion, a problem that limits the performances of Cu-supported catalysts. Not only was the success of using β-CD in improving Cu dispersion and reducibility revealed through physicochemical analysis, but a meticulous inspection of the interactions taking place within the synthesized system, from solution stage to that of calcined product, exposed the role of β-CD at each step of the Cu/Hap catalyst preparation, evidencing the occurrence of interactions between β-CD molecules and both Cu^{2+} ions derived from copper precursor and Ca^{2+} ions of hydroxyapatite support. Finally, an investigation of manganese speciation in Mn/Hap catalysts with different Mn loadings was carried out. Results indicated an increase in Mn average oxidation state (AOS) going hand in hand with that of Mn content. However, a lower Mn AOS turned out to be more beneficial for the catalyst's reducibility.

Keywords: Heterogeneous catalysts; VOC; Toluene; Hydroxyapatite; Binary Cu-Mn oxides; β-cyclodextrin; Cu dispersion; Manganese speciation.

Résumé

L'utilisation de procédés catalytiques dans la réduction de la pollution de l’air est répandue et considérée comme l'une des méthodes les plus prometteuses pour l'élimination des polluants atmosphériques. Les catalyseurs hétérogènes sont des outils efficaces pour limiter les émissions toxiques, tels que les composés organiques volatils (COV), parmi lesquels le toluène a été sélectionné comme molécule modèle à utiliser dans cette étude. L'hydroxyapatite ($Ca_{10}(PO_4)_6(OH)_2$), qui s'est avérée, grâce à des études antérieures, être extrêmement utile dans le domaine de la gestion de l'environnement, en raison de sa structure particulière et de ses propriétés attrayantes, a été choisie pour être le support de la phase active dans le travail en cours. Les oxydes de cuivre et de manganèse, oxydes de métaux de transition qui s'étaient révélés très actifs dans l'oxydation totale du toluène dans le passé, ont été désignés pour le rôle de phases actives dans les catalyseurs supportés sur hydroxyaptite (Hap) actuellement préparés. Tout d'abord, un examen approfondi de l'utilisation des oxydes binaires Cu-Mn supportés sur Hap avec différentes compositions atomiques Cu/Mn (2; 1; 0,5) a été réalisé. Cette étude a montré que les catalyseurs à oxydes binaires étaient plus efficaces que les catalyseurs à oxyde de métal de transition unique et a déterminé une valeur optimale du rapport molaire Cu/Mn égale à 2. Deuxièmement, la β-cyclodextrine (β-CD), un agent complexant organique, a été employée pour résoudre la mauvaise dispersion des espèces de cuivre, un problème qui limite les performances des catalyseurs Cu supportés. Non seulement le succès de l'utilisation de la β-CD dans l'amélioration de la dispersion et de la réductibilité du Cu a été démontré par analyses physicochimiques, mais une inspection minutieuse des interactions qui ont lieu au sein du système synthétisé, du stade de solution à celui de produit calciné, a illustré le rôle de la β-CD à chaque étape de la préparation du catalyseur Cu/Hap, mettant en évidence l'occurrence d'interactions entre les molécules de β-CD et les ions Cu^{2+} provenant du précurseur de cuivre ainsi que les ions Ca^{2+} du support hydroxyapatite. Enfin, une enquête sur la spéciation du manganèse dans les catalyseurs Mn/Hap avec différentes teneurs de Mn a été effectuée. Les résultats ont indiqué une augmentation du degré d'oxydation moyen du Mn (DOM) allant de pair avec celle de la teneur en Mn. Cependant, un faible DOM de Mn s’est avéré plus avantageux pour la réductibilité du catalyseur.

Mots-clés: Catalyseurs hétérogènes; COV; Toluène; Hydroxyapatite; Oxydes binaires Cu-Mn; β-cyclodextrine; Dispersion du Cu; Spéciation du manganèse.

Table of Contents

Introduction

Air pollution constitutes a major hazard to human health, for it accounts for an estimated 4.2 million deaths per year (World Health Organization (WHO), 2019). While an enhancement in air quality was noted in many countries, owing to efficient emission control technologies, in other parts of the world air quality kept on suffering from severe deterioration. In fact, around 91% of the world's population lives in areas where air quality levels surpass WHO limits. Moreover, seeing as air quality is intimately connected with earth's climate, implementing robust and high-performing air-cleanup strategies will not only lessen the weight of illnesses ascribable to air pollution, but also play a role in resolving the problem of climate change.

Volatile Organic Compounds (VOC) are considered to be main contributors towards air pollution. The term VOC refers to a broad range of organic compounds which can rapidly evaporate to air as a result of their high vapor pressure and low boiling point. European Directive 2004/42/CE provides an even more precise definition of the term, by identifying VOC as "any organic compound having an initial boiling point less than or equal to 250 °C measured at a standard pressure of 101.3 kPa". VOC are emitted to the atmosphere from various biogenic (vegetation, oceans, soils etc.) and anthropogenic (motor vehicles, agriculture, industry etc.) sources. Although the biogenic sources are generally predominant over anthropogenic sources, in certain situations the anthropogenic emissions can dominate, e.g. in industrialized and densely populated regions.

To eliminate these pollutants from gas streams, different technologies have been developed and put to practice. Thermal incineration is the most common process which requires high temperatures (> 1000 °C) to achieve the total combustion of highly concentrated VOC. However, seeing as this technique entails high energy consumption, making it thus rather costly, as well as produces undesirable by-products such as dioxins and carbon monoxide in the incinerator flue gas, an alternative method for VOC removal must be utilized. Catalytic oxidation represents a much more effective and economically viable alternative to the formerly discussed process, by completely oxidizing VOC into CO_2 and water under much lower temperature and potentially increasing the reaction rate [1].

Among the VOC, toluene, with the chemical formula $C_6H_5CH_3$, is an aromatic hydrocarbon extensively employed as an organic solvent for paints, printing inks, adhesives, and antiseptics because of its great capacity to dissolve organic substances. This aromatic VOC is also present in car exhausts and cigarette smoke, and has a relatively high photochemical ozone creation potential (POCP = 77) [2]. In addition, toluene has a toxic effect on health. Indeed, in mild cases, its vapors can be irritating to the eyes and the upper respiratory tract, as well as cause headaches. Furthermore, in severe cases, exposure to very high concentrations can cause loss of consciousness and death. It follows that finding effective means of abating toluene emission into atmosphere, is of the outmost importance. Accordingly, it seemed highly appropriate to choose toluene as a probe molecule in this study.

Catalysts based on noble metals and transition metal oxides have been successfully applied in the past for the total oxidation of toluene. While on one hand noble metal catalysts such as Pt, Pd, and Au were found to be highly active, their equally high cost limited their application. Transition metal oxides (TMO), on the other hand, which are more cost-efficient, have demonstrated great catalytic performances in toluene's complete incineration, with an activity sometimes comparable, or even on some occasion superior, to that of noble metal based catalysts. Among said transition metal oxides, copper oxide and manganese oxide have proven to be most rewarding in terms of activity and selectivity [3], [4]. Hence, both of these TMO (CuO_x and MnO_y) were selected as active species in this work.

TMO catalysts can be either unsupported or supported on a carrier material. However, considering that higher dispersion of the active components can be achieved over supported catalysts, these latter would exhibit higher efficiency in the total oxidation of toluene and be therefore a more catalytically favorable choice. Hydroxyapatite (Hap), a calcium phosphate material whose general formula is $Ca_{10}(PO_4)_6(OH)_2$, is considered to be very valuable for air clean-up applications, owing to its outstanding characteristics: great adsorption capacities, acid-base adjustability, ion-exchange capability, and good thermal stability [5]. Previous reports have shown that these unique features of this material have granted Hap with exceptional carrier traits, leading towards the enhancement of catalytic performances. This has encouraged its current use as active phase support in the present research.

Consequently, in this study, hydroxyapatite supported copper and/or manganese based catalysts will be prepared and examined in the total oxidation of toluene. As a first step, the possibility of creating a synergic effect by combining both copper and manganese oxides will be meticulously investigated. Subsequently, seeing as both the dispersion of the metal oxide species and the oxidation states of the metals are of great importance in determining their catalytic activities, efforts will be made towards improving the first (metal oxide dispersion) in the case of copper-based catalysts, and evaluating the second (metal oxidation state) in the case of manganese-based catalysts.

In order to attain enhanced copper species dispersion and reducibility, an organic complexing agent, β-cyclodextrin (β-CD), will be used. This oligosaccharide has already been successfully employed by other researchers for upgrading the dispersion and reducibility of active species over a carrier material, an action which effectively prompted a rise in the catalytic performances of the synthesized catalyst [6]. Hence, the use of β-CD as active phase dispersant looks to be a very promising strategy.

This PhD manuscript will be divided into six chapters. In Chapter I, a literature review on the structure, properties, and environmental applications of hydroxyapatite will be first provided, followed by a report on the catalytic use of copper and manganese oxides for the complete oxidation of toluene, subsequent to which, the necessity of employing β-CD to achieve higher Cu dispersion will be full outlined, and finally the impact of Mn speciation on the catalytic performances of Mn-based catalysts will be clearly indicated. Chapter II will be dedicated to presenting the catalysts synthesis protocols as well as the experimental conditions adopted during the physicochemical characterizations and catalytic performances evaluation. The remaining four chapters will be devoted to unveiling the results derived from the inspection of the presently prepared catalytic systems, tested in toluene's complete oxidation. Thus, Chapter III will discuss all data pertaining to the study of binary Cu-Mn oxides supported on hydroxyapatite catalysts. As for Chapter IV, it will be assigned to presenting the effects of a β-CD-assisted synthesis on the resulting properties and catalytic performances of the obtained Cu-supported catalyst. Chapter V will strongly focus on the role played by β-CD at each step of the Cu/Hap catalyst preparation. Regarding Chapter VI, it will deal with the determination of manganese speciation in Mn-based catalysts all while investigating its effect on the physicochemical properties of these Mn-bearing materials. This manuscript will be lastly wrapped up with a general conclusion which will highlight the main contributions of this work, in addition to shedding some light on future perspectives.

[1] M. S. Kamal, S. A. Razzak, and M. M. Hossain, « Catalytic oxidation of volatile organic compounds (VOCs)–A review », *Atmos. Environ.*, vol. 140, p. 117–134, 2016.

[2] R. G. Derwent, M. E. Jenkin, S. M. Saunders, and M. J. Pilling, « Photochemical ozone creation potentials for organic compounds in northwest Europe calculated with a master chemical mechanism », *Atmos. Environ.*, vol. 32, n° 14-15, p. 2429–2441, 1998.

[3] Z. Sihaib, F. Puleo, J. M. Garcia-Vargas, L. Retailleau, C. Descorme, L. F. Liotta, J. L. Valverde, S. Gil, and A. Giroir-Fendler, « Manganese oxide-based catalysts for toluene oxidation », *Appl. Catal. B Environ.*, vol. 209, p. 689–700, 2017.

[4] S. C. Kim, « The catalytic oxidation of aromatic hydrocarbons over supported metal oxide », *J. Hazard. Mater.*, vol. 91, n° 1, p. 285–299, 2002.

[5] M. Ibrahim, M. Labaki, J.-M. Giraudon, and J.-F. Lamonier, « Hydroxyapatite, a multifunctional material for air, water and soil pollution control: A review », *J. Hazard. Mater.*, vol. 383, p. 121–139, 2020.

[6] L. Bai, F. Wyrwalski, J.-F. Lamonier, A. Y. Khodakov, E. Monflier, and A. Ponchel, « Effects of β-cyclodextrin introduction to zirconia supported-cobalt oxide catalysts: From molecule-ion associations to complete oxidation of formaldehyde », *Appl. Catal. B Environ.*, vol. 138, p. 381–390, 2013.

Chapter I: Literature Survey

This chapter will begin by giving a brief outline on the structure of hydroxyapatite (Hap), a material which will be employed as a catalyst support in the current work, followed by a literature report on data regarding Hap and its use in environmental remediation applications. Secondly, a discussion revolving around the catalytic use of copper and manganese oxides for the complete oxidation of toluene will be thoroughly conducted, seeing as both these transition metal oxides have been selected for the role of active phases in this study. Thirdly, the need for incorporating a complexing agent, such as β-cyclodextrin, into the synthesis process of Cu-supported catalyst will be firmly established, subsequent to a description of the difficulties faced concerning the maintaining of good Cu dipersion with increasing Cu loading. Finally, the importance of performing an in-depth investigation of Mn speciation in manganese-bearing materials will be clearly pointed out, as will the influence that Mn loading exerts on Mn speciation in the resulting manganese supported solids.

1.1. Hydroxyapatite, a multifunctional material for air, water and soil pollution control

1.1.1. Introduction

Calcium phosphates form a privileged class of biomaterials because of their good biocompatibility, their possibility of biodegradability and their possible bioreactivity. Depending on the Ca/P ratio, several families of calcium orthophosphates can be defined such as pyrophosphate (Ca/P = 1), octacalcium phosphate (Ca/P = 1.33), tricalcium phosphate (Ca/P = 1.5), hydroxyapatite (Ca/P = 1.67) and tetracalcium phosphate (Ca/P = 2).

Calcium phosphates are part of the apatites of the general formula $Me_{10}(XO_4)_6Y_2$ and which crystallize in the hexagonal system (space group: P6 3/m), where:

- (Me) represents a generally divalent cation (Ca^{2+}, Sr^{2+}, Ba^{2+}, Pb^{2+}, ...) which can be replaced by monovalent cations (Na^+, Rb^+, Cs^+, K^+...), trivalent cations (Re^{3+} (rare earths), Al^{3+}, An^{3+} (actinides)...) and tetravalent cations (U^{4+}, Pu^{4+}, Th^{4+}...) ;
- (XO_4) is an anionic tetrahedron often trivalent such as PO_4^{3-}, AsO_4^{3-}, VO_4^{3-} that can be substituted by a tetravalent group (SiO_4^{4-}, GeO_4^{4-}...) or even bivalent (SO_4^{2-}, CO_3^{2-}, HPO_4^{2-} …) ;
- Y is a site occupied by an anion that is often monovalent (F^-, HO^-, Cl^-...) and sometimes bivalent (O^{2-}, CO_3^{2-}...). Vacancies can also be found on the Y site.

The most common natural apatites are calcium phosphates of stoichiometry close to the general formula $Ca_{10}(PO_4)_6Y_2$ where Y = HO^-, F^-, Cl^-, where the fluoroapatite (Y = F^-) is the most thermodynamically stable.

Hydroxyapatite (Hap), whose general formula is $Ca_{10}(PO_4)_6(OH)_2$, is the primary mineral component of bone and teeth and the main factor responsible for their hardness and strength. This bio-inspired material is of great interest in many fields because of its remarkable structure and inherent properties. To cite a few, hydroxyapatite is considered to be very valuable for medical purposes in which it can be used as bone repairing material [1]–[3] or as biocompatible coating for bioimplant materials that suffer from high degradation rate [4], [5]. Moreover, Hap finds many applications in pharmaceutical industries where it is applied as a protein delivery media [6], [7] and drug releasing agent [8]–[10]. Hap is also substantially used in chemical industries where chromatography on hydroxyapatite columns constitutes a powerful technique for separation of proteins and nucleic acids [11], [12]. Additionally, seeing as nowadays more and more efforts are being made towards environmental remediation industry [13], with the focus being shifted towards the development of new and improved ways of eliminating air [14], soil [15], [16] and water [17], [18] pollution, the use of Hap can prove to be highly benefic for the removal of contaminants present in gas, liquid and solid phases.

In fact, employing hydroxyapatite in air, water and soil clean-up will not only constitute a sustainable, safe and clean method for pollutants' removal from contaminated sites, but also make up for a valuable resource recovery route, since Hap can be successfully obtained from biological sources, such as mineral rocks, plants…, and more importantly from waste, among which essentially figure animal bones (fish bones, chicken bone …), as well as biogenic products (eggshells, mussel shells …).

To put it concisely, an insight will be first provided into the structure and defining properties of hydroxyapatite in order to better understand its significant value and vital contribution to the field of environmental management. Following this, an extensive survey of the various applications of Hap in catalysis, whether as a catalyst/photocatalyst or as the active phase support, will allow highlighting the diversified and numerous practical applications of this calcium phosphate complex in catalytic reactions, showcasing its contribution in attaining better catalytic performances.

1.1.2. Hydroxyapatite material

1.1.2.1. Structure

Hap crystallizes in the hexagonal system (P63/m space group) and the approximate lattice parameters are: a = 9.37 Å and c = 6.88 Å. It is important to note that there are two crystallographically different Ca atoms. Hence, the general formula of the Hap can be rewritten as $Ca(I)_4Ca(II)_6(PO_4)_6(OH)_2$. In fact, as can be seen in Figure 1.1, the framework of hydroxyapatite can be described as a compact assemblage of tetrahedral PO_4 groups where each PO_4 tetrahedron is shared by one column, and delimit two types of unconnected channels. The first channel has a diameter of 2.5 Å and is bordered by Ca^{2+} ions (denoted Ca (I)). The second type, which plays an important role in the acid-base and electrical properties of apatite-type solids, has a diameter of around 3.5 Å, is bordered by triangular Ca^{2+} ions (denoted Ca(II)), and hosts the OH groups along the c-axis in order to balance the positive charge of the matrix [19]–[21].

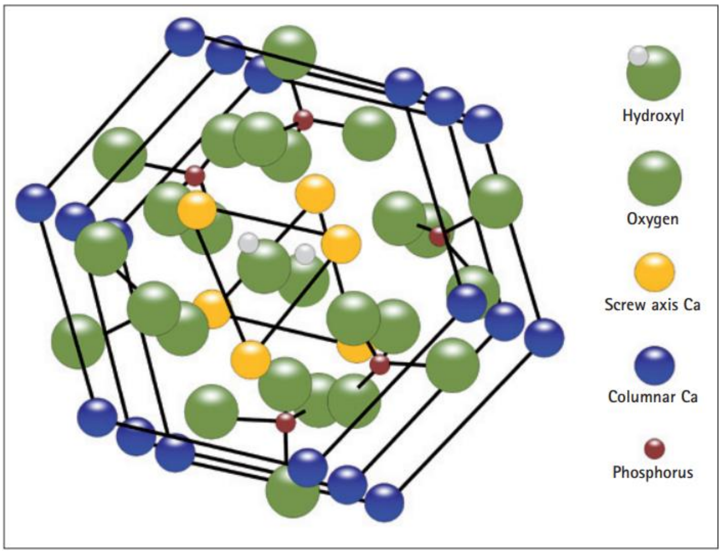

Figure 1.1. Illustration of the structure of hydroxyapatite [22].

The aforementioned Hap allows large variations in compositions, and, as a matter of fact, can be a highly non-stoichiometric solid. Stoichiometric Hap (Hap-S) has the chemical formula $Ca_{10}(PO_4)_6(OH)_2$ where the ratio Ca/P is of 1.67. Calcium deficient Hap (Hap-D) has a Ca/P ratio less than 1.67 and its chemical formula is $Ca_{10-x}(HPO_4)_x(PO_4)_{6-x}(OH)_{2-x}$ with $0 < x < 1$, and finally carbonate-rich hydroxyapatite (Hap-E) with the chemical formula $Ca_{10-x}(PO_4)_{6-x}(CO_3)_x(OH)_{2-x}$, or $Ca_{10-y}Na_y[(PO_4)_{6-y}(CO_3)_y][(OH)_{2-2x}(CO_3)_x]$ in case sodium is present, has a Ca/P ratio higher than 1.67 [23], [24].

Furthermore, Hap is poorly soluble in water and insoluble in alkaline solutions. It is, however, soluble in acids because both PO_4^{3-} and HO^- react with H^+ [25], [26]:

$$\mathrm{Ca_{10}(PO_4)_6(OH)_2} + 14\,\mathrm{H^+} \rightarrow 10\,\mathrm{Ca^{2+}} + 6\,\mathrm{H_2PO_4{}^-} + 2\,\mathrm{H_2O} \qquad (1.1)$$

This apatitic biomaterial has attracted much attention in numerous applications due to its varied useful properties, which we will strive to clearly outline in the upcoming part.

1.1.2.2. Properties

1.1.2.2.1. Adsorption capacities

The adsorption properties of a material are of significance when exploring environmental remediation technologies and the catalytic activity of heterogeneous surfaces. Indeed, on the one hand, the adsorbent material can contribute to the removal of pollutants by retaining them on its surface, and on the other hand, it can facilitate the catalytic process seeing as an adsorption followed by an activation of the reactants on the surface of catalysts constitutes a critical step in catalytic reactions.

It is well-known that hydroxyapatite possesses great adsorption capacities, a property which favored its use in chromatographic columns for the separation of proteins, nucleic acids and viruses [11], [27]–[34].

Indeed, literature reports Hap as having two distinct binding sites, C and P sites, present on its surface. C sites, which consists of calcium ions are positively charged, and preferentially adsorb acid molecules, while P sites which consists of phosphate groups are negatively charged, and preferentially adsorb basic molecules [35], [36].

In addition, hydroxyapatite presents two types of crystal planes, each displaying its characteristic atomic arrangement. In fact, whereas the a(b)-planes expose, primarily, positively charged Ca ions, the c-planes expose negatively charged phosphate and hydroxyl groups. This fact encouraged researchers to examine the possibility of obtaining a selective adsorption behavior, depending on the orientation of prepared Hap material. The work of Zhuang *et al.* [37], demonstrated the validity of this hypothesis, since the study of the adsorption of bovine serum albumin (BSA), an acidic protein, and lysozyme (LSZ), a basic protein, onto synthesized Hap particles with preferred orientation to the c- and a(b)-axes, resulted in a high specificity for the adsorption of BSA and LSZ, on a- and c-oriented hydroxyapatite, respectively.

Moreover, it is really important to realize that based on the properties of the adsorbate, it is possible to improve Hap’s adsorption performances by simply adjusting certain parameters to better fit the required application. For example, a most influential parameter that should be taken into account when synthesizing Hap in the aim of utilizing its adsorption properties, is the molar ratio Ca/P. A variation of this ratio could either enhance or worsen Hap’s adsorption efficiency, depending on the acido-basicity nature of the adsorbate. Since an increase of the molar ratio Ca/P would be beneficial in the case of an acidic molecule's adsorption, yet disadvantageous in the adsorption of a basic compound [7].

1.1.2.2.2. Acid-base adjustability

In the field of heterogeneous catalysis, the acid-base properties of solid catalysts are known to play a key-role in their catalytic performance; the number and strength of the acid/base sites being crucial factors driving the activity and selectivity of many catalytic reactions, not only in acid-base transformations but also in reduction and oxidation reactions.

Hap has the rare property of containing both acid and basic sites in its inherent structure. This property is strongly correlated to the Ca/P atomic ratio in the calcium phosphate compound. Thus, it can be modified accordingly in order to obtain the desired acidic and/or basic function [38], [39].

In fact, the higher the Ca/P ratio is, the lower the acid site density and the higher the basic site density is. Indeed, at Ca/P ratio of 1.50, Hap acts as an acid catalyst. However, when Ca/P = 1.67, hydroxyapatite demonstrates basic behavior; and so, when the Ca/P ratio is between 1.50 and 1.67, Hap develops both acidic and basic attributes. Therefore, deficient Haps are considered to be acid solids, and the nearer we draw to the stoichiometric apatite (predominantly basic) the more basic the solids are. This was verified by various authors through different Hap catalyzed reactions. Studies of the reactivity of ethanol over hydroxyapatite revealed an association between the Ca/P ratio of Hap catalysts and selectivity to certain products [40], [41]. Ethylene was the main product when the Ca/P ratio of the catalysts was low (Ca/P ratio of 1.50), the acid solid catalyzing predominantly the dehydration reaction, whereas the best selectivity for 1,3-butadiene was observed for Ca/P ratio of 1.62, where the apatitic structure displayed a relative balance of acid and basic sites. On the other hand, acetaldehyde, the dehydrogenation product of ethanol, was mainly produced over Hap catalysts with high Ca/P ratios. Other reactions were also examined and exhibited many similarities to the one described previously [38], [39], [42].

In order to better understand the correlation between the Ca/P ratio and the acid-base properties, it is important to note that the acidity of Hap derives from two types of acid sites: Brönsted acid sites and Lewis acid sites, illustrated by Silvester *et al.* [38] in Figure 1.2. HPO_4^{2-} species act as the former while Ca^{2+} or HO^- vacancies result in the latter. This explains why calcium-deficient apatite HapD has a higher number of acid sites. This is due to the contribution from HPO_4^{2-} groups, abundantly present in this type of apatite, or HO^- vacancies. Hence, HapD is more acid and contains more Brönsted acid sites, when compared to stoichiometric and calcium-rich hydroxyapatite [38], [40], [43].

What is more, regarding water decontamination processes which involve, among other things, metal trapping on a suitable adsorbent material, surface properties such as surface acido-basicity of the Hap matrix can play an important role in determining the predominance of a particular metal immobilization mechanism. Hence, it was useful to not only measure the acid-base properties of hydroxyapatite in air [38] but also in water [44], since it would serve to evaluate the characteristics of Hap's surface under real working conditions (decontamination of metal-polluted waters). Surface acid and basic sites of hydroxyapatite solid can be measured in gas phase by Thermo-Programmed Desorption of NH_3 (TPD-NH_3) and of CO_2 (TPD-CO_2), respectively, whereas in liquid phase, they can be assessed by titration with solutions of 2-phenylethylamine (PEA) and benzoic acid (BA), respectively. Interestingly, researchers found that even though stoichiometric Hap is a basic rather than an acidic material, in water it only exhibits acidic property because Hap's basic sites are too weak to provide it with lively basicity [44].

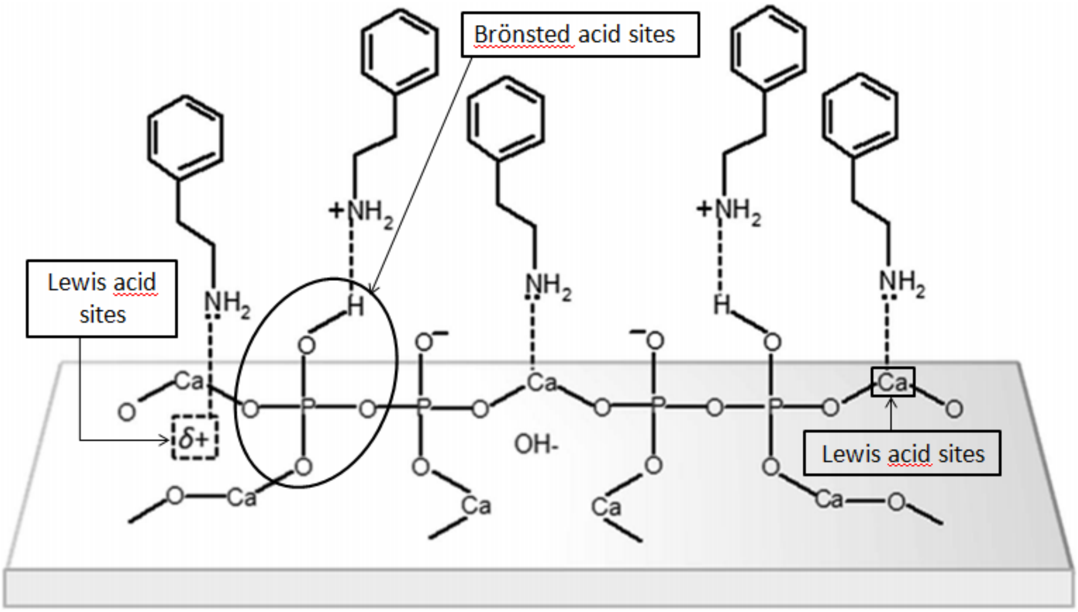

Figure 1.2. Model of 2-phenylethylamine (used as a probe molecule) adsorption over Lewis and Brönsted acid sites on the surface of apatites [(δ+) = HO^- vacancies] [38].

An additional noteworthy point to consider is the possibility of tuning the surface's acido-basicity by cationic and anionic substitutions [38], [39], [45]–[47]. For example, the addition of sodium ions causes a slight increase in the basicity of hydroxyapatite materials [39], whereas acidity is largely enhanced by replacing HO^- by CO_3^{2-} anions [46]. As a matter of fact, this remarkable substitution aptitude will be further discussed below.

1.1.2.2.3. Ion-exchange capability

Ion-exchange is one of the most common and effective treatment methods used in pollution control. Through the removal of hazardous ionic impurities and the recovery of toxic and valuable metals from hostile surroundings (nuclear waste), ion-exchange materials play an increasing role in waste minimization and management.

This is why it is important to mention that the apatite lattice is very flexible. Thus, it is very tolerant of substitutions and allows the presence of defects and vacancies. The substitution can occur in either the cationic or the anionic sites. When it comes to the first one, calcium ions can be replaced by different metal ions such as transition metals [48]–[52] (Cu^{2+}, Mn^{2+}, Ni^{2+}, Zn^{2+}, Cd^{2+}, Co^{2+}…), alkaline earth metals [50], [53] (Mg^{2+}, Sr^{2+}, Ba^{2+}…) and many other cations [50], [54] (Pb^{2+}, Al^{3+}, La^{3+}…).

However, the determination of the occupation site remains delicate. Indeed, as explained above, there are two types of nonequivalent sites when it comes to calcium ions denoted Ca(I) and Ca(II). Discerning an ion's preferential position requires better understanding of the parameters that govern a cation's affinity to a specific site. According to Zhu *et al*. [50], the preferential occupancy of metal ions can be explained mainly by ionic radius and electronegativity of the metal ions, Ca(II) sites being preferentially occupied by cations with bigger ionic radius or electronegativity than Ca^{2+}. Hence, these authors were able to illustrate the reason for all of Cd^{2+} (similar ionic radius but bigger electronegativity), Sr^{2+} (similar electronegativity but bigger ionic radius) and Pb^{2+} ions (bigger ionic radius and electronegativity) preferential occupancy of the Ca(II) sites in the apatite structure. These findings were also verified by other researchers [51], [55], [56] who confirmed larger ions' stronger preference towards Ca(II) site and smaller ones towards the Ca(I) site and corroborated electronegativity's impact on the distribution of the cations between the two positions.

Moreover, it is important to discuss the factors that influence the facility of the exchange process. Following the results obtained from their work, Wakamura *et al.* [52] were able to establish that the ion-exchange with Ca^{2+} seems to depend more on the cations' charge density than on its ionic radius, an ion with larger charge density displacing more easily calcium ions than an ion of a similar ionic size.

As for anionic substitutions, they involve either HO^- or PO_4^{3-} ions or both. HO^- can be replaced by F^- [57]–[61], Cl^- [60]–[62], Br^- [61], [63], O^{2-} [64] or CO_3^{2-} [65], [66] and PO_4^{3-} by HPO_4^{2-} [67], AsO_4^{3-} [68], [69], VO_4^{3-} [70], [71], SO_4^{2-} [57], SiO_4^{4-} [72] or CO_3^{2-} [57], [65], [66]. In the case of carboapatites, the replacement with carbonate ions can occur at two different sites as can be seen in the following formula $Ca_{10-x/2}[(PO_4)_{6-x}(CO_3)_x][(OH)_{2-2y}(CO_3)_y]$. The substitution of hydroxyl and phosphate ions by carbonate, leads to A and B type carbonated hydroxyapatite respectively [73], [74]. Some studies went even further and identified three structural locations for the carbonate ions by differentiating between two types of channel positions: type A1 (apatite channel, oriented with two oxygen atoms close to the c-axis) and type A2 (stuffed channel position) [75]. It was also shown that the location site of CO_3^{2-} is strongly dependent on the synthesis method used to prepare carboapatites. In fact, type A apatite can be obtained by synthesizing the material at high temperature (∼900 °C) or by heating the hydroxyapatite in a CO_2 atmosphere at temperatures of 900–1000 °C for 15–144 h, or also, by soaking stoichiometric Hap in an aqueous solution saturated in carbon dioxide for up to 2 months. Conversely, B type carbonated hydroxyapatite results from low temperatures (∼400 °C) synthesis by precipitation at elevated pH [46], [76].

In short, Hap's ion exchange capacity has been widely explored in numerous works, in order to incorporate certain entities into the apatite structure [48], [54], [55], [77]–[84]. These added substances can alter the physicochemical properties of the material and its effectiveness, thus, inducing the enhancement of Hap's catalytic activity and performance all while maintaining its overall structure.

1.1.2.2.4. Thermal stability

Thermal stability is one of the determining factors of a catalyst lifetime, seeing as thermal sintering is a major cause of irreversible catalyst deactivation. Therefore, when choosing a material to be utilized in environmental remediation processes, its thermal stability is regarded as an important consideration.

Hence, it comes as a significant value that another primary characteristic of hydroxyapatite is its good thermal and chemical stability. In fact, it is one of the major reasons that make it an attractive material choice and an excellent candidate for biomedical applications [85]–[89]. Hap maintains its stability at a wide pH and temperature range. However, it is known to start to decompose into other phases such as tricalcium phosphate (TCP; $Ca_3(PO_4)_2$) at temperatures higher than 800 °C [90]–[93]:

$$\mathrm{Ca_{10}(PO_4)_6(OH)_2 \rightarrow 3\ \beta\text{-}Ca_3(PO_4)_2 + CaO + H_2O} \quad (1.2)$$

Nevertheless, there are certain factors influencing Hap's stability and upon which the latter is intrinsically dependent. Indeed, among these factors figure the apatite's stoichiometry as well as the synthesis conditions. It has actually been reported that stoichiometry plays a key role in apatite's stability, non-stoichiometric hydroxyapatites (Ca/P ratios different from 1.67) being less thermally stable than stoichiometric ones. In fact, research has shown that Hap with Ca/P = 1.68 can reach temperatures up to 1450 °C without decomposing over a period of 3 h, consequently making stoichiometry a most looked-for criteria owing to the stability it provides at high temperatures [94]–[96]. Furthermore, Fang *et al.* [97] found an optimum thermal stability (up to 1370 °C) for Hap samples prepared by hydrothermal method, whereas Hap synthesized by hydrolysis of brushite started to decompose at about 700 °C. In a different study, calcium phosphates which were synthesized by a modified wet chemical precipitation route where calcium hydroxide was homogenized with planetary mill resulted in a highly thermally stable (up to 1300 °C) hydroxyapatite, hence, demonstrating the effect of synthesis parameters on the apatite's stability [98].

Moreover, the incorporation of ions into the hydroxyapatite structure can also affect the crystal lattice properties, therefore enhancing or diminishing Hap's thermal and chemical stability. For example, the introduction of fluoride ions into the apatite lattice ($Ca_{10}(PO_4)_6(OH)_{2-2x}F_{2x}$) with varying amounts ($x = 0, 0.2, 0.4$, and 1.0, in HA, HA02F, HA04F and FA, respectively) improves the thermal and chemical stability when $x > 0.4$ by hindering the decomposition process, as evidenced by Figure 1.3, and by ameliorating Hap's corrosion resistance [99]–[110]. Other substitutions can, on the contrary, reduce the material's stability by increasing its solubility such as strontium, magnesium, manganese, and carbonate substitutions [111]–[113].

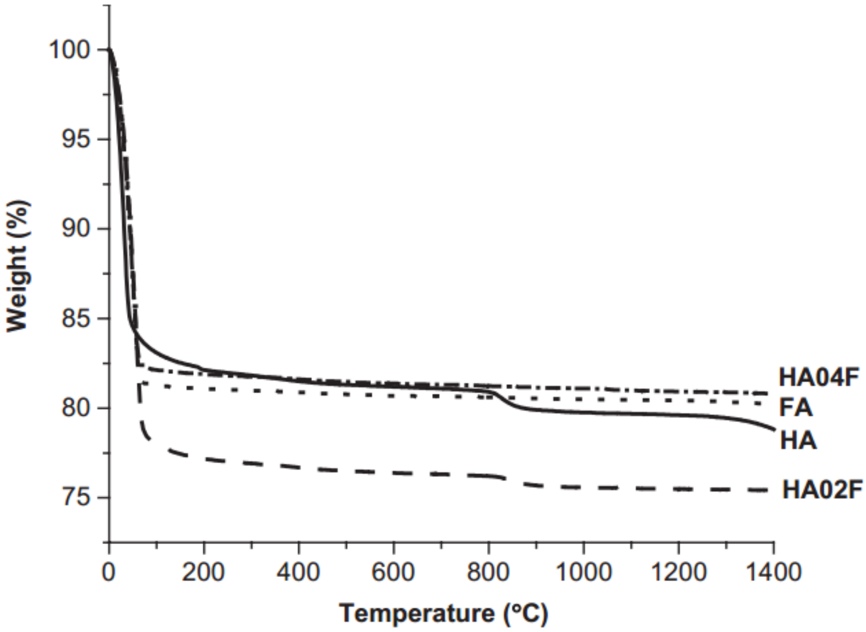

Figure 1.3. TGA (thermogravimetric analysis) data of HA (hydroxyapatite), FHA (fluorine-substituted hydroxyapatite: HA04F and HA02F) and FA (fluoroapatite) powders heated to 1400 °C in dry air [104].

1.1.2.3. Factors that make Hap an environment-friendly material

Hydroxyapatite is considered to be an environment-friendly material for many reasons, among which figure its non-toxicity and biocompatibility. This latter, combined with its excellent osteoconductive property, have led to Hap playing a vital role in clinical applications such as drug delivery [114], bone tissue regeneration [115], as well as various other fields which help in reducing the environmental pollution.

Besides its intrinsic properties and environmental applications, another aspect makes this calcium phosphate compound particularly attractive from an environmental point of view. It is actually its capacity to be derived from natural sources, and more precisely from waste. Indeed, Hap has been successfully obtained from animal waste such as fish bones [116]–[118], chicken bone [119], fish scales [117], [120]–[123], eggshells [124]–[126], and mussel shells [127], all of which were found to constitute important bioresources for hydroxyapatite production. Nonetheless, it is important to mention that hydroxyapatite derived from natural sources differ from synthetic Hap in terms of lower purity, higher degree of substitution and deficiency, lower specific surface area value (4.49 $m^2.g^{-1}$ for natural phosphates [128] while that of synthetic Hap can attain 100 $m^2.g^{-1}$ and more) and consequently, poorer sorption capacities [128]–[135]. Indeed, bio-sources of Hap contain small amounts of inorganic compounds other than Hap, such as $Ca_4O(PO_4)_2$, $NaCaPO_4$, $Ca_3(PO_4)_2$, CaO, and MgO. In addition, through Hap's substitution ability, natural apatite contains some fluoride or chloride in place of hydroxide and some metal ions (aluminum, iron, copper, zinc…) in place of Ca^{2+}. Finally, organic matters are also present within natural apatitic materials. All of these alterations in the compound's purity and therefore in the obtained Ca/P value [128], [132], can have a direct influence on the efficiency of hydroxyapatite used in environmental remediation applications. This is why, a pre-treatment of naturally derived Hap is usually conducted before its use, in order to eliminate remaining organic matter and attain a pure hydroxyapatite phase, which would result in a Hap material with comparable properties and efficiency as synthetic hydroxyapatite.

What is important to understand is that this generation of Hap from waste does not only offer economic benefits since it relies on the use of cheap, natural, and undesirable materials, but also, contributes in achieving a sustainable development by being an active part in the global waste management process. In other words, solids which would have accumulated, creating thus a pollution source, endangering human, animal, and vegetation's health, are in this way being utilized for the production of very sought-out product.

All of the above cited factors lead to hydroxyapatite being branded an environment-friendly material, making it very suitable for different environmentally related applications. In fact, hydroxyapatite has found numerous applications as adsorbent for wastewater and soil treatment. It was shown to not only be highly efficient in metal [44], [136]–[157], inorganic [158]–[164] and organic compounds' [165]–[169] removal, but to be also superior to other conventional adsorbents such as activated carbon [170], [171], zeolite [167], silica [162], [167] and others [146], [162], [167] due to Hap's formerly indicated remarkable properties. However, as mentioned before, the present report will be solely focused around the use of Hap in the field of catalysis in the aim of environmental remediation.

1.1.3. Hap in catalytic reactions

1.1.3.1. As a catalyst and photocatalyst

Volatile organic compounds (VOC), emitted from a variety of sources including industrial processes and transportation activities, constitute a well-known class of air pollutants. One of the most effective, inexpensive and environmentally compatible solutions for the removal of these pollutants is their total oxidation in the presence of a catalyst. The advantages of catalytic oxidation on thermal oxidation are the reduction of energy consumption since the catalyst lowers the oxidation temperature, and the promotion of efficiency since it directs the selectivity towards the desired products (CO_2 and H_2O).

Among said VOC, formaldehyde (HCHO), which is a short-chain oxygenated compound, is recognized as being a carcinogenic VOC and thus a major hazard to human health. Although HCHO catalytic oxidation is usually carried out over precious metal catalysts such as platinum or palladium, recent studies have shown that hydroxyapatite is not just catalytically active in the combustion of formaldehyde but that it also exhibits an excellent performance at room temperature, which makes this non-precious metal catalyst an ideal candidate for HCHO removal [172], [173]. Furthermore, when the activity of hydroxyapatite was compared with that of a supported precious metal catalyst, Pd (3 wt%) / γ-Al_2O_3, results revealed that at room temperature the conversion of formaldehyde was ca. 45% for Hap, only slightly lower than for the Pd catalyst (ca. 57%). However, while formaldehyde conversion over Hap remained stable at 45% for the first 2 h of reaction at room temperature before dropping to 28% after running for 10 h, the catalytic activity of Pd-based catalyst decreased rapidly from 57% to 33%. Finally but most importantly, Hap displayed higher mass-specific and turnover rate values than Pd (3 wt%) / γ-Al_2O_3; all of which goes to demonstrate hydroxyapatite's good catalytic performances (good activity and stability) when it comes to HCHO combustion under ambient conditions [172]. It should be noted that Hap's catalytic activity was attributed to the hydroxyl groups bonded with the channel Ca^{2+}. Indeed, these groups would play an important role in activating/oxidizing the formaldehyde compound, assisting thus the catalytic process.

Hap was, in addition, tested as a possible catalyst for the oxidation of other VOC, namely gaseous toluene, ethyl acetate and iso-propanol [24], and was found equally active in the oxidative decomposition of these volatile organic compounds at 400–500 °C. In fact, in this case, the oxidation of the studied organic compounds was instigated by the activation of oxygen due to the electron trapped on vacancy in Hap, this electron being generated by thermal excitation.

On another note, chlorinated organic compounds, whose treatment is vital in order to prevent their harmful effects on the environment and health, have also found a viable catalyst option in hydroxyapatite. In fact, calcium deficient Hap manifested a good performance in the oxidative decomposition of trichloroethylene vapor at 400–500 °C and was able to capture as well the Cl species since only a small amount of HCl was found in the effluent gas [174], [175]. It was supposed that Cl^- would replace HO^- in hydroxyapatite, producing thus chloroapatite. The same was shown to be true in the study conducted by Nishikawa *et al.* [176], where chlorobenzene was oxidatively decomposed at 400–500 °C, over calcium deficient Hap (DAp), with the major part of Cl being seized by the calcium phosphate catalyst according to the data reported in Table 1.1.

Just as Hap was proven to be a performant catalyst in the previously mentioned fields, it was also revealed to display good photocatalytic activity whether combined with other photocatalytic materials [177]–[194], or undoped [195]–[200]. Indeed, it was explained that under UV irradiation the electronic state of the surface phosphate group will be altered and produce a vacancy on hydroxyapatite, and then an electron transfer occurs from the vacancy formed in apatitic structure to atmospheric oxygen present on Hap resulting in the formation of $O_2^{\cdot -}$ radicals, which will oxidize the pollutant compounds [201], [202]. Thus, the addition of Hap improved the photocatalytic performance of commonly known photocatalysts such as TiO_2 [177]–[180]. In fact, TiO_2/Hap composite proved to be highly efficient in the photodegradation of dyes [177]–[180] and organic pollutants such as pentachlorophenol [187] and formaldehyde [188]. Moreover, TiO_2/Hap composite was shown to be highly active in photocatalytic nitric oxides (NOx) removal [190]–[192] where it demonstrated a superior photocatalytic activity compared to pure TiO_2 component. This improved behavior, acquired by hydroxyapatite incorporation, was credited to an enhanced chemisorption of NO due to a greater amount of surface OH groups, as well as to higher separation efficiency and faster transfer of the photo-generated electron-holes pairs. Furthermore, it should be noted, that a study examining undoped hydroxyapatite has demonstrated that the latter manifested a better performance in the photocalatytic degradation of the 17α-methyltestosterone hormone than TiO_2 and nickel or copper-doped Hap [198].

Up until this moment, we have reported the use of Hap in catalysis as a catalyst and photocatalyst, and demonstrated its added value in each of these departments. However, one important aspect of the catalytic applications of Hap remains to be seen, which is none other than the use of hydroxyapatite as a support for an active phase in various environmentally oriented catalytic reactions.

Table 1.1. Cl^- amounts in fresh and reacted DAp[a] [176].

	Cl^-/DAp ($mg.g^{-1}$)		A/B[c]
	(A) Found	(B) Calcd[b]	%
Fresh	None	-	-
Reacted	1.6	1.86	86

[a] Reaction conditions: chlorobenzene = 40.1 ppm (v/v); DAp = 1 g; reaction temperature = 450 °C. [b] Theoretical amounts when the DAp was completely chlorinated with chlorobenzene reacted. [c] Cl^- amount in DAp to Cl amount in decomposed chlorobenzene.

1.1.3.2. As a support for an active phase

Due to its textural and structural characteristics, hydroxyapatite is of considerable interest as catalyst's support in numerous oxidation processes. In fact, in alkane oxidation reactions such as methane combustion, Hap's tunable acidic and basic properties were found to be of particular consequence on the catalytic activity. Previous studies had shown, that catalysts' basic sites could be held responsible for the activation of methane. This, therefore, explains the choice of hydroxyapatite as metal carrier in several works [81], [203]–[205]. A study conducted by Boukha *et al.* [205], using Pd loaded Hap, led to results with similar performance in methane's oxidation to that of conventional Pd/Al_2O_3 catalysts, thus, proving the apatite material's efficiency as a carrier in this reaction. In addition to hydroxyapatite's modulable acid/base properties, its relatively high surface area came into play in the oxidation of 1,2-dichloroethane, catalyzed by cobalt supported on Hap [206]. Tests showed that the good dispersion of cobalt active species, led to a significant improvement in the catalytic activity, when compared to bulk Co_3O_4 catalyst.

As for aromatics and aldehydes' combustion, in a work conducted by Wang *et al.* [207], hydroxyapatite was reported to enhance the thermal stability of gold against sintering. A detailed examination showed that apatite's phosphate groups were the source of gold nanoparticles stabilization at lower temperature (≤400 °C), while hydroxyl group were at the origin of higher temperature stability (≤600 °C). To better point out Hap's stabilizing effect, a comparison was made between Au/CeO_2/Hap and Au/CeO_2 catalysts, both calcined at 600 °C, in formaldehyde oxidation reaction. Results indicated a high HCHO conversion for the Au/CeO_2/Hap material (98% conversion) in opposition to Au/CeO_2 that only gave 5% HCHO conversion because of its poor stability in regard to sintering. Furthermore, toluene's total oxidation, assessed over various metals supported on hydroxyapatite, led to the conclusion of oxidation activity being related to the high dispersion of active species as well as the carrier's acid characteristics. In fact, the support's acidic centers heighten the prospect of an electrophilic attack of adsorbed oxygen, hence, the oxidation of toluene molecules; the electrons trapped in Hap's vacancies are considered as accountable for oxygen activation. Indeed, palladium loaded on hydroxyapatite were more performant than Pd supported on classical alumina in total toluene combustion. The specific rates on apatites supports were four to six times higher even though the palladium content was lower on Hap (0.25 wt% of Pd on Hap vs 0.4 wt% of Pd on Al_2O_3)

[23]. This was also true when the active phase used was manganese. The toluene conversion increased when passing from Mn supported on alumina (Mn-Al) to the one supported on hydroxyapatite (MnNit-Hap and MnAc-Hap), and that no matter the nature of the precursor used (manganese nitrate: MnNit or manganese acetate: MnAc) to incorporate manganese active species on Hap (Figure 1.4) [208]. Besides, a paper examining the total oxidation of toluene over Cu supported on Hap materials [209] revealed good catalytic activity for very low Cu loadings (2.5 wt%), which was correlated with the presence of acid sites with a moderate strength, provided by none other than the hydroxyapatite support, as well as finely dispersed CuO species on the Hap. Hydroxyapatite's acidic properties were also found to be responsible for methanol's activation in a study conducted by Aellach *et al.* [210] over calcium-deficient and stoichiometric hydroxyapatites promoted by cobalt, for the catalytic oxidation of methanol. Indeed, the authors found that while the redox properties of Co_3O_4 entities formed on the catalyst's surface were mainly responsible for the catalytic activity of the supported material, an enhancement in the catalytic performances could be noted when replacing a stoichiometric Hap support with a calcium-deficient one. The specific role of this Ca-deficient support in that particular case was explained by the presence of surface acid sites in the form of HPO_4^{2-} species and surface cationic vacancies, believed as accountable for methanol activation at low temperature, resulting thus in improved catalytic activity. Moreover, Hap's ion-exchange capacity, as well as its great recyclability permitted for a synthesized Cu doped Hap catalyst to be reused in the oxidation of formaldehyde without significant loss in its catalytic activity [211].

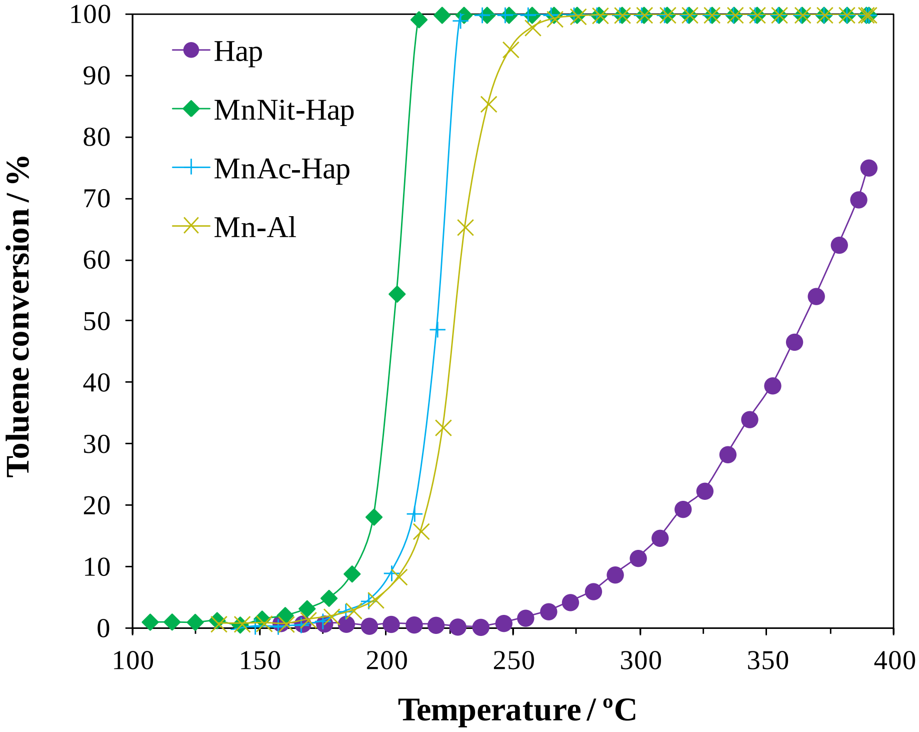

Figure 1.4. Toluene conversion over the catalysts (GHSV = 30,000 mL.h^{-1}.g^{-1}; 800 ppmv toluene in air) [208].

Studies for the applicability of hydroxyapatite supported gold in CO elimination processes, were conducted by several researchers [212]–[219]. The aim was to find a support whose properties would amplify the reactivity of nanosized gold. As already mentioned above, Hap succeeded in enhancing the stability of Au nanoparticles creating a highly durable catalyst. This renders the apatitic material an ideal alternative to metal oxide supports such as $CuMn_2O_3$ and TiO_2, hindered by a rapid deactivation caused by Au crystals' growth; these carriers becoming thus, unsuitable for long term use [215]. What is more, Domínguez *et al.* [214] revealed Hap's implication in the enhancement of the catalytic activity, in the oxidation of CO at room temperature. Apparently, structural vacancies in the apatite structure can activate oxygen to produce peroxide species which are behind CO's room temperature oxidation.

Besides Hap's use as a support for catalysts applied in the oxidation of toxic pollutants, it was also employed as carrier material for catalysts examined in the reduction of NOx [48], [78], [220]–[225], where owing to its ability to highly disperse active species [48], [78], [220] and good basic properties [221]–[223], hydroxyapatite proved to be more conductive than a series of traditional supports (Al_2O_3, TiO_2, SiO_2, ZrO_2, TiO_2–ZrO_2 and Ga_2O_3) for achieving high DeNOx activity.

Moreover, Hap aroused considerable interest in view of its potential use as host material for compounds employed in hydrogen production, derived either from hydrides' hydrolysis [226]–[232] or methane conversion [233]–[237]. Indeed this support's flexibility via its high ion-exchange ability resulted in catalysts being more efficient when supported on Hap solid than on other materials.

Finally, the suitability of Hap as support for desulfurization processes was also confirmed through several works [80], [238]–[240]. These researches showed that in the case of apatite supported NiMo catalysts, the presence of superficial HPO_4^{2-} groups and related surface defects, which by acting as grafting sites of Ni-Mo oxides facilitate the dispersion of these active species, were at the origin of this material's higher activity when compared to industrial alumina supported NiMo catalyst, despite having lower specific surface area.

All of the aforementioned appraisal of Hap's role in environmental remediation culminates in one single fact: hydroxyapatite is a perfectly suitable, and highly promising bio-inspired material for various environmental applications. The unique features of this material accord it with exceptional carrier traits resulting in the enhancement of catalytic performances. Therefore, in the particular case of toluene total oxidation, which is the target reaction of the current work, Hap will be used as host to selected active species. The reasons that inspired the choice of these active species will be the focus of the upcoming section.

1.2. Choice of Cu-Mn as active phase

1.2.1. Mn-based catalysts for toluene total oxidation

As is commonly known, the choice of catalyst is crucial in catalytic oxidation technology. Indeed, to attain high efficiency for toluene elimination and high selectivity towards target products (CO_2 and H_2O), the development of economical and efficient catalysts is required. While noble metals-based catalysts have been shown to exhibit great catalytic activity in toluene total oxidation [23], [241]–[243], their high price and low-resistance to poisons [244]–[246] limits their applicability. Alternatively, transition metal oxides appear as more attractive substitutes due to their low cost and high resistance to poisons, despite being slightly less active than noble metals in most cases.

Among the transition metal oxides, manganese oxides have attracted much attention in recent years due to their excellent performances in the removal of VOC. A study conducted by Lahousse *et al.* [247] has shown that γ-MnO_2 manifests even better catalytic activity than supported noble metal solid, Pt/TiO_2, for the removal of various VOC. Regarding, the total oxidation of toluene, both bulk [248]–[261] and supported Mn oxides [208], [262]–[274] have proven to be highly efficient catalysts, owing to a combination of factors, namely their strong oxygen storage/release ability and excellent redox properties. In fact, MnO_x-based materials revealed enhanced catalytic performances compared to other transition metal oxide-based solids, in the removal of toluene. For instance, in the case of bulk MnO_x catalysts, manganese oxide demonstrated higher catalytic activity than both iron oxide [251] and cerium oxide [258] in the total oxidation of toluene; even more interestingly, the work of Sihaib *et al.* [255] showed manganese oxide to be more active than commercial Pd/Al_2O_3 catalyst in low temperature range (< 225 °C) because of its very high reducibility. Furthermore, in terms of supported Mn oxide solids, several studies performed over metal oxides supported on clinoptilolite-type zeolite [269], [270] indicated that among the various clinoptilolite-supported transition metal oxides (MnO_2, Co_3O_4, Fe_2O_3, CuO) which were tested in the catalytic incineration of toluene, it was the one bearing manganese oxide that turned out to be the most active and durable. The authors attributed the improved catalytic performance to a higher acidity of the surface of the Mn-based compound compared to the other tested catalysts; the acid property being in other words enhanced by MnO_2 incorporation. In addition, an investigation of toluene oxidation at room temperature over HZSM-5-supported Mn and Ag materials [271], revealed greater catalytic activity in the case of Mn/HZSM-5. This was explained as being due to a higher ratio of oxygen vacancies over lattice oxygen (O_V/O_l, determined by X-ray photoelectron spectroscopy (XPS) analysis) on Mn/HZSM-5 catalyst compared to Ag/HZSM-5, leading to an improvement in the mobility of lattice oxygen as well as the generation of reactive oxygen species, which ultimately resulted in enhanced activity in toluene oxidation process.

On another note, it has been demonstrated that for supported manganese oxide catalysts, the nature of the used support produces a significant effect on the catalytic activity of the resulting material in toluene total oxidation. Indeed, previous works examining the influence of the support on the catalytic behavior of Mn supported catalysts [264], [273], [274] have shown that among several materials including Al_2O_3, SiO_2, TiO_2, ZrO_2, and MCM-41, the use of alumina as carrier is more beneficial for the obtained catalytic performances. Jung *et al.* [274] ascribed this to the fact that Mn supported on alumina exhibits higher O_V/O_l ratio than when supported on other type of materials.

However, a recent study conducted by Chlala *et al.* [208] has shown that manganese oxide supported on hydroxyapatite has proven to be even more efficient than alumina supported MnO_x solid. This finding was rationalized as being the result of a difference in the nature of the active phase, induced by a change of the support. In fact, as has been reported in the previous section on hydroxyapatite material, one of the remarkable characteristics of Hap is its ion-exchange ability. Hence, in this particular case, a diffusion of manganese into the support, mainly as Mn^{2+} (by substitution of Ca^{2+} cations) leads to surface enrichment in calcium ions which promotes the formation of well-dispersed Mn species, resulting thus in an enhanced toluene oxidation performance.

Therefore, the choice of an Mn-based material on the one hand, and of a hydroxyapatite support on the other, appear to constitute a fitting combination in the project of developing an efficient catalyst for toluene total oxidation.

1.2.2. Cu-based catalysts for toluene total oxidation

Besides manganese oxide, another transition metal oxide was found to be high-performing in the complete oxidation of toluene. It is none other than CuO. Indeed, the work of Wang *et al.* [275], [276] revealed that when a screening for the optimal catalyst was conducted among different metal species (Cu, Fe, Mn, Cr, Co, Mo, Ni) supported on γ-Al_2O_3 materials, examined in the catalytic incineration of toluene, CuO/γ-Al_2O_3 was found to be the most active of seven catalysts tested. The authors attributed the higher activity of CuO/γ-Al_2O_3 to an enhanced adsorption capacity of toluene and O_2, resulting thus in an increase of toluene conversion efficiency. In another study conducted by Kim [277], investigating the catalytic activity of metals (Cu, Mn, Fe, V, Mo, Co, Ni, Zn)/γ-Al_2O_3 in the complete oxidation of toluene, the superior activity of Cu loaded on γ- Al_2O_3 was once again demonstrated, when compared to that of the other materials probed. In fact, the activity of alumina supported metal oxide compounds, with respect to the metal used, was observed to follow the sequence: Cu > Mn > Fe > V > Mo > Co > Ni > Zn. Saqer *et al.* [278] who also explored the effect of the nature of metal oxide employed in Al_2O_3-supported M_xO_y catalysts (M_xO_y = CuO, MnO, V_2O_5, Cr_2O_3, CeO_2, MgO, Nd_2O_3, CsO, ZrO_2) on toluene conversion efficiency remarked that CuO/Al_2O_3 was by far the most active catalyst in the tested M_xO_y/Al_2O_3 series. The authors stated that the activity of this set of catalysts was essentially determined by the redox properties of M_xO_y species, meaning that CuO being the most reducible among the metal oxides assessed is what led to CuO/Al_2O_3 being the most active material in the series. Other works on silica [279] and titania [280] -supported copper oxide evidenced yet again the benefits gained in terms of catalytic activity by choosing Cu over other metals, which was ascribed as being due to the formation of well-dispersed copper species on the surface of the support.

Similarly to Mn-based materials where the nature of the support has great consequence on the performance of the resulting catalyst, the choice of carrier compound exerts a great influence on the catalytic efficiency in the case of supported copper oxide solids as well. Indeed, in an investigation carried out by Wang *et al.* [276] over Cu supported catalysts applied for the complete combustion of toluene, four different supports (CeO_2, γ-Al_2O_3, TiO_2, and V_2O_5) were examined in order to define the optimal combination. Results revealed CuO/CeO_2 to be the most active among the tested materials followed by CuO/γ-Al_2O_3. The better performance of CuO/CeO_2 and CuO/γ-Al_2O_3 catalysts was attributed to better dispersion of the active species and enhanced adsorption of reactants (O_2 and toluene). The importance of obtaining well-dispersed Cu^{II} entities on the carrier's surface was further confirmed by the observations made by Kim [277] which indicated that the catalytic activity of copper-based solids supported on different materials (γ-Al_2O_3, TiO_2, SiO_2) follows the same sequence as that of copper dispersion degree on those carrier materials; both going thusly: γ-Al_2O_3 > TiO_2 > SiO_2. The variance of Cu dispersion with respect to supports was credited to strong metal-support interaction (SMSI), which when enhanced, depending on the nature of the support, causes a decrease in copper particle size and hence an increase in copper dispersion. A comparison between the catalytic performances towards toluene total oxidation of Cu dispersed on FAU Zeolite and ZrO_2 supports, showed that copper had a better affinity for zirconia which was correlated with the oxygen mobility property of the carrier leading to easily reducible CuO particles [281]. Moreover, when the oxygen mobility characteristic was further improved by adding yttrium to ZrO_2 support, the efficiency of the Cu-bearing material became even greater than before.

Many more examples showcasing the impact of the support on the behavior of Cu-supported catalysts have been given in literature. As a way of summarizing the data previously recorded regarding this subject, an overview of the catalytic properties (T_{50}) of the various Cu-based materials (various metal loadings and supports) obtained in the total oxidation of toluene (various concentrations) are reported in Table 1.2. This extensive survey calls attention to the great catalytic activity exhibited by Cu dispersed on Hap, examined in the study conducted by Chlala *et al.* [209], in which the good catalytic performance was attributed not only to the presence of well dispersed CuO species but also to the contribution of Hap in toluene activation, by means of its weak acid properties. This makes the use of hydroxyapatite-supported copper catalyst seem as an attractive solution for the removal of toluene molecules.

Table 1.2. Literature reported data on Cu-based catalysts examined in toluene total oxidation.

Catalyst	Cu loading (wt%)	Toluene (ppm)	VHSV [a] ($m^3.kg^{-1}.h^{-1}$) [GHSV [b] (h^{-1})]	T_{50} [c] (°C)	Reference
Cu/Hap	2.5	800	30 [15000]	215	[209]
$Cu/\gamma\text{-}Al_2O_3$	5	900	6	275	[277]
$Cu/\gamma\text{-}Al_2O_3$	5	4000	[4500]	277	[276]
$Cu/\gamma\text{-}Al_2O_3$	15	1000	200	305	[282]
$CuO/\gamma\text{-}Al_2O_3$	10	930	[40000]	≈ 330	[283]
$CuO/\gamma\text{-}Al_2O_3$-Cord	10	930	[40000]	≈ 337	[283]
CuO/Cord	10	930	[40000]	≈ 340	[283]
Cu/SiO_2	5	900	6	≈ 325	[277]
CuO/SiO_2	10	880	[1.2]	≈ 317	[279]
CuO/SBA-15	10	880	[1.2]	≈ 325	[279]
Cu/SBA-16	9	880	[1.2]	≈ 337	[284]
Cu/TiO_2	20	300	36	182	[285]
Cu/TiO_2	5	4000	[4500]	≈ 327	[276]
Cu/TiO_2	5	900	6	≈ 283	[277]
Cu/NaFAU	5	1000	60	≈ 253	[281]
Cu/ZrO_2	5	1000	60	≈ 245	[281]
$CuO/Ce_{0.8}Zr_{0.2}O_2$	8	4400	[33000]	207	[286]
Cu/CeO_2	5	4000	[4500]	≈ 207	[276]
Cu/V_2O_5	5	4000	[4500]	≈ 352	[276]
CuO/HCLT	9.5	1000	[15000]	330	[269]

[a] Volume hourly space velocity. [b] Gas hourly space velocity. [c] Temperature for a 50% conversion of toluene.

1.2.3. Binary Cu-Mn based catalysts for toluene total oxidation

Based on the two previous sections (1.2.1 and 1.2.2) emphasizing the advantages of both Cu and Mn-based catalysts, the use of a binary copper-manganese oxide looks to be a promising strategy for further improving the performance of the materials employed in the total oxidation of toluene. In fact, it has already been reported in literature that bulk [287]–[292] and supported [282], [288], [293]–[295] Cu-Mn binary oxides can be considered as efficient catalysts in toluene oxidation, for which they exhibit higher catalytic activity than the single metal counterparts.

The good performances of Cu-Mn oxides in toluene oxidation have been said to be due to segregated $CuO/\gamma\text{-}Mn_2O_3$, the presence of Cu allowing an enhanced catalytic activity of the manganese oxide for which active sites may be derived from the presence of Mn^{3+} in the near surface of the catalyst [292]. Other teams ascribed the enhanced catalytic activity to the formation of a mixed copper manganese oxide spinel phase allowing easier electron transfer between copper and manganese cations [288], [293]–[295]. Behar *et al.* [288] reported on bulk $Cu_{1.5}Mn_{1.5}O_4$ particles (10 nm) prepared from ionotropic alginate gel able to completely oxidize toluene at ≈ 240 °C.

Cu-Mn binary oxides supported on conventional supports such as alumina [282], [295], [296], titania [288], and silica [294], have been studied so far.

In the case of alumina supported Cu-Mn oxides, Saqer *et al.* [282] attributed the enhanced catalytic activity to the better dispersion of segregated M_xO_y (M = Cu, Mn) species, their increased reducibility (reactivity of surface oxygen), and their lower tendency to form coke deposits under reaction conditions. Li *et al.* [295] reported the best activity for a Cu/Mn atomic ratio of 1 on catalysts pretreated with H_2 in line with the formation of the spinel phase $Cu_{1.5}Mn_{1.5}O_4$. However, it was found that the presence of water vapor had a negative effect on catalytic activity. Wang *et al.* [296] associated improved catalytic activity with the presence of highly dispersed Cu-O-Mn clusters in which part of the Cu^{2+} occupies the tetrahedral vacancies (TV) of alumina support, this strong interaction between Cu and Mn results in better redox properties. Considering titania, the Cu-Mn oxide supported on TiO_2 obtained by incipient wetness impregnation shows an overall activity lower than for the unsupported $Cu_{1.5}Mn_{1.5}O_4$ [288].

Considering the silica based support, it was found that MCM-41-supported Cu-Mn oxide showed better activity than conventional amorphous silica, β-zeolite, and ZSM-5-supported Cu-Mn catalysts [294]. It was supposed that highly dispersed Cu-Mn mixed oxides on mesoporous structure possibly provide active sites for the complete oxidation of toluene on the mesoporous catalysts.

On another note, regarding the influence of the variation of the Cu/Mn ratio on the toluene conversion activity of these binary oxides, literature results appear to be rather ambiguous on this point. Thus, in the case of the studies carried out by Li *et al.* [295], and Hu *et al.* [289], on the series of molar ratios Cu/Mn = 0.5; 1 and 2, tested for complete oxidation of toluene, the optimal ratio was found to be 1. While Wang *et al.* [296], noted that among the series of Cu/Mn molar ratios ranging from 0.4 to 1.7, the optimal ratio obtained corresponded to Cu/Mn = 0.8, signaling, overall, an order of activity which would follow the manganese ratio in these bimetallic catalysts. This observation was also made in other previous works [297], [298], where the mixed Cu-Mn catalysts rich in Mn, were considered to be much more active than those rich in Cu (having a Cu/Mn molar ratio greater than 1). This would result from a better activity of the mixed Cu-Mn phases when they are associated with manganese oxide phases such as Mn_2O_3 (mixed catalysts rich in Mn), rather than when they are associated with copper oxide phases such as CuO (mixed catalysts rich in Cu). Indeed, according to Lu *et al.* [298], the MnO_x phases would constitute the oxygen supply and transmission center, supplying the active phase of mixed Cu-Mn oxides with active oxygen, thereby allowing the organic molecules to be completely oxidized. Moreover, in the studies which proposed the $Cu_{1.5}Mn_{1.5}O_4$ spinel phase as being the catalytically active phase in bimetallic copper-manganese oxides, the better performance of solids with a lower copper content was explained by the fact that the excess copper (corresponding to a Cu/(Cu + Mn) molar ratio > 0.30), was not incorporated in the spinel phase. Indeed, this excess was rather present as a separate phase of CuO, responsible for the decrease in catalytic activity, due to the covering of active sites with excessive amounts of copper [299], [300]. Finally, Huang *et al.* [301] found, for their part, that a Cu/Mn molar ratio of 0.5 led to a better oxidation performance of toluene, due to the formation of the $CuMn_2O_4$ phase, responsible for the catalytic activity of the mixed Cu-Mn oxides.

Therefore, it would be interesting to disperse both these active metal species (Cu and Mn) on multifunctional hydroxyapatite support and to evaluate the impact of varying the Cu/Mn molar ratio on the resulting catalytic performances of the obtained Hap supported binary Cu-Mn materials, in the complete oxidation of toluene.

Nonetheless, it would also be of great significance to reexamine the notions that remain either unresolved or insufficiently probed, in each of these transition metal (TM) oxides, individually. This would help develop high performance Cu and Mn-based catalysts for toluene total oxidation. Matters connected with Cu-supported solids will be discussed first, followed by those associated with Mn-bearing materials.

1.3. Dispersion of copper species over Cu-supported catalysts

1.3.1. Effect of Cu loading on the dispersion of Cu entities

As was shown above the high efficiency of Cu-based catalysts in toluene total oxidation is strongly contingent on the good dispersion of copper species on the surface of the support. However, a problem is presented regarding the maintaining of a good Cu dispersion when wanting to increase the loading of copper within the supported catalyst. Wang [275] examined this particular issue when investigating the best choice of catalyst for the incineration of toluene. Indeed, having concluded through his research that $CuO/\gamma\text{-}Al_2O_3$ was the optimal catalyst among seven other tested, he thought of inspecting the repercussions of altering the Cu content (1; 3; 5; 7 and 9 wt% Cu) of this optimal catalyst on catalytic performance. It was supposed that with CuO being the active species, an increase in its amount would lead to improved catalytic activity. Nonetheless, a continuous rise in the Cu loading was not conductive to good toluene conversion efficiency. Indeed, a Cu content of about 5 wt% was found to be the most suitable in terms of resulting catalytic performances. A higher amount of Cu on the support produced large CuO crystals, worsening the dispersion of CuO species and entailing a decrease in the amount of active sites, which thus prompted a decline in toluene conversion. Another study also pointed out the difficulty faced by increasing the Cu loading above 5 wt% for alumina supported copper catalysts [277]. It was noted that when the copper amount grew from 5 to 15 wt%, the evolution of toluene conversion followed, on the contrary, a decreasing trend. Results indicated that while Cu loadings lower than 5 wt% are unfavorable for the oxidation activity of the material due to the insufficiency of active sites, higher Cu loadings are also catalytically detrimental, but in this case because of a change in copper state induced by an increase in Cu amount: copper is mostly present as isolated copper ions at 5 wt% loading, these entities being more easily reduced than bulk CuO formed at Cu content > 5 wt%. Similar conclusions were drawn by Larsson *et al.* [280] who conducted a study over titania-supported copper oxide catalysts and explained the activity decline provoked by an increase in Cu loading with the formation of different types of copper species dependent on the Cu amount, one consisting of dispersed Cu^{2+} species possessing high catalytic activity for toluene combustion and the other being bulk CuO which contributes little to the sample's activity. An analogous pattern of decreasing activity with increasing copper content was observed for copper dispersed on zirconia [302] and zeolite [303] materials, ascribed once again to a decrease in CuO species dispersion, these latter becoming less accessible and therefore less active for toluene oxidation.

It should also be highlighted that apart from being instrumental in acquiring good catalytic activity for toluene combustion, the formation of well-dispersed Cu species significantly affects the stability of the copper-containing material as well. Indeed, Meng *et al.* [285] declared that an increased dispersion of the CuO species can enhance the catalyst's water resistance.

Thus it seems essential that a solution be found for the hurdle caused by the impossibility of increasing copper loading without adversely impacting the copper dispersion on the surface of the support; poor copper dispersion inducing deterioration in the catalytic performances of the Cu-based materials. In the case of hydroxyapatite-supported Cu catalysts, results showed that the highest Cu content viable before a problem with obtaining good copper dispersion arises is 2.5 wt% of Cu [209]. Consequently, the goal would be to find a way to surpass this so far optimal loading for Cu/Hap materials while preserving a good dispersion of Cu^{II} entities on Hap surface.

1.3.2. Means of enhancing Cu dispersion

According to all of the previously reported data regarding Cu-based catalysts, generation of highly dispersed active copper species is extremely important for the catalytic performances in toluene total oxidation. One of the key factors for obtaining high metal dispersed catalysts is choosing a proper copper precursor for the preparation of the copper supported material. Indeed, a study conducted by Lee *et al.* [304] revealed that the dispersion degree of copper oxide was profoundly affected by the nature of Cu precursor used. Among the three examined precursors (copper nitrate, sulfate, and chloride), the one prepared with copper nitrate resulted in the catalyst with the highest activity, due to the formation of highly dispersed Cu particles. Furthermore, another work investigating the dispersion of copper species on mesoporous silica SBA-15 support indicated a dependence of the dispersion behavior of CuO on the type of copper precursor employed, the aggregation of CuO particles becoming more and more favorable in the increasing order: nitrate < acetate < chloride [305]. Therefore, it does seem that a Cu nitrate precursor constitutes a most appropriate choice if we aim to promote the dispersion of copper species on the hydroxyapatite support.

Another frequently adopted approach, that favors high dispersions of the active phase, is the addition of an organic complexing agent to the impregnation solution. In fact, when dispersed in solution the copper species tend to aggregate together, increasing thus the Cu particle size and leading towards a decline in catalytic activity. It follows then that the selection of a dispersing agent is important in preparing highly efficient catalysts, for it determines the properties of the copper-bearing material by influencing the size of Cu species formed on the surface of the support. Among the complexing agents which have been successfully used for improving the dispersion of Cu entities figures:

- ethylene diamine tetra acetic acid (EDTA), used as chelating agent when preparing copper coating on alumina powder [306].
- ethylenediamine (en), complexing Cu(II) ions that were deposited on a silica surface [307].
- hexadecyl trimethyl ammonium bromide (CTAB), incorporated into the impregnation solution designed for the synthesis of CuO/CeO_2 catalyst [308].
- β-cyclodextrin, assisting the dispersion of Cu particles on top of mesoporous silica support [309]. A further examination of this organic compound will be presently performed.

1.3.3. β-cyclodextrin

1.3.3.1. Structure

Cyclodextrins (CDs) are macrocyclic oligosaccharides that are composed of α-(1,4) linked glucopyranose subunits. Cyclodextrins are produced from starch by enzymatic degradation and possess a toroid-shaped molecular structure. Cyclodextrins are of three types: α-, β-, and γ-cyclodextrin which are composed of six, seven, and eight α-(1,4) linked glycosyl units, respectively. While the height of the CD cavity is the same (≈ 8 Å) for all three types, the number of glucopyranose units determine the internal diameter of the cavity as ≈ 6 Å, 8 Å, and 10 Å for α-CD, β-CD, and γ-CD, respectively, as shown in Figure 1.5.

The structure of the CDs, together with the particular orientation of the various hydroxyl functions of the glucopyranose units, gives them a characteristic amphiphilic character; a relatively hydrophobic central cavity lined with carbon and hydrogen atoms, and a relatively hydrophilic exterior filled with primary (carried by the C_6 carbons around the narrow opening of the cone) and secondary hydroxyl groups (carried by the C_2 and C_3 carbons around the broad opening of the cone) [310], [311].

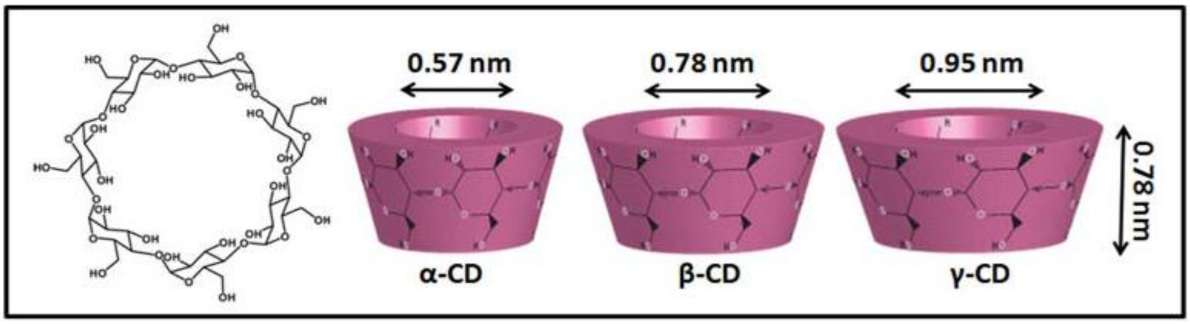

Figure 1.5. Schematic representations of the chemical structure of β-CD and approximate dimensions of α-, β-, and γ-cyclodextrins. From reference [312].

Of the three above mentioned types of cyclodextrin, β-CD is the most widely used and represents at least 95% of all produced and consumed CDs. This is due to several reasons among which figure price, availability, cavity dimensions, etc… What is more, it has generally shown to be the most useful in complexation processes [313], [314].

1.3.3.2. Inclusion complexes and molecule-ion adducts formation

The amphiphilic character of cyclodextrins accord them with the capacity of forming inclusion complexes, with CDs playing the role of host molecules able to include in their cavity hydrophobic guests, resulting thus host–guest complexes. Complex formation is a dimensional fit between host cavity and guest molecule. Therefore, only an appropriately sized non-polar moiety can enter the cyclodextrin cavity to form an inclusion complex. In fact, the latter is not accompanied by the formation or break of any covalent bonds, ensuing a non-permanent binding of guest molecules within the CD host. Complexes can be formed either in solution or in the crystalline state, and water is typically the solvent of choice [311], [314]. By temporarily locking or caging guest molecules within the host cavity, cyclodextrins can exert a powerful effect on the physicochemical properties of the obtained material. Therefore, the use of cyclodextrins can prove to be really advantageous in the field of heterogeneous catalysis.

In the particular case of copper interaction with cyclodextrins, previous investigations carried out by Matsui and co-workers [315]–[317], examining the complexation of Cu(II) ions by β-CD in alkaline solutions by means of pH-metric, conductometric titrations and polarimetric measurements have shown that an inclusion 2:1 complex between copper (II) and β-CD is formed. The process consisted of a cross-linking of the two pairs of deprotonated C_2 and C_3 secondary hydroxyl groups of adjacent glucopyranose units by the =Cu(OH)(O)Cu= ion bridge, as illustrated in Figure 1.6.

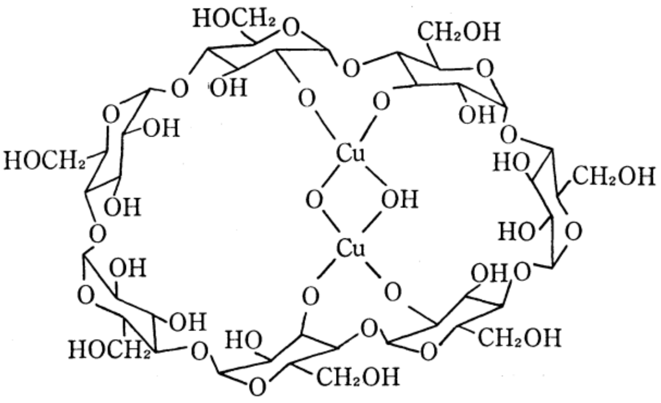

Figure 1.6. The suggested structure of the Cu(II)-β-CD complex . From reference [316].

Another study conducted by Ribeiro *et al.* [318], in which the authors used electrical conductivity and diffusion measurements to inspect the interactions between copper (II) chloride and β-CD, revealed a favorable tendency of the β-CD system to incorporate Cu^{2+} in the internal cavity rather than Cl^-, or for the cavity to remain unassociated. This further supported the previous suggestion of a Cu-CD inclusion complex. However, it should be stressed out that the works of both Matsui *et al.* [315]–[317] and Ribeiro *et al.* [318] indicated that the proposed complex would be highly stable in basic conditions (due to the deprotonation of β-CD hydroxyl-groups), but not at neutral pH, where the chelating property of β-CD would be much weaker.

Actually, it should be noted that a metal-CD interaction does not necessarily involve the formation of an inclusion complex. In fact, the metal ion can react with the hydroxyl groups of the CD molecule resulting in a hydroxy-complex which is not an inclusion complex, but rather a supramolecular adduct [319]–[321].

Indeed, the work of Kurokawa *et al.* [322] probing the interaction of β-cyclodextrin with copper(II) chloride in neutral aqueous solutions declared the occurrence of an adduct which is not a guest-“inclusion” compound but a novel kind of capped CD compound in which the $CuCl_2$ moiety is hydrogen-bonded at the rim of the primary-hydroxy side. This notion was later expanded on by Song *et al.* [323] whose research was also centered around the interactions taking place between copper chloride and β-cyclodextrin in neutral conditions. Their results evidenced the occurrence of molecule-ion interactions between β-CD and Cu^{2+} ions as well as Cl^- ions, leading to a weakening of ionic bonds in $CuCl_2$.

1.3.3.3. Use as active phase dispersant

Several authors have demonstrated that the controlled addition of β-cyclodextrin during the impregnation step could have a considerable favorable effect on the dispersion and reducibility of supported cobalt species and on their catalytic behavior in the complete oxidation of formaldehyde [324], [325] and Fischer-Tropsch synthesis [326]. Bai *et al.* [324] studied the effect of the β-CD to cobalt ratio used in the impregnating solution on the overall catalytic performance, and found an optimal value of 0.1. Indeed, at this ratio value, a drop in light-off temperature of ca. 15 °C (T_{50}) in the oxidation of formaldehyde could be obtained. Based on the optimal ratio of 0.1, which would theoretically correspond to approximately 2 OH groups per cobalt ion (seeing as β-CD has 21 OH groups in total), these authors suggested a probable formation of adducts of Co^{2+} with β-CD, in which the cobalt center would be coordinated to two O atoms of adjacent hydroxyl groups of β-CD. The formation of these complexes helped diminish the risk of particle aggregation by preventing the interactions of cobalt ions together, and their subsequent decomposition led to having smaller and more reducible supported cobalt oxide particles. What is more, the same group of authors established that the nature of cobalt precursor used during impregnation step, and its affinity for β-CD can strongly affect the final properties of the cobalt oxide catalysts [325]. Indeed, while a negative impact resulted from the co-impregnation of β-CD and cobalt acetate due to a lack of preferential interactions between these two, conversely, in the case of nitrate and acetylacetonate precursors, the co-impregnation of cobalt and β-CD over zirconia induced a promotion of the catalytic activity, by a joint effect of an improved Co_3O_4 particle dispersion and greater cobalt reducibility.

The impact of β-CD proved to be beneficial as well for nickel based materials. An investigation conducted over a series of Ni/Al_2O_3 catalysts confirmed that the use of cyclodextrins led towards a much higher Ni dispersion and narrower distribution of Ni particle sizes, as well as an increase in the availability of reduced surface nickel species [327]. This translated into enhanced catalytic properties in the direct amination of alcohols. Moreover, employing cyclodextrin-assisted catalysts gave rise to better robustness of the solids by lessening the nickel leaching during reaction. Furthermore, CO_2 reforming of methane over Ni/SBA-15 catalysts prepared with β-cyclodextrin during impregnation step was also examined [328], [329]. The results revealed that using β-CD generated smaller NiO particles that exhibited stronger interactions with the SBA-15 support. These Ni/SBA-15-CD solids manifested higher conversions and stronger abilities to resist carbon deposition.

Finally, Cu loaded MCM-41 and KIT-6 prepared by β-CD assisted co-impregnation method (Cu/MCM-41-CD and Cu/KIT-6-CD) for in situ catalytic upgrading of bio-oil derived from the fast pyrolysis of biomass was investigated by Karnjanakom *et al.* [309]. Authors found that using β-CD allowed attaining a better dispersion of Cu species on MCM-41 and KIT-6, which led to Cu/MCM-41-CD and Cu/KIT-6-CD materials showcasing an enhanced catalytic activity for promoting the deoxygenation from the bio-oil when compared with conventionally prepared catalysts (Cu/MCM-41 and Cu/KIT-6). In addition, a CD-assisted co-impregnation can upgrade the anti-coke formation ability and stability of catalyst.

The aforementioned data promotes the choice of β-cyclodextrin as complexing agent, to be used in the synthesis of Cu loaded on Hap materials, as an instrument for achieving high Cu dispersion for high Cu loadings.

Still, one area of interest is kept pending, revolving around manganese oxide based catalysts. More to the point, it regards Mn speciation. The following section will deal with this topic, focusing, on one hand, on the role that Mn speciation plays in the catalytic performances outcome, and on the other hand, on its susceptibility to the content of Mn employed, in the preparation of Mn supported catalyst.

1.4. Speciation of Mn

1.4.1. Effect of Mn speciation on the catalytic performances of Mn-based solids tested in toluene total oxidation

In last decade, considerable efforts have been made in order to enhance the catalytic performance of Mn_xO_y materials by focusing on various essential factors, which are valence, phase structure, morphology, and particle size. Among these several parameters, Mn valence plays a key role in obtaining high performance catalysts. Indeed, numerous studies have shown the catalytic activity of Mn-based solids to be decidedly dependent on the oxidation state of manganese [248], [253], [257],

[330]. When Kim *et al.* [248] investigated the catalytic combustion of toluene over different manganese oxide catalysts (Mn_3O_4, Mn_2O_3, and MnO_2), their results revealed a sequence of catalytic activity which went as follows: $Mn_3O_4 > Mn_2O_3 > MnO_2$. What was deemed to be responsible for the improved behavior of Mn_3O_4 compound was its higher oxygen mobility and surface area, compared to the other two Mn_xO_y solids. Moreover, the superior activity of Mn_3O_4 was again demonstrated in other works examining the catalytic conduct of manganese oxides in toluene total oxidation [253], [257], [330]. Santos *et al.* [330] found that while the presence of Mn_3O_4 favors an increase in the catalytic performances due to a rise in the reactivity and mobility of lattice oxygen, that of Mn_2O_3 leads, on the contrary, to an opposite effect. However, it ought to be noted that the activity of hausmannite (Mn_3O_4) can be upgraded even further by the addition of Mn_5O_8, as has been indicated by the research of Deng *et al.* [257]. These authors signaled that a mixture of tetragonal hausmannite Mn_3O_4 and monoclinic Mn_5O_8 results in better toluene conversion efficiency owing to a promotion of the oxygen mobility and an increase of the amount of surface adsorbed oxygen. Sun *et al.* [249] focused their investigations on manganese oxide octahedral molecular sieves (OMS) among which figures cryptomelane (OMS-2) whose chemical composition is KMn_8O_{16}. It was stated that what provides cryptomelane with excellent catalytic activity in the complete combustion of toluene, is the coexistence of multiple Mn valences in its framework (Mn^{4+}, Mn^{3+}, and Mn^{2+}). Besides, Li *et al.* [251] who conducted an evaluation of the toluene conversion efficiency over different manganese oxide catalysts ($LaMnO_3$, OMS, and Mn_2O_3) also commented on the impressive oxidation activity of OMS compound for which they discerned the best performance, that they ascribed to both higher reducibility and specific surface area.

On another note, in accordance with what was said in the beginning of the preceding paragraph, the catalytic performances of Mn_xO_y materials are also contingent on the phase structure of the manganese oxide. This was clearly proven by the work of Li *et al.* [252] in which they evidenced that by varying the phase structure of MnO_2 the resulting catalytic conduct varies as well. Indeed, among the various manganese dioxide polymorphs synthesized (β-, α-, γ-, and δ-MnO_2), δ-MnO_2 was the most active: the catalytic activity in toluene oxidation followed the sequence of β- < α- < γ- < δ-MnO_2. The poorest behavior of β-MnO_2 is largely due its extreme small surface area. Whereas, in the case of α-MnO_2, its weaker activity compared to that of γ- and δ-MnO_2, is a consequence of fewer amounts of Mn^{4+} and lattice oxygen on its surface. Last but not least, what confers to δ-MnO_2 better catalytic oxidation activity than γ-MnO_2 resides in its special hierarchical structure which facilitates toluene adsorption on its surface. Additionally, this study showed that for MnO_2 materials having a δ phase structure, the crystallinity degree and morphology also affect toluene catalytic oxidation activity, but to a lesser extent than phase structure. Results indicated that a decrease of crystallinity degree and particle size contributed in improving the catalytic performances of δ-MnO_2.

The influence of the morphology of manganese dioxide catalysts on the observed catalytic behavior was put heavily into focus in a study conducted by Wang *et al.* [256] in which toluene's removal efficiency was found to decrease in the order of rod-like α-MnO_2 > tube-like α-MnO_2 > flower-like Mn_2O_3 > wire-like α-MnO_2. The superior performance of the well-defined morphologically manganese dioxide, α-MnO_2 nanorods, was attributed to its high oxygen adsorbed species concentration and low-temperature reducibility.

All of the above goes to show the momentous impact that Mn speciation has on the catalytic performances of Mn-based catalysts evaluated in toluene total oxidation.

1.4.2. Effect of Mn loading on Mn speciation in Mn_xO_y supported catalysts examined in toluene total oxidation reaction

A consensus has thus been reached regarding the clear dependence of the catalytic activity of Mn-based materials on Mn speciation. However, what literature data has also shown is the existence of a direct relationship between Mn loading and the average oxidation state of Mn in supported manganese oxide catalysts, which induces a direct influence on the resulting catalytic activity of the Mn-bearing compounds, tested in toluene complete oxidation [263], [268], [272].

A paper investigating the effect of four different Mn loadings (1, 5, 10, and 20 wt%) on the total oxidation of toluene by ozone using alumina-supported manganese oxide catalysts revealed the occurrence of a correlation between the manganese amount and the attained Mn oxidation state [263]. This led to obvious disparities in the noted catalytic conduct of the various Mn-based catalysts. It was found that the catalysts with lower Mn loadings were more active in toluene conversion, which was explained by an activity order of the solids associated with the oxidation state of Mn present in these solids. Indeed, results conveyed that catalysts with lower Mn amount, up to 10 wt%, were essentially composed of Mn_2O_3. On the other hand, those with Mn loading greater than 10 wt% were formed by mixtures of MnO_2 and Mn_2O_3. Seeing as materials with lower Mn oxidation states are more favorable for the instigation of ozone decomposition process due to their higher activity in electrons transfer to ozone, it is to be expected that the catalysts with lower Mn loadings would manifest a higher toluene oxidation rate owing to their higher rate of ozone decomposition to atomic oxygen.

Another study conducted by Aboukaïs *et al.* [268] over titania-supported manganese oxide compounds, examined the total oxidation of toluene. It was perceived that the content of manganese dispersed on TiO_2 exerted a significant effect on the catalytic activity of the obtained material. Among the several tested Mn loadings (2.5; 3.5; 5; and 6 wt%), a maximum of activity was noted for the 5% Mn/TiO_2 catalyst. The authors connected the oxidation activity of the manganese oxide catalysts with the reducibility and mobility of oxygen derived from Mn_xO_y phases on one hand, as well as with the presence of the redox couple Mn^{3+}/Mn^{4+} in the Mn/TiO_2 catalyst on the other hand. Given that when the amount of Mn is increased further than 5 wt% (6% Mn/TiO_2), large particles of Mn_2O_3 emerge, it follows that the catalytic activity decreases with the increase in Mn loading.

Finally, concerning manganese oxide supported on hydroxyapatite catalysts, Chlala *et al.* [272] showed that the preparation of MnxHap materials with different Mn loadings (x = 2.5; 5.0; 10; 20; and 30 Mn wt%), resulted in a divergence in the observed catalytic performances, Mn10Hap being the one to exhibit the best resistance to deactivation among the tested solids. X-Ray Photoelectron Spectroscopy (XPS) results indicated an increase in manganese average oxidation state going hand in hand with that of Mn content in MnxHap solids. Thus, a scheme was proposed which consisted in an initial incorporation of Mn^{2+} into Hap, succeeded by manganese dispersion on the Hap surface, eventually leading to the formation of $Mn_2O_3/\varepsilon\text{-}MnO_2$ particles (identified by XRD analysis) when Mn loading increases beyond a certain value (10 wt% Mn).

As can be seen, more work needs to be done to thoroughly evaluate the effects of Mn speciation on toluene conversion efficiency of Hap supported Mn catalysts. In addition, a more rigorous appraisal of the influence of Mn loading on the nature and location of produced Mn species ought to be performed, via analysis techniques, suitable for carrying out this type of study.

Finally, in conclusion to this chapter, a presentation of the methodology which guided this thesis's work will be carried out below.

1.5. Objectives and strategies adopted for this thesis

As already mentioned earlier, previous work investigating the use of copper and manganese oxides supported on hydroxyaptite using wet impregnation process, showed good activity and selectivity towards CO_2 for both of these transition metal oxides based materials, in the catalytic oxidation of toluene [208], [209]. Moreover, a study of the effect of Cu and Mn content on the catalytic performances of these solids in the targeted catalytic reaction, revealed that the best performances for toluene oxidation in terms of T_{50} (°C) could be achieved in the case of copper supported Hap for Cu loading of 2.5 wt% (215), whereas in the case of Mn, it is attained at 10 wt% (220).

Therefore, the aim of this thesis work is to optimize the preparation method and experimental conditions that are used, in the hope of enhancing the catalytic performances of these TM oxides in toluene's total combustion.

As a first attractive strategy for improving the performances of the catalysts, synthesis of binary Cu-Mn oxides, which have already been reported in literature to be efficient catalysts for VOC oxidation, will be conducted. An investigation of the behavior of binary Cu-Mn/Hap catalysts, accompanied by a comparison of their activity with that of the single oxide counterparts in toluene's removal process, will take place. This would either confirm or disprove the hypothesis of a synergistic interaction between Cu and Mn. Moreover, an evaluation of the effect that varying the Cu/Mn molar ratio (Cu/Mn = 2; 1; 0.5) can have on the Cu-Mn oxide catalysts will be carried out, in order to determine the optimal Cu/Mn ratio for these hydroxyapatite-supported materials (chapter III).

The second strategy for upgrading the catalytic behavior of these TM oxide based catalysts, and more precisely the Cu supported Hap materials, is to ameliorate the dispersion of copper species on the apatitic support through the use of organic complexant, β-cyclodextrin. Not only will the properties and catalytic performances of the resulting materials be examined (chapter IV), but a comprehensive study into the role played by β-CD during Cu/Hap synthesis will also be performed, monitored by Raman and ToF-SIMS analysis (chapter V).

Finally, a probing of manganese speciation in Mn-based catalysts will be the focus of chapter VI. Indeed, Mn/Hap solids, prepared with various manganese loadings (2.5; 5; 10; and 20 wt% of Mn), will be characterized by different physico-chemical techniques, among which figure XRD, Raman, XANES, H_2-TPR, and XPS. The results derived from these several methods will be compared with those obtained for different Mn_xO_y reference compounds, which have been synthesized in the current work, offering thus an extensive database that will be conductive for drawing appropriate conclusions. This will lead towards a better understanding of the nature of active Mn species involved in the catalytic oxidation of toluene, allowing for future optimization of the highly promising Mn/Hap catalytic system.

References

[1] K. Ioku, "Tailored bioceramics of calcium phosphates for regenerative medicine," *J. Ceram. Soc. Jpn.*, vol. 118, n^{o} 1381, p. 775–783, 2010.

[2] I. Sopyan, M. Mel, S. Ramesh, and K. A. Khalid, "Porous hydroxyapatite for artificial bone applications," *Sci. Technol. Adv. Mater.*, vol. 8, n^{o} 1, p. 116–123, 2007.

[3] S. Mondal, U. Pal, and A. Dey, "Natural origin hydroxyapatite scaffold as potential bone tissue engineering substitute," *Ceram. Int.*, vol. 42, n^{o} 16, p. 18338–18346, 2016.

[4] M. A. Surmeneva, A. A. Ivanova, Q. Tian, R. Pittman, W. Jiang, J. Lin, H. H. Liu, and R. A. Surmenev, "Bone marrow derived mesenchymal stem cell response to the RF magnetron sputter deposited hydroxyapatite coating on AZ91 magnesium alloy," *Mater. Chem. Phys.*, vol. 221, p. 89–98, 2019.

[5] M. A. Surmeneva, T. M. Mukhametkaliyev, H. Khakbaz, R. A. Surmenev, and M. B. Kannan, "Ultrathin film coating of hydroxyapatite (HA) on a magnesium–calcium alloy using RF magnetron sputtering for bioimplant applications," *Mater. Lett.*, vol. 152, p. 280–282, 2015.

[6] H. Fu, M. N. Rahaman, R. F. Brown, and D. E. Day, "Evaluation of BSA protein release from hollow hydroxyapatite microspheres into PEG hydrogel," *Mater. Sci. Eng. C*, vol. 33, n^{o} 4, p. 2245–2250, 2013.

[7] S. K. Swain and D. Sarkar, "Study of BSA protein adsorption/release on hydroxyapatite nanoparticles," *Appl. Surf. Sci.*, vol. 286, p. 99–103, 2013.

[8] B. Palazzo, M. C. Sidoti, N. Roveri, A. Tampieri, M. Sandri, L. Bertolazzi, F. Galbusera, G. Dubini, P. Vena, and R. Contro, "Controlled drug delivery from porous hydroxyapatite grafts: An experimental and theoretical approach," *Mater. Sci. Eng. C*, vol. 25, no. 2, p. 207–213, 2005.

[9] D. R. K. Weerasuriya, W. Wijesinghe, and R. M. G. Rajapakse, "Encapsulation of anticancer drug copper bis (8-hydroxyquinoline) in hydroxyapatite for pH-sensitive targeted delivery and slow release," *Mater. Sci. Eng. C*, vol. 71, p. 206–213, 2017.

[10] J. S. Son, M. Appleford, J. L. Ong, J. C. Wenke, J. M. Kim, S. H. Choi, and D. S. Oh, "Porous hydroxyapatite scaffold with three-dimensional localized drug delivery system using biodegradable microspheres," *J. Controlled Release*, vol. 153, no. 2, p. 133–140, 2011.

[11] L. J. Cummings, M. A. Snyder, and K. Brisack, "Chapter 24 Protein Chromatography on Hydroxyapatite Columns," in *Methods in Enzymology*, vol. 463, R. R. B. and M. P. Deutscher, Ed. Academic Press, p. 387–404, 2009.

[12] C. Tibbetts, K. Johansson, and L. Philipson, "Hydroxyapatite chromatography and formamide denaturation of adenovirus DNA," *J. Virol.*, vol. 12, no. 2, p. 218–225, 1973.

[13] W. Condit, E. Hawley, H. Rectanus, and R. Deeb, "Global trends in the environmental remediation industry," *J. Environ. Manage.*, vol. 204, p. 705‑708, 2017.

[14] H. Wu, H. Yan, Y. Quan, H. Zhao, N. Jiang, and C. Yin, "Recent progress and perspectives in biotrickling filters for VOCs and odorous gases treatment," *J. Environ. Manage.*, vol. 222, p. 409–419, 2018.

[15] M. Shaaban, L. Van Zwieten, S. Bashir, A. Younas, A. Núñez-Delgado, M. Chhajro, K. A. Kubar, U. Ali, M. S. Rana, and M. A. Mehmood, “A concise review of biochar application to agricultural soils to improve soil conditions and fight pollution,” *J. Environ. Manage.*, vol. 228, p. 429–440, 2018.

[16] D. Wlóka, A. Placek, M. Smol, A. Rorat, D. Hutchison, and M. Kacprzak, “The efficiency and economic aspects of phytoremediation technology using Phalaris arundinacea L. and Brassica napus L. combined with compost and nano SiO_2 fertilization for the removal of PAH’s from soil,” *J. Environ. Manage.*, vol. 234, p. 311–319, 2019.

[17] C. R. Holkar, A. J. Jadhav, D. V. Pinjari, N. M. Mahamuni, and A. B. Pandit, “A critical review on textile wastewater treatments: possible approaches,” *J. Environ. Manage.*, vol. 182, p. 351–366, 2016.

[18] M. Kumari and A. K. Saroha, “Performance of various catalysts on treatment of refractory pollutants in industrial wastewater by catalytic wet air oxidation: A review,” *J. Environ. Manage.*, vol. 228, p. 169–188, 2018.

[19] J. C. Elliott, R. M. Wilson, and S. E. P. Dowker, “Apatite structures,” *Adv. X-Ray Anal.*, vol. 45, p. 172–181, 2002.

[20] J. C. Elliot, *Structure and Chemistry of the Apatites and Other Calcium Phosphates 1994*. Amsterdam: Elsevier, 1994.

[21] J. D. Pasteris, “Structurally incorporated water in bone apatite: A cautionary tale,” in *Calcium Phosphates: Structure, Synthesis, Properties, and Applications*, R. B. Heimann, Éd. New York: Nova Science Publishers, Inc., 2012, p. 63–94.

[22] P. A. Brunton, R. P. W. Davies, J. L. Burke, A. Smith, A. Aggeli, S. J. Brookes, and J. Kirkham, “Treatment of early caries lesions using biomimetic self-assembling peptides–a clinical safety trial,” *Br. Dent. J.*, vol. 215, no. 4, 6 pages, 2013.

[23] D. Chlala, M. Labaki, J.-M. Giraudon, O. Gardoll, A. Denicourt-Nowicki, A. Roucoux, and J.-F. Lamonier, “Toluene total oxidation over Pd and Au nanoparticles supported on hydroxyapatite,” *Comptes Rendus Chim.*, vol. 19, no. 4, p. 525–537, 2016.

[24] H. Nishikawa, T. Oka, N. Asai, H. Simomichi, T. Shirai, and M. Fuji, “Oxidative decomposition of volatile organic compounds using thermally-excited activity of hydroxyapatite,” *Appl. Surf. Sci.*, vol. 258, n^{o} 14, p. 5370–5374, 2012.

[25] D. Meza, I. A. Figueroa, C. Flores-Morales, and M. C. Piña-Barba, “Nano hydroxyapatite crystals obtained by colloidal solution,” *Rev. Mex. Física*, vol. 57, n^{o} 6, p. 471–474, 2011.

[26] R. Li, K. Chen, G. Li, G. Han, S. Yu, J. Yao, and Y. Cai, “Structure design and fabrication of porous hydroxyapatite microspheres for cell delivery,” *J. Mol. Struct.*, vol. 1120, p. 34–41, 2016.

[27] G. Bernardi, “Chromatography of proteins on hydroxyapatite,” vol. 27, B.-M. in Enzymology, Ed. Academic Press, p. 471–479, 1973.

[28] A. Tiselius, S. Hjerten, and Ö. Levin, “Protein chromatography on calcium phosphate columns,” *Arch. Biochem. Biophys.*, vol. 65, n^{o} 1, p. 132–155, 1956.

[29] G. Bernardi, “Chromatography of proteins on hydroxyapatite,” vol. 22, B.-M. in Enzymology, Ed. Academic Press, p. 325–339, 1971.

[30] T. Kadoya, “High-performance liquid chromatography of proteins on a ceramic hydroxyapatite with volatile buffers,” *J. Chromatogr. A*, vol. 515, p. 521–525, 1990.

[31] T. Itagaki, M. Yoshida, S. Abe, H. Omichi, and Y. Nishihira, “Separation of human tear proteins with ceramic hydroxyapatite high-performance liquid chromatography,” *J. Chromatogr. B. Biomed. Sci. App.*, vol. 620, n^{o} 1, p. 149–152, 1993.

[32] G. Bernardi, “Chromatography of nucleic acids on hydroxyapatite columns,” vol. 21, B.-M. in Enzymology, Ed. Academic Press, p. 95–139, 1971.

[33] T. Watanabe, K. Makitsuru, H. Nakazawa, S. Hara, T. Suehiro, A. Yamamoto, T. Hiraide, and T. Ogawa, “Separation of double-strand DNA fragments by high-performance liquid chromatography using a ceramic hydroxyapatite column,” *Anal. Chim. Acta*, vol. 386, no. 1–2, p. 69–75, 1999.

[34] T. Kawasaki, S. Takahashi, and K. Ideda, “Hydroxyapatite high-performance liquid chromatography: column performance for proteins,” *Eur. J. Biochem.*, vol. 152, no. 2, p. 361–371, 1985.

[35] K. Kandori, S. Mizumoto, S. Toshima, M. Fukusumi, and Y. Morisada, “Effects of heat treatment of calcium hydroxyapatite particles on the protein adsorption behavior,” *J. Phys. Chem. B*, vol. 113, no. 31, p. 11016–11022, 2009.

[36] G. Yin, Z. Liu, J. Zhan, F. Ding, and N. Yuan, “Impacts of the surface charge property on protein adsorption on hydroxyapatite,” *Chem. Eng. J.*, vol. 87, n^{o} 2, p. 181–186, 2002.

[37] Z. Zhuang and M. Aizawa, “Protein adsorption on single-crystal hydroxyapatite particles with preferred orientation to a (b)-and c-axes,” *J. Mater. Sci. Mater. Med.*, vol. 24, n^{o} 5, p. 1211–1216, 2013.

[38] L. Silvester, J.-F. Lamonier, R.-N. Vannier, C. Lamonier, M. Capron, A.-S. Mamede, F. Pourpoint, A. Gervasini, and F. Dumeignil, “Structural, textural and acid–base properties of carbonate-containing hydroxyapatites,” *J. Mater. Chem. A*, vol. 2, no. 29, p. 11073–11090, 2014.

[39] C. Lamonier, J.-F. Lamonier, B. Aellach, A. Ezzamarty, and J. Leglise, “Specific tuning of acid/base sites in apatite materials to enhance their methanol thiolation catalytic performances,” *Catal. Today*, vol. 164, n^{o} 1, p. 124–130, 2011.

[40] T. Tsuchida, J. Kubo, T. Yoshioka, S. Sakuma, T. Takeguchi, and W. Ueda, “Reaction of ethanol over hydroxyapatite affected by Ca/P ratio of catalyst,” *J. Catal.*, vol. 259, n^{o} 2, p. 183–189, 2008.

[41] L. Silvester, J.-F. Lamonier, J. Faye, M. Capron, R.-N. Vannier, C. Lamonier, J.-L. Dubois, J.-L. Couturier, C. Calais, and F. Dumeignil, “Reactivity of ethanol over hydroxyapatite-based Ca-enriched catalysts with various carbonate contents,” *Catal. Sci. Technol.*, vol. 5, no. 5, p. 2994–3006, 2015.

[42] C. L. Kibby and W. K. Hall, “Dehydrogenation of alcohols and hydrogen transfer from alcohols to ketones over hydroxyapatite catalysts,” *J. Catal.*, vol. 31, n^{o} 1, p. 65–73, 1973.

[43] S. Diallo-Garcia, M. B. Osman, J.-M. Krafft, S. Casale, C. Thomas, J. Kubo, and G. Costentin, "Identification of Surface Basic Sites and Acid–Base Pairs of Hydroxyapatite," *J. Phys. Chem. C*, vol. 118, no. 24, p. 12744–12757, 2014.

[44] M. Ferri, S. Campisi, M. Scavini, C. Evangelisti, P. Carniti, and A. Gervasini, "In-depth study of the mechanism of heavy metal trapping on the surface of hydroxyapatite," *Appl. Surf. Sci.*, vol. 475, p. 397–409, 2019.

[45] S. C. Oh, Y. Wu, D. T. Tran, I. C. Lee, Y. Lei, and D. Liu, "Influences of cation and anion substitutions on oxidative coupling of methane over hydroxyapatite catalysts," *Fuel*, vol. 167, p. 208–217, 2016.

[46] N. S. Resende, M. Nele, and V. M. Salim, "Effects of anion substitution on the acid properties of hydroxyapatite," *Thermochim. Acta*, vol. 451, n° 1, p. 16–21, 2006.

[47] S. C. Oh, Y. Lei, H. Chen, and D. Liu, "Catalytic consequences of cation and anion substitutions on rate and mechanism of oxidative coupling of methane over hydroxyapatite catalysts," *Fuel*, vol. 191, p. 472–485, 2017.

[48] H. Tounsi, S. Djemal, C. Petitto, and G. Delahay, "Copper loaded hydroxyapatite catalyst for selective catalytic reduction of nitric oxide with ammonia," *Appl. Catal. B Environ.*, vol. 107, n° 1, p. 158–163, 2011.

[49] K. Matsunaga, H. Murata, T. Mizoguchi, and A. Nakahira, "Mechanism of incorporation of zinc into hydroxyapatite," *Acta Biomater.*, vol. 6, n° 6, p. 2289–2293, 2010.

[50] K. Zhu, K. Yanagisawa, R. Shimanouchi, A. Onda, and K. Kajiyoshi, "Preferential occupancy of metal ions in the hydroxyapatite solid solutions synthesized by hydrothermal method," *J. Eur. Ceram. Soc.*, vol. 26, n° 4, p. 509–513, 2006.

[51] L. Veselinović, L. Karanović, Z. Stojanović, I. Bračko, S. Marković, N. Ignjatović, and D. Uskoković, "Crystal structure of cobalt-substituted calcium hydroxyapatite nanopowders prepared by hydrothermal processing," *J. Appl. Crystallogr.*, vol. 43, no. 2, p. 320–327, 2010.

[52] M. Wakamura, K. Kandori, and T. Ishikawa, "Surface structure and composition of calcium hydroxyapatites substituted with Al (III), La (III) and Fe (III) ions," *Colloids Surf. Physicochem. Eng. Asp.*, vol. 164, n° 2, p. 297–305, 2000.

[53] D. Laurencin, N. Almora-Barrios, N. H. de Leeuw, C. Gervais, C. Bonhomme, F. Mauri, W. Chrzanowski, J. C. Knowles, R. J. Newport, and A. Wong, "Magnesium incorporation into hydroxyapatite," *Biomaterials*, vol. 32, no. 7, p. 1826–1837, 2011.

[54] K. Kandori, S. Toshima, M. Wakamura, M. Fukusumi, and Y. Morisada, "Effects of modification of calcium hydroxyapatites by trivalent metal ions on the protein adsorption behavior," *J. Phys. Chem. B*, vol. 114, n° 7, p. 2399–2404, 2010.

[55] Z. Opre, J.-D. Grunwaldt, M. Maciejewski, D. Ferri, T. Mallat, and A. Baiker, "Promoted Ru–hydroxyapatite: designed structure for the fast and highly selective oxidation of alcohols with oxygen," *J. Catal.*, vol. 230, n° 2, p. 406–419, 2005.

[56] Z. Opre, "Catalytic oxidation over transition metal containing hydroxyapatites," PhD Thesis, ETH Zurich, 2007.

[57] M. Veiderma, K. Tõnsuaadu, R. Knubovets, and M. Peld, "Impact of anionic substitutions on apatite structure and properties," *J. Organomet. Chem.*, vol. 690, n° 10, p. 2638–2643, 2005.

[58] M. Hidouri, K. Bouzouita, F. Kooli, and I. Khattech, "Thermal behaviour of magnesium-containing fluorapatite," *Mater. Chem. Phys.*, vol. 80, n° 2, p. 496–505, 2003.

[59] G. C. Silva, L. Ma, O. Hemmers, and D. Lindle, "Micro-structural characterization of precipitation-synthesized fluorapatite nano-material by transmission electron microscopy using different sample preparation techniques," *Micron*, vol. 39, n° 3, p. 269–274, 2008.

[60] J. S. Prener, "The Growth and Crystallographic Properties of Calcium Fluor-and Chlorapatite Crystals," *J. Electrochem. Soc.*, vol. 114, n° 1, p. 77–83, 1967.

[61] P. Rulis, L. Ouyang, and W. Y. Ching, "Electronic structure and bonding in calcium apatite crystals: Hydroxyapatite, fluorapatite, chlorapatite, and bromapatite," *Phys. Rev. B*, vol. 70, n° 15, p. 155104, 2004.

[62] J. C. Elliott and R. A. Young, "Conversion of single crystals of chlorapatite into single crystals of hydroxyapatite," *Nature*, vol. 214, no. 5091, p. 904–906, 1967.

[63] E. J. Duff, "Orthophosphates-XI Bromoapatite: Stability of solid solutions of bromoapatite with other calcium apatites under aqueous conditions," *J. Inorg. Nucl. Chem.*, vol. 34, n° 1, p. 101–108, 1972.

[64] J. C. Trombe and G. Montel, "Some features of the incorporation of oxygen in different oxidation states in the apatitic lattice—I On the existence of calcium and strontium oxyapatites," *J. Inorg. Nucl. Chem.*, vol. 40, n° 1, p. 15–21, 1978.

[65] J.-P. Lafon, E. Champion, and D. Bernache-Assollant, "Processing of AB-type carbonated hydroxyapatite $Ca_{10-x}(PO_4)_{6-x}(CO_3)_x(OH)_{2-x-2y}(CO_3)_y$ ceramics with controlled composition," *J. Eur. Ceram. Soc.*, vol. 28, no. 1, p. 139–147, 2008.

[66] J. Barralet, S. Best, and W. Bonfield, "Carbonate substitution in precipitated hydroxyapatite: an investigation into the effects of reaction temperature and bicarbonate ion concentration," *J. Biomed. Mater. Res.*, vol. 41, n° 1, p. 79–86, 1998.

[67] K. Ishikawa, P. Ducheyne, and S. Radin, "Determination of the Ca/P ratio in calcium-deficient hydroxyapatite using X-ray diffraction analysis," *J. Mater. Sci. Mater. Med.*, vol. 4, n° 2, p. 165–168, 1993.

[68] W. Dungkaew, K. J. Haller, A. E. Flood, and J. F. Scamehorn, "Arsenic removal by precipitation with Calcium phosphate hydroxyapatite," in *Adv. Mater. Res.*, vol. 506, p. 413–416, 2012.

[69] P. P. Mahapatra, L. M. Mahapatra, and B. Mishra, "Physicochemical studies on solid solutions of calcium phosphorus arsenic hydroxyapatites," *Bull. Chem. Soc. Jpn.*, vol. 62, n° 10, p. 3272–3277, 1989.

[70] C. B. Boechat, J.-G. Eon, A. M. Rossi, C. A. de Castro Perez, and R. A. da S. San Gil, "Structure of vanadate in calcium phosphate and vanadate apatite solid solutions," *Phys. Chem. Chem. Phys.*, vol. 2, n° 18, p. 4225–4230, 2000.

[71] S. Sugiyama, T. Osaka, Y. Hirata, and K.-I. Sotowa, “Enhancement of the activity for oxidative dehydrogenation of propane on calcium hydroxyapatite substituted with vanadate,” *Appl. Catal. A-Gen.*, vol. 312, p. 52–58, 2006.

[72] I. R. Gibson, S. M. Best, and W. Bonfield, “Chemical characterization of silicon-substituted hydroxyapatite,” *J. Biomed. Mater. Res. A*, vol. 44, n^{o} 4, p. 422–428, 1999.

[73] Y. Suetsugu, Y. Takahashi, F. P. Okamura, and J. Tanaka, “Structure analysis of A-type carbonate apatite by a single-crystal X-ray diffraction method,” *J. Solid State Chem.*, vol. 155, n^{o} 2, p. 292–297, 2000.

[74] M. E. Fleet and X. Liu, “Coupled substitution of type A and B carbonate in sodium-bearing apatite,” *Biomaterials*, vol. 28, n^{o} 6, p. 916–926, 2007.

[75] M. E. Fleet, X. Liu, and P. L. King, “Accommodation of the carbonate ion in apatite: An FTIR and X-ray structure study of crystals synthesized at 2–4 GPa,” *Am. Mineral.*, vol. 89, n^{o} 10, p. 1422–1432, 2004.

[76] I. R. Gibson and W. Bonfield, “Novel synthesis and characterization of an AB-type carbonate-substituted hydroxyapatite,” *J. Biomed. Mater. Res.*, vol. 59, n^{o} 4, p. 697–708, 2002.

[77] G. Liu, J. W. Talley, C. Na, S. L. Larson, and L. G. Wolfe, “Copper doping improves hydroxyapatite sorption for arsenate in simulated groundwaters,” *Environ. Sci. Technol.*, vol. 44, n^{o} 4, p. 1366–1372, 2010.

[78] J. Jemal, H. Tounsi, K. Chaari, C. Petitto, G. Delahay, S. Djemel, and A. Ghorbel, “NO reduction with NH_3 under oxidizing atmosphere on copper loaded hydroxyapatite,” *Appl. Catal. B Environ.*, vol. 113, p. 255–260, 2012.

[79] M. Khachani, M. Kacimi, A. Ensuque, J.-Y. Piquemal, C. Connan, F. Bozon-Verduraz, and M. Ziyad, “Iron–calcium–hydroxyapatite catalysts: Iron speciation and comparative performances in butan-2-ol conversion and propane oxidative dehydrogenation,” *Appl. Catal. A Gen.*, vol. 388, no. 1, p. 113–123, 2010.

[80] M. Riad and S. Mikhail, “Oxidative desulfurization of light gas oil using zinc catalysts prepared via different techniques,” *Catal. Sci. Technol.*, vol. 2, no. 7, p. 1437–1446, 2012.

[81] S. Sugiyama, Y. Iguchi, H. Nishioka, T. Minami, T. Moriga, H. Hayashi, and J. B. Moffat, “Effects of the thermal stability and the fine structure changes of strontium hydroxyapatites ion-exchanged with lead on methane oxidation in the presence and absence of tetrachloromethane,” *J. Catal.*, vol. 176, no. 1, p. 25–34, 1998.

[82] T. Matsuda, C. Yamanaka, and M. Ikeya, “ESR study of Gd^{3+} and Mn^{2+} ions sorbed on hydroxyapatite,” *Appl. Radiat. Isot.*, vol. 62, no. 2, p. 353–357, 2005.

[83] Y. Li, J. Ho, and C. P. Ooi, “Antibacterial efficacy and cytotoxicity studies of copper (II) and titanium (IV) substituted hydroxyapatite nanoparticles,” *Mater. Sci. Eng. C*, vol. 30, no. 8, p. 1137–1144, 2010.

[84] Y. Masuyama, K. Yoshikawa, N. Suzuki, K. Hara, and A. Fukuoka, “Hydroxyapatite-supported copper(II)-catalyzed azide–alkyne [3+2] cycloaddition with neither reducing agents nor bases in water,” *Tetrahedron Lett.*, vol. 52, no. 51, p. 6916–6918, 2011.

[85] Y. Liu and Y. Peng, *Advanced Material Engineering: Proceedings of the 2015 International Conference on Advanced Material Engineering*. World Scientific, 2015.

[86] D. J. Green, *An Introduction to the Mechanical Properties of Ceramics*. Cambridge University Press, 1998.

[87] J.-A. Epinette and M. T. Manley, *Fifteen Years of Clinical Experience with Hydroxyapatite Coatings in Joint Arthroplasty*. Springer Science & Business Media, 2003.

[88] L.-H. Fu, Y.-J. Liu, M.-G. Ma, X.-M. Zhang, Z.-M. Xue, and J.-F. Zhu, "Microwave-Assisted Hydrothermal Synthesis of Cellulose/Hydroxyapatite Nanocomposites," *Polymers*, vol. 8, no. 9, p. 316–328, 2016.

[89] A. H. Yoruç, A. Karakaş, A. Koyun, and T. Yildiz, "Comparison of Properties of Hydroxyapatite Powders Synthesized by Chemical and Biomimetic Techniques," *Acta Phys. Pol. A*, vol. 121, n^{o} 1, p. 233–235, 2012.

[90] B. El Idrissi, K. Yamni, A. Yacoubi, and A. Massit, "A novel method to synthesize nanocrystalline hydroxyapatite: Characterization with X-ray diffraction and infrared spectroscopy," *J. Appl. Chem.*, vol. 7, p. 107–112, 2014.

[91] H. Eslami, M. Solati-Hashjin, and M. Tahriri, "Synthesis and characterization of nanocrystalline fluorinated hydroxyapatite powder by modified wet-chemical process," *J. Ceram. Process. Res.*, vol. 9, p. 224–229, 2008.

[92] R. W. N. Nilen and P. W. Richter, "The thermal stability of hydroxyapatite in biphasic calcium phosphate ceramics," *J. Mater. Sci. Mater. Med.*, vol. 19, n^{o} 4, p. 1693–1702, 2008.

[93] M. R. Ribeiro Alves, A. D. G. Zuñiga, R. de C. S. Sousa, and C. Zacchi Scolforo, "The Process of Separating Bovine Serum Albumin Using Hydroxyapatite and Active Babassu Coal (Orbignya martiana)," *Sci. World J.*, vol. 2016, 9 pages, 2016.

[94] V. P. Orlovskii, V. S. Komlev, and S. M. Barinov, "Hydroxyapatite and hydroxyapatite-based ceramics," *Inorg. Mater.*, vol. 38, n^{o} 10, p. 973–984, 2002.

[95] R. Barbucci, *Integrated Biomaterials Science*. Springer Science & Business Media, 2007.

[96] D. Malina, K. Biernat, and A. Sobczak-Kupiec, "Studies on sintering process of synthetic hydroxyapatite," *Acta Biochim. Pol.*, vol. 60, n^{o} 4, p. 851–855, 2013.

[97] Y. Fang, D. K. Agrawal, and D. M. Roy, "Thermal stability of synthetic hydroxyapatite," *in* P. W. Brown and B. Constantz, *Hydroxyapatite and Related Materials*. CRC Press, 1994.

[98] K. Salma, L. Berzina-Cimdina, and N. Borodajenko, "Calcium phosphate bioceramics prepared from wet chemically precipitated powders," *Process. Appl. Ceram.*, vol. 4, n^{o} 1, p. 45–51, 2010.

[99] Y. Cai, S. Zhang, X. Zeng, and D. Sun, "Effect of fluorine incorporation on long-term stability of magnesium-containing hydroxyapatite coatings," *J. Mater. Sci. Mater. Med.*, vol. 22, n^{o} 7, p. 1633–1638, 2011.

[100] P. Kanchana and C. Sekar, “Influence of sodium fluoride on the synthesis of hydroxyapatite by gel method,” *J. Cryst. Growth*, vol. 312, n° 6, p. 808–816, 2010.

[101] E. Karamian, M. Abdellahi, A. Khandan, and S. Abdellah, “Introducing the fluorine doped natural hydroxyapatite-titania nanobiocomposite ceramic,” *J. Alloys Compd.*, vol. 679, p. 375–383, 2016.

[102] S. Kapoor, U. Batra, and K. Suchita, “Investigation on influence of fluorine substitution on structural, thermal and in-vitro behaviour of nanodimensional hydroxyapatite,” *J. Chem. Pharm. Res.*, vol. 8(3), p. 281–288, 2016.

[103] B. Nasiri-Tabrizi, A. Fahami, F. Ebrahimi, and R. Ebrahimi-Kahrizsangi, *New Frontiers in Mechanosynthesis: Hydroxyapatite-and Fluorapatite-Based Nanocomposite Powders*. INTECH Open Access Publisher, 2012.

[104] Y. Chen and X. Miao, “Thermal and chemical stability of fluorohydroxyapatite ceramics with different fluorine contents,” *Biomaterials*, vol. 26, n° 11, p. 1205–1210, 2005.

[105] Y. Wang, S. Zhang, X. Zeng, L. L. Ma, W. Weng, W. Yan, and M. Qian, “Osteoblastic cell response on fluoridated hydroxyapatite coatings,” *Acta Biomater.*, vol. 3, no. 2, p. 191–197, 2007.

[106] S. Zhang, Z. Xianting, W. Yongsheng, C. Kui, and W. Wenjian, “Adhesion strength of sol–gel derived fluoridated hydroxyapatite coatings,” *Surf. Coat. Technol.*, vol. 200, n° 22–23, p. 6350–6354, 2006.

[107] E.-J. Lee, S.-H. Lee, H.-W. Kim, Y.-M. Kong, and H.-E. Kim, “Fluoridated apatite coatings on titanium obtained by electron-beam deposition,” *Biomaterials*, vol. 26, n° 18, p. 3843–3851, 2005.

[108] H.-W. Kim, H.-E. Kim, and J. C. Knowles, “Fluor-hydroxyapatite sol–gel coating on titanium substrate for hard tissue implants,” *Biomaterials*, vol. 25, n° 17, p. 3351–3358, 2004.

[109] S. Zhang, *Hydroxyapatite Coatings for Biomedical Applications*. CRC Press, 2013.

[110] J. Park and R. S. Lakes, *Biomaterials: An Introduction*. Springer Science & Business Media, 2007.

[111] D. N. Ungureanu, N. Angelescu, Z. Bacinschi, E. V. Stoian, and C. Z. Rizescu, “Thermal stability of chemically precipitated hydroxyapatite nanopowders,” *Int. J. Biol. Biomed. Eng.*, vol. 5, no. 2, p. 57–64, 2011.

[112] S. Kuśnieruk, J. Wojnarowicz, A. Chodara, T. Chudoba, S. Gierlotka, and W. Lojkowski, “Influence of hydrothermal synthesis parameters on the properties of hydroxyapatite nanoparticles,” *Beilstein J. Nanotechnol.*, vol. 7, n° 1, p. 1586–1601, 2016.

[113] M. Zilm, S. D. Thomson, and M. Wei, “A Comparative Study of the Sintering Behavior of Pure and Manganese-Substituted Hydroxyapatite,” *Materials*, vol. 8, n° 9, p. 6419–6436, 2015.

[114] S. Mondal, S. V. Dorozhkin, and U. Pal, “Recent progress on fabrication and drug delivery applications of nanostructured hydroxyapatite,” *Wiley Interdiscip. Rev. Nanomed. Nanobiotechnol.*, vol. 10, n° 4, 32 pages, 2018.

[115] I. Denry and L. T. Kuhn, “Design and characterization of calcium phosphate ceramic scaffolds for bone tissue engineering,” *Dent. Mater.*, vol. 32, n° 1, p. 43–53, 2016.

[116] M. Boutinguiza, J. Pou, R. Comesaña, F. Lusquiños, A. De Carlos, and B. León, “Biological hydroxyapatite obtained from fish bones,” *Mater. Sci. Eng. C*, vol. 32, n° 3, p. 478–486, 2012.

[117] C. Piccirillo, R. C. Pullar, D. M. Tobaldi, P. L. Castro, and M. E. Pintado, “Hydroxyapatite and chloroapatite derived from sardine by-products,” *Ceram. Int.*, vol. 40, n° 8, p. 13231–13240, 2014.

[118] A. Pal, S. Paul, A. R. Choudhury, V. K. Balla, M. Das, and A. Sinha, “Synthesis of hydroxyapatite from Lates calcarifer fish bone for biomedical applications,” *Mater. Lett.*, vol. 203, p. 89–92, 2017.

[119] R. Rajesh, A. Hariharasubramanian, and Y. D. Ravichandran, “Chicken Bone as a Bioresource for the Bioceramic (Hydroxyapatite),” *Phosphorus Sulfur Silicon Relat. Elem.*, vol. 187, n° 8, p. 914–925, 2012.

[120] N. Muhammad, Y. Gao, F. Iqbal, P. Ahmad, R. Ge, U. Nishan, A. Rahim, G. Gonfa, and Z. Ullah, “Extraction of biocompatible hydroxyapatite from fish scales using novel approach of ionic liquid pretreatment,” *Sep. Purif. Technol.*, vol. 161, p. 129–135, 2016.

[121] B. Mondal, S. Mondal, A. Mondal, and N. Mandal, “Fish scale derived hydroxyapatite scaffold for bone tissue engineering,” *Mater. Charact.*, vol. 121, p. 112–124, 2016.

[122] W. Pon-On, P. Suntornsaratoon, N. Charoenphandhu, J. Thongbunchoo, N. Krishnamra, and I. M. Tang, “Hydroxyapatite from fish scale for potential use as bone scaffold or regenerative material,” *Mater. Sci. Eng. C*, vol. 62, p. 183–189, 2016.

[123] Y. Chai and M. Tagaya, “Simple preparation of hydroxyapatite nanostructures derived from fish scales,” *Mater. Lett.*, vol. 222, p. 156–159, 2018.

[124] I. Abdulrahman, H. I. Tijani, B. Mohammed, H. Saidu, H. Yusuf, M. Ndejiko Jibrin, and S. Mohammed, “From garbage to biomaterials: an overview on egg shell based hydroxyapatite,” *J. Mater.*, vol. 2014, 6 pages, 2014.

[125] R. Bardhan, S. Mahata, and B. Mondal, “Processing of natural resourced hydroxyapatite from eggshell waste by wet precipitation method,” *Adv. Appl. Ceram.*, vol. 110, n° 2, p. 80–86, 2011.

[126] A. A. Baba, I. T. Oduwole, F. O. Salami, F. A. Adekola, and S. E. Adeboye, “Synthesis of hydroxyapatite from waste egg-shell by Precipitation method,” *Ife J. Sci.*, vol. 15, n° 3, p. 435–443, 2013.

[127] M. I. Jones, H. Barakat, and D. A. Patterson, “Production of hydroxyapatite from waste mussel shells,” in *IOP Conference Series: Materials Science and Engineering*, vol. 18, p. 192002–192005, 2011.

[128] T. Kaluđerović Radoičić and S. Raičević, “In situ lead stabilization using natural and synthetic apatite,” *Chem. Ind. Chem. Eng. QuarterlyCICEQ*, vol. 14, n° 4, p. 269–271, 2008.

[129] S. Joschek, B. Nies, R. Krotz, and A. Göpferich, “Chemical and physicochemical characterization of porous hydroxyapatite ceramics made of natural bone,” *Biomaterials*, vol. 21, n° 16, p. 1645–1658, 2000.

[130] S. El Asri, A. Laghzizil, T. Coradin, A. Saoiabi, A. Alaoui, and R. M'hamedi, "Conversion of natural phosphate rock into mesoporous hydroxyapatite for heavy metals removal from aqueous solution," *Colloids Surf. Physicochem. Eng. Asp.*, vol. 362, n° 1‑3, p. 33–38, 2010.

[131] W. Admassu and T. Breese, "Feasibility of using natural fishbone apatite as a substitute for hydroxyapatite in remediating aqueous heavy metals," *J. Hazard. Mater.*, vol. 69, n° 2, p. 187–196, 1999.

[132] K. Haberko, M. M. Bućko, J. Brzezińska-Miecznik, M. Haberko, W. Mozgawa, T. Panz, A. Pyda, and J. Zarębski, "Natural hydroxyapatite—its behaviour during heat treatment," *J. Eur. Ceram. Soc.*, vol. 26, no. 4–5, p. 537–542, 2006.

[133] C. Y. Ooi, M. Hamdi, and S. Ramesh, "Properties of hydroxyapatite produced by annealing of bovine bone," *Ceram. Int.*, vol. 33, n° 7, p. 1171–1177, 2007.

[134] T. Leventouri, "Synthetic and biological hydroxyapatites: crystal structure questions," *Biomaterials*, vol. 27, n° 18, p. 3339–3342, 2006.

[135] Y. Zhou, D. Chang, and J. Chang, "Preparation of nano-structured pig bone hydroxyapatite for high-efficiency adsorption of Pb^{2+} from aqueous solution," *Int. J. Appl. Ceram. Technol.*, vol. 14, n° 6, p. 1125–1133, 2017.

[136] J. V. Flores-Cano, R. Leyva-Ramos, F. Carrasco-Marin, A. Aragón-Piña, J. J. Salazar-Rabago, and S. Leyva-Ramos, "Adsorption mechanism of Chromium(III) from water solution on bone char: effect of operating conditions," *Adsorption*, vol. 22, n° 3, p. 297–308, 2016.

[137] I. Mobasherpour, E. Salahi, and M. Pazouki, "Comparative of the removal of Pb^{2+}, Cd^{2+} and Ni^{2+} by nano crystallite hydroxyapatite from aqueous solutions: Adsorption isotherm study," *Arab. J. Chem.*, vol. 5, n° 4, p. 439–446, 2012.

[138] M. Hadioui, P. Sharrock, M.-O. Mecherri, V. Brumas, and M. Fiallo, "Reaction of lead ions with hydroxylapatite granules," *Chem. Pap.*, vol. 62, n° 5, p. 516–521, 2008.

[139] Q. Y. Ma, S. J. Traina, T. J. Logan, and J. A. Ryan, "In Situ Lead Immobilization by Apatite," *Env. Sci Technol*, vol. 27, n° 9, p. 1803–1810, 1993.

[140] J. Reichert and J. G. P. Binner, "An evaluation of hydroxyapatite-based filters for removal of heavy metal ions from aqueous solutions," *J. Mater. Sci.*, vol. 31, n° 5, p. 1231–1241, 1996.

[141] S. M. Mousa, N. S. Ammar, and H. A. Ibrahim, "Removal of lead ions using hydroxyapatite nano-material prepared from phosphogypsum waste," *J. Saudi Chem. Soc.*, vol. 20, n° 3, p. 357–365, 2016.

[142] Y. Feng, J.-L. Gong, G.-M. Zeng, Q.-Y. Niu, H.-Y. Zhang, C.-G. Niu, J.-H. Deng, and M. Yan, "Adsorption of Cd (II) and Zn (II) from aqueous solutions using magnetic hydroxyapatite nanoparticles as adsorbents," *Chem. Eng. J.*, vol. 162, no. 2, p. 487–494, 2010.

[143] Q. Y. Ma, S. J. Traina, T. J. Logan, and J. A. Ryan, "Effects of aqueous Al, Cd, Cu, Fe (II), Ni, and Zn on Pb immobilization by hydroxyapatite," *Environ. Sci. Technol.*, vol. 28, n° 7, p. 1219–1228, 1994.

[144] Q. Y. Ma, T. J. Logan, S. J. Traina, and J. A. Ryan, “Effects of NO_3^-, Cl^-, F^-, SO_4^{2-}, and CO_3^{2-} on Pb^{2+} immobilization by hydroxyapatite,” *Environ. Sci. Technol.*, vol. 28, no. 3, p. 408–418, 1994.

[145] X. Chen, J. V. Wright, J. L. Conca, and L. M. Peurrung, “Effects of pH on heavy metal sorption on mineral apatite,” *Environ. Sci. Technol.*, vol. 31, n° 3, p. 624–631, 1997.

[146] S. Chen, M. Xu, Y. Ma, and J. Yang, “Evaluation of different phosphate amendments on availability of metals in contaminated soil,” *Ecotoxicol. Environ. Saf.*, vol. 67, n° 2, p. 278–285, 2007.

[147] X. Chen, J. V. Wright, J. L. Conca, and L. M. Peurrung, “Evaluation of heavy metal remediation using mineral apatite,” *Water. Air. Soil Pollut.*, vol. 98, n° 1‑2, p. 57–78, 1997.

[148] M. Srinivasan, C. Ferraris, and T. White, “Cadmium and lead ion capture with three dimensionally ordered macroporous hydroxyapatite,” *Environ. Sci. Technol.*, vol. 40, n° 22, p. 7054–7059, 2006.

[149] Y. Xu, F. W. Schwartz, and S. J. Traina, “Sorption of Zn^{2+} and Cd^{2+} on hydroxyapatite surfaces,” *Environ. Sci. Technol.*, vol. 28, n° 8, p. 1472–1480, 1994.

[150] M. Prasad, H. Xu, and S. Saxena, “Multi-component sorption of Pb (II), Cu (II) and Zn (II) onto low-cost mineral adsorbent,” *J. Hazard. Mater.*, vol. 154, n° 1‑3, p. 221–229, 2008.

[151] J. G. del Rıo, P. J. Morando, and D. S. Cicerone, “Natural materials for treatment of industrial effluents: comparative study of the retention of Cd, Zn and Co by calcite and hydroxyapatite. Part I: batch experiments,” *J. Environ. Manage.*, vol. 71, n° 2, p. 169–177, 2004.

[152] O. Og and A. Fa, “Removal of Iron and Manganese from Aqueous Solution Using Hydroxyapatite Prepared from Cow Bone,” *Res. Rev. J. Mater. Sci.*, vol. 6, n° 2, p. 59–72, 2018.

[153] A. Corami, S. Mignardi, and V. Ferrini, “Cadmium removal from single- and multi-metal (Cd+Pb+Zn+Cu) solutions by sorption on hydroxyapatite,” *J. Colloid Interface Sci.*, vol. 317, n° 2, p. 402–408, 2008.

[154] S. Campisi, C. Castellano, and A. Gervasini, “Tailoring the structural and morphological properties of hydroxyapatite materials to enhance the capture efficiency towards copper(II) and lead(II) ions,” *New J. Chem.*, vol. 42, n° 6, p. 4520–4530, 2018.

[155] I. Mobasherpour, E. Salahi, and M. Pazouki, “Removal of nickel (II) from aqueous solutions by using nano-crystalline calcium hydroxyapatite,” *J. Saudi Chem. Soc.*, vol. 15, n° 2, p. 105–112, 2011.

[156] I. D. Smičiklas, S. K. Milonjić, P. Pfendt, and S. Raičević, “The point of zero charge and sorption of cadmium (II) and strontium (II) ions on synthetic hydroxyapatite,” *Sep. Purif. Technol.*, vol. 18, n° 3, p. 185–194, 2000.

[157] C.-K. Lee, H.-S. Kim, J.-H. Kwon, C.-K. Lee, H.-S. Kim, and J.-H. Kwon, “The removal of heavy metals using hydroxyapatite,” *Environ. Eng. Res.*, vol. 10, no. 5, p. 205–212, 2005.

[158] S. Gao, R. Sun, Z. Wei, H. Zhao, H. Li, and F. Hu, “Size-dependent defluoridation properties of synthetic hydroxyapatite,” *J. Fluor. Chem.*, vol. 130, n° 6, p. 550–556, 2009.

[159] G. E. J. Poinern, M. K. Ghosh, Y.-J. Ng, T. B. Issa, S. Anand, and P. Singh, “Defluoridation behavior of nanostructured hydroxyapatite synthesized through an ultrasonic and microwave combined technique,” *J. Hazard. Mater.*, vol. 185, n° 1, p. 29–37, 2011.

[160] M. Mourabet, A. El Rhilassi, H. El Boujaady, M. Bennani-Ziatni, R. El Hamri, and A. Taitai, “Removal of fluoride from aqueous solution by adsorption on hydroxyapatite (HAp) using response surface methodology,” *J. Saudi Chem. Soc.*, vol. 19, n° 6, p. 603–615, 2015.

[161] S. Gao, J. Cui, and Z. Wei, “Study on the fluoride adsorption of various apatite materials in aqueous solution,” *J. Fluor. Chem.*, vol. 130, n° 11, p. 1035–1041, 2009.

[162] X. Fan, D. J. Parker, and M. D. Smith, “Adsorption kinetics of fluoride on low cost materials,” *Water Res.*, vol. 37, n° 20, p. 4929–4937, 2003.

[163] S. Kongsri, K. Janpradit, K. Buapa, S. Techawongstien, and S. Chanthai, “Nanocrystalline hydroxyapatite from fish scale waste: Preparation, characterization and application for selenium adsorption in aqueous solution,” *Chem. Eng. J.*, vol. 215, p. 522–532, 2013.

[164] F. Monteil-Rivera, M. Fedoroff, J. Jeanjean, L. Minel, M.-G. Barthes, and J. Dumonceau, “Sorption of selenite (SeO_3^{2-}) on hydroxyapatite: an exchange process,” *J. Colloid Interface Sci.*, vol. 221, n° 2, p. 291–300, 2000.

[165] A. I. Adeogun, E. A. Ofudje, M. A. Idowu, S. O. Kareem, S. Vahidhabanu, and B. R. Babu, “Biowaste-Derived Hydroxyapatite for Effective Removal of Reactive Yellow 4 Dye: Equilibrium, Kinetic, and Thermodynamic Studies,” *ACS Omega*, vol. 3, n° 2, p. 1991–2000, 2018.

[166] N. Barka, S. Qourzal, A. Assabbane, A. Nounah, and Y. Ait-Ichou, “Removal of Reactive Yellow 84 from aqueous solutions by adsorption onto hydroxyapatite,” *J. Saudi Chem. Soc.*, vol. 15, n° 3, p. 263–267, 2011.

[167] W. Wei, L. Yang, W. Zhong, J. Cui, and Z. Wei, “Poorly crystalline hydroxyapatite: A novel adsorbent for enhanced fulvic acid removal from aqueous solution,” *Appl. Surf. Sci.*, vol. 332, p. 328–339, 2015.

[168] W. Wei, R. Sun, J. Cui, and Z. Wei, “Removal of nitrobenzene from aqueous solution by adsorption on nanocrystalline hydroxyapatite,” *Desalination*, vol. 263, n° 1‑3, p. 89–96, 2010.

[169] K. Lin, J. Pan, Y. Chen, R. Cheng, and X. Xu, “Study the adsorption of phenol from aqueous solution on hydroxyapatite nanopowders,” *J. Hazard. Mater.*, vol. 161, n° 1, p. 231–240, 2009.

[170] C. Stötzel, F. A. Müller, F. Reinert, F. Niederdraenk, J. E. Barralet, and U. Gbureck, “Ion adsorption behaviour of hydroxyapatite with different crystallinities,” *Colloids Surf. B Biointerfaces*, vol. 74, n° 1, p. 91–95, 2009.

[171] S. J. Coleman, P. R. Coronado, R. S. Maxwell, and J. G. Reynolds, “Granulated activated carbon modified with hydrophobic silica aerogel-potential composite materials for the removal of uranium from aqueous solutions,” *Environ. Sci. Technol.*, vol. 37, n° 10, p. 2286–2290, 2003.

[172] J. Xu, T. White, P. Li, C. He, and Y.-F. Han, “Hydroxyapatite foam as a catalyst for formaldehyde combustion at room temperature,” *J. Am. Chem. Soc.*, vol. 132, n° 38, p. 13172–13173, 2010.

[173] Y. Sun, Z. Qu, D. Chen, H. Wang, F. Zhang, and Q. Fu, “Formaldehyde catalytic oxidation over hydroxyapatite modified with various organic molecules,” *Chin. J. Catal.*, vol. 35, n^{o} 12, p. 1927–1936, 2014.

[174] H. Nishikawa, S. Ikeda, and H. Monma, “Characterization of calcium-deficient hydroxyapatite after a catalytic reaction with trichloroethylene vapor,” *Bull. Chem. Soc. Jpn.*, vol. 66, n^{o} 9, p. 2570–2573, 1993.

[175] H. Nishikawa and H. Monma, “Vapor phase decomposition with dechlorination of organic chlorinated compounds over calcium-deficient hydroxyapatite,” *Phosphorus Res. Bull.*, vol. 3, p. 115–118, 1993.

[176] H. Nishikawa and H. Monma, “Oxidative decomposition of chlorobenzene over calcium-deficient hydroxyapatite,” *Bull. Chem. Soc. Jpn.*, vol. 67, n^{o} 9, p. 2454–2456, 1994.

[177] C. Piccirillo, C. J. Denis, R. C. Pullar, R. Binions, I. P. Parkin, J. A. Darr, and P. M. L. Castro, “Aerosol assisted chemical vapour deposition of hydroxyapatite-embedded titanium dioxide composite thin films,” *J. Photochem. Photobiol. Chem.*, vol. 332, p. 45–53, 2017.

[178] S. Ji, S. Murakami, M. Kamitakahara, and K. Ioku, “Fabrication of titania/hydroxyapatite composite granules for photo-catalyst,” *Mater. Res. Bull.*, vol. 44, n^{o} 4, p. 768–774, 2009.

[179] H. Anmin, L. Tong, L. Ming, C. Chengkang, L. Huiqin, and M. Dali, “Preparation of nanocrystals hydroxyapatite/TiO_2 compound by hydrothermal treatment,” *Appl. Catal. B Environ.*, vol. 63, n^{o} 1, p. 41–44, 2006.

[180] A. Sahibed-dine, F. Bentiss, and M. Bensitel, “The photocatalytic degradation of methylene bleu over TiO_2 catalysts supported on hydroxyapatite,” *J. Mater.*, vol. 8, n^{o} 4, p. 1301–1311, 2017.

[181] H. Han, X. Qian, Y. Yuan, M. Zhou, and Y. Chen, “Photocatalytic Degradation of Dyes in Water Using TiO_2/Hydroxyapatite Composites,” *Water. Air. Soil Pollut.*, vol. 227, n^{o} 12, p. 461–466, 2016.

[182] Y. Chai, J. Ding, L. Wang, Q. Liu, J. Ren, and W.-L. Dai, “Enormous enhancement in photocatalytic performance of Ag_3PO_4/HAp composite: A Z-scheme mechanism insight,” *Appl. Catal. B Environ.*, vol. 179, p. 29–36, 2015.

[183] X. Liu, J. Ma, and J. Yang, “Visible-light-driven amorphous Fe(III)-substituted hydroxyapatite photocatalyst: Characterization and photocatalytic activity,” *Mater. Lett.*, vol. 137, p. 256–259, 2014.

[184] S. Murgolo, I. Moreira, M. Piccirillo, P. Castro, G. Ventrella, C. Cocozza, and G. Mascolo, “Photocatalytic Degradation of Diclofenac by Hydroxyapatite–TiO_2 Composite Material: Identification of Transformation Products and Assessment of Toxicity,” *Materials*, vol. 11, no. 9, p. 1779–1794, 2018.

[185] E. M. Brazón, C. Piccirillo, I. S. Moreira, and P. M. L. Castro, “Photodegradation of pharmaceutical persistent pollutants using hydroxyapatite-based materials,” *J. Environ. Manage.*, vol. 182, p. 486–495, 2016.

[186] C. El Bekkali, H. Bouyarmane, M. El Karbane, S. Masse, A. Saoiabi, T. Coradin, and A. Laghzizil, “Zinc oxide-hydroxyapatite nanocomposite photocatalysts for the degradation of

ciprofloxacin and ofloxacin antibiotics," *Colloids Surf. Physicochem. Eng. Asp.*, vol. 539, p. 364–370, 2018.

[187] J. Xie, X. Meng, Z. Zhou, P. Li, L. Yao, L. Bian, X. Gao, and Y. Wei, "Preparation of titania/hydroxyapatite (TiO_2/HAp) composite photocatalyst with mosaic structure for degradation of pentachlorophenol," *Mater. Lett.*, vol. 110, p. 57–60, 2013.

[188] M. Hu, Z. Yao, X. Liu, L. Ma, Z. He, and X. Wang, "Enhancement mechanism of hydroxyapatite for photocatalytic degradation of gaseous formaldehyde over TiO_2/hydroxyapatite," *J. Taiwan Inst. Chem. Eng.*, vol. 85, p. 91–97, 2018.

[189] M. Wakamura, H. Tanaka, Y. Naganuma, N. Yoshida, and T. Watanabe, "Surface structure and visible light photocatalytic activity of titanium–calcium hydroxyapatite modified with Cr (III)," *Adv. Powder Technol.*, vol. 22, n^o 4, p. 498–503, 2011.

[190] T. Giannakopoulou, N. Todorova, G. Romanos, T. Vaimakis, R. Dillert, D. Bahnemann, and C. Trapalis, "Composite hydroxyapatite/TiO_2 materials for photocatalytic oxidation of NO_x," *Mater. Sci. Eng. B*, vol. 177, no. 13, p. 1046–1052, 2012.

[191] J. Yao, Y. Zhang, Y. Wang, M. Chen, Y. Huang, J. Cao, W. Ho, and S. Cheng Lee, "Enhanced photocatalytic removal of NO over titania/hydroxyapatite (TiO_2/HAp) composites with improved adsorption and charge mobility ability," *RSC Adv.*, vol. 7, no. 40, p. 24683–24689, 2017.

[192] A. Mitsionis, T. Vaimakis, C. Trapalis, N. Todorova, D. Bahnemann, and R. Dillert, "Hydroxyapatite/titanium dioxide nanocomposites for controlled photocatalytic NO oxidation," *Appl. Catal. B Environ.*, vol. 106, n^o 3, p. 398–404, 2011.

[193] M. Pratap Reddy, A. Venugopal, and M. Subrahmanyam, "Hydroxyapatite-supported Ag–TiO_2 as Escherichia coli disinfection photocatalyst," *Water Res.*, vol. 41, n^o 2, p. 379–386, 2007.

[194] C. Hu, J. Guo, J. Qu, and X. Hu, "Efficient destruction of bacteria with Ti(IV) and antibacterial ions in co-substituted hydroxyapatite films," *Appl. Catal. B Environ.*, vol. 73, n^o 3, p. 345–353, 2007.

[195] W. Liu, G. Qian, B. Zhang, L. Liu, and H. Liu, "Facile synthesis of spherical nano hydroxyapatite and its application in photocatalytic degradation of methyl orange dye under UV irradiation," *Mater. Lett.*, vol. 178, p. 15–17, 2016.

[196] J. H. Shariffuddin, M. I. Jones, and D. A. Patterson, "Greener photocatalysts: hydroxyapatite derived from waste mussel shells for the photocatalytic degradation of a model azo dye wastewater," *Chem. Eng. Res. Des.*, vol. 91, n^o 9, p. 1693–1704, 2013.

[197] M. P. Reddy, A. Venugopal, and M. Subrahmanyam, "Hydroxyapatite photocatalytic degradation of calmagite (an azo dye) in aqueous suspension," *Appl. Catal. B Environ.*, vol. 69, n^o 3‑4, p. 164–170, 2007.

[198] D. L. Savaris, R. de Matos, and C. A. Lindino, "Degradation of 17α-methyltestosterone by hydroxyapatite catalyst," *Rev. Ambiente Água*, vol. 13, n^o 1, 9 pages, 2018.

[199] H. Tanaka, E. Tsuda, H. Nishikawa, and M. Fuji, "FTIR studies of adsorption and photocatalytic decomposition under UV irradiation of dimethyl sulfide on calcium hydroxyapatite," *Adv. Powder Technol.*, vol. 23, n^o 1, p. 115–119, 2012.

[200] H. Nishikawa, “A high active type of hydroxyapatite for photocatalytic decomposition of dimethyl sulfide under UV irradiation,” *J. Mol. Catal. Chem.*, vol. 207, n° 2, p. 149–153, 2004.

[201] H. Nishikawa, “Surface changes and radical formation on hydroxyapatite by UV irradiation for inducing photocatalytic activation,” *J. Mol. Catal. Chem.*, vol. 206, n° 1, p. 331–338, 2003.

[202] H. Nishikawa, “Photocatalytic activity of hydroxyapatite based on photo-induced excitation,” *Phosphorus Res. Bull.*, vol. 17, p. 101–104, 2004.

[203] S. Sugiyama, T. Minami, H. Hayashi, M. Tanaka, and J. B. Moffat, “Surface and bulk properties of stoichiometric and nonstoichiometric strontium hydroxyapatite and the oxidation of methane,” *J. Solid State Chem.*, vol. 126, n° 2, p. 242–252, 1996.

[204] S. Sugiyama, T. Minami, T. Higaki, H. Hayashi, and J. B. Moffat, “High selective conversion of methane to carbon monoxide and the effects of chlorine additives in the gas and solid phases on the oxidation of methane on strontium hydroxyapatites,” *Ind. Eng. Chem. Res.*, vol. 36, n° 2, p. 328–334, 1997.

[205] Z. Boukha, M. Kacimi, M. Ziyad, A. Ensuque, and F. Bozon-Verduraz, “Comparative study of catalytic activity of Pd loaded hydroxyapatite and fluoroapatite in butan-2-ol conversion and methane oxidation,” *J. Mol. Catal. Chem.*, vol. 270, n° 1, p. 205–213, 2007.

[206] Z. Boukha, J. González-Prior, B. de Rivas, J. R. González-Velasco, R. López-Fonseca, and J. I. Gutiérrez-Ortiz, “Synthesis, characterisation and behaviour of Co/hydroxyapatite catalysts in the oxidation of 1,2-dichloroethane,” *Appl. Catal. B Environ.*, vol. 190, p. 125–136, 2016.

[207] Y. Wang, B. Chen, M. Crocker, Y. Zhang, X. Zhu, and C. Shi, “Understanding on the origins of hydroxyapatite stabilized gold nanoparticles as high-efficiency catalysts for formaldehyde and benzene oxidation,” *Catal. Commun.*, vol. 59, p. 195–200, 2015.

[208] D. Chlala, J.-M. Giraudon, N. Nuns, C. Lancelot, Rose-Noëlle Vannier, M. Labaki, and J.-F. Lamonier, “Active Mn species well dispersed on Ca^{2+} enriched apatite for total oxidation of toluene,” *Appl. Catal. B Environ.*, vol. 184, p. 87–95, 2016.

[209] D. Chlala, J.-M. Giraudon, N. Nuns, M. Labaki, and J.-F. Lamonier, “Highly Active Noble-Metal-Free Copper Hydroxyapatite Catalysts for the Total Oxidation of Toluene,” *ChemCatChem*, vol. 9, n° 12, p. 2275–2283, 2017.

[210] B. Aellach, A. Ezzamarty, J. Leglise, C. Lamonier, and J.-F. Lamonier, “Calcium-deficient and stoichiometric hydroxyapatites promoted by Cobalt for the catalytic removal of oxygenated Volatile Organic Compounds,” *Catal. Lett.*, vol. 135, n° 3‑4, p. 197–206, 2010.

[211] Z. Qu, Y. Sun, D. Chen, and Y. Wang, “Possible sites of copper located on hydroxyapatite structure and the identification of active sites for formaldehyde oxidation,” *J. Mol. Catal. Chem.*, vol. 393, p. 182–190, 2014.

[212] Z. Boukha, J. L. Ayastuy, J. R. González-Velasco, and M. A. Gutiérrez-Ortiz, “CO elimination processes over promoter-free hydroxyapatite supported palladium catalysts,” *Appl. Catal. B Environ.*, vol. 201, p. 189–201, 2017.

[213] J. Huang, L.-C. Wang, Y.-M. Liu, Y. Cao, H.-Y. He, and K.-N. Fan, “Gold nanoparticles supported on hydroxylapatite as high performance catalysts for low temperature CO oxidation,” *Appl. Catal. B Environ.*, vol. 101, n° 3, p. 560–569, 2011.

[214] M. I. Domínguez, F. Romero-Sarria, M. A. Centeno, and J. A. Odriozola, “Gold/hydroxyapatite catalysts: Synthesis, characterization and catalytic activity to CO oxidation,” *Appl. Catal. B Environ.*, vol. 87, n° 3, p. 245–251, 2009.

[215] N. Phonthammachai, Z. Ziyi, G. Jun, H. Y. Fan, and T. J. Whitea, “Synthesis of high performance hydroxyapatite-gold catalysts for CO oxidation,” *Gold Bull.*, vol. 41, n° 1, p. 42–50, 2008.

[216] J.-D. Wang, J.-K. Liu, Y. Lu, D.-J. Hong, and X.-H. Yang, “Catalytic performance of gold nanoparticles using different crystallinity hap as carrier materials,” *Mater. Res. Bull.*, vol. 55, p. 190–197, 2014.

[217] A. Venugopal and M. S. Scurrell, “Hydroxyapatite as a novel support for gold and ruthenium catalysts: Behaviour in the water gas shift reaction,” *Appl. Catal. A-Gen.*, vol. 245, n° 1, p. 137–147, 2003.

[218] K. Zhao, B. Qiao, J. Wang, Y. Zhang, and T. Zhang, “A highly active and sintering-resistant Au/FeOx–hydroxyapatite catalyst for CO oxidation,” *Chem. Commun.*, vol. 47, n° 6, p. 1779–1781, 2011.

[219] K. Zhao, B. Qiao, Y. Zhang, and J. Wang, “The roles of hydroxyapatite and FeO_x in a Au/FeO_x hydroxyapatite catalyst for CO oxidation,” *Chin. J. Catal.*, vol. 34, n° 7, p. 1386–1394, 2013.

[220] P. A. Kumar, M. P. Reddy, L. K. Ju, and H. H. Phil, “Novel silver loaded hydroxyapatite catalyst for the selective catalytic reduction of NO_x by propene,” *Catal. Lett.*, vol. 126, n° 1‑2, p. 78–83, 2008.

[221] C. Huang, Z. Ma, P. Xie, Y. Yue, W. Hua, and Z. Gao, “Hydroxyapatite-supported rhodium catalysts for N_2O decomposition,” *J. Mol. Catal. Chem.*, vol. 400, p. 90–94, 2015.

[222] C. Huang, Y. Jiang, Z. Ma, P. Xie, Y. Lin, T. Meng, C. Miao, Y. Yue, W. Hua, and Z. Gao, “Correlation among preparation methods/conditions, physicochemical properties, and catalytic performance of Rh/hydroxyapatite catalysts in N_2O decomposition,” *J. Mol. Catal. Chem.*, vol. 420, p. 73–81, 2016.

[223] Y. Lin, T. Meng, and Z. Ma, “Catalytic decomposition of N_2O over RhO_x supported on metal phosphates,” *J. Ind. Eng. Chem.*, vol. 28, p. 138–146, 2015.

[224] M. Schiavoni, S. Campisi, P. Carniti, A. Gervasini, and T. Delplanche, “Focus on the catalytic performances of Cu-functionalized hydroxyapatites in NH_3-SCR reaction,” *Appl. Catal. A-Gen.*, vol. 563, p. 43–53, 2018.

[225] S. Campisi, M. G. Galloni, F. Bossola, and A. Gervasini, “Comparative performance of copper and iron functionalized hydroxyapatite catalysts in NH_3-SCR,” *Catal. Commun.*, vol. 123, p. 79–85, 2019.

[226] J. W. Jaworski, S. Cho, Y. Kim, J. H. Jung, H. S. Jeon, B. K. Min, and K.-Y. Kwon, "Hydroxyapatite supported cobalt catalysts for hydrogen generation," *J. Colloid Interface Sci.*, vol. 394, p. 401–408, 2013.

[227] D. Özhava and S. Özkar, "Rhodium(0) nanoparticles supported on hydroxyapatite nanospheres and further stabilized by dihydrogen phosphate ion: A highly active catalyst in hydrogen generation from the methanolysis of ammonia borane," *Int. J. Hydrog. Energy*, vol. 40, n^{o} 33, p. 10491–10501, 2015.

[228] S. Akbayrak, P. Erdek, and S. Özkar, "Hydroxyapatite supported ruthenium(0) nanoparticles catalyst in hydrolytic dehydrogenation of ammonia borane: Insight to the nanoparticles formation and hydrogen evolution kinetics," *Appl. Catal. B Environ.*, vol. 142–143, p. 187–195, 2013.

[229] M. Rakap and S. Özkar, "Hydroxyapatite-supported palladium(0) nanoclusters as effective and reusable catalyst for hydrogen generation from the hydrolysis of ammonia-borane," *Int. J. Hydrog. Energy*, vol. 36, n^{o} 12, p. 7019–7027, 2011.

[230] M. Rakap and S. Özkar, "Hydroxyapatite-supported cobalt(0) nanoclusters as efficient and cost-effective catalyst for hydrogen generation from the hydrolysis of both sodium borohydride and ammonia-borane," *Catal. Today*, vol. 183, n^{o} 1, p. 17–25, 2012.

[231] H. Durak, M. Gulcan, M. Zahmakiran, S. Ozkar, and M. Kaya, "Hydroxyapatite-nanosphere supported ruthenium (0) nanoparticle catalyst for hydrogen generation from ammonia-borane solution: kinetic studies for nanoparticle formation and hydrogen evolution," *RSC Adv.*, vol. 4, n^{o} 55, p. 28947–28955, 2014.

[232] D. Celik, S. Karahan, M. Zahmakıran, and S. Özkar, "Hydrogen generation from the hydrolysis of hydrazine-borane catalyzed by rhodium (0) nanoparticles supported on hydroxyapatite," *Int. J. Hydrog. Energy*, vol. 37, n^{o} 6, p. 5143–5151, 2012.

[233] Z. Boukha, M. Kacimi, M. F. R. Pereira, J. L. Faria, J. L. Figueiredo, and M. Ziyad, "Methane dry reforming on Ni loaded hydroxyapatite and fluoroapatite," *Appl. Catal. A-Gen.*, vol. 317, n^{o} 2, p. 299–309, 2007.

[234] B. Rêgo De Vasconcelos, L. Zhao, P. Sharrock, A. Nzihou, and D. Pham Minh, "Catalytic transformation of carbon dioxide and methane into syngas over ruthenium and platinum supported hydroxyapatites," *Appl. Surf. Sci.*, vol. 390, p. 141–156, 2016.

[235] S. J. Lee, J. H. Jun, S.-H. Lee, K. J. Yoon, T. H. Lim, S.-W. Nam, and S.-A. Hong, "Partial oxidation of methane over nickel-added strontium phosphate," *Appl. Catal. A Gen.*, vol. 230, no. 1, p. 61–71, 2002.

[236] Y. Matsumura, S. Sugiyama, H. Hayashi, N. Shigemota, K. Saitoh, and J. B. Moffat, "Strontium hydroxyapatites: catalytic properties in the oxidative dehydrogenation of methane to carbon oxides and hydrogen," *J. Mol. Catal.*, vol. 92, n^{o} 1, p. 81–94, 1994.

[237] J. H. Jun, T.-J. Lee, T. H. Lim, S.-W. Nam, S.-A. Hong, and K. J. Yoon, "Nickel–calcium phosphate/hydroxyapatite catalysts for partial oxidation of methane to syngas: characterization and activation," *J. Catal.*, vol. 221, n^{o} 1, p. 178–190, 2004.

[238] N. El Azarifi, A. El Ouassouli, M. Lakhdar, A. Ezzamarty, C. Moreau, A. Travert, and J. Leglise, "Catalyst made of NiMo sulfide supported on hydroxyapatite: Influence of Al addition on

support properties and on the catalytic conversion of thiophene," *J. Phys. IV France*, vol. 123, p. 203–206, 2005.

[239] N. Elazarifi, M. A. Chaoui, A. El Ouassouli, A. Ezzamarty, A. Travert, J. Leglise, L.-C. de Ménorval, and C. Moreau, "Hydroprocessing of dibenzothiophene, 1-methylnaphthalene and quinoline over sulfided NiMo-hydroxyapatite-supported catalysts," *Catal. Today*, vol. 98, no. 1, p. 161–170, 2004.

[240] H. Wang, C. Wang, B. Xiao, L. Zhao, J. Zhang, Y. Zhu, and X. Guo, "The hydroxyapatite nanotube as a promoter to optimize the HDS reaction of NiMo/TiO_2 catalyst," *Catal. Today*, vol. 259, Part 2, p. 340–346, 2016.

[241] H. L. Tidahy, M. Hosseni, S. Siffert, R. Cousin, J.-F. Lamonier, A. Aboukaïs, B.-L. Su, J.-M. Giraudon, and G. Leclercq, "Nanostructured macro-mesoporous zirconia impregnated by noble metal for catalytic total oxidation of toluene," *Catal. Today*, vol. 137, n^o 2‑4, p. 335–339, 2008.

[242] V. P. Santos, S. A. Carabineiro, P. B. Tavares, M. F. Pereira, J. J. Órfão, and J. L. Figueiredo, "Oxidation of CO, ethanol and toluene over TiO_2 supported noble metal catalysts," *Appl. Catal. B Environ.*, vol. 99, n^o 1, p. 198–205, 2010.

[243] M. J. Patterson, D. E. Angove, and N. W. Cant, "The effect of carbon monoxide on the oxidation of four C_6 to C_8 hydrocarbons over platinum, palladium and rhodium," *Appl. Catal. B Environ.*, vol. 26, n^o 1, p. 47–57, 2000.

[244] N. W. Cant, D. E. Angove, and M. J. Patterson, "The effects of residual chlorine on the behaviour of platinum group metals for oxidation of different hydrocarbons," *Catal. Today*, vol. 44, n^o 1‑4, p. 93–99, 1998.

[245] M. Paulis, H. Peyrard, and M. Montes, "Influence of chlorine on the activity and stability of Pt/Al_2O_3 catalysts in the complete oxidation of toluene," *J. Catal.*, vol. 199, n^o 1, p. 30–40, 2001.

[246] S. Benard, M. Ousmane, L. Retailleau, A. Boreave, P. Vernoux, and A. Giroir-Fendler, "Catalytic removal of propene and toluene in air over noble metal catalyst," *Can. J. Civ. Eng.*, vol. 36, n^o 12, p. 1935–1945, 2009.

[247] C. Lahousse, A. Bernier, P. Grange, B. Delmon, P. Papaefthimiou, T. Ioannides, and X. Verykios, "Evaluation of γ-MnO_2 as a VOC removal catalyst: comparison with a noble metal catalyst," *J. Catal.*, vol. 178, n^o 1, p. 214–225, 1998.

[248] S. C. Kim and W. G. Shim, "Catalytic combustion of VOCs over a series of manganese oxide catalysts," *Appl. Catal. B Environ.*, vol. 98, n^o 3‑4, p. 180–185, 2010.

[249] H. Sun, S. Chen, P. Wang, and X. Quan, "Catalytic oxidation of toluene over manganese oxide octahedral molecular sieves (OMS-2) synthesized by different methods," *Chem. Eng. J.*, vol. 178, p. 191–196, 2011.

[250] Y. Lyu, C. Li, X. Du, Y. Zhu, Y. Zhang, and S. Li, "Catalytic oxidation of toluene over MnO_2 catalysts with different Mn (II) precursors and the study of reaction pathway," *Fuel*, vol. 262, p. 116610–116618, 2020.

[251] J. Li, L. Li, W. Cheng, F. Wu, X. Lu, and Z. Li, “Controlled synthesis of diverse manganese oxide-based catalysts for complete oxidation of toluene and carbon monoxide,” *Chem. Eng. J.*, vol. 244, p. 59–67, 2014.

[252] K. Li, C. Chen, H. Zhang, X. Hu, T. Sun, and J. Jia, “Effects of phase structure of MnO_2 and morphology of δ-MnO_2 on toluene catalytic oxidation,” *Appl. Surf. Sci.*, vol. 496, p. 143662–143671, 2019.

[253] T. Garcia, J. M. López, A. Mayoral, Y. Zhang, R. Arenal, D. Alonso-Domínguez, M. P. Pico, M. L. López, A. Dejoz, and I. Álvarez-Serrano, “Green synthesis of cavity-containing manganese oxides with superior catalytic performance in toluene oxidation,” *Appl. Catal. A-Gen.*, vol. 582, p. 117107–117135, 2019.

[254] X. Zhang, H. Zhao, Z. Song, J. Zhao, M. Zhao, Y. Xing, P. Zhang, and N. Tsubaki, “Influence of hydrothermal synthesis temperature on the redox and oxygen mobility properties of manganese oxides in the catalytic oxidation of toluene,” *Transit. Met. Chem.*, vol. 44, n^o 7, p. 663–670, 2019.

[255] Z. Sihaib, F. Puleo, J. M. Garcia-Vargas, L. Retailleau, C. Descorme, L. F. Liotta, J. L. Valverde, S. Gil, and A. Giroir-Fendler, “Manganese oxide-based catalysts for toluene oxidation,” *Appl. Catal. B Environ.*, vol. 209, p. 689–700, 2017.

[256] F. Wang, H. Dai, J. Deng, G. Bai, K. Ji, and Y. Liu, “Manganese oxides with rod-, wire-, tube-, and flower-like morphologies: highly effective catalysts for the removal of toluene,” *Environ. Sci. Technol.*, vol. 46, n^o 7, p. 4034–4041, 2012.

[257] Q.-F. Deng, T.-Z. Ren, and Z.-Y. Yuan, “Mesoporous manganese oxide nanoparticles for the catalytic total oxidation of toluene,” *React. Kinet. Mech. Catal.*, vol. 108, n^o 2, p. 507–518, 2013.

[258] M. Duplancic, V. Tomasic, S. Kurajica, I. Minga, and K. M. Valkaj, “A comparative study of toluene oxidation on different metal oxides,” *Chem. Eng. Trans.*, vol. 57, p. 889–894, 2017.

[259] X. Zeng, G. Cheng, Q. Liu, W. Yu, R. Yang, H. Wu, Y. Li, M. Sun, C. Zhang, and L. Yu, “Novel Ordered Mesoporous γ-MnO_2 Catalyst for High-Performance Catalytic Oxidation of Toluene and o-Xylene,” *Ind. Eng. Chem. Res.*, vol. 58, n^o 31, p. 13926–13934, 2019.

[260] H. Sun, Z. Liu, S. Chen, and X. Quan, “The role of lattice oxygen on the activity and selectivity of the OMS-2 catalyst for the total oxidation of toluene,” *Chem. Eng. J.*, vol. 270, p. 58–65, 2015.

[261] X. Zhang, Z. Ma, Z. Song, H. Zhao, W. Liu, M. Zhao, and J. Zhao, “Role of Cryptomelane in Surface-Adsorbed Oxygen and Mn Chemical Valence in MnO_x during the Catalytic Oxidation of Toluene,” *J. Phys. Chem. C*, vol. 123, n^o 28, p. 17255–17264, 2019.

[262] J. Guan, D. Wang, H. Yuan, Y. Guo, and J. Dai, “Experimental Study on Catalytic Oxidation of Toluene with Manganese Catalysts and Ozone at Low Temperature,” in *IOP Conference Series: Earth and Environmental Science*, vol. 310, p. 042028–042035, 2019.

[263] E. Rezaei, J. Soltan, and N. Chen, “Catalytic oxidation of toluene by ozone over alumina supported manganese oxides: Effect of catalyst loading,” *Appl. Catal. B Environ.*, vol. 136, p. 239–247, 2013.

[264] E. Rezaei and J. Soltan, “Low temperature oxidation of toluene by ozone over MnO_x/γ-alumina and MnO_x/MCM-41 catalysts,” *Chem. Eng. J.*, vol. 198, p. 482–490, 2012.

[265] P. Liu, H. He, G. Wei, D. Liu, X. Liang, T. Chen, J. Zhu, and R. Zhu, “An efficient catalyst of manganese supported on diatomite for toluene oxidation: Manganese species, catalytic performance, and structure-activity relationship,” *Microporous Mesoporous Mater.*, vol. 239, p. 101–110, 2017.

[266] Y. Qin, H. Wang, C. Dong, and Z. Qu, “Evolution and enhancement of the oxygen cycle in the catalytic performance of total toluene oxidation over manganese-based catalysts,” *J. Catal.*, vol. 380, p. 21–31, 2019.

[267] L. Qin, X. Huang, B. Zhao, Y. Wang, and J. Han, “Iron oxide as a promoter for toluene catalytic oxidation over Fe–Mn/γ-Al_2O_3 catalysts,” *Catal. Lett.*, p. 1–13, 2019.

[268] A. Aboukaïs, E. Abi-Aad, and B. Taouk, “Supported manganese oxide on TiO_2 for total oxidation of toluene and polycyclic aromatic hydrocarbons (PAHs): characterization and catalytic activity,” *Mater. Chem. Phys.*, vol. 142, n^o 2, p. 564–571, 2013.

[269] G. S. P. Soylu, Z. Özçelik, and İ. Boz, “Total oxidation of toluene over metal oxides supported on a natural clinoptilolite-type zeolite,” *Chem. Eng. J.*, vol. 162, n^o 1, p. 380–387, 2010.

[270] Z. Özçelik, G. S. P. Soylu, and İ. Boz, “Catalytic combustion of toluene over Mn, Fe and Co-exchanged clinoptilolite support,” *Chem. Eng. J.*, vol. 155, n^o 1‑2, p. 94–100, 2009.

[271] J. Li, H. Na, X. Zeng, T. Zhu, and Z. Liu, “In situ DRIFTS investigation for the oxidation of toluene by ozone over Mn/HZSM-5, Ag/HZSM-5 and Mn–Ag/HZSM-5 catalysts,” *Appl. Surf. Sci.*, vol. 311, p. 690–696, 2014.

[272] D. Chlala, A. Griboval-Constant, N. Nuns, J.-M. Giraudon, M. Labaki, and J.-F. Lamonier, “Effect of Mn loading onto hydroxyapatite supported Mn catalysts for toluene removal: Contribution of PCA assisted ToF-SIMS,” *Catal. Today*, vol. 307, p. 41–47, 2018.

[273] G. S. Pozan, “Effect of support on the catalytic activity of manganese oxide catalyts for toluene combustion,” *J. Hazard. Mater.*, vol. 221, p. 124–130, 2012.

[274] S.-C. Jung, Y.-K. Park, H. Y. Jung, U. I. Kang, J. W. Nah, and S. C. Kim, “Effects of calcination and support on supported manganese catalysts for the catalytic oxidation of toluene as a model of VOCs,” *Res. Chem. Intermed.*, vol. 42, n^o 1, p. 185–199, 2016.

[275] C.-H. Wang, “Al_2O_3-supported transition-metal oxide catalysts for catalytic incineration of toluene,” *Chemosphere*, vol. 55, n^o 1, p. 11–17, 2004.

[276] C.-H. Wang, S.-S. Lin, C.-L. Chen, and H.-S. Weng, “Performance of the supported copper oxide catalysts for the catalytic incineration of aromatic hydrocarbons,” *Chemosphere*, vol. 64, n^o 3, p. 503–509, 2006.

[277] S. C. Kim, “The catalytic oxidation of aromatic hydrocarbons over supported metal oxide,” *J. Hazard. Mater.*, vol. 91, n^o 1, p. 285–299, 2002.

[278] S. M. Saqer, D. I. Kondarides, and X. E. Verykios, “Catalytic activity of supported platinum and metal oxide catalysts for toluene oxidation,” *Top. Catal.*, vol. 52, n^o 5, p. 517–527, 2009.

[279] M. Popova, Á. Szegedi, Z. Cherkezova-Zheleva, A. Dimitrova, and I. Mitov, “Toluene oxidation on chromium-and copper-modified SiO_2 and SBA-15,” *Appl. Catal. A-Gen.*, vol. 381, n° 1‑2, p. 26–35, 2010.

[280] P.-O. Larsson, A. Andersson, L. R. Wallenberg, and B. Svensson, “Combustion of CO and toluene; characterisation of copper oxide supported on titania and activity comparisons with supported cobalt, iron, and manganese oxide,” *J. Catal.*, vol. 163, n° 2, p. 279–293, 1996.

[281] H. L. Tidahy, S. Siffert, F. Wyrwalski, J.-F. Lamonier, and A. Aboukaïs, “Catalytic activity of copper and palladium based catalysts for toluene total oxidation,” *Catal. Today*, vol. 119, n° 1, p. 317–320, 2007.

[282] S. M. Saqer, D. I. Kondarides, and X. E. Verykios, “Catalytic oxidation of toluene over binary mixtures of copper, manganese and cerium oxides supported on γ-Al_2O_3,” *Appl. Catal. B Environ.*, vol. 103, n° 3, p. 275–286, 2011.

[283] F. Jiancai, C. Xiao, X. I. A. Qibin, X. I. Hongxia, and L. I. Zhong, “Effect of relative humidity on catalytic combustion of toluene over copper based catalysts with different supports,” *Chin. J. Chem. Eng.*, vol. 17, n° 5, p. 767–772, 2009.

[284] Á. Szegedi, M. Popova, K. Lázár, S. Klébert, and E. Drotár, “Impact of silica structure of copper and iron-containing SBA-15 and SBA-16 materials on toluene oxidation,” *Microporous Mesoporous Mater.*, vol. 177, p. 97–104, 2013.

[285] L. Meng and H. Zhao, “Low-temperature complete removal of toluene over highly active nanoparticles CuO-TiO_2 synthesized via flame spray pyrolysis,” *Appl. Catal. B Environ.*, vol. 264, p. 118427–118436, 2020.

[286] Q.-F. Deng, T.-Z. Ren, B. Agula, Y. Liu, and Z.-Y. Yuan, “Mesoporous $Ce_xZr_{1-x}O_2$ solid solutions supported CuO nanocatalysts for toluene total oxidation,” *J. Ind. Eng. Chem.*, vol. 20, n° 5, p. 3303–3312, 2014.

[287] Z. Ye, J.-M. Giraudon, N. Nuns, P. Simon, N. De Geyter, R. Morent, and J.-F. Lamonier, “Influence of the preparation method on the activity of copper-manganese oxides for toluene total oxidation,” *Appl. Catal. B Environ.*, vol. 223, p. 154–166, 2018.

[288] S. Behar, P. Gonzalez, P. Agulhon, F. Quignard, and D. Świerczyński, “New synthesis of nanosized Cu–Mn spinels as efficient oxidation catalysts,” *Catal. Today*, vol. 189, n° 1, p. 35–41, 2012.

[289] J. Hu, W. B. Li, and R. F. Liu, “Highly efficient copper-doped manganese oxide nanorod catalysts derived from CuMnO hierarchical nanowire for catalytic combustion of VOCs,” *Catal. Today*, vol. 314, p. 147–153, 2018.

[290] Y. Liu, L. Jia, Y. Lin, Y. Zhao, L. Sun, H. Ma, H. Kameyama, M. Sakurai, and Y. Guo, “Catalytic Combustion of Toluene over Cu–Mn Mixed Oxide Catalyst,” *J. Chem. Eng. Jpn.*, vol. 51, n° 9, p. 769–777, 2018.

[291] D. A. Aguilera, A. Perez, R. Molina, and S. Moreno, “Cu–Mn and Co–Mn catalysts synthesized from hydrotalcites and their use in the oxidation of VOCs,” *Appl. Catal. B Environ.*, vol. 104, n° 1‑2, p. 144–150, 2011.

[292] H. C. Genuino, S. Dharmarathna, E. C. Njagi, M. C. Mei, and S. L. Suib, “Gas-phase total oxidation of benzene, toluene, ethylbenzene, and xylenes using shape-selective manganese oxide and copper manganese oxide catalysts,” *J. Phys. Chem. C*, vol. 116, n^o 22, p. 12066–12078, 2012.

[293] H. J. Kim, S. W. Choi, C. S. Lee, B. Wielage, S. Bae, S. O. Obare, and H. I. Inyang, “Oxidation of Toluene on γ-Al_2O_3 Supported Copper–Manganese Catalysts,” *Environ. Eng. Sci.*, vol. 28, n^o 12, p. 827–833, 2011.

[294] W. B. Li, M. Zhuang, T. C. Xiao, and M. L. H. Green, “MCM-41 supported Cu- Mn catalysts for catalytic oxidation of toluene at low temperatures,” *J. Phys. Chem. B*, vol. 110, n^o 43, p. 21568–21571, 2006.

[295] X. Li, L. Wang, Q. Xia, Z. Liu, and Z. Li, “Catalytic oxidation of toluene over copper and manganese based catalysts: Effect of water vapor,” *Catal. Commun.*, vol. 14, n^o 1, p. 15–19, 2011.

[296] H. Wang, Y. Lu, Y. Han, C. Lu, H. Wan, Z. Xu, and S. Zheng, “Enhanced catalytic toluene oxidation by interaction between copper oxide and manganese oxide in Cu-O-Mn/γ-Al_2O_3 catalysts,” *Appl. Surf. Sci.*, vol. 420, p. 260–266, 2017.

[297] G. J. Hutchings, A. A. Mirzaei, R. W. Joyner, M. R. H. Siddiqui, and S. H. Taylor, “Effect of preparation conditions on the catalytic performance of copper manganese oxide catalysts for CO oxidation,” *Appl. Catal. A-Gen.*, vol. 166, n^o 1, p. 143–152, 1998.

[298] H. Lu, X. Kong, H. Huang, Y. Zhou, and Y. Chen, “Cu–Mn–Ce ternary mixed-oxide catalysts for catalytic combustion of toluene,” *J. Environ. Sci.*, vol. 32, p. 102–107, 2015.

[299] J. Papavasiliou, G. Avgouropoulos, and T. Ioannides, “Combined steam reforming of methanol over Cu–Mn spinel oxide catalysts,” *J. Catal.*, vol. 251, n^o 1, p. 7–20, 2007.

[300] Q. Tang, X. Gong, P. Zhao, Y. Chen, and Y. Yang, “Copper–manganese oxide catalysts supported on alumina: physicochemical features and catalytic performances in the aerobic oxidation of benzyl alcohol,”, *Appl. Catal. A-Gen.*, vol. 389, n^o 1‑2, p. 101–107, 2010.

[301] Q. Huang, Z. Zhang, Y. Chen, S. Zhu, and S. Shen, “Catalytic Combustion of Toluene with a Novel Mixed Cu.Mn Oxides Catalyst Supported on Cordierite,” *J. Chem. Eng. Jpn.*, vol. 43, n^o 4, p. 413–420, 2010.

[302] A. Białas, T. Kondratowicz, M. Drozdek, and P. Kuśtrowski, “Catalytic combustion of toluene over copper oxide deposited on two types of yttria-stabilized zirconia,” *Catal. Today*, vol. 257, p. 144–149, 2015.

[303] D. Romero, D. Chlala, M. Labaki, S. Royer, J.-P. Bellat, I. Bezverkhyy, J.-M. Giraudon, and J.-F. Lamonier, “Removal of toluene over NaX zeolite exchanged with Cu^{2+},” *Catalysts*, vol. 5, n^o 3, p. 1479–1497, 2015.

[304] E.-K. Lee, H.-S. Kim, K.-D. Jung, O.-S. Joo, and Y.-G. Shul, “Influence of copper precursors in the steam reforming of methanol over $Cu/SnO_2/SiO_2$ catalysts,” *React. Kinet. Catal. Lett.*, vol. 81, n^o 1, p. 177–181, 2004.

[305] Y. Yin, W.-J. Jiang, X.-Q. Liu, Y.-H. Li, and L.-B. Sun, “Dispersion of copper species in a confined space and their application in thiophene capture,” *J. Mater. Chem.*, vol. 22, n^o 35, p. 18514–18521, 2012.

[306] W. H. Lin and H. F. Chang, "Effect of chelating agents on the structure of electroless copper coating on alumina powder," *Surf. Coat. Technol.*, vol. 107, n^o 1, p. 48–54, 1998.

[307] O. Clause, L. Bonneviot, M. Che, M. Verdaguer, F. Villain, D. Bazin, and H. Dexpert, "Contrôle des étapes d'adsorption électrostatique et de greffage du complexe bis (éthylénediamine) cuivre (II) sur un gel de silice," *J. Chim. Phys.*, vol. 86, p. 1767–1775, 1989.

[308] S. U. N. Shuaishuai, M. A. O. Dongsen, and Y. U. Jun, "Enhanced CO oxidation activity of CuO/CeO_2 catalyst prepared by surfactant-assisted impregnation method," *J. Rare Earths*, vol. 33, n^o 12, p. 1268–1274, 2015.

[309] S. Karnjanakom, G. Guan, B. Asep, X. Hao, S. Kongparakul, C. Samart, and A. Abudula, "Catalytic upgrading of bio-oil over Cu/MCM-41 and Cu/KIT-6 prepared by β-cyclodextrin-assisted co-impregnation method," *J. Phys. Chem. C*, vol. 120, no. 6, p. 3396–3407, 2016.

[310] E. M. Del Valle, "Cyclodextrins and their uses: a review," *Process Biochem.*, vol. 39, n^o 9, p. 1033–1046, 2004.

[311] J. Szejtli, "Introduction and general overview of cyclodextrin chemistry," *Chem. Rev.*, vol. 98, n^o 5, p. 1743–1754, 1998.

[312] P. Blach, S. Fourmentin, D. Landy, F. Cazier, and G. Surpateanu, "Cyclodextrins: a new efficient absorbent to treat waste gas streams," *Chemosphere*, vol. 70, n^o 3, p. 374–380, 2008.

[313] J. Szejtli, "Utilization of cyclodextrins in industrial products and processes," *J. Mater. Chem.*, vol. 7, n^o 4, p. 575–587, 1997.

[314] F. Kayaci, H. S. Sen, E. Durgun, and T. Uyar, "Electrospun nylon 6,6 nanofibers functionalized with cyclodextrins for removal of toluene vapor," *J. Appl. Polym. Sci.*, vol. 132, n^o 18, 11 pages, 2015.

[315] Y. Matsui, "Complexes of copper (II) with cyclodextrins," *Bull. Chem. Soc. Jap.*, vol. 45, n^o 10, p. 3229, 1972.

[316] Y. Matsui, T. Kurita, M. Yagi, T. Okayama, K. Mochida, and Y. Date, "The formation and structure of Copper (II) complexes with cyclodextrins in an alkaline solution," *Bull. Chem. Soc. Jpn.*, vol. 48, n^o 7, p. 2187–2191, 1975.

[317] K. Mochida and Y. Matsui, "Kinetic study on the formation of a binuclear complex between copper (II) and cyclodextrin," *Chem. Lett.*, vol. 5, n^o 9, p. 963–966, 1976.

[318] A. C. F. Ribeiro, M. A. Esteso, V. M. M. Lobo, A. J. M. Valente, S. M. N. Simões, A. J. F. N. Sobral, L. Ramos, H. D. Burrows, A. M. Amado, and A. M. Amorim da Costa *et al.*, "Interactions of Copper (II) Chloride with β-Cyclodextrin in Aqueous Solutions," *J. Carbohydr. Chem.*, vol. 25, n^o 2‑3, p. 173–185, 2006.

[319] L. X. Song, M. Wang, Z. Dang, and F. Y. Du, "Meaningful differences in spectral performance, thermal behavior, and heterogeneous catalysis between ammonium molybdate tetrahydrate and its adduct of β-cyclodextrin," *J. Phys. Chem. B*, vol. 114, n^o 9, p. 3404–3410, 2010.

[320] E. Norkus, "Metal ion complexes with native cyclodextrins. An overview," *J. Incl. Phenom. Macrocycl. Chem.*, vol. 65, n^o 3‑4, p. 237–248, 2009.

[321] D. Prochowicz, A. Kornowicz, I. Justyniak, and J. Lewiński, “Metal complexes based on native cyclodextrins: Synthesis and structural diversity,” *Coord. Chem. Rev.*, vol. 306, p. 331–345, 2016.

[322] G. Kurokawa, M. Sekii, T. Ishida, and T. Nogami, “Crystal structure of a molecular complex from native β-cyclodextrin and copper (II) chloride,” *Supramol. Chem.*, vol. 16, n^o 5, p. 381–384, 2004.

[323] L. X. Song, J. Yang, L. Bai, F. Y. Du, J. Chen, and M. Wang, “Molecule-ion interaction and its effect on electrostatic interaction in the system of copper chloride and β-cyclodextrin,” *Inorg. Chem.*, vol. 50, n^o 5, p. 1682–1688, 2011.

[324] L. Bai, F. Wyrwalski, J.-F. Lamonier, A. Y. Khodakov, E. Monflier, and A. Ponchel, “Effects of β-cyclodextrin introduction to zirconia supported-cobalt oxide catalysts: From molecule-ion associations to complete oxidation of formaldehyde,” *Appl. Catal. B Environ.*, vol. 138, p. 381–390, 2013.

[325] L. Bai, F. Wyrwalski, M. Safariamin, R. Bleta, J.-F. Lamonier, C. Przybylski, E. Monflier, and A. Ponchel, “Cyclodextrin-cobalt (II) molecule-ion pairs as precursors to active Co_3O_4/ZrO_2 catalysts for the complete oxidation of formaldehyde: Influence of the cobalt source,” *J. Catal.*, vol. 341, p. 191–204, 2016.

[326] A. Jean-Marie, A. Griboval-Constant, A. Y. Khodakov, E. Monflier, and F. Diehl, “β-Cyclodextrin for design of alumina supported cobalt catalysts efficient in Fischer–Tropsch synthesis,” *Chem. Commun.*, vol. 47, n^o 38, p. 10767–10769, 2011.

[327] A. Tomer, F. Wyrwalski, C. Przybylski, J.-F. Paul, E. Monflier, M. Pera-Titus, and A. Ponchel, “Facile preparation of Ni/Al_2O_3 catalytic formulations with the aid of cyclodextrin complexes: Towards highly active and robust catalysts for the direct amination of alcohols,” *J. Catal.*, vol. 356, p. 111–124, 2017.

[328] H. Liu, Y. Li, H. Wu, T. Miyake, and D. He, “CO_2 reforming of methane over Ni/SBA-15 prepared with β-cyclodextrin–Role of β-cyclodextrin in Ni dispersion and performance,” *Int. J. Hydrog. Energy*, vol. 38, n^o 35, p. 15200–15209, 2013.

[329] H. Liu, Y. Li, H. Wu, H. Takayama, T. Miyake, and D. He, “Effects of β-cyclodextrin modification on properties of Ni/SBA-15 and its catalytic performance in carbon dioxide reforming of methane,” *Catal. Commun.*, vol. 28, p. 168–173, 2012.

[330] V. P. Santos, M. F. R. Pereira, J. J. M. Órfão, and J. L. Figueiredo, “The role of lattice oxygen on the activity of manganese oxides towards the oxidation of volatile organic compounds,” *Appl. Catal. B Environ.*, vol. 99, n^o 1‑2, p. 353–363, 2010.

Chapter II: Experimental Protocols and Techniques: synthesis, physicochemical characterizations and catalytic tests

2.1. Materials preparation

2.1.1. Synthesis of the stoichiometric Hap support

Stoichiometric hydroxyapatite, with a Ca/P molar ratio of 1.67, was prepared by a co-precipitation technique [1], according to the following equation:

$$10\ \mathrm{Ca(NO_3)_2} + 6\ \mathrm{NH_4H_2PO_4} + 14\ \mathrm{NH_3.H_2O} \rightarrow \mathrm{Ca_{10}(PO_4)_6(OH)_2} + 20\ \mathrm{NH_4NO_3} + 12\ \mathrm{H_2O} \quad (2.1)$$

150 mL of an aqueous solution of $Ca(NO_3)_2.4H_2O$ (0.0835 mole, Riedel-de Haën, purity ≥ 98%) was added dropwise to 500 mL of a $NH_4H_2PO_4$ solution (0.05 mole, Fluka; purity ≥ 99%) under stirring. The pH was maintained at 10 by properly adding ammonia (25%; Scharlau) to the reaction media. The procedure was conducted under reflux. A white precipitate is obtained. The maturation duration was 1 h under constant stirring. After filtration, washing with hot deionized water, and drying (80 °C for 18 h), a calcination step was performed in dry air (400 °C for 4 h, 2 $°C.min^{-1}$) to get the Hap support.

2.1.2. Synthesis of the Cu_xMn_yHap catalysts (10 wt% of TM)

CuHap: In a typical experiment, 1.76 g of $Cu(NO_3)_2.3H_2O$ (Sigma Aldrich, purity ≥ 99%) was dissolved in 50 mL of deionized water and the apatitic support (4.0 g) was then added. The pH of the Cu(II) nitrate aqueous solution (50 mL) was 4.0. This pH turned out to be 4.6 when the Hap support (solid) was added to the Cu(II) solution (50 mL). Rotary evaporation (Büchi Rotavapor R-114) was used to remove water under the following conditions: temperature of the water bath = 60 °C, rotational speed = 20 $rotations.min^{-1}$ (rpm), pressure = 70 mbar. After 30 min of evaporation (volume of the solution: 35 mL), the pH decreased to 4.3 and remained stable at this value after further evaporation of the solution. The recovered powder was dried and calcined in similar conditions to those relative to the Hap support.

MnHap: The synthesis was carried in a similar way as for CuHap using $Mn(NO_3)_2.4H_2O$ (Sigma Aldrich purity ≥ 97%) as Mn(II) precursor.

The $CuMn_2$Hap, CuMnHap, and Cu_2MnHap samples (Cu/Mn molar ratio: 0.5 ; 1 ; 2) were synthesized by dissolving the suitable Cu(II) and Mn(II) precursors in 50 mL of deionized water and subsequently treated in a similar manner to before. The weight percentages of Cu and Mn were 3.66% and 6.34%, 5.36% and 4.64%, 6.98% and 3.02% for $CuMn_2$Hap, CuMnHap, and Cu_2MnHap, respectively.

2.1.3. Synthesis of 10 Cu/Hap and 10 Cu-CD/Hap

The copper oxide catalyst with a theoretical copper content of 10 wt%, derived from β-CD-assisted synthesis was prepared by a wet impregnation technique inspired by the work of Bai *et al.* [2]. In a round bottom flask, 1.7559 g (7.19 mmol) of copper (II) nitrate trihydrate (Sigma Aldrich, purity ≥ 99%) was added to 50 mL of an aqueous solution containing 0.8156 g of native β-CD ($C_{42}H_{70}O_{35}$, M = 1134 $g.mol^{-1}$, Roquette Frères) so as to have a molar ratio of cyclodextrin to copper equal to 0.1. The solution was kept under constant stirring for 2 hours at room temperature. The Hap support (4 g) was then added to the copper-β-CD suspension and then stirred again for 2 supplementary hours. The resulting mixture was placed in a rotary evaporator (Büchi Rotavapor R-114, 60 °C, 20 rpm, 70 mbar) to remove water. The recovered solid was dried overnight in an oven at 80 °C, resulting in a blue colored powder with a tint of green, shown in Figure 2.1-a. Then, it was calcined under air flow at 400 °C for 10 h, leading to a dark gray powder (Figure 2.1-b). The so-obtained catalyst is denoted as 10 Cu-CD/Hap. A conventional copper oxide catalyst, with Cu loading of 10 wt%, prepared with the same procedure, but without addition of β-CD and with a smaller calcination time at 400 °C (4 h instead of 10 h) is designated as 10 Cu/Hap. This conventional catalyst was characterized by a blue color after drying step and a light grey color after calcination step (Figure 2.1). Dried samples are labeled with the suffix D.

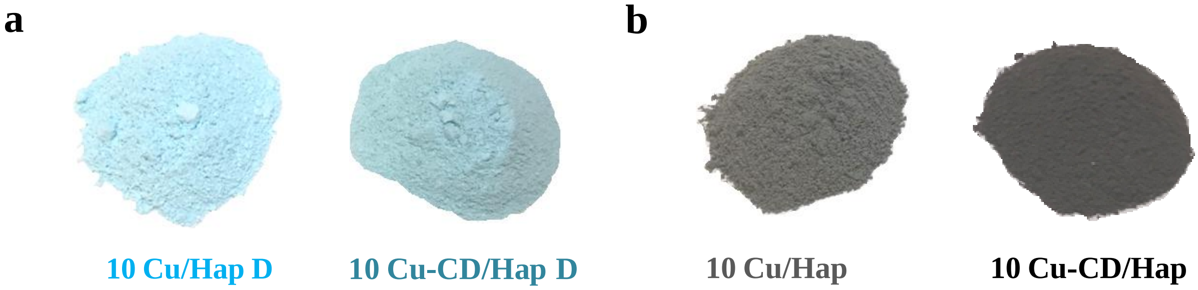

Figure 2.1. Dried a) and calcined b) 10 Cu/Hap and 10 Cu-CD/Hap samples.

2.1.4. Synthesis of Cu doped Hap (CuDHap)

To 25 mL of distilled water were added 25 mL of ammonia (25%; Scharlau) and 1 g of dried 10 Cu/Hap D. A suspension of light blue particles in a dark blue fluid appeared, as noted in Figure 2.2-a. The mixture was kept under constant stirring for 5 hours at room temperature. Afterwards, a centrifugation was performed at the speed of 4000 rpm for 45 min. A light blue sediment was obtained as displayed in Figure 2.2-b.

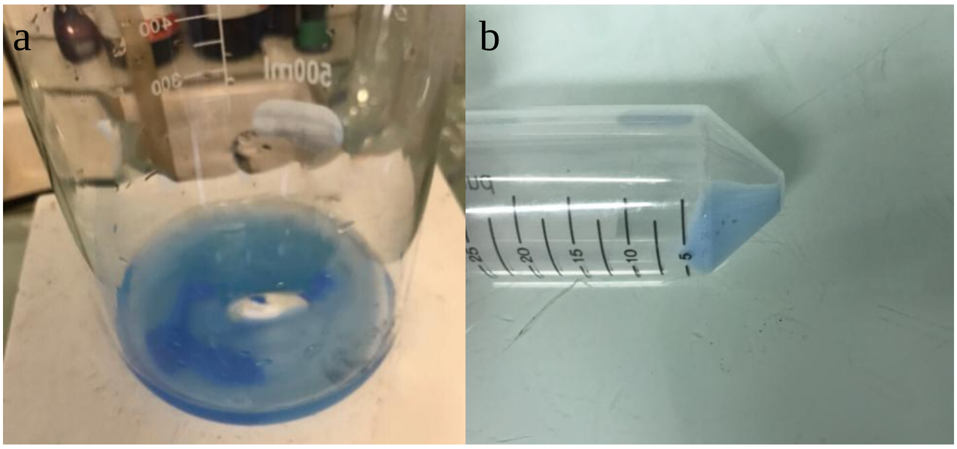

Figure 2.2. a) Suspension formed after addition of 10 Cu/Hap D to an aqueous solution of ammonia. b) Light blue sediment obtained after centrifugation of mixture shown in a).

The thus obtained blue sediment was dried in an oven at 80 °C overnight. The recovered blue product, presented in Figure 2.3-a, was finally calcined in dry air (400 °C for 4 h, 2 °C.min^{-1}) resulting in the final compound which retained a blue, albeit slightly less bright, color (Figure 2.3-b). This compound corresponds to copper-doped hydroxyapatite and will be hereafter labeled CuDHap.

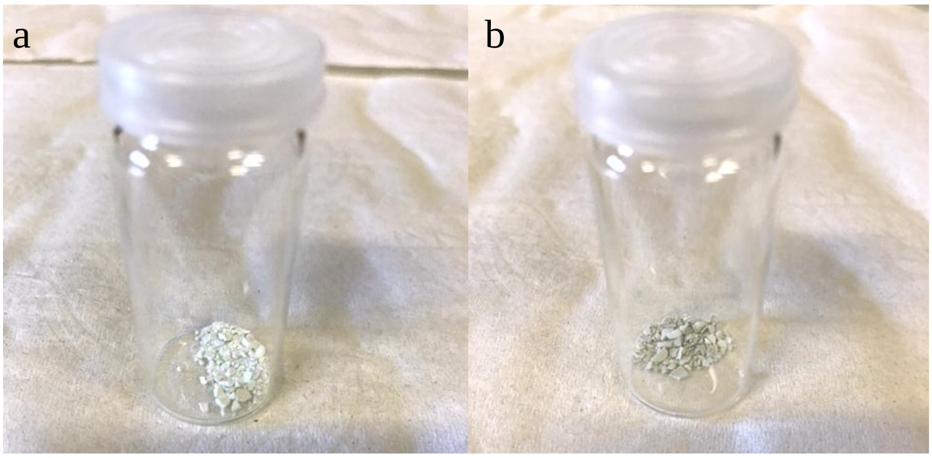

Figure 2.3. Dried a) and calcined b) CuDHap.

2.1.5. Synthesis of $Cu(NO_3)_2$

In a round bottom flask, 1.7559 g (7.19 mmol) of copper (II) nitrate trihydrate (Sigma Aldrich, purity ≥ 99%) was added to 50 mL of distilled water. The solution, represented in Figure 2.4-a, was first characterized by Raman spectroscopy before beginning the process of removing the water solvent by rotary evaporator (Büchi Rotavapor R-114) in which the following conditions were adopted: 60 °C, 20 rpm, and 70 mbar. However, with the current set of experimental conditions, complete solvent evaporation could not be achieved, as could be clearly observed in Figure 2.4-b. After removing the flask from the evaporation setup, the 3 mL of remaining solution were investigated by Raman analysis before being reinserted in rotary evaporator. However, the initially adopted conditions were modified: the temperature of the heating bath was increased to 90 °C and the pressure was reduced to 50 mbar. Owing to these more severe experimental conditions the solvent was entirely removed (Figure 2.4-c) and the resulting humid product was analyzed by Raman.

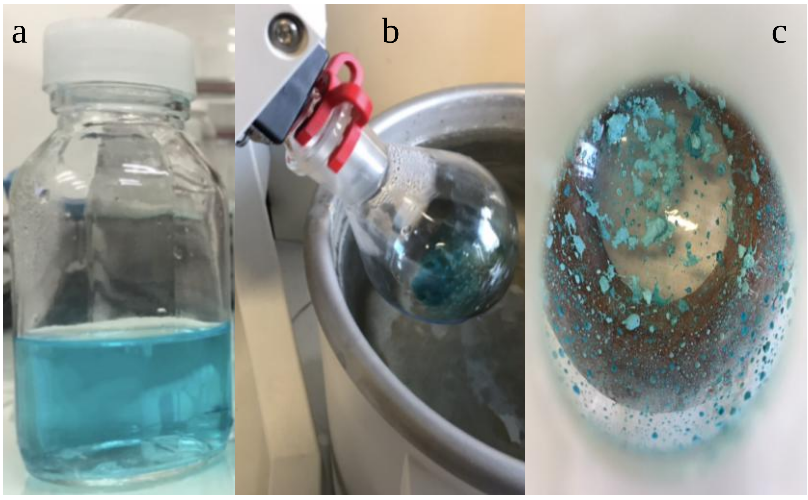

Figure 2.4. Copper nitrate aqueous solution a) before removal of the solvent; b) with 3 mL of solvent remaining; c) after complete removal of solvent.

2.1.6. Synthesis of $CuCD_x$ (x = 0.05; 0.1; 0.2)

In a round bottom flask, 1.7559 g (7.19 mmol) of copper (II) nitrate trihydrate (Sigma Aldrich, purity ≥ 99%) was added to 50 mL of an aqueous solution containing 0.8156 g of native β-CD ($C_{42}H_{70}O_{35}$, M = 1134 $g.mol^{-1}$, Roquette Frères) so as to have a molar ratio of cyclodextrin to copper equal to 0.1. The colloidal suspension was kept under constant stirring for 2 hours at room temperature. The same procedure was conducted for the preparation of two other $CuCD_x$ mixtures, where the amount of native β-CD added was changed to 0.4078 and 1.6312 g, so as to have β-CD/Cu molar ratios of 0.05 and 0.2, respectively. In the course of the 2 hours of stirring following the addition of β-CD the limpidity of the mixture gradually increased. The three mixtures of $CuCD_x$ with different β-CD/Cu molar ratios (0.05; 0.1 and 0.2) are illustrated in Figure 2.5. It can be seen that with increasing values of this ratio the mixtures evolve from homogeneous solution to suspension, consisting of a blue fluid containing white suspended particles.

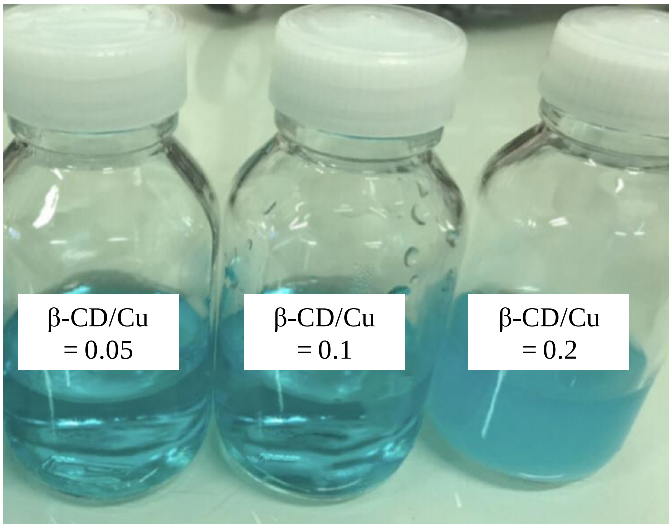

Figure 2.5. $CuCD_x$ (x = 0.05; 0.1; 0.2).

The 50 mL colloidal solution $CuCD_{0.1}$ was placed in a rotary evaporator (Büchi Rotavapor R-114, 60 °C, 20 rpm, 70 mbar) to remove water. After elimination of 35 mL of water, the rotation was stopped, the round bottom flask elevated from the heating bath, the pressure increased to 1 bar and finally the round bottom flask removed from the setup in order to conduct a Raman analysis on the remaining 15 mL of aqueous mixture. Once the Raman analysis completed, the flask containing the remaining Cu/β-CD mixture was placed once more in the rotary evaporator under the initial evaporation conditions to proceed with the removal of the solvent. However, under these conditions, all remaining water could not be eliminated and 3 mL of solvent persisted inside the round bottom flask and were analyzed by Raman spectroscopy. Subsequently, the flask was placed, with its content, in an oven at 80 °C and kept overnight. The recovered powder had a homogeneous green color, shown in Figure 2.6, and was designated by Cu/β-CD D.

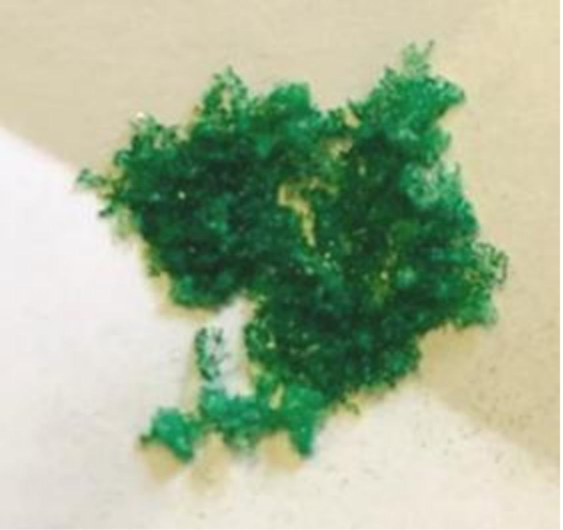

Figure 2.6. Dried powder of Cu/β-CD D.

2.1.7. Synthesis of β-CD/Hap D

In a round bottom flask, 4 g (3.98 mmol) of calcined Hap support was added to 50 mL of an aqueous solution containing 0.8156 g of native β-CD ($C_{42}H_{70}O_{35}$, M = 1134 g.mol^{-1}, Roquette Frères). The solution was kept under constant stirring for 2 hours at room temperature. The resulting mixture was placed in a rotary evaporator (Büchi Rotavapor R-114, 60 °C, 20 rpm, 70 mbar) to remove water. The retrieved solid was dried overnight in an oven at 80 °C, resulting in a white powder.

2.1.8. Synthesis of Mn_xO_y standards

2.1.8.1. Synthesis of ε-MnO_2

For the synthesis of ε-MnO_2, the following procedure was adopted: 1.0 g of perovskite $LaMnO_3$ was added to 50 mL of a 10 mol.L^{-1} nitric acid (65 ~ 70%, Alfa Aesar) solution and stirred at room temperature for 15 h continuously. Afterwards, the suspension was centrifuged at the speed of 4000 rpm for 15 min. The sediment was resuspended in water and centrifuged again, in the same conditions, twice. The obtained product was dried at 80 °C overnight and finally calcined in dry air (300 °C for 2 h, 2 °C.min^{-1}) to get the ε-MnO_2 standard.

2.1.8.2. Synthesis of β-MnO_2

β-MnO_2 was prepared as follows: ammonium persulphate $(NH_4)_2.S_2O_8$ (98%, Sigma-Aldrich) was employed as an oxidizing agent for manganese sulphate monohydrate, $MnSO_4.H_2O$ (99%, Merck). 0.04 mole of $(NH_4)_2.S_2O_8$ were dissolved in 200 mL of distilled water, then added dropwise, under constant stirring, to 0.04 mole of $MnSO_4.H_2O$ dissolved in 200 mL of distilled water as well and heated at 85 °C. The gradual formation of a black precipitate of MnO_2 can be perceived in the course of the reaction. Once the reactant addition completed (≈ 1 h), the suspension was further stirred for 5 h, then filtered and washed with hot deionized water. The resulting black product was dried at 85 °C overnight and finally calcined in dry air (400 °C for 5 hours, 2 °C.min^{-1}) to obtain β-MnO_2 compound.

2.1.8.3. Synthesis of Mn_2O_3

High purity Mn_2O_3 powder (98%) was purchased from Alfa-Aesar, and used as standard in the present study.

2.1.8.4. Synthesis of γ-MnOOH

γ-MnOOH was synthesized using a simple hydrothermal method. 3 mL of absolute ethanol were added to 47 mL of aqueous solution of $KMnO_4$ (0.1 mol.L^{-1}) under intensive stirring at room temperature, which was maintained for 45 min. The resulting mixture was placed and sealed inside a Teflon-lined stainless steel autoclave, then heated at 140 °C for one day. Afterwards, the autoclave was rapidly cooled down to room temperature by means of tap water. Subsequently, a filtration of the formed light brown precipitate was conducted, followed by a washing step with distilled water till obtainment of a neutral pH, and finally the product was dried at 80 °C overnight.

2.1.8.5. Synthesis of Mn_5O_8

Mn_5O_8 was prepared according to the method described thusly: A certain amount of the previously synthesized γ-MnOOH was placed in an alumina crucible and heated at 400 °C in flowing N_2 atmosphere for 2 h. Following this, the light brown γ-MnOOH powder was altered into a blackish compound, signaling the occurrence of a phase transition.

2.1.8.6. Synthesis of Mn_3O_4

Mn_3O_4 was acquired through a reduction process involving $KMnO_4$ and glycerol. The addition, drop-wise, of 50 mL of glycerol (0.4 mol.L^{-1}) to 100 mL of $KMnO_4$ (0.3 mol.L^{-1}) solution, under vigorous stirring for 1 min (1200 rpm) at room temperature, resulted in the formation of a gel. The latter was set aside and aged for 72 h, still at room temperature. Following this aging step, the gel was heated at 80 °C for 5 h to eliminate excess water. Subsequently, the deposit was washed with 400 mL of water and centrifuged to remove any remaining impurities. Lastly, the material was dried in an oven at 80 °C, resulting in the formation of the final black product.

2.1.8.7. Synthesis of MnO

The synthesis of MnO was carried out through a reduction route as well, this time involving β-MnO_2. 0.5 g of the above prepared β-MnO_2 were heated at 500 °C for 3 h with a heating rate of 2 °C.min^{-1} in H_2 atmosphere. A grey powder was obtained, corresponding to the MnO product.

2.1.9. Synthesis of x Mn/Hap catalysts (with x = 2.5; 5; 10; 20 wt%)

Samples consisting of hydroxyapatite support loaded with 2.5, 5, 10, and 20 wt% of manganese (x Mn/Hap) were prepared through a wet impregnation procedure which will be summarized as follows: In the case of 10 Mn/Hap for example, 4 g of Hap were added to a 50 mL of 0.81 mol.L^{-1} aqueous solution of $Mn(NO_3)_2.4H_2O$ (Sigma–Aldrich, purity ≥ 97%). The solvent of the obtained mixture was eliminated in a rotary evaporator (60 °C, 20 rpm, 70 mbar). The resulting solid was subsequently dried overnight at 80 °C, before being at last calcined at 400 °C for 4 h under air flow. The as acquired sample is designated as 10 Mn/Hap.

2.2. Methods of characterization

2.2.1. X-Ray Diffraction (XRD)

Powder XRD measurements were performed on a laboratory X-ray diffractometer (Bruker AXS D8 Advance powder diffractometer equipped with a LynxEye Super Speed detector) using a Cu-Kα radiation (λ = 1.5418 Å), with a step of 0.02 ° in the 2θ range of 10 – 55 ° and a count time of 5 s. The sample was ground gently, then filled in the depression of the XRD sample holder and smoothed flat. Identification of crystalline phases was made using EVA software, by comparison to reference patterns registered in Powder Diffraction Files (PDF) of the International Centre for Diffraction Data (ICDD) database. The Scherrer equation given below, was employed for the calculation of the mean crystallite size of Hap supported Cu and/or Mn oxide catalysts:

$$\mathrm{D}\ (\text{Å}) = \frac{k\lambda}{\beta\cos\theta} \qquad (2.2)$$

where D is the crystallite size in Angström, k a dimensionless shape factor taken as 0.9, λ is the wavelength of the Kα radiation in Angström, θ the diffraction angle in radians, and β full peak width at half-maximum intensity in radians after subtracting the instrumental line broadening using LaB_6 as an internal reference.

Regarding quantitative analysis conducted over XRD results, it should be noted that a quick semi-quantitative method for the determination of the concentration of a phase in a sample of phase mixtures relies on the use of the values of I/Icor provided from the ICDD database. I/Icor is the ratio of the intensity of the strongest line of the sample to the intensity of the strongest line (reflection (113)) of trigonal corundum (alpha alumina) for the 50% – 50% (weight) mixture of the 2 phases. I/Icor constitutes a special case of RIR, "Reference Intensity Ratio", a procedure used for carrying out quantitative analysis. Thus, the weight fractions of a mixture of two phases “x” and “y” will be given by [3], [4]:

$$\frac{X_x}{Xy} = \frac{I_{(hkl)x}}{I_{(hkl)y}} * \frac{I/I_{cor\ y}}{I/I_{cor\ x}} \qquad (2.3)$$

where X denotes the weight fraction of the phase and I the intensity of the diffraction line.

2.2.2. N_2 physisorption analysis

Nitrogen adsorption-desorption measurements were conducted with a Micromeritics Tristar II Surface Areas and Porosity apparatus. The specific surface areas were calculated according to the BET (Brunauer, Emmet, and Teller) method, based on the evaluation of the quantity of physisorbed N_2, whereas, pore volume and size distribution were determined by the BJH (Barrett, Joyner, and Halenda) method. Prior to data collection, each sample (≈ 500 mg) was outgassed under vacuum at 200 °C for 2 h.

2.2.3. Scanning Electron Microscopy (SEM)

Scanning electron micrographs were recorded on a JEOL JSM 7500F operating at an accelerating voltage of 5 kV. Prior to analysis, a thin chromium coating was performed on the samples in order to reduce potential charging effect.

2.2.4. Thermal Analysis coupled with Mass Spectrometry (TGA/DSC-MS)

A thermal analysis balance instrument, model: SDT 2960 DSC-TGA X, was used to conduct simultaneous Thermal Gravimetric Analysis and Differential Scanning Calorimetry (TGA/DSC) under an atmosphere of 20% O_2 in He (100 $mL.min^{-1}$). The sample was heated at a rate 5 $°C.min^{-1}$ from 25 °C to 1000 °C. A Pfeiffer vacuum Omnistar GSD 320 mass spectrometer was coupled to the exit of the TGA/DSC analysis instrument, allowing the monitoring of the following selected m/z signals: m/z = 12, 14, 16, 17, 18, 28, 30, 44, and 46.

2.2.5. Infrared spectroscopy (IR)

2.2.5.1. Transmission Fourier Transform Infrared spectroscopy (FTIR)

FTIR spectra were recorded at room temperature, under vacuum, in a spectral range spanning from 200 to 4000 cm^{-1}, while using a Nicolet 460 spectrometer. These spectra were an average of 256 scans with a spectral resolution of 4 cm^{-1}. Thin, disk-shaped pellets of the catalysts were prepared by compressing 30 mg of powder derived from an intimate mixture of 1 mg of the sample combined with 100 mg of dried KBr. A spectrum of an empty cell was first recorded. This spectrum served as a background spectrum, which would be subsequently subtracted from that of the samples analyzed.

2.2.5.2. Attenuated Total Reflectance-Fourier Transform Infrared spectroscopy (ATR-FTIR)

The different infrared spectra were obtained using a Thermoscientific Nicolet iS50 attenuated total reflectance-Fourier transform infrared (ATR-FTIR) spectrometer. The spectra were recorded using a Deuterated Tri-Glycine Sulfate (DTGS) pyroelectric detector. Samples were directly pressed between the detector window and a diamond crystal. The number of scans was set at 64 with a resolution of 2 cm^{-1}. Spectra were measured over a far-infrared range of 1800 – 80 cm^{-1} and a mid-infrared range of 4000 – 400 cm^{-1}. Changing the beamsplitter between measurements so as to be able to collect the far-infrared portion of the spectrometer was easily accomplished with the automatic beamsplitter exchanger (ABX) on the Nicolet iS50 spectrometer. The unique ABX design allows automated switching between measurement modes through a simple click on the desired infrared range achieved *via* the use of the OMNIC software.

2.2.6. Temperature Programmed Reduction coupled with Mass Spectrometry (H_2-TPR/MS)

The H_2-temperature-programmed reduction (H_2-TPR) experiments were conducted using a Micromeritics Autochem II (2920) instrument, equipped with a U-shaped quartz reactor. Prior to starting the analysis, fresh (200 mg) and used catalysts (100 mg) were treated in Ar at 150 °C for 1 h. After cooling down, the H_2-TPR measurements were conducted in 5 vol% H_2/Ar gaseous mixture (50 $mL.min^{-1}$) from room temperature to 800 °C (10 $°C.min^{-1}$). The amount of consumed H_2 was measured by a thermal conductivity detector (TCD) and calculated from the integrated peak areas of the profiles. The produced water was confined in a cold trap composed of isopropanol and liquid nitrogen before reaching the detector. The outlet gases were identified through the study of m/z signals, acquired by coupling the H_2-TPR instrument with a mass spectrometer (MS).

2.2.7. X-Ray Photoelectron Spectroscopy (XPS)

XPS analysis was performed on an AXIS Ultra DLD Kratos spectrometer equipped with a monochromatic Al-Kα source (hν = 1486.6 eV), operating at 120 W. Irradiation is performed at ambient temperature, under ultra-vacuum conditions (base pressure: 10^{-9} mbar). The photoelectron spectra were calibrated using the C 1s signal detected at a binding energy of 284.8 eV from contaminant carbon. Data treatment was conducted using CasaXPS software. Two recordings of Cu 2p core level XPS spectra were carried out: one at the beginning and one at the end of XPS analysis, in order to monitor the potential occurrence of an XPS-induced reduction of copper particles during data acquisition. The average oxidation state (AOS) of Mn was calculated, based on the magnitude of the Mn 3s multiplet splitting. Finally, XPS quantification was performed from the study of peak core levels of Ca 2p, P 2p, O 1s, Cu 2p, and/or Mn 2p (depending on whether Cu and /or Mn are present in the sample). However, it should be noted that the measured areas of the main peaks obtained cannot be used directly for the calculation of atomic percentages and ratios between different elements. Indeed, a preliminary correction is required. The latter will take into account 3 factors which are: T, the transmission function of the spectrometer; σ, the photoionization cross section, defined as the probability of emission of the electron by photoionization, represented by RSF (Relative Sensitivity Factors) in Casa XPS; and λ or MFP, the mean free path of photoelectrons in the solid, which is the distance traveled by an electron between two inelastic shocks.

Thus, the approach to be adopted for an XPS quantitative analysis, would consist simply, after subtraction of a defined background (linear, shirley, or other…), to divide the raw peak area by the three factors mentioned above, and as presented in the following equation:

$$\text{Corrected area} = \frac{\text{Raw area}}{\text{T x RSF x MFP}} \qquad (2.4)$$

The values thus normalized, having removed instrumental and sample artefacts, can be used for calculating atomic ratios and percentages.

Nevertheless, it ought to be pointed out that in the particular case of binary copper-manganese Hap supported samples, further steps were taken for the XPS quantification of Cu in order to remove the Mn Auger contribution from the total envelope of the Cu 2p core level. This was performed according to the method described in the work of Ye *et al.* [5].

Last but not least, regarding the curve fitting conducted in the case of Mn/Hap catalysts using the Mn_xO_y reference compounds envelopes, the operation consisted simply in creating asymmetric lineshapes derived from the Mn 2p envelope of these Mn_xO_y reference compounds with the intention of then employing each of the extracted peak shapes as component in a peak model. The procedure was carried out in a similar manner to that adopted for the removal of the Mn Auger contribution from the total envelope of the Cu 2p core level and it can be described as follows:

In order to determine the contribution of the different types of Mn oxides to the Mn 2p spectrum of Mn/Hap catalysts, the data from the Mn 2p region of each of the Mn_xO_y reference compounds will be used to create a lineshape, assumed to represent the presence of the respective Mn_xO_y phase in the Mn-based catalysts. As said above, the intention will be to use the extracted peak shape as a component in a peak model. Components in peak models are designed to represent the signal above background and therefore the data in the region must be background subtracted using a background typical for the data to which the component is intended for use. Therefore, we used a shirley background for both the Mn 2p region of Mn_xO_y reference compounds from which a peak model is to be created, and for the region created in the Mn 2p VAMAS block of the Mn/Hap catalysts, where the defined Mn 2p lineshape will be introduced.

Background subtraction is performed on the Test Data property page of the Spectrum Processing dialog window. It is important for the component based on data to be appropriately defined, which means that the block identifier must begin with the % character. The % prefix to the block identifier causes the normalization of the lineshape when used in peak models. Without the % character the data would need additional manual processing.

The full width at half-maximum (FWHM) for lineshapes based on data should be fixed at unity. Hence, a value of 1 must be put into the FWHM field for the component using the lineshape, and introduce the # character without any numerical value into the constraint field, resulting in stable and fixed parameter at the current value i.e. 1. A similar constraint will be performed for the position of the component with the latter fixed at the value noted for the lineshape corresponding to each of the Mn_xO_y reference compounds respectively.

Finally, for each Mn/Hap catalyst, the Mn 2p peaks present in the Mn 2p core level spectra, will be relied on to accomplish a good fitting of the intensity of the Mn 2p component, for which a fixed synthetic lineshape, already constructed based on the Mn 2p region in the Mn_xO_y reference compounds, will be attributed.

2.2.8. Raman

Raman spectra were collected with an XploRA PLUS Raman Microscope (HORIBA Jobin Yvon) equipped with a CCD silicon detector cooled by means of a Peltier device. Raman analysis was conducted using a laser wavelength of 532 nm with an output power of 20 mW, which was reduced by attenuation filters to 0.2 mW on the sample. However, for the Cu/β-CD D product, even under these conditions, which correspond to the lowest laser power, the sample was subjected to local heating, resulting in its thermal degradation. Thus, in this particular situation, the solid was covered by a thin layer of water which defocuses the laser impact and accords improved heat dispersion, therefore preventing the material's degradation.

For all conducted analysis, a 100X std objective was employed resulting in a laser spot of 0.72 µm. The Raman spectrometer was controlled using the software package LabSpec 6. The presented spectra corresponded to the average of 5 scans with 1800 s acquisition time for each scan. The spatial resolution was about 100 µm. All measurements were taken at room temperature. Preceding Raman analysis a calibration step was performed using a silicon wafer characterized by the Si line at $\bar{\upsilon} = 520.7\ cm^{-1}$.

In the case of solutions' Raman analysis, the solutions were placed in 3500 µL quartz macro cuvette (THORLABS) which in turn was inserted in a cuvette holder. No attenuation filters were used and the acquisition time was reduced to 180 s.

Regarding image acquisition, the system is equipped with standard white light illumination of the sample. A colour camera linked to the software allowed the sample to be visualised, and the image to be captured on the computer and saved.

2.2.9. Time of Flight Secondary Ion Mass Spectrometry (ToF-SIMS)

Time-of-Flight Secondary Ion Mass Spectrometry (ToF-SIMS) data were collected using a TOF·SIMS^5 spectrometer (ION-TOF GmbH Germany) equipped with a bismuth liquid metal ion gun (LMIG). Spectra were generated with a pulsed 25 keV Bi^{3+} primary ion beam (≈ 0.25 pA target current) bombarding the sample, and were gathered in 500 µm × 500 µm areas. The primary ion fluence was maintained below the static mode limit of 10^{12} ions.cm^{-2}. A pulsed, low energy (≈ 20 eV) electron flood gun was used for charge neutralization. A cycle time of 270 µs was employed resulting in data acquisition over a mass range of m/z = 0 – 6500 for both positive and negative secondary ions. The secondary ions were identified by their exact mass, coupled with the appropriate intensities for the expected isotope pattern.

2.2.10. X-Ray Absorption Spectroscopy (XAS)

Before reporting the experimental procedure, it should be first noted that all XAS experiments were conducted by Dr Asma TOUGERTI and Dr Jean-Marc GIRAUDON. In the current work, X-ray emission and high energy resolution fluorescence detection (HERFD)-XAS spectra were collected, meaning that the incident energy was varied around Mn K absorption edge in the range of 6530 – 6620 eV while the fluorescence detection energy was fixed to K_β emission line with energy at 6491.5 eV. Regarding the overall setup, Mn K edge HERFD-XAS spectra were recorded at SOLEIL synchrotron facility (Gif sur Yvette, France) on the GALAXIES beamline [6]. The energy of the incident radiation was selected using fixed-exit Si(111) double-crystal monochromator. Mn K edge HERFD-XAS and spectra were recorded with spherically bent crystals in a Rowland geometry: the K_β fluorescence line of cobalt, a germanium crystal Ge (220) was used. A bag filled with helium was positioned between the sample and the analyzer crystal to limit the absorption of the fluorescence signal by air. The fluorescence signal was then collected on the avalanche photodiode detector (APD). The sample placed on the *in situ* catalytic cell [7] was heated up to 400 °C with a ramp of 2 °C.min^{-1}. The following experimental conditions were adopted for carrying out the tests:

- All Mn-bearing compounds were diluted in boron nitride (BN) to 1% in order to avoid self-absorption.
- The bottle used for conducting the in situ reduction experiments consisted of a 5 vol.% H_2/N_2 gaseous mixture with a 30 mL.min^{-1} flow rate.
- For each test 100 mg of the Mn-bearing sample was used.

In the upcoming XANES (X-ray absorption near edge structure) analysis of the results derived from the experiments conducted above, no detailed discussion of the pre-edge feature will be performed, seeing as pre-edge measured using HERFD may result in the modification of some spectral features in the pre-edge region [8]–[11].

2.3. Catalytic activity tests

The catalytic tests were performed at atmospheric pressure in a continuous-flow fixed-bed Pyrex reactor. For each test, 200 mg of catalyst were placed in the reactor which was set in an electric furnace. Two thermocouples were employed, one fixed to the exterior of the reactor and one placed into a thermowell, positioned in the middle of the catalyst bed, in order to perform an ongoing monitoring of the reaction temperature. Toluene vapors were generated through the use of a stainless steel saturator electrically heated by a temperature controller instrument (Watlow SD series). Both mass flow controllers and toluene heating temperature were adjusted to control the toluene concentration and space velocity.

Regarding the catalytic tests carried out over Cu_xMn_yHap catalysts, the reactive gas mixture consisted of 800 ppmv of toluene diluted in dry air (100 mL.min^{-1}) corresponding to a gas hourly space velocity (GHSV) of 14500 h^{-1}. The catalysts were activated in air at 390 °C for 2 h (75 mL.min^{-1}) then submitted to the reactive mixture for 1 h before decreasing the temperature from 390 °C to 25 °C at a rate of 0.5 °C.min^{-1}. As for the conducted stability tests, following an activation step at 200 °C for 2 h in air flow (75 mL.min^{-1}), the catalysts were exposed to the reactive mixture at 200 °C for 24 h. At the end of each stability test, no more reactive gaseous mixture was sent to the catalyst, the furnace was turned off and the system cooled down to room temperature under static conditions.

Regarding the 72 h stability tests performed on 10 Cu/Hap and 10 Cu-CD/Hap, the reactive gas mixture consisted first of 200 ppmv (from 0 to 24 h), then 400 ppmv (from 24 to 48 h), and finally 800 ppmv (from 48 to 72 h) of toluene diluted in dry air (100 mL.min^{-1}) corresponding to a gas hourly space velocity (GHSV) of 14500 h^{-1}. Prior to each stability test, the samples were activated in dry air at 390 °C for 2 h (75 mL.min^{-1}). Then, the temperature was decreased to 250 °C, and the catalyst was exposed to the reactive gaseous mixture for 72 h. The catalyst was kept in flowing air (90 – 300 min) during the stabilization of the new toluene concentration. At the end of each stability test, no more reactive gaseous mixture was sent to the catalyst, the furnace was turned off and the system cooled down to room temperature under static conditions. The used catalysts were labeled with the suffix U.

The concentrations of the gaseous reactants and products were assessed by gas chromatograph (7860A Agilent Gas Chromatograph) equipped with two detectors and two columns: a Thermal Conductivity Detector (TCD) that identifies permanent gases (CO, CO_2, etc.), separated on a Restek Shin Carbon ST/Silco HP NOC 80/100 micro packed column; and a Flame Ionization Detector (FID) that recognizes hydrocarbons and aromatic compounds (toluene, benzene, etc.), separated on a capillary column CP-Wax 52 CB: 25 m, Ø 0.25 mm × 1.2 µm.

Toluene conversion (C_t) was evaluated by the following equation:

$$C_t\ (\%) = \frac{[\text{toluene}]_i - [\text{toluene}]_t}{[\text{toluene}]_i} \times 100 \quad (2.5)$$

where $[\text{toluene}]_i$ and $[\text{toluene}]_t$ correspond, respectively, to toluene inlet and outlet concentrations.

CO_2 yield was calculated as follows:

$$C_{CO_2}\ (\%) = \frac{[CO_2]_t \times 100}{7 \times [\text{toluene}]_i} \qquad (2.6)$$

where $[CO_2]_t$ was the CO_2 outlet concentration.

The standardised rates of toluene conversion r_{190} and r_{250} expressed in mole of reacted toluene per hour and per mol of transition metal (TM), were determined according to:

$$r = \frac{\text{ppmv Tol} \times F_T \times C_t}{V_m \times n_{TM}} \qquad (2.7)$$

where F_T was the total volumetric flow rate (L.h^{-1}), C_t the toluene conversion at 190 °C (in the case of r_{190}) or 250 °C (in the case of r_{250}), V_m the molar volume equal to 24.4 L.mol^{-1}, and n_{TM} the total amount of TM. It should be noted that the temperatures of 190 °C and 250 °C were selected because they correspond to the light-off temperatures, defined as the temperatures at which 50% of toluene is converted, of the most active catalysts among Cu_xMn_yHap and 10 Cu(-CD)/Hap catalysts, respectively.

The productivity (P) expressed in mole of toluene converted into CO_2 per hour was quantified as follows:

$$\mathrm{P\ (mol\ CO_2.h^{-1})} = \frac{\mathrm{ppmv\ Tol} \times \mathrm{F_T} \times \mathrm{C_{CO_2}}}{\mathrm{V_m}} \qquad (2.8)$$

References

[1] L. Silvester, J.-F. Lamonier, R.-N. Vannier, C. Lamonier, M. Capron, A.-S. Mamede, F. Pourpoint, A. Gervasini, and F. Dumeignil, « Structural, textural and acid–base properties of carbonate-containing hydroxyapatites », *J. Mater. Chem. A*, vol. 2, no. 29, p. 11073–11090, 2014.

[2] L. Bai, F. Wyrwalski, J.-F. Lamonier, A. Y. Khodakov, E. Monflier, and A. Ponchel, « Effects of β-cyclodextrin introduction to zirconia supported-cobalt oxide catalysts: From molecule-ion associations to complete oxidation of formaldehyde », *Appl. Catal. B Environ.*, vol. 138, p. 381–390, 2013.

[3] P. Gravereau, *Introduction à la pratique de la diffraction des rayons X par les poudres*. France: Université Bordeaux 1, 2011.

[4] S. Hillier, « Accurate quantitative analysis of clay and other minerals in sandstones by XRD: comparison of a Rietveld and a reference intensity ratio (RIR) method and the importance of sample preparation », *Clay Miner.*, vol. 35, n° 1, p. 291–302, 2000.

[5] Z. Ye, J.-M. Giraudon, N. Nuns, P. Simon, N. De Geyter, R. Morent, and J.-F. Lamonier, « Influence of the preparation method on the activity of copper-manganese oxides for toluene total oxidation », *Appl. Catal. B Environ.*, vol. 223, p. 154–166, 2018.

[6] J.-P Rueff, J. M. Ablett, D. Ceolin, D. Prieur, T. Moreno, V. Baledent, B. Lassalle-Kaiser, J. E. Rault, M. Simon, and A. Shukla, « The GALAXIES beamline at the SOLEIL synchrotron: inelastic X-ray scattering and photoelectron spectroscopy in the hard X-ray range », *J. Synchrotron Radiat.*, vol. 22, n° 1, p. 175–179, 2015.

[7] C. La Fontaine, L. Barthe, A. Rochet, and V. Briois, « X-ray absorption spectroscopy and heterogeneous catalysis: Performances at the SOLEIL's SAMBA beamline », *Catal. Today*, vol. 205, p. 148–158, 2013.

[8] A. Bordage, V. Trannoy, O. Proux, H. Vitoux, R. Moulin, and A. Bleuzen, « In situ site-selective transition metal K-edge XAS: a powerful probe of the transformation of mixed-valence compounds », *Phys. Chem. Chem. Phys.*, vol. 17, n° 26, p. 17260–17265, 2015.

[9] P. Glatzel, R. Alonso-Mori, and D. Sokaras, « Hard x-ray photon-in/photon-out spectroscopy: instrumentation, theory and applications », *X-Ray Absorpt. X-Ray Emiss. Spectrosc. Theory Appl.*, vol. 1, p. 125–153, 2016.

[10] A. A. Guda, N. Smolentsev, M. Rovezzi, E. M. Kaidashev, V. E. Kaydashev, A. N. Kravtsova, V. L. Mazalova, A. P. Chaynikov, E. Weschke, and P. Glatzel, « Spin-polarized electronic structure of the core–shell ZnO/ZnO: Mn nanowires probed by X-ray absorption and emission spectroscopy », *J. Anal. At. Spectrom.*, vol. 28, n° 10, p. 1629–1637, 2013.

[11] X. Wang, F. M. de Groot, and S. P. Cramer, « Spin-polarized x-ray emission of 3 d transition-metal ions: a comparison via K α and K β detection », *Phys. Rev. B*, vol. 56, n° 8, p. 4553–4564, 1997.

Chapter III: Binary Cu-Mn oxides supported on hydroxyapatite materials for Toluene Total Oxidation

3.1. Introduction

As has been previously discussed in the literature review chapter, the use of transition metal oxides (TMO) as a cost efficient alternative to noble metal based catalysts in the total oxidation of toluene has become the focus of many recent studies. Among said TMO, copper and manganese oxides have generated a lot of attention due to their superior catalytic activity and selectivity towards the desired products (CO_2 and H_2O) [1]–[3]. Therefore, the use of a binary copper-manganese oxide can be an attractive strategy to improve the performance of the catalyst in the total oxidation of toluene. In that way, it has already been reported in the literature that bulk [4]–[9] and supported [5], [10]–[13] Cu-Mn binary oxides can be considered as efficient catalysts in toluene oxidation, for which they exhibit higher catalytic activity than the single metal counterparts.

Important parameters such as the methods of synthesis, total TM loading, temperature of calcination, nature of the support, play key roles in tuning the optimized Cu/Mn ratio for the oxidation in toluene oxidation.

The present work will focus on dispersing these active metal species by wet co-impregnation method on an unconventional support, which is hydroxyapatite (Hap), a non-toxic, low cost, and naturally abundant material with exceptional properties [14]. Previous studies which have aimed to study the effect of TM content on the performances of copper [15] and manganese [16], [17] based active phases dispersed on Hap in the total oxidation of toluene, have found it to be correlated with the speciation and dispersion of the TM. For the TM-based Hap supported catalysts (TM = Cu, Mn), the maximum of activity is achieved for a low amount of Cu (wt%: 2.5%) compared with those of 5-10 wt% for Mn.

With the objective to improve the catalyst efficiency, this study investigates the catalytic performances of binary Cu-Mn oxides dispersed on Hap in toluene oxidation considering a TM content of 10 wt%, to be compared with those of the single supported TMO counterparts, through the tuning of the Cu/Mn molar ratio (2; 1; 0.5). The catalytic performances will be correlated with the physicochemical properties of the catalysts.

3.2. Decomposition of the Dried Impregnated Cu_xMn_yHapD Samples: Thermogravimetric Analysis (TGA)

The mode of decomposition of the dried impregnated samples (Cu_xMn_yHapD) was investigated using TGA technique. The resulting traces are given in Figure 3.1 and all noted weight losses are listed in Appendix A, Table AA.1. The TGA traces (Figure 3.1-a) are rather similar for all samples. The first weight loss from 50 °C to 160 °C is ascribed to the departure of water. The second stage of decomposition which takes place in the temperature range of about 160-400 °C is attributed to the decomposition of NO_3^- [18]. It is found that the temperature of the large DTG peak (in °C) increases with Cu content owing to: MnHapD (190) < Cu_2MnHapD (300) < CuHapD (335) (Figure 3.1-b). Furthermore, based on the theoretical NO_3^- content in the Cu(II)/Mn(II) precursors and taking into account the H_2O removal contribution at low temperature, it is found that 82, 88, and 95% of the initial nitrate content decompose for CuHapD, Cu_2MnHapD and MnHapD, respectively. These results show that some remaining NO_3^- related species can be retained by the samples after calcinations performed at 400 °C for 4 h.

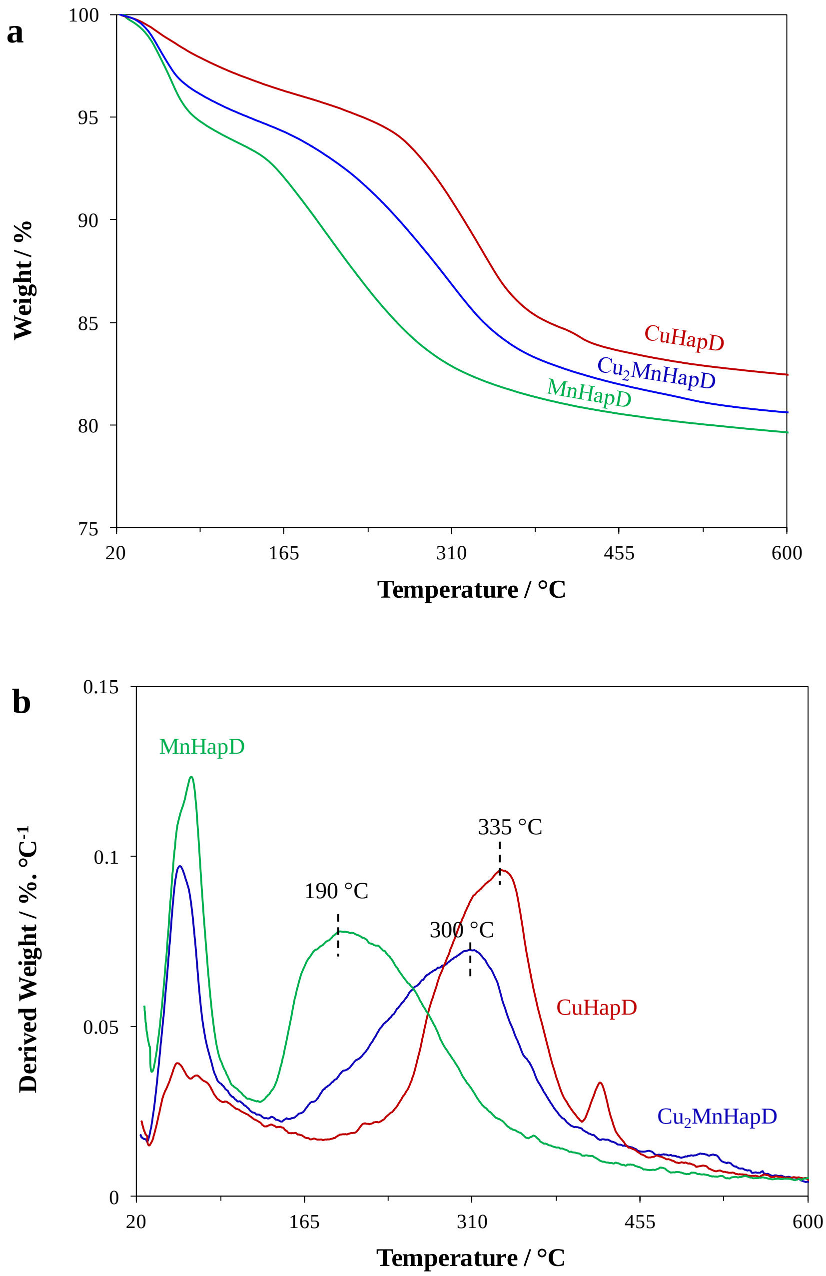

Figure 3.1. TGA (a) and DTG (b) curves of dried CuHapD, $Cu_2MnHapD$ and MnHapD samples.

3.3. Structural, Morphological and Textural Characterizations

The X-ray diffractograms of the fresh Cu_xMn_yHap samples and of the Hap support are shown in Figure 3.2.

The characteristic peaks of Hap agree with those corresponding to the hexagonal phase $Ca_5(PO_4)_3(OH)$ (PDF n ° 00-009-0432). It is found that the Full Width at Half Maximum (FWHM) for the (0 0 2) reflection is low as compared to the other ones in line with the presence of anisotropic crystallites as reported earlier in the literature [19], [20].

In Table 3.1 are listed two mean crystallite sizes obtained by the Scherrer equation from the FWHM of the peaks positioned at 10.9 ° and 25.9 ° relative to the (1 0 0) and (0 0 2) planes, respectively. This allows us to determine a length to thickness ratio of the crystallite through the determination of the $D_{c(002)}/D_{c(100)}$ ratio which is of 1.81 for the Hap support. This ratio increases with the addition of Cu and/or Mn to get the highest value of 2.08 for CuHap. Thus, the addition of TM leads to slightly more elongated crystallite as compared to that of the Hap support as already observed by Chala *et al.* [16] for MnHap samples.

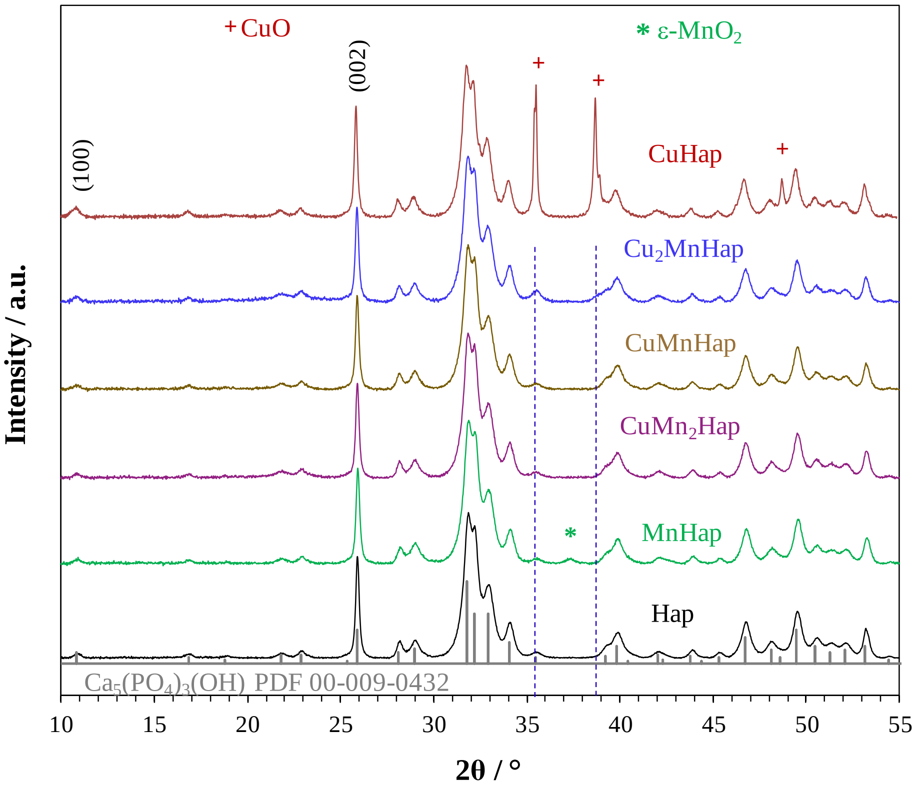

Figure 3.2. XRD patterns of pure Hap and Cu_xMn_yHap samples.

In addition to the characteristic peaks of Hap, we detect the presence of new peaks for the CuHap and MnHap solids. Indeed, the CuHap sample exhibits new peaks positioned at 2θ = 35.6 °, 38.8 °, and 48.8 ° associated with monoclinic CuO tenorite (PDF n ° 04-007-1375). The narrow sharp peaks are consistent with a mean crystallite size of 45 nm (see Table 3.1), in line with that of 42 nm reported by Chlala *et al*. [15], indicating that the addition of copper on Hap by wet impregnation results in poor CuO dispersion for a 10 wt% of Cu.

The X-ray diffractogram of MnHap shows a new distinct broad peak located at 2θ = 37.1 ° which can be tentatively attributed to the akhtenskite ε-MnO_2 (PDF n ° 00-030-0820) phase (Figure AA.1) which was not previously detected in similar conditions [17].

Regarding the binary oxide materials, for the Cu-rich sample, we observe an increase in intensity and broadness of the peak located at 2θ = 35.5 ° and of the shoulder at 2θ = 38.7 °. However, the broadness of the peaks precludes discriminating a CuO from a related Cu-Mn spinel phase as shown in Figure 3.3.

Table 3.1. Mean crystallite size (D_C) of Hap support and of TM related detected phases.

Sample	$D_{c(002)}$ [nm]	$D_{c(100)}$ [nm]	$D_{c(002)}/D_{c(100)}$	$D_c^{[a]}$ CuO [nm]	D_c ε-MnO_2 [nm]
	(002)	(100)	(002)/(100)		
Hap	36	20	1.81	-	-
CuHap	39	19	2.08	45	-
Cu_2MnHap	37	20	1.85	-	-
CuMnHap	37	18	1.99	-	-
CuMn_2Hap	38	21	1.81	-	-
MnHap	35	18	1.90	-	16

[a] : determined from the peak at 2θ = 48.8 °

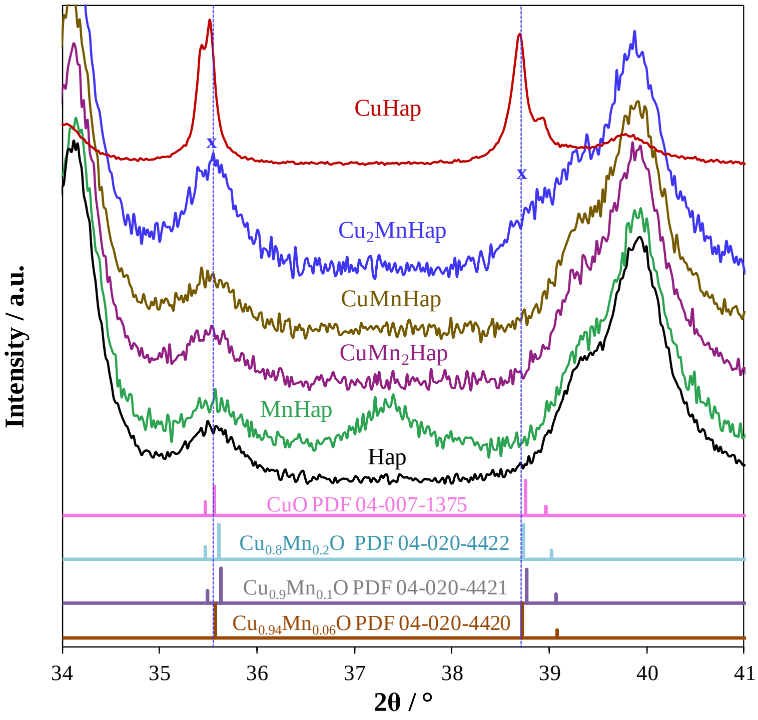

Figure 3.3. X-ray diffractograms of the Cu_xMn_yHap solids in the 2θ = 34-41 ° range. The intensity of the diffractogram of CuHap was divided by 10.

By opposition, for the enriched Mn samples, *i.e.* CuMnHap and CuMn_2Hap, we do not observe any additional peaks to those of the pure Hap, which could be explained either by a high dispersion of the TMO phase(s) or/and by the formation of supported amorphous TMO phase(s).

The anisotropy observed by XRD was also evidenced through SEM analysis (Figure 3.4). Indeed, some bundles of fiber-like particles are observed for all our samples, indicating an anisotropic growth of the particles with a length varying from 50 nm to almost 400 nm for all samples.

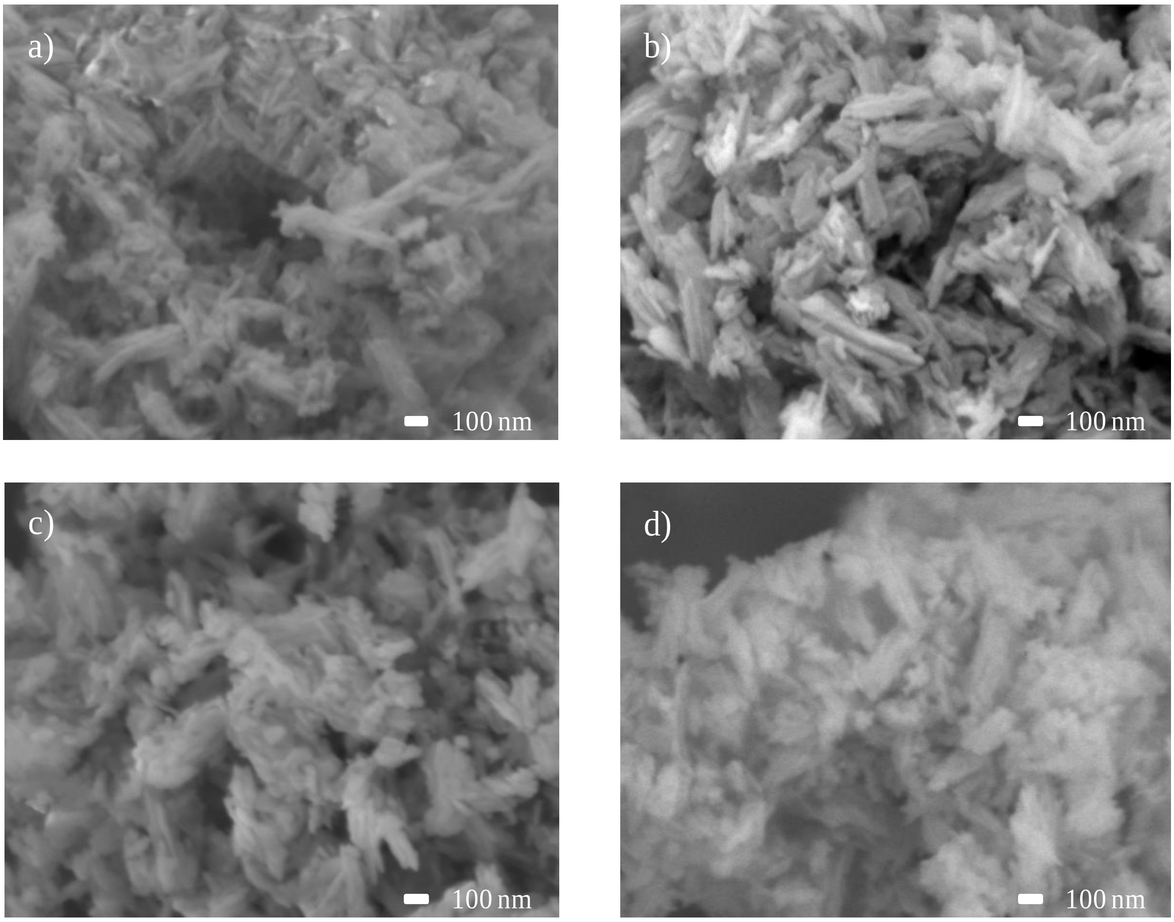

Figure 3.4. SEM images of a) Hap, b) CuHap, c) CuMnHap and d) MnHap.

The main textural properties of the samples are summarized in Table 3.2. The Hap support has a specific surface area of 102 $m^2.g^{-1}$ and a pore volume of 0.70 $cm^3.g^{-1}$. When adding Cu and/or Mn, both the BET surface area and pore volume values decrease. This decrease is higher in the case of CuHap, due most probably to some pore blockage by CuO particles.

Table 3.2. Textural properties and H_2-TPR results.

Sample	SSA[a] [$m^2.g^{-1}$]	Vp[b] [$cm^3.g^{-1}$]	$n(H_2)_{th}$[c] [$mmol.g^{-1}$]	$n(H_2)_{ex}$[d] [$mmol.g^{-1}$]
Hap	102	0.70	-	-
CuHap	71	0.46	5.51 (1.58)	4.96
Cu_2MnHap	78	0.49	2.67 (1.65)	1.99
CuMnHap	79	0.54	1.83 (1.69)	1.19
$CuMn_2Hap$	86	0.56	1.46 (1.73)	0.98
MnHap	78	0.51	1.78 (1.82)	0.67

[a] Specific surface area. [b] Pore volume. [c] Experimental amount of H_2 consumed on the fresh catalysts; Theoretical amount of H_2 consumed (see text). [d] Experimental amount of H_2 consumed on the used catalysts.

3.4. Redox Characterization: Temperature Programmed Reduction (H_2-TPR) Coupled with Mass Spectrometry (MS)

The H_2-TPR profiles of the calcined materials are illustrated in Figure 3.5 and the quantitative results are reported in Table 3.2. As expected the pure apatitic support does not exhibit any reduction peak (not shown here) [21], [22]. For MnHap, one peak of H_2 consumption at 370 °C was observed, followed by a tail. The trace relative to CuHap is complex showing at high temperature a strong H_2 consumption due to overlapping peaks at 452 °C and 485 °C while a low temperature H_2-consumption is also observed. By opposition the H_2-TPR profiles of the Cu-Mn based materials show only two overlapping peaks in a narrow temperature range. Interestingly, the onset of H_2 consumption decreases while the peak enlargement increases with the increase of Cu content.

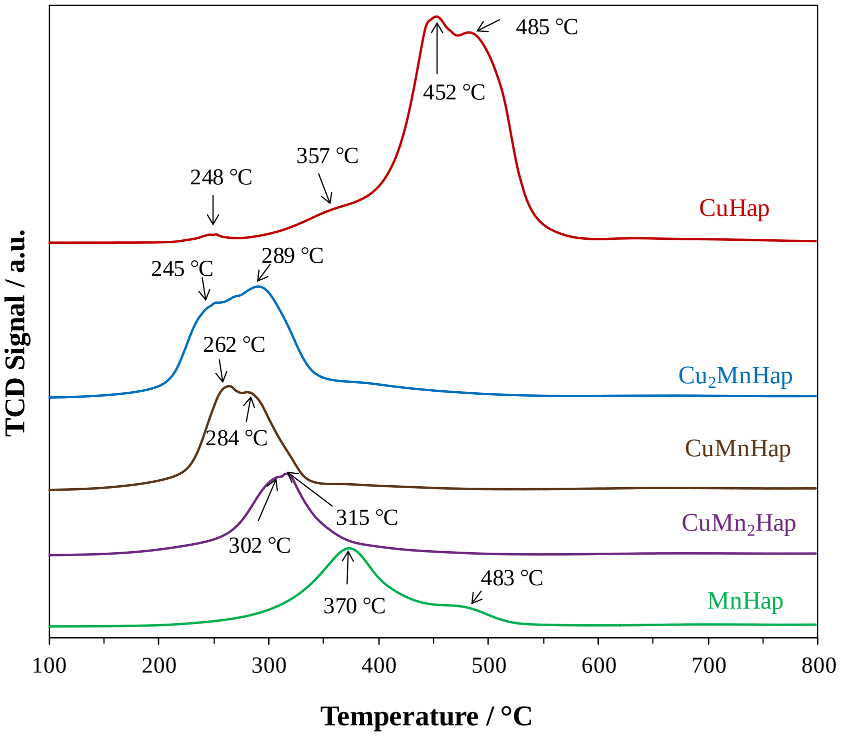

Figure 3.5. H_2-TPR profiles of Cu_xMn_yHap solids calcined at 400 °C.

The experimental H_2 consumptions expressed per g of catalyst $n(H_2)_{ex}$ increase with Cu content from 1.46 ($CuMn_2Hap$) to 5.51 (CuHap). These values were compared to the theoretical ones $n(H_2)_{th}$ regarded as maximum values assuming Cu(+II) → Cu(0) and Mn(+IV) → Mn(II) reductions. We noticed that $n(H_2)_{ex}$ exceeds $n(H_2)_{th}$ for Cu/Mn atomic ratio ≥ 1.0. This can be explained by taking into account that some reducible NO_3^- related entities are retained in the materials after calcination. This assumption is supported by the FT-IR results exhibiting the characteristic unreacted nitrate band at 1386 cm^{-1} whose relative intensity increases with Cu content (not shown here) as already observed by Chlala *et al.* [15].

On purpose, the degradation modes of the NO_3^- species have been monitored using mass spectroscopy through the evolution of m/z signals 17, 28, 30 and 44 characteristic of NH_3, N_2, NO and N_2O as a function of temperature (Figure AA.2). For the Cu-Mn based catalysts the evolution of these m/z signals over time are rather similar. A peak of high intensity at m/z = 30 is observed, followed by a narrow less intense peak at m/z = 28 while the contributions at m/z = 17 and 44 are negligible. Hence, during the H_2-TPR experiments it turns out that the NO_3^- entities are reduced into NO then into N_2 while the contributions of gaseous N_2O and NH_3 appear to be negligible. Such scheme of NO_3^- degradation holds also for the MnHap sample. However, in that case the relative contribution of N_2 is less pronounced.

Taking into account the ability of Cu(0) to efficiency reduce the nitrate entities at low temperature, the T_{NO} value has been taken as a reference to describe the reducibility of the materials: the easier the reducibility of the materials, the lower T_{NO} is. Thereby, as seen in Figure 3.6 the solids can be ranked according to the increasing temperature of NO appearance T_{NO} (°C): Cu_2MnHap (174) < CuMnHap (188) < CuHap (200) < $CuMn_2$Hap (212) < MnHap (236). For the Cu-Mn related catalysts it turns out that T_{NO} decreases with an increase of Cu content showing that high relative Cu content promotes the reducibility of the materials. It should also be noted that T_{NO} is lower for Cu/Mn = 2 and 1 as compared to those relative to the single TM based catalyst.

Additionally, the H_2-TPR profile of the fresh Cu-Mn based catalysts exhibits a typical profile similar to those of mixed Cu-Mn oxides [23], [24] in line with the co-impregnation method.

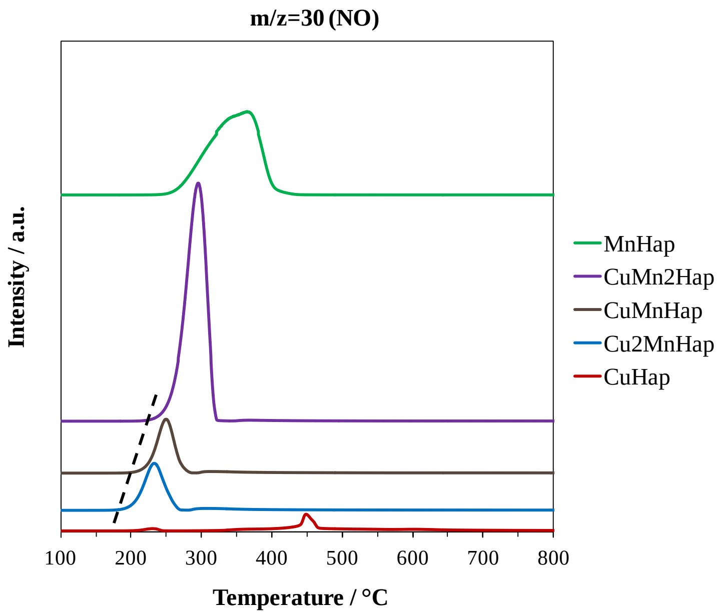

Figure 3.6. Evolution of the m/z = 30 (NO) signal for the Cu_xMn_yHap solids.

3.5. Surface Characterizations

3.5.1. XPS Results

Figure 3.7 gives the Cu 2p core level XPS spectra for the fresh samples and the pertinent results are given in Table 3.3. The Cu $2p_{3/2}$ binding energy (BE) for CuHap is at 932.8 ± 0.1 eV considering the first and second recorded XPS spectra while the FWHM decreases from 3.4 eV to 2.7 eV. By opposition, for all the Cu_xMn_yHap samples, the Cu $2p_{3/2}$ BEs are much higher, located at 934.1 ± 0.1 eV with FWHM of 3.2 ± 0.3 eV and I_{sat}/Ipp ratio about twice higher than that of CuHap, in line with a Cu(II). However, considering the second Cu 2p XPS, it is observed for all samples a significant Cu $2p_{3/2}$ BE decrease accompanied with a decrease of FWHM and I_{sat}/Ipp ratio. Based on all these observations, it is concluded that XPS induces reduction of copper at different extents as already observed [15]. Copper is significantly reduced on CuHap considering the first XPS spectra, while a partial copper reduction is observed for the Cu_xMn_yHap samples regarding the second recording XPS spectra**.** Such different behaviors in terms of copper reduction can be tentatively ascribed to the presence of a mixed CuMn oxide which stabilizes the Cu towards XPS photons.

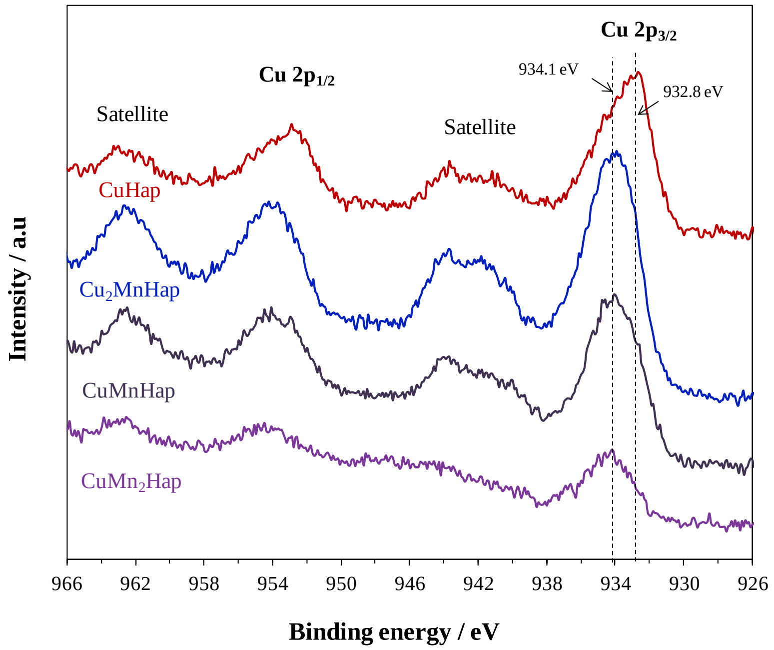

Figure 3.7. 1st recording of the Cu 2p XPS core levels.

Table 3.3. XPS based data obtained for the fresh and used catalysts.

Sample	Cu $2p_{3/2}$[a]	FWHM Cu $2p_{3/2}$[a]	I_{sat}/I_{pp}[a]	Cu $2p_{3/2}$[b]	FWHM Cu $2p_{3/2}$[b]	I_{sat}/I_{pp}[b]	ΔE	Mn AOS[c]	Mn/Cu
CuHap	932.8	3.42	0.38	932.7	2.69	0.35	0.1	-	-
Cu_2MnHap	933.9	3.40	0.60	933.4	3.26	0.49	0.5	2.6	1.1
CuMnHap	934.0	3.50	0.65	933.1	3.14	0.49	0.9	2.6	2.0
$CuMn_2Hap$	934.4	3.04	0.69	933.4	2.78	0.56	1	2.7	5.3
MnHap	-	-	-	-	-	-	-	3.1	-
CuHapU	933.3	4.20	0.44	933.3	3.45	0.29	0	-	-
$Cu_2MnHapU$	933.7	3.66	0.51	933.3	3.07	0.32	0.4	2.0	1.1
CuMnHapU	934.2	3.20	0.55	933.3	3.20	0.38	0.9	2.0	2.3
$CuMn_2HapU$	934.4	4.14	0.62	933.4	3.58	0.49	1	2.3	5.1
MnHapU	-	-	-	-	-	-	-	2.5	-

[a] Data obtained for 1st recording. [b] Data obtained for 2nd recording. [c] Mn average oxidation state.

The Mn 3s core levels for the Mn containing samples have been investigated. From the splitting between the two multiplet spin components, a Mn average oxidation state (AOS) has been estimated which gives a value of 3.1 for MnHap while those for Cu_xMn_yHap decrease to 2.7-2.6.

The Mn/Cu atomic ratio compared to the nominal Mn/Cu shows a Mn surface enrichment which becomes more pronounced with increasing Mn content.

3.5.2. Time of Flight Secondary Ions Mass Spectrometry (ToF-SIMS)

Regarding the Hap support, the peaks displayed in the positive ToF-SIMS spectra include Ca^+ (m/z = 40), CaH^+ (m/z = 41), CaO^+ (m/z = 56), $CaOH^+$ (m/z = 57) and Ca_2O^+ (m/z = 96), $Ca_2PO_3^+$ (m/z = 159), $Ca_2PO_4^+$ (m/z = 175), $CaPO_3H^+$ (m/z = 120), $CaPO_4H_2^+$ (m/z = 137), $Ca_2PO_3H^+$ (m/z = 160), $Ca_3P_2O_3H^+$ (m/z = 231), $Ca_4P_2O_4H^+$ (m/z = 287), $Ca_5P_2O_5H^+$ (m/z = 343) and $Ca_5(PO_4)_3^+$ (m/z = 485) which are the characteristic secondary ions observed for $Ca_5(PO_4)_3(OH)$ [25]–[29]. In the negative polarity, O^- (m/z = 16), HO^- (m/z = 17), P^- (m/z = 31), PO^- (m/z = 47), PO_2^- (m/z = 63), and PO_3^- (m/z = 79) are found. It should be mentioned that some mineral impurities such as Na^+ (m/z = 23), Mg^+ (m/z = 24), K^+ (m/z = 39) and some hydrocarbons $C_xH_yO_z^+$ were detected as well. Additionally, all samples exhibit the NO^- (m/z = 30), NO_2^- (m/z = 46) and NO_3^- (m/z = 62) secondary ions in line with residual nitrate after calcination.

The existence of interactions between the TM and hydroxyapatite in TMHap (TM = Cu or Mn) materials is evidenced by the presence of a series of cluster ions involving TM and Ca or P and both (see Tables 3.4, 3.5, 3.6). Based on these results, it is found that Cu and Mn preferentially interact with Ca rather than P. This statement has already been reported in the case of Hap supported Mn samples by Chlala *et al.* [17]. These observations suggest the occurrence of an ion (Ca-Cu/Mn) exchange at the uttermost layers of the samples.

Table 3.4. List of ToF-SIMS positive ion fragments detected in copper containing solids

$Cu_xCa_vO_zH_w^+$	$Cu_xP_tO_zH_w^+$	$Cu_xCa_vP_tO_zH_w^+$	$Cu_xO_zH_w^+$
CuCaO	n.d.[a]	Cu_2CaPO_4	Cu ; ^{65}Cu
$^{65}CuCaO$		$^{65}CuCuCaPO_4$	Cu_2 ; $^{65}CuCu$; $^{65}Cu_2$
$CuCaO_2$		$^{65}Cu_2CaPO_4$	Cu_3 ; $^{65}CuCu_2$;
$CuCaO_2H$			Cu_2O ; $^{65}CuCuO$; $^{65}Cu_2O$
$CuCaO_3$			Cu_3O ; $^{65}CuCu_2O$; $^{65}Cu_2CuO$
$CuCa_3O_4$			Cu_3O_2 ; $^{65}CuCu_2O_2$
$CuCa_2O_3H$			Cu_4O_2 ; $^{65}CuCu_3O_2$; $^{65}Cu_2Cu_2O_2$
$CuCa_3O_4H$			Cu_5O_2 ; $^{65}CuCu_4O_2$; $^{65}Cu_2Cu_3O_2$; $^{65}Cu_3Cu_3O_2$
Cu_2CaO_2H			Cu_5O_3 ; $^{65}CuCu_4O_3$; $^{65}Cu_2Cu_3O_3$
$^{65}CuCuCaO_2H$			Cu_6O_3 ; $^{65}CuCu_5O_3$; $^{65}Cu_2Cu_4O_3$; $^{65}Cu_3Cu_3O_3$
$^{65}Cu_2CaO_2H$			Cu_2OH ; $^{65}CuCuOH$; $^{65}Cu_2OH$
			Cu_3O_2H

[a] Not detected.

Table 3.5. List of ToF-SIMS positive ion fragments detected in manganese containing solids

$Mn_yCa_vO_zH_w^+$	$Mn_yP_tO_zH_w^+$	$Mn_yCa_vP_tO_zH_w^+$	$Mn_yO_zH_w^+$
MnCaO	$MnPO_2$	Mn_2CaPO_5	Mn
$MnCaO_2$		Mn_2CaPO_4H	Mn_2
Mn_2CaO_2			MnO
Mn_2CaO_3			Mn_2O
Mn_3CaO_4			Mn_2O_2
$MnCa_2O_2$			Mn_2O_4
$MnCa_2O_3$			Mn_2O_5
$Mn_2Ca_2O_4$			Mn_3O_2
$MnCaO_2H$			Mn_3O_3
Mn_2CaO_3H			Mn_2O_2H
$MnCa_2O_3H$			$Mn_2O_2H_2$
			Mn_3O_3H

Interestingly for the CuMn based samples, the ToF-SIMS spectra in positive polarity exhibit a series of mixed $Cu_xMn_yO_zH_w^+$ (x = 1; y = 1; z = 0,1; w = 0-2) ions (see Table 3.6).

Table 3.6. List of ToF-SIMS positive secondary ions detected in Cu-Mn based solids

$Cu_xMn_yCa_vO_zH_w^+$	$Cu_xMn_yP_tO_zH_w^+$	$Cu_xMn_yCa_vP_tO_zH_w^+$	$Cu_xMn_yO_zH_w^+$
n.d.[a]	CuMnPH	n.d.[a]	CuMn
	$CuMnPH_2$		$^{65}CuMn$
	$^{65}CuMnPH_2$		CuMnO
			$^{65}CuMnO$
			CuMnOH
			$^{65}CuMnOH$

[a] Not detected.

For example the ToF-SIMS (+) spectrum of Cu_2MnHap in the m/z 133-138 range displayed in Figure 3.8 evidences the $CuMnO^+$ and $CuMnOH^+$ secondary ions. The presence of such ions proves the formation of mixed Cu-O-Mn oxide. However, it is not possible to identify the mixed oxide phase just based on the ToF-SIMS fragmentation patterns. In parallel, in order to evaluate the relative surface density of Cu-O-Mn interactions the ToF-SIMS intensity ratio $CuMnO^+/(Cu^++Mn^+)$ for the

Cu_xMn_yHap solids has been determined. This allows classifying the catalysts by decreasing intensity ratio to get the following sequence: Cu_2MnHap (0.057) > CuMnHap (0.040) > $CuMn_2Hap$ (0.025). This result highlights the greater contribution of Cu-O-Mn interactions for Cu_2MnHap.

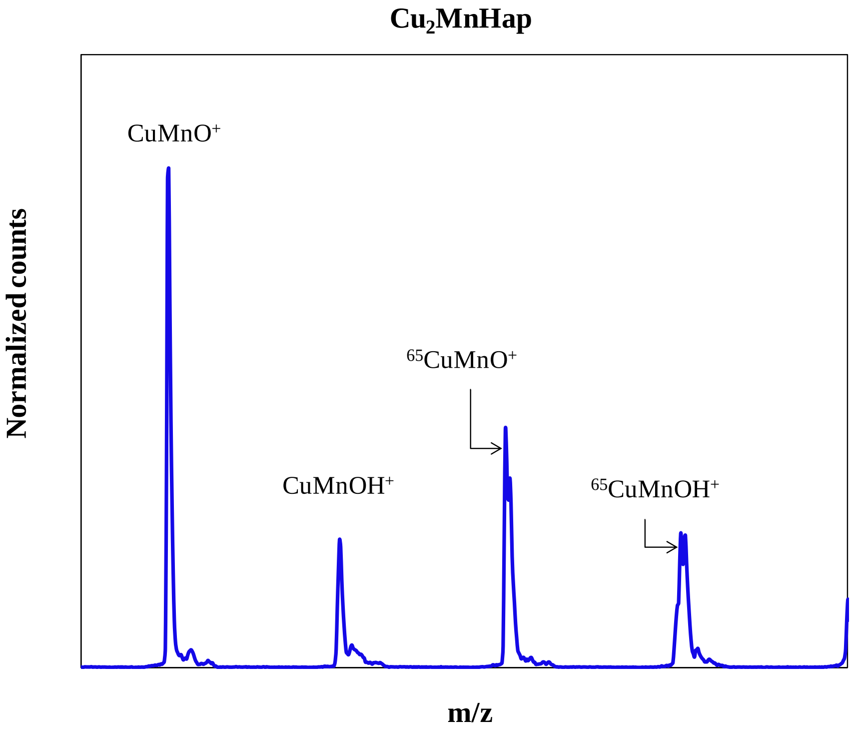

Figure 3.8. ToF-SIMS (+) spectrum in the m/z 133–138 range collected from the Cu_2MnHap sample.

3.6. Catalytic Oxidation of Toluene

The conversion of toluene into CO_2 over Hap and Cu_xMn_yHap catalysts as a function of temperature is given in Figure 3.9. It should be noted that the toluene conversion is significantly enhanced by the addition of single TM with good redox properties over the hydroxyapatite support. Additionally, the catalysts perform even better when adding Cu and Mn on the support by co-impregnation. Toluene conversion into CO_2 based on T_{50} (CO_2) (temperature at which 50% of toluene is converted into CO_2 in °C) decreases in the following order: Cu_2MnHap (196) > CuMnHap (202) ≈ $CuMn_2Hap$ (205) > MnHap (210) >> CuHap (255). 90% of toluene conversion was achieved for CuHap and MnHap at temperatures of 302 °C and 224 °C, respectively, while a temperature below 220 °C was required for Cu-Mn based catalysts. Indeed, the same order of decreasing activity was maintained for all catalysts for both T_{90} (CO_2) and T_{10} (CO_2) (see Table AA.2).

Considering a standardised conversion rate determined at 190 °C (r_{190}), the catalysts can be ranked by decreasing activity ($/10^{-2}$ h^{-1}) following the same previous sequence: Cu_2MnHap (2.57) > CuMnHap (2.04) > $CuMn_2Hap$ (1.59) > MnHap (1.13) >> CuHap (0.13). It should be noted that r_{190} for Cu_2MnHap catalyst is 2 times higher and 20 times higher compared to those obtained with MnHap and CuHap, respectively.

T_{50} (CO_2) as a function of the Mn/(Cu+Mn) molar ratio (Figure 3.10) shows a parabolic resembling curve indicating a better activity in terms of specific activity for the supported mixed oxides. It should be noted that the specific activity is the highest for a Cu/Mn ratio of 2.0. Moreover, the production of

CO is lower over Cu-Mn based catalysts as compared to those of the single TMHap samples, to become non-detectable over the Cu_2MnHap sample (Figure AA.3) in line with previous studies showing a better activity for CO oxidation into CO_2 for such Cu/Mn stoichiometry [30], [31]. Figure 3.10 clearly shows a nice correlation between the catalytic activity in terms of T_{50} (CO_2) and the reducibility of the catalysts in terms of the onset reduction temperature (T_{or}). This correlation highlights the importance of the redox behaviour of the catalysts for such reaction.

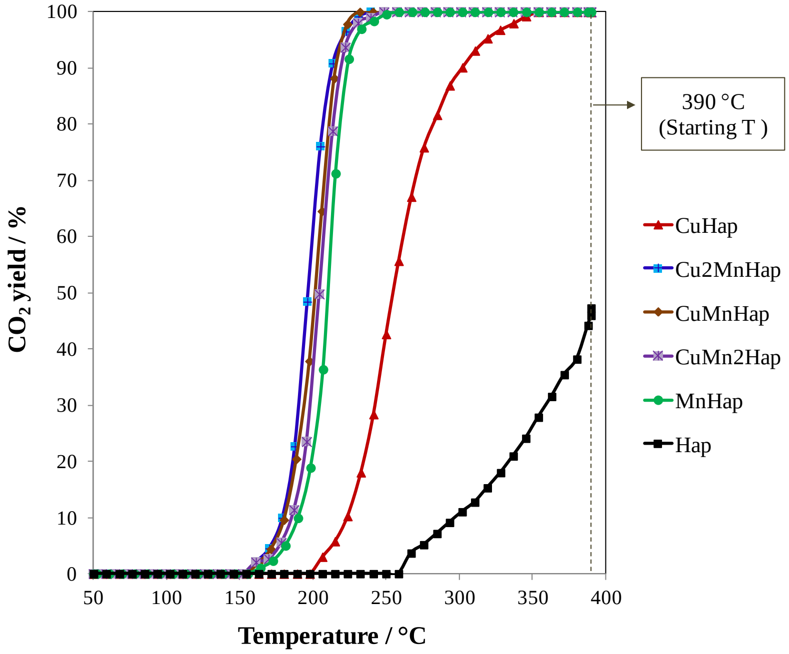

Figure 3.9. CO_2 yield for Cu_xMn_yHap catalysts (GHSV = 14,500 h^{-1}; 800 ppmv toluene in air).

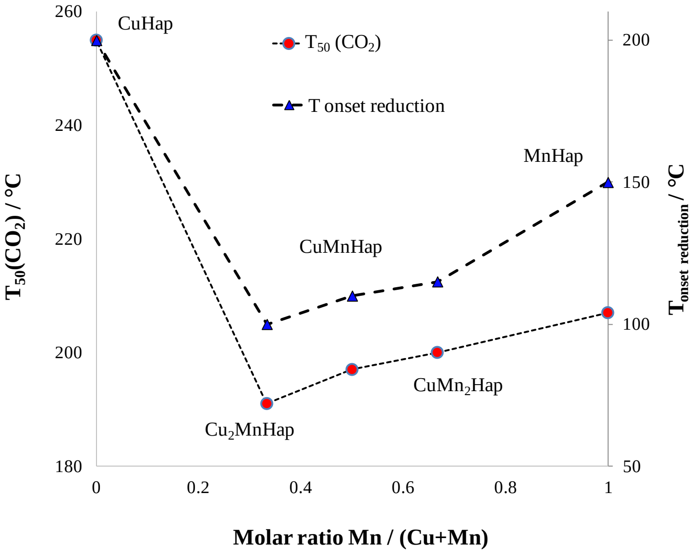

Figure 3.10. T_{50} (CO_2) (left axis) and $T_{onset\ reduction}$ (right axis) vs. Mn/(Cu+Mn) molar ratio.

Interestingly, as shown in figure 3.11, the standardised rate r_{190} increases linearly with the $CuMnO^+/(Cu^++Mn^+)$ ToF-SIMS intensity ratio. It is recognized that the formation of Cu-O-Mn entities, in which the polar covalent Mn-O bond is weakened by the presence of Cu, promotes oxygen lability [32], [33]. Furthermore, the electron transfer between copper and manganese cations is made easier.

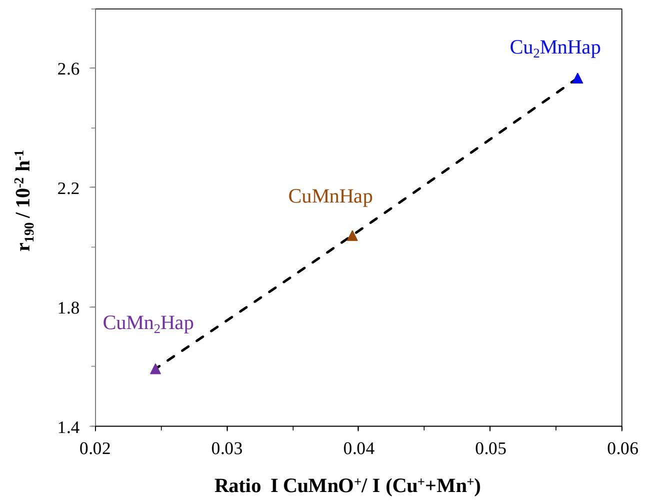

Figure 3.11. r_{190} as a function of $CuMnO^+$/ Cu^++Mn^+ intensity ratio for the mixed Cu_xMn_yHap catalysts.

3.7. Stability Tests

Stability tests of Cu_xMn_yHap catalysts were conducted at 200 °C in similar conditions to those of the catalytic tests. As can be seen in Figure 3.12, a decrease in toluene conversion is noted for all Cu_xMn_yHap catalysts. A quantification of the deactivation resistance of our catalysts was performed through the use of an activity coefficient a_{200} determined by calculating the ratio of toluene conversion after 24 h of test to that obtained at the beginning of the test. The evolution of the values of a_{200} as a function of Mn/(Cu+Mn) molar ratio is given in Figure 3.13. Therefore, the used catalysts can be ranked by decreasing resistance towards deactivation: CuHap >> MnHap > Cu_2MnHap ≈ CuMnHap ≈ $CuMn_2Hap$.

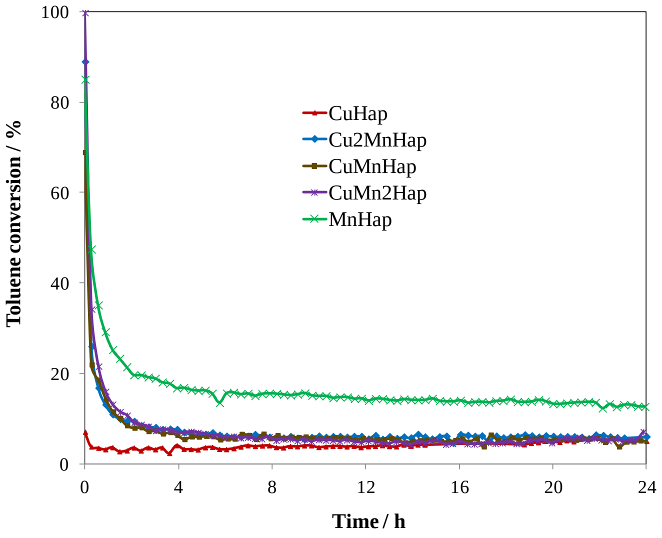

Figure 3.12. Time course for toluene oxidation over Cu_xMn_yHap catalysts activated at 200 °C. Feed composition: 800 ppmv toluene in air, T_{test} = 200 °C.

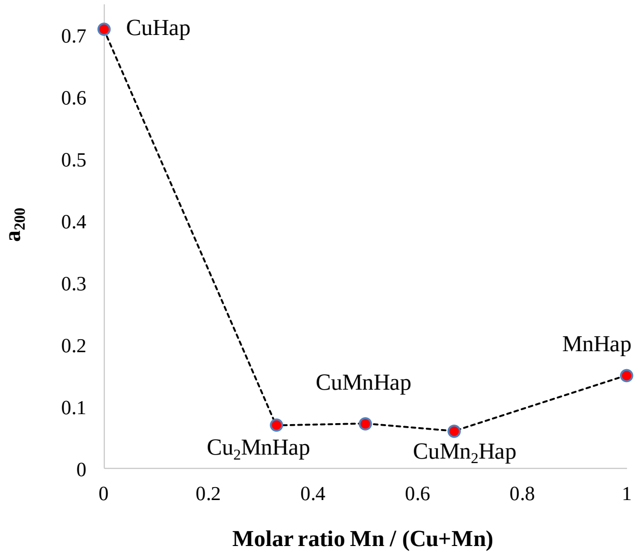

Figure 3.13. Evolution of activity coefficient a_{200} as a function of Mn/(Cu+Mn) molar ratio.

The effect of the temperature of activation was investigated in the case of CuMnHap. Increasing the temperature from 200 °C to 390 °C allows quadrupling the toluene conversion which amounts now to 18% as observed in Figure 3.14.

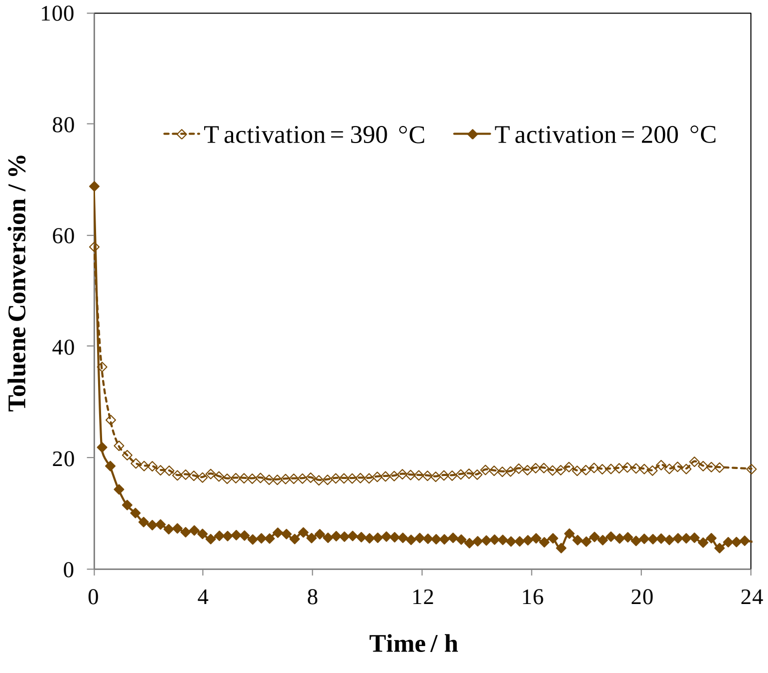

Figure 3.14. Time course for toluene oxidation over CuMnHap catalyst activated either at 200 °C or 390 °C. Feed composition: 800 ppmv toluene in air, T_{test} = 200 °C.

3.8. Characterizations after Stability Tests

In order to get insight about the deactivation, additional characterizations have been performed on the used catalysts. The XRD patterns of the Cu_xMn_yHapU samples reveal no modification in the positions and relative intensities of the peaks previously observed in fresh samples, nor does it reveal any new crystalline phase.

By opposition the reducibility of the used catalysts is significantly altered compared to that of the fresh catalysts in terms of H_2-TPR profiles as shown in Figure 3.15 and in terms of H_2 consumption amount (Table 3.2). For the CuHapU and $Cu_2MnHapU$ samples it is found that $n(H_2)_{ex}$ is higher than $n(H_2)_{th}$ indicating that NO_3^- related moieties are still incorporated in the catalysts. For the MnHapU sample is found a very complex H_2-TPR trace showing at least five overlapping contributions. Furthermore, the H_2 consumption amount is low and results in a Mn AOS of 2.7 highlighting the reduction of the MnO_x species. For the used CuMn based catalysts, it is found that the onset reduction temperature is all the lower when the Cu content is higher, as previously observed for the fresh samples. All the traces are initially composed of an intense narrow peak followed by a complex tail constituted of overlapping components in a wide temperature window (up to 700 °C). Furthermore, a global H_2-consumption decrease is noted compared to that observed on the fresh samples, which becomes all the more pronounced the higher the Mn content is.

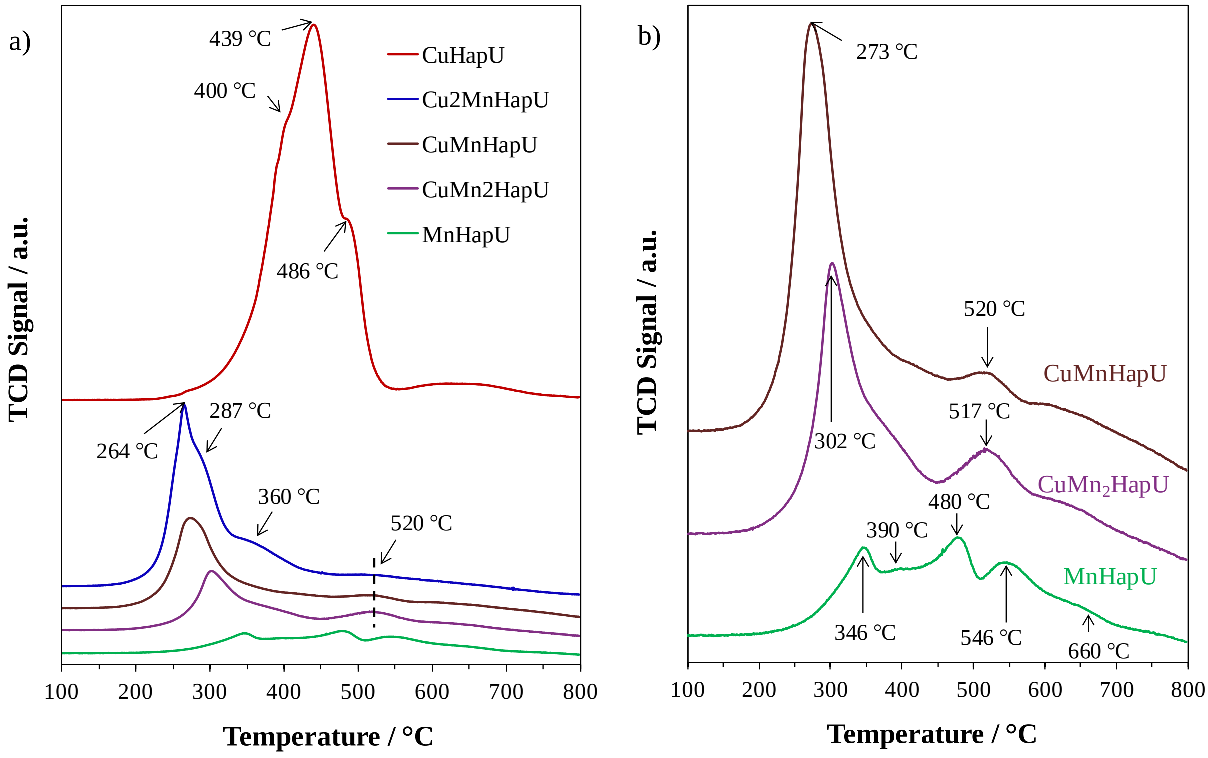

Figure 3.15. a) H_2-TPR reduction profiles for Cu_xMn_yHapU solids and b) zoom of the H_2-TPR reduction profiles for CuMnHapU, $CuMn_2HapU$ and MnHapU.

Interestingly, it should be noticed that the amount of H_2-TPR consumed for the low temperature peak corresponds to the total conversion of Cu(II) into Cu(0) within the margin of uncertainty (see Table 3.7). As a consequence, the H_2-TPR profiles of these two CuMn based catalysts consist in the successive reductions of Cu(II) into Cu(0) and of Mn^{x+} into Mn(II). Taking into account the remaining amount of H_2 consumed in the TPR experiments, a Mn AOS of 2.8 and 2.6 has been estimated for the CuMnHapU and $CuMn_2HapU$ samples, respectively. Therefore, the Mn entities appear more reduced after the stability test as previously noticed [16]. The total oxidation of toluene over Cu-Mn mixed oxide can be described by a Mars-van Krevelen model in which the toluene is oxidized by the catalyst and the gaseous dioxygen restore the oxidized state of the catalyst. Taking this model into account, the Mn reoxidation can be herein the rate limiting step of the process. A possible decomposition of the mixed $Cu_xMn_yO_z$ species present in fresh Cu-Mn samples into CuO and MnO_x after catalytic reaction could account for such behavior.

Table 3.7. H_2 consumption amounts and Mn AOS

Sample	$n(H_2)_{th}$ [a] [mmol.g^{-1}]	$n(H_2)_{ex}$ [b] [mmol.g^{-1}]	Mn AOS [c]
CuMnHapU	0.84	0.84	2.8
$CuMn_2HapU$	0.58	0.65	2.6
MnHapU	-	-	2.7

[a] Theoretical amount of H_2 consumed corresponding to the reduction of CuO to Cu^0. [b] Experimental amount of H_2 consumed relative to the low temperature reduction peak considered as symmetric. [c] Manganese average oxidation state.

This assumption is in line with the work of Papavasiliou *et al.* [34]. In this study the performances of Cu–Mn spinel oxide materials were investigated in steam reforming of methanol. A decomposition of the spinel was noted following the catalytic reaction. It was claimed that the difficulty in oxidizing Mn(II) leads to the spinel decomposition. To conclude, such a similar behaviour may have likely occurred in our experiments.

Cu 2p core level XPS spectra for the used samples that are illustrated in Figure 3.16 show that the copper state is still (+II) for the supported Cu-Mn oxides (Table 3.3). By opposition the Mn AOS decreases after durability test (Table 3.3) while the Mn/Cu atomic ratios remain practically unchanged.

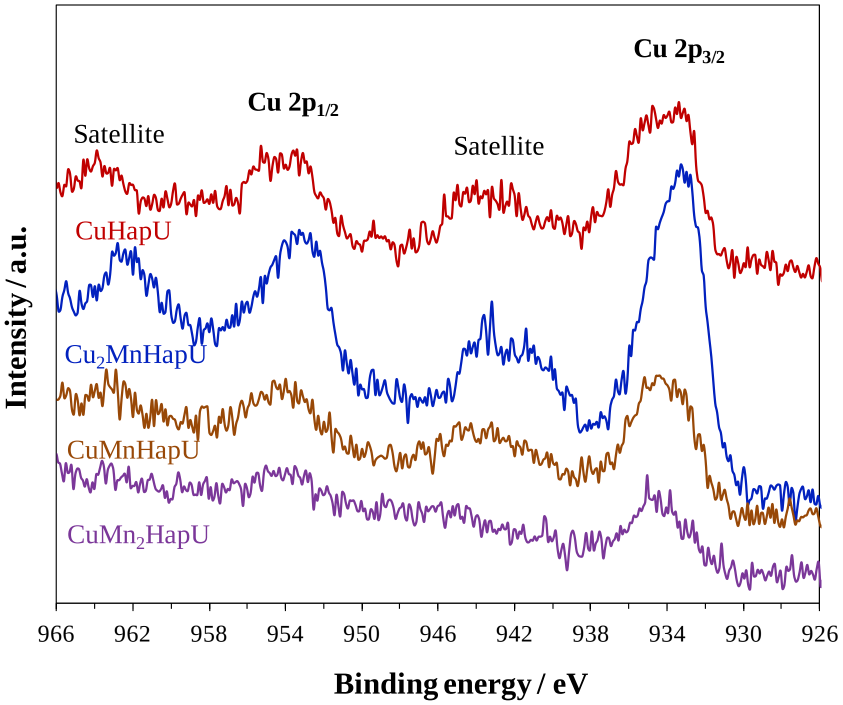

Figure 3.16. 1st recording of Cu 2p for Cu_xMn_yHapU samples.

3.9. Conclusion

Hydroxyapatite supported binary Cu-Mn (TM: 10 wt%) oxides with different atomic Cu/Mn composition (2 ; 1 ; 0.5), were successfully synthesized by co-impregnation and calcined at 400 °C for 4 h. The performances of these catalysts were compared to those of the single TM in the catalytic oxidation of toluene in dry air. Adding Cu to Mn promotes in any case the total oxidation of toluene into CO_2 with the highest activity and CO_2 selectivity obtained for the catalyst having a Cu/Mn molar ratio of 2. These improved catalytic performances could be correlated with improved reducibility induced by the presence of supported a mixed copper-manganese phase. However, the catalysts deactivate with time. Such a deactivation of Hap supported Cu-Mn based oxides with time may be explained by a decomposition of the mixed entities.

References

[1] Y. Peng, L. Zhang, L. Chen, D. Yuan, G. Wang, X. Meng, and F.-S. Xiao, « Catalytic performance for toluene abatement over Al-rich Beta zeolite supported manganese oxides », *Catal. Today*, vol. 297, p. 182–187, 2017.

[2] D. Romero, D. Chlala, M. Labaki, S. Royer, J.-P. Bellat, I. Bezverkhyy, J.-M. Giraudon, and J.-F. Lamonier, « Removal of toluene over NaX zeolite exchanged with Cu^{2+} », *Catalysts*, vol. 5, n° 3, p. 1479–1497, 2015.

[3] C.-H. Wang, « Al_2O_3-supported transition-metal oxide catalysts for catalytic incineration of toluene », *Chemosphere*, vol. 55, n° 1, p. 11–17, 2004.

[4] Z. Ye, J.-M. Giraudon, N. Nuns, P. Simon, N. De Geyter, R. Morent, and J.-F. Lamonier, « Influence of the preparation method on the activity of copper-manganese oxides for toluene total oxidation », *Appl. Catal. B Environ.*, vol. 223, p. 154–166, 2018.

[5] S. Behar, P. Gonzalez, P. Agulhon, F. Quignard, and D. Świerczyński, « New synthesis of nanosized Cu–Mn spinels as efficient oxidation catalysts », *Catal. Today*, vol. 189, n° 1, p. 35–41, 2012.

[6] J. Hu, W. B. Li, and R. F. Liu, « Highly efficient copper-doped manganese oxide nanorod catalysts derived from CuMnO hierarchical nanowire for catalytic combustion of VOCs », *Catal. Today*, vol. 314, p. 147–153, 2018.

[7] Y. Liu, L. Jia, Y. Lin, Y. Zhao, L. Sun, H. Ma, H. Kameyama, M. Sakurai, and Y. Guo, « Catalytic Combustion of Toluene over Cu–Mn Mixed Oxide Catalyst », *J. Chem. Eng. Jpn.*, vol. 51, n° 9, p. 769–777, 2018.

[8] D. A. Aguilera, A. Perez, R. Molina, and S. Moreno, « Cu–Mn and Co–Mn catalysts synthesized from hydrotalcites and their use in the oxidation of VOCs », *Appl. Catal. B Environ.*, vol. 104, n° 1‑2, p. 144–150, 2011.

[9] H. C. Genuino, S. Dharmarathna, E. C. Njagi, M. C. Mei, and S. L. Suib, « Gas-phase total oxidation of benzene, toluene, ethylbenzene, and xylenes using shape-selective manganese oxide and copper manganese oxide catalysts », *J. Phys. Chem. C*, vol. 116, n° 22, p. 12066–12078, 2012.

[10] H. J. Kim, S. W. Choi, C. S. Lee, B. Wielage, S. Bae, S. O. Obare, and H. I. Inyang, « Oxidation of Toluene on γ-Al_2O_3 Supported Copper–Manganese Catalysts », *Environ. Eng. Sci.*, vol. 28, n° 12, p. 827–833, 2011.

[11] W. B. Li, M. Zhuang, T. C. Xiao, and M. L. H. Green, « MCM-41 supported Cu- Mn catalysts for catalytic oxidation of toluene at low temperatures », *J. Phys. Chem. B*, vol. 110, n° 43, p. 21568–21571, 2006.

[12] S. M. Saqer, D. I. Kondarides, and X. E. Verykios, « Catalytic oxidation of toluene over binary mixtures of copper, manganese and cerium oxides supported on γ-Al_2O_3 », *Appl. Catal. B Environ.*, vol. 103, n° 3, p. 275–286, 2011.

[13] X. Li, L. Wang, Q. Xia, Z. Liu, and Z. Li, « Catalytic oxidation of toluene over copper and manganese based catalysts: Effect of water vapor », *Catal. Commun.*, vol. 14, n° 1, p. 15–19, 2011.

[14] M. Ibrahim, M. Labaki, J.-M. Giraudon, and J.-F. Lamonier, « Hydroxyapatite, a multifunctional material for air, water and soil pollution control: A review », *J. Hazard. Mater.*, vol. 383, p. 121–139, 2020.

[15] D. Chlala, J.-M. Giraudon, N. Nuns, M. Labaki, and J.-F. Lamonier, « Highly Active Noble-Metal-Free Copper Hydroxyapatite Catalysts for the Total Oxidation of Toluene », *ChemCatChem*, vol. 9, n° 12, p. 2275–2283, 2017.

[16] D. Chlala, J.-M. Giraudon, N. Nuns, C. Lancelot, R.-N. Vannier, M. Labaki, and J.-F. Lamonier, « Active Mn species well dispersed on Ca^{2+} enriched apatite for total oxidation of toluene », *Appl. Catal. B Environ.*, vol. 184, p. 87–95, 2016.

[17] D. Chlala, A. Griboval-Constant, N. Nuns, J.-M. Giraudon, M. Labaki, and J.-F. Lamonier, « Effect of Mn loading onto hydroxyapatite supported Mn catalysts for toluene removal: Contribution of PCA assisted ToF-SIMS », *Catal. Today*, vol. 307, p. 41–47, 2018.

[18] D. Chlala, « Étude de l'ajout de métaux (Pt, Pd, Mn et Cu) sur hydroxyapatite: apport de la flexibilité du support dans l'oxydation catalytique totale du toluène », PhD Thesis, University of Lille, 2015.

[19] L. Silvester, J.-F. Lamonier, R.-N. Vannier, C. Lamonier, M. Capron, A.-S. Mamede, F. Pourpoint, A. Gervasini, and F. Dumeignil, « Structural, textural and acid–base properties of carbonate-containing hydroxyapatites », *J. Mater. Chem. A*, vol. 2, n° 29, p. 11073–11090, 2014.

[20] B. Maaten, J. Moussa, C. Desmarets, P. Gredin, P. Beaunier, T. Kanger, K. Tõnsuaadu, D. Villemin, and M. Gruselle, « Cu-modified hydroxy-apatite as catalyst for Glaser–Hay C—C homo-coupling reaction of terminal alkynes », *J. Mol. Catal. Chem.*, vol. 393, p. 112–116, 2014.

[21] Z. Qu, Y. Sun, D. Chen, and Y. Wang, « Possible sites of copper located on hydroxyapatite structure and the identification of active sites for formaldehyde oxidation », *J. Mol. Catal. Chem.*, vol. 393, p. 182–190, 2014.

[22] C. Wen, Y. Cui, X. Chen, B. Zong, and W.-L. Dai, « Reaction temperature controlled selective hydrogenation of dimethyl oxalate to methyl glycolate and ethylene glycol over copper-hydroxyapatite catalysts », *Appl. Catal. B Environ.*, vol. 162, p. 483–493, 2015.

[23] F. C. Buciuman, F. Patcas, and T. Hahn, « A spillover approach to oxidation catalysis over copper and manganese mixed oxides », *Chem. Eng. Process. Process Intensif.*, vol. 38, n° 4‑6, p. 563–569, 1999.

[24] V. H. Vu, J. Belkouch, A. Ould-Dris, and B. Taouk, « Catalytic oxidation of volatile organic compounds on manganese and copper oxides supported on titania », *AIChE J.*, vol. 54, n° 6, p. 1585–1591, 2008.

[25] H. B. Lu, C. T. Campbell, D. J. Graham, and B. D. Ratner, « Surface characterization of hydroxyapatite and related calcium phosphates by XPS and TOF-SIMS », *Anal. Chem.*, vol. 72, n° 13, p. 2886–2894, 2000.

[26] R. França, T. D. Samani, G. Bayade, L. Yahia, and E. Sacher, « Nanoscale surface characterization of biphasic calcium phosphate, with comparisons to calcium hydroxyapatite and β-tricalcium phosphate bioceramics », *J. Colloid Interface Sci.*, vol. 420, p. 182–188, 2014.

[27] R. Oriňaková, A. Oriňak, M. Kupková, M. Hrubovčáková, L. Škantárová, A. Turoňová, L. M. Bučková, C. Muhmann, and H. M. Arlinghaus, « Study of Electrochemical Deposition and Degradation of Hydroxyapatite Coated Iron Biomaterials », *Int. J. Electrochem. Sci.*, vol. 10, p. 659–670, 2015.

[28] S. R. Leadley, M. C. Davies, C. C. Ribeiro, M. A. Barbosa, A. J. Paul, and J. F. Watts, « Investigation of the dissolution of the bioceramic hydroxyapatite in the presence of titanium ions using ToF-SIMS and XPS », *Biomaterials*, vol. 18, nº 4, p. 311–316, 1997.

[29] M. J. Ziglo, A. E. Nelson, G. Heo, and P. W. Major, « Argon laser induced changes to the carbonate content of enamel », *Appl. Surf. Sci.*, vol. 255, nº 15, p. 6790–6794, 2009.

[30] E. C. Njagi, C.-H. Chen, H. Genuino, H. Galindo, H. Huang, and S. L. Suib, « Total oxidation of CO at ambient temperature using copper manganese oxide catalysts prepared by a redox method », *Appl. Catal. B Environ.*, vol. 99, nº 1–2, p. 103–110, 2010.

[31] L. Shi, Z.-H. Hu, G.-M. Deng, and W.-C. Li, « Carbon monoxide oxidation on copper manganese oxides prepared by selective etching with ammonia », *Chin. J. Catal.*, vol. 36, nº 11, p. 1920–1927, 2015.

[32] W. Y. Hernández, M. A. Centeno, F. Romero-Sarria, S. Ivanova, M. Montes, and J. A. Odriozola, « Modified cryptomelane-type manganese dioxide nanomaterials for preferential oxidation of CO in the presence of hydrogen », *Catal. Today*, vol. 157, nº 1-4, p. 160–165, 2010.

[33] W. Y. Hernández, M. A. Centeno, S. Ivanova, P. Eloy, E. M. Gaigneaux, and J. A. Odriozola, « Cu-modified cryptomelane oxide as active catalyst for CO oxidation reactions », *Appl. Catal. B Environ.*, vol. 123, p. 27–35, 2012.

[34] J. Papavasiliou, G. Avgouropoulos, and T. Ioannides, « Combined steam reforming of methanol over Cu–Mn spinel oxide catalysts », *J. Catal.*, vol. 251, nº 1, p. 7–20, 2007.

Chapter IV: High efficiency of Cu/Hap catalyst in toluene oxidation through β-CD assisted synthesis.

4.1. Introduction

The performances of hydroxyapatite-supported Cu-based catalysts in the total oxidation of toluene have been limited thus far by the inability to increase the copper loading within the material without deteriorating its catalytic behavior, due to the negative effect a Cu amount higher than 2.5 wt% has on copper dispersion on the hydroxyapatite (Hap) support [1]. Thus, the objective of the following work will be to increase copper loadings on Hap support while maintaining good copper dispersion and reducibility, in order to improve the productivity of Cu/Hap catalysts in the total oxidation of toluene.

Over the past two decades, significant efforts have been focused on the generation of highly dispersed active copper species. On the one hand, the effect of the nature of the counter-anion of Cu(II) precursors has been investigated (nitrate, sulfate, acetate, and chloride) and copper(II) nitrate has led to the best dispersion of Cu particles leading towards the highest catalytic activity [2], [3]. In fact, in regards with Hap supported Cu catalysts, a previous study showed that among several copper precursors (nitrate, chloride and acetate), the catalyst prepared with Cu-nitrate led to the best catalytic performance while use of Cu-acetate as Cu-precursor caused some modification of the hydroxyapatite surface with enrichment of carbonate groups, with these latter tightly retaining Cu^{2+} species, causing them to be less prompt to react and thus being detrimental for the catalytic activity [4]. On the other hand, investigations regarding the use of an organic complexing agent to favor high dispersion and reducibility of Cu entities showed very promising results as well. Among the complexing agents which have been successfully used for improving the dispersion of Cu entities figures β-cyclodextrin [5].

Cyclodextrins (CD), which are macrocyclic oligosaccharides composed of α-(1,4) linked glucopyranose sub-units, have been receiving a lot of interest lately, emerging as potential tools for the development of well performing catalysts. Indeed, owing to their amphiphilic character, cyclodextrins are capable of forming inclusion complexes, with CD playing the role of host molecules able to include in their cavity hydrophobic guests, resulting thus in host–guest complexes [6], [7]. However, some metal ions can interact with hydroxyl groups of the CD molecule generating supramolecular adducts, or molecule-ion adducts, rather than inclusion complexes [8]–[10]. Of the three known types of CD (α-, β-, and γ-), β-cyclodextrin (β-CD) is the most widely involved in complexation processes [11], [12]. In fact, Bai *et al.* [8], [10] have demonstrated that the controlled addition of β-cyclodextrin during the impregnation step led towards the enhancement of the dispersion and reducibility of zirconia supported cobalt species, which induced a catalytic behavior upgrade in the complete oxidation of formaldehyde. They established that the nature of cobalt precursor used during impregnation step was very important seeing as its affinity for β-CD can strongly affect the final properties of the cobalt oxide catalysts [10]. Out of several examined cobalt precursors, cobalt nitrate emerged as a good precursor choice due to the occurrence of preferential interactions between this precursor and the hydroxyl sites located at the rim of β-CD cavity (either on the primary or secondary rim). β-CD played the role of a scaffold molecule that concentrated the cobalt ions at its close vicinity thus succeeding in forming more stable complexes of cobalt ions with β-CD which allowed for a better control of cobalt oxide nucleation during calcination, leading to a higher dispersion and reducibility of Co_3O_4 species. Moreover, these authors noticed that the performance of the catalyst was highly dependent on the β-CD to cobalt ratio used in the impregnating solution, finding an optimal value of

0.1. They explained their finding by proposing the formation of supramolecular adducts of Co^{2+} with β-CD, in which the cobalt center would be coordinated by two O atoms present at the β-CD rim.

The aim of this work will be to mimic what has been previously done by Bai *et al.* [8], [10] for supported cobalt species, but while employing a different transition metal (Cu instead of Co) and support material (Hap instead of ZrO_2).

Regarding copper interaction with cyclodextrins, previous investigations carried out by Matsui and co-workers [13]–[15], examining the complexation of Cu(II) ions by β-CD in alkaline solutions have shown that an inclusion 2:1 complex between copper (II) and β-CD is formed. This suggestion of a Cu-CD inclusion complex was further supported by the study of Ribeiro *et al.* [16] which revealed a favorable tendency of the β-CD system to incorporate Cu^{2+} in the internal cavity. However, both group of authors signaled that the proposed complex would be highly stable in basic conditions (due to the deprotonation of β-CD hydroxyl-groups), but not at neutral pH, where the chelating property of β-CD would be much weaker. Indeed, this was proven to be true through the works of Kurokawa *et al.* [17] and Song *et al.* [18], which inspected the interaction of β-CD with copper(II) chloride in neutral aqueous solutions. Their results indicated that rather than forming inclusion compounds, molecule-ion interactions occurred between β-CD and Cu^{2+} ions as well as Cl^- ions, which induced a weakening of ionic bonds in $CuCl_2$. Therefore, in the upcoming study, all synthesis will be conducted in neutral conditions to promote the formation of supramolecular adducts of Cu^{2+} with β-CD which will favor molecule-ion interactions between β-CD and Cu^{2+} cations along with NO_3^- anions, while weakening the ionic bonds in $Cu(NO_3)_2$, thereby preventing copper agglomeration and improving nitrate elimination efficiency during calcination step.

Furthermore, in the particular case of using hydroxyapatite as a support material, it should be reminded that Hap possesses exceptional properties among which figure its ion-exchange ability and great adsorption capacity. Thus, Hap presents a great affinity for copper cations through ion-exchange with its Ca^{2+} ions (with a maximum substitution rate of 6.6 wt% being reached) and surface complexation with its anionic adsorption sites (hydroxyl and phosphate groups) [19], [20]. Previous works have shown that several locations for copper entities on Hap are possible depending on the copper content and methods of copper addition [4], [21], [22]. In fact, depending on copper loading, copper cations will be more or less likely to interact with the support: active metal phase will tend to disperse as monolayer at low metal loading, thus favoring the bigger portion of metal phase to be surrounded by the carrier atoms, leading to strong metal–support interaction. While the double-layer and multi-layer of metal dispersion engendered by high metal loading will lessen the number of neighboring support's atom around metal species on the catalyst surface, entailing weaker metal–support interaction [23]. Strong interactions between the active phase and the support can be detrimental to the performances of the catalyst seeing as the reducibility of Hap-supported metal oxides has been shown to decrease when interaction with the Hap support becomes stronger [24], [25]. Thus, the use of β-CD will prevent the occurrence of strong metal-support interaction (SMSI) by acting as a chemical spacer between both copper entities (thus avoiding copper agglomeration) and copper species and the Hap support (thus avoiding the encapsulation of copper active species between layers of hydroxyapatite).

In this work the objective is to prepare efficient copper/Hap based catalysts (Cu wt%: 10) in toluene oxidation taking advantage of β-CD to enhance the dispersion and reducibility of the copper active phases. The strategy consists in forming macromolecular adducts between the copper-based precursor and β-CD, for which the methodology given by the work of Bai *et al.* [8], [10] will be used as reference. Thus, the conditions given by these authors to obtain macromolecular adducts will be adopted in this study (molar ratio β-CD/Cu = 0.1; neutral pH). In order to verify if the adopted method is successful in yielding efficient Cu/Hap catalysts in the total oxidation of toluene, catalytic tests are performed on 10 Cu-CD/Hap and the results are then compared with those of a reference catalyst (10 Cu/Hap). Any eventual improvement in the catalytic performances will be explained through a detailed study of the physicochemical properties of the developed materials by a set of complementary techniques which are XRD, TGA-DSC/MS, ATR-FTIR, H_2-TPR/MS, and XPS, allowing to determine whether an enhancement in the dispersion and reducibility of copper active species can be achieved through the use of β-CD.

4.2. Dried precursors

4.2.1. XRD

To gain further insight into the occurrence of interactions involving β-CD material which could have a significant impact on the nature and crystallite size of resulting Cu entities, XRD analysis was performed. The powder X-ray diffraction patterns of 10 Cu/Hap D and 10 Cu-CD/Hap D samples are shown in Figure 4.1-a. The XRD diffractograms of both compounds display the characteristic peaks relative to the hexagonal hydroxyapatite phase (PDF n ° 00-009-0432) with a P63/m space group. Additional peaks located at 2θ = 12.8 ° and 36.5 ° in both 10 Cu/Hap D and 10 Cu-CD/Hap D diffractograms are ascribed to copper hydroxynitrate, $Cu_2(OH)_3(NO_3)$, naturally found in the mineral called gerhardtite (PDF n ° 75-1779) and whose structure representation is given in Figure 4.2.

This basic Cu(II) salt which is known to be formed by careful heating of $Cu(NO_3)_2.3H_2O$ at 80 °C [26], [27] was previously shown on dried copper-loaded hydroxyapatite systems using incipient wetness impregnation method [28]. In fact, during the first stage of $Cu(NO_3)_2{\cdot}3H_2O$ thermal decomposition, which takes place between 40 and 80 °C, a dehydration process accompanied by significant hydrolysis occur, involving the splitting of bonds in $Cu(NO_3)_2.2.5H_2O$ and the addition of the hydrogen cation and the hydroxide anion of water to nitrate anions and copper nitrate entities, respectively, resulting thus in the release of HNO_3 and the formation of crystalline gerhardtite phase [27]:

$$\mathrm{Cu(NO_3)_2.3H_2O_{(cr)}} \rightarrow \mathrm{Cu(NO_3)_2.2.5H_2O_{(cr)}} + 0.5\ \mathrm{H_2O_{(g)}} \quad (4.1)$$

$$2\ \mathrm{Cu(NO_3)_2.2.5H_2O_{(cr)}} \rightarrow \mathrm{Cu_2(OH)_3(NO_3)_{(cr)}} + 2\ \mathrm{H_2O_{(g)}} + 3\ \mathrm{HNO_3}_{(g)} \quad (4.2)$$

The mean crystallite size based on the Scherrer equation from the peak located at 2θ = 12.8 ° is of the same order of magnitude for the 10 Cu/Hap D and 10 Cu-CD/Hap D samples with values of 84 nm and 96 nm, respectively. It should also be noted that none of the multiple peaks in the 10-25 ° 2θ range characteristic of the XRD pattern of pure β-CD (Figure 4.1-b) in accordance with literature reports [29], [30] can be observed for 10 Cu-CD/Hap D. The visual absence of any β-CD related peak can be the result of its very weak signal compared to that of copper entities (molar ratio β-CD/Cu = 0.1). Indeed, a similar outcome was reported in the work of Ye *et al.* [31] examining β-CD doped Cu-catalysts (0 < β-CD Mass fraction < 0.3), where the strong relative intensities of the peaks related to copper entities masked the weaker β-CD characteristic ones. Hence, based on XRD results, no difference can be perceived between the two samples considering their XRD patterns which both show the presence of gerhardtite. However, no further conclusion can be drawn at this stage.

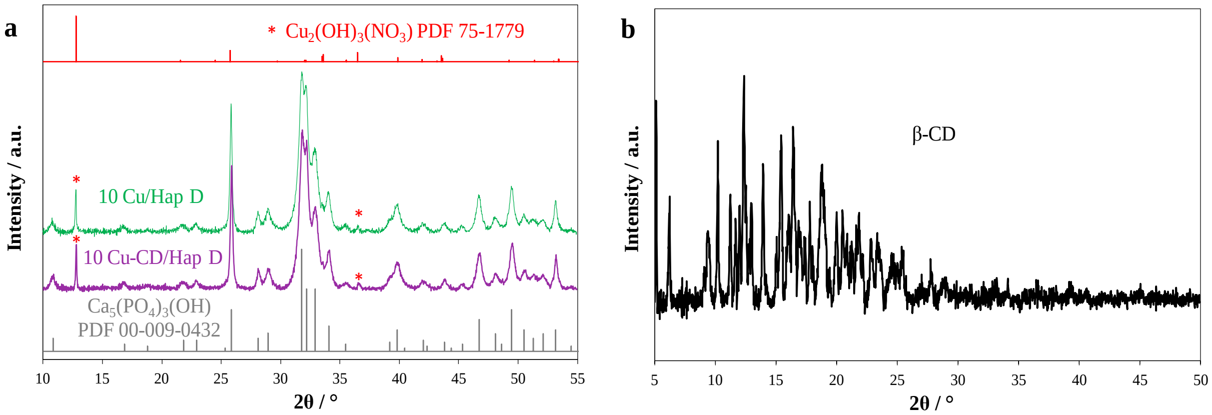

Figure 4.1. XRD patterns of a) 10 Cu/Hap D, 10 Cu-CD/Hap D and of b) pure β-CD.

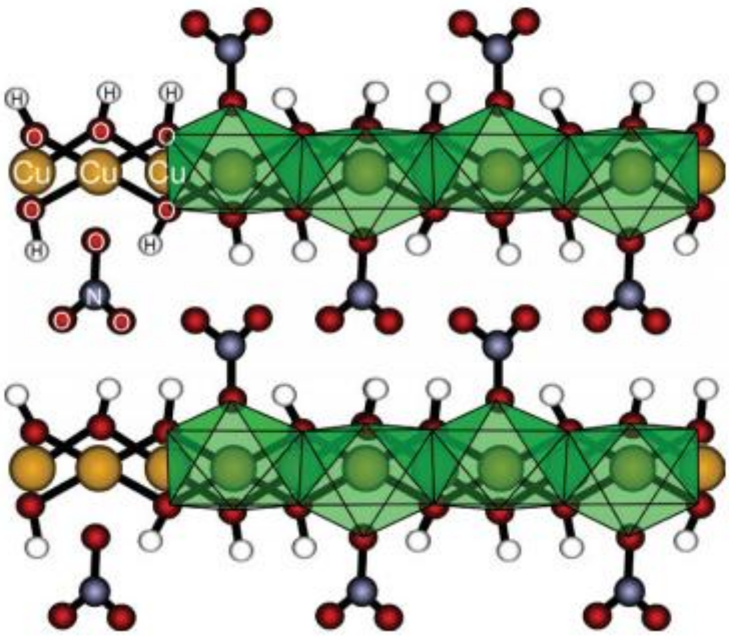

Figure 4.2. Schematic representation of the structure of copper hydroxynitrate, ($Cu_2(OH)_3NO_3$). From reference [32].

4.2.2. TGA/DSC-MS

TGA/DSC-MS experiments were performed over 10 Cu/Hap D, 10 Cu-CD/Hap D in order to investigate the effect of β-CD on the degradation pathway of the dried samples in flowing dry air. The resulting TGA/DTG and TGA/DSC traces are given in Figure 4.3 and the related data are listed in Table 4.1. For the 10 Cu/Hap D sample a total weight loss of 17.6% is observed within the whole temperature range from 20 °C to 600 °C. The DTG curve shows three peaks at 65 °C, 320 °C, and 415 °C corresponding to three distinct steps. The first endothermic step is attributed to the loss of adsorbed water [33] in line with H_2O evolution (m/z = 18, 17; Figure 4.3-c). The second and third processes are also endothermic. NO (m/z = 30, 14; Figure 4.3-d) as well as H_2O (Figure 4.3-c) are detected at the exit of the reactor during the second weight loss which takes place between 200 and 400 °C (Table AB.1). The concomitant detection of such gaseous species results from thermal decomposition of copper hydroxynitrate in accordance with previous works [34], [35]. Indeed, Schildermans *et al.* [34] who conducted their study under an atmosphere of dry N_2 indicated that the thermal decomposition of gerhardtite generates CuO *via* H_2O and HNO_3 removal which decomposes into NO and NO_2. However, in this case, despite conducting the experiments in O_2 atmosphere no significant presence of NO_2 can be detected (no notable evolution of the signal m/z = 46; Figure 4.3-d). Finally, the third endothermic step, characterized by a weight loss of 1.2 wt%, occurring between 400 and 450 °C can be due to the decomposition of related nitrate species probably incorporated in the Hap support in line with NO removal [36].

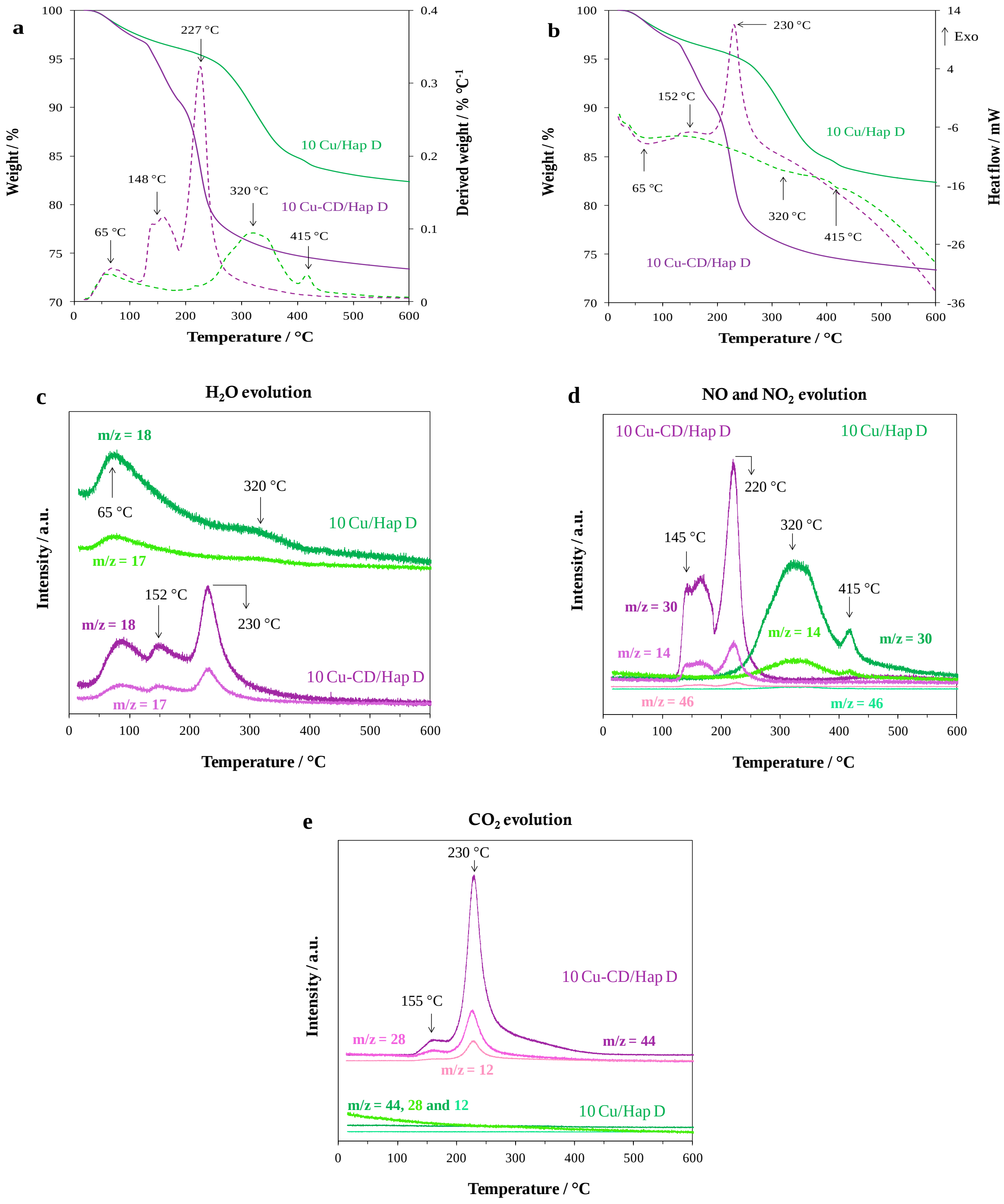

Figure 4.3. TGA-DTG a), TGA-DSC b) and MS signals corresponding to the evolution of H_2O c), NO, NO_2 d), and CO_2 e) in 10 Cu/Hap D and 10 Cu-CD/Hap D samples.

As expected in the case of 10 Cu-CD/Hap D sample, a higher total weight loss of 26.6% is observed due to the initial presence of β-CD, whose total decomposition should result in a theoretical weight loss of 12.4%. The DTG trace reveals again a three step decomposition process and the temperatures relative to the peaks are now 65 °C, 148 °C and 227 °C (Figure 4.3-a). The first endothermic process leading to a slight weight loss of 3.1%, observed from 20 °C to 120 °C, is due to the release of adsorbed water as well as water molecules present in the cavity of β-CD [37]. The latter is known to rapidly absorb water at ambient conditions [38] which can be usually eliminated between 50 and 100 °C [39]. This is consistent with the evolution of signal intensity for m/z = 17 and 18 (Figure 4.3-c). By opposition, the second and third processes taking place at 120 °C-190 °C and 190 °C-350 °C are both exothermic owing to the decomposition of β-CD, as proven by the detection of CO_2 (m/z = 44, 28, 12; Figure 4.3-e) and H_2O (m/z = 18, 17; Figure 4.3-c) in these two processes. A release of NO and NO_2 to a small extent (m/z = 30, 14 and 46; Figure 4.3-d) is also observed for each of these two steps. Based on the trace of m/z = 30 it is found that the nitrate thermal decomposition starts at 120 °C as compared to 200 °C for 10 Cu/Hap D. These nitrate species are supposed to belong to the gerhardtite in close vicinity of β-CD in accordance with simultaneous release of H_2O and CO_2. The third process is consistent with the complete degradation of gerhardtite to generate NO and H_2O and of the concomitant degradation of β-CD to give CO_2 and H_2O.

The constant weight loss observed after 450 °C (1.3 wt%, 10 Cu/Hap D) and 350 °C (2 wt%, 10 Cu-CD/Hap D) is mainly due to the dehydroxylation of the Hap [40], [41].

Therefore, it appears clearly from these experiments that the addition of β-CD in the sample accelerates significantly the thermal decomposition of copper supported phases, as proven by the lower temperature decomposition values found for 10 Cu-CD/Hap. Moreover, the elimination of nitrate becomes more efficient with the assistance of β-CD, as demonstrated by the evolution of m/z = 30 signal which undergoes a considerable shift towards lower temperature in 10 Cu-CD/Hap. This conclusion validates the occurrence of preferential interactions between β-CD and copper entities, this latter resulting in a weakening of the interactions between NO_3^- related species and Hap support.

Table 4.1. TGA based data for 10 Cu/Hap D and 10 Cu-CD/Hap D solids.

Sample	Global weight loss (%)	Experimental weight loss (%)		
		1st step	2nd step	3rd step
10 Cu/Hap D	17.6	4.1 (20 - 200 °C)	11 (200 - 400 °C)	1.2 (400 - 450 °C)
10 Cu-CD/Hap D	26.6	3.1 (20 - 120 °C)	6.4 (120 - 190 °C)	15.1 (190 - 350 °C)

4.3. Calcined catalysts

4.3.1. XRD

The diffractograms of 10 Cu/Hap (calcined at 400 °C for 4 h), 10 Cu-CD/Hap (calcined at 400 °C for 10 h) and Hap solids are shown in Figure 4.4. In addition to the diffraction peaks characteristic of the hexagonal $Ca_5(PO_4)_3(OH)$ phase (PDF n ° 00-009-0432), two intense peaks are observed at 2θ = 35.5 ° and 38.8 ° as well as a less intense peak at 2θ = 48.7 ° which are ascribed to the monoclinic phase of CuO (tenorite, PDF n ° 00-048-1548) (Figure 4.4-a). However, it is to be noted that the apparent peak at 2θ = 35.5 ° is due to overlapping peaks at 2θ = 35.47 ° and 2θ = 35.56 ° relative to CuO and that of

Hap at 2θ = 35.48 °. As for the other apparent peak at 2θ = 38.8 °, it is formed by two overlapping peaks at 2θ = 38.75 ° and 2θ = 38.97 ° ascribed to CuO (Figure 4.4-b). Based on these observations, the estimated value of 45 nm for the mean CuO crystallite size was obtained from the corrected FWHM of the peak at 2θ = 48.7 ° (Figure AB.1). This is in accordance with the value given by Chlala *et al.* [1] of 42 nm for a similar preparation. By opposition, the X-ray diffraction pattern of 10 Cu-CD/Hap shows broad and less intense reflections related to CuO indicating the presence of small CuO crystallites.

From these various observations it can be concluded that the addition of β-cyclodextrin can induce the formation of smaller CuO crystallites. This beneficial effect could be again explained by preferential interactions between β-CD and $Cu_2(OH)(NO_3)_2$ preventing the growth of CuO crystallites during the calcination step.

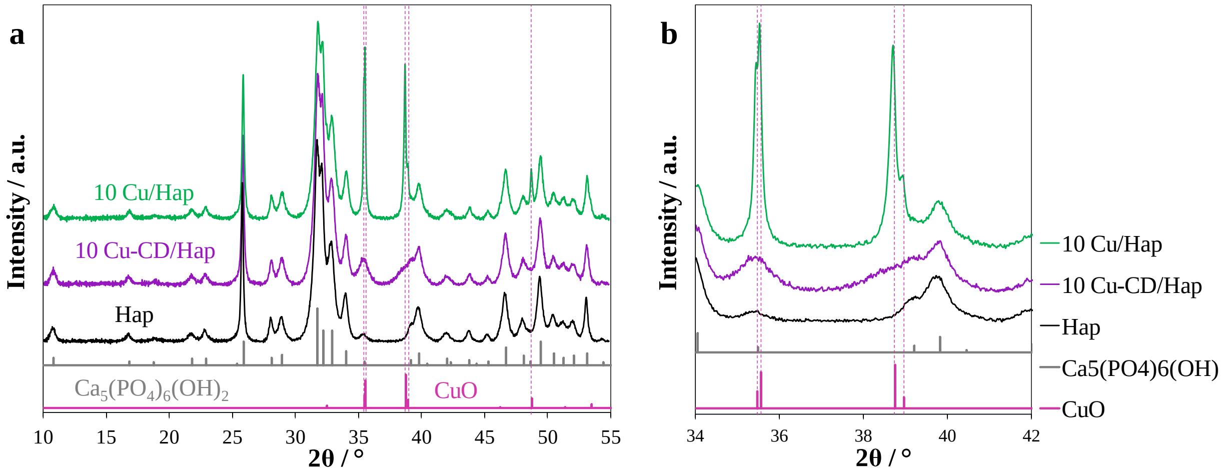

Figure 4.4. a) XRD patterns of 10 Cu/Hap, 10 Cu-CD/Hap and Hap samples; b) a zoom in the 2θ range of 34-42 °.

4.3.2. ATR-FTIR

The samples were additionally analyzed by ATR-FTIR spectroscopy to determine the purity of the samples. The ATR-FTIR spectra of 10 Cu/Hap and 10 Cu-CD/Hap solids are shown in Figure 4.5. The ATR-FTIR spectrum of Hap shows characteristic bands assigned to the PO_4^{3-} groups at 1100 and 1030 cm^{-1} (υ_3); 602 and 565 cm^{-1} (υ_4); and 962 cm^{-1} (υ_1) [42]. These phosphate bands are regarded as the IR fingerprint of hydroxyapatite material [43]. In addition, two absorption bands were observed at 633 cm^{-1} and 3573 cm^{-1}, corresponding to the deformation and stretching modes of OH ions, respectively [44]. Finally, weak bands corresponding to CO_3^{2-} species resulting from the dissolution of atmospheric CO_2 into the reaction medium during the preparation of Hap, were located at 875, 1413 and 1446 cm^{-1}. The position of these bands are in accordance with a type B substitution (CO_3^{2-} replacing PO_4^{3-}) [45], [46]. The ATR-FTIR spectra of the 10 Cu/Hap and 10 Cu-CD/Hap samples are similar to that of Hap apart from the presence of a weak band at 1386 cm^{-1} attributed to residual free nitrates for 10 Cu/Hap [47]. The ATR-FTIR spectrum of 10 Cu-CD/Hap solid (Figure 4.5-b) shows no band associated with the vibrational modes of pure β-CD [48]–[50], suggesting the complete elimination of the cyclodextrin.

Thus, the use of β-CD allows to get rid of the free nitrate species in accordance with the TGA/DSC-MS experiment.

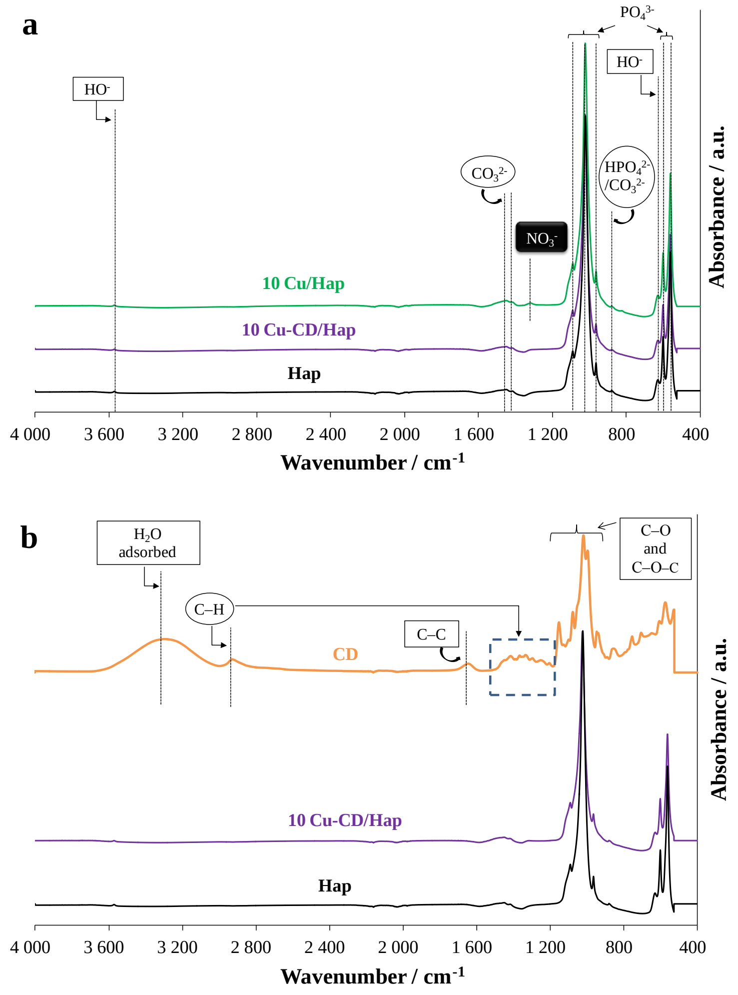

Figure 4.5. ATR-FTIR spectra of Hap, 10 Cu-CD/Hap, along with a) 10 Cu/Hap and b) pure β-CD.

4.3.3. H_2-TPR/MS

The reducibility of 10 Cu/Hap and 10 Cu-CD/Hap samples was investigated using H_2-TPR coupled with mass spectrometry, with the aim of determining whether the use of β-CD is capable of enhancing the reducibility of the copper supported active phases. The H_2-TPR profiles are shown in Figure 4.6 and the quantitative results are reported in Table 4.2. The two H_2-TPR profiles differ in the onset temperature of H_2-consumption and in the number of peaks. Indeed, the onset reduction temperature shifts toward a lower temperature of 85 °C for 10 Cu-CD/Hap as compared to 156 °C for 10 Cu/Hap. Three reduction peaks at 234 °C, 290 °C and 450 °C are observed in the temperature range of 150 °C-500 °C for 10 Cu/Hap while only a broad peak centered at 237 °C is observed for 10 Cu-CD/Hap in the temperature range of 80 °C-280 °C.

It has to be noted that the total H_2 consumption $n(H_2)_{ex}$ values of 2.81 and 1.99 mmoles per gram of catalyst for 10 Cu/Hap and 10 Cu-CD/Hap, respectively, exceed the theoretical one $n(H_2)_{th}$ of 1.58 based on the assumption that Cu^{2+} is completely reduced into metallic Cu. This H_2 overconsumption implies the reduction of nitrates retained on Hap. The reduction of nitrates into NO operates at low temperature, while N_2 and NH_3 are detected as the temperature increases (Figure 4.7-a). Such an evolution follows the reaction scheme given below of the catalytic hydrogenation of nitrate species over copper bearing materials proposed in previous investigations [51], [52]:

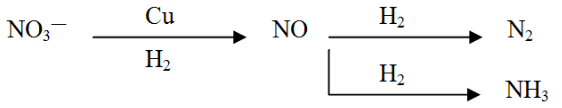

$$NO_3^{-} \xrightarrow[H_2]{Cu} NO \xrightarrow{H_2} N_2$$
$$NO \xrightarrow{H_2} NH_3$$

(4.3)

The reduction of some related NO_3^- species takes place also when considering the reduction of 10 Cu-CD/Hap, owing to the same pathways as for 10 Cu/Hap but to a minor extent (Figure 4.7-b). However, contrary to 10 Cu/Hap the release of CO_2 (m/z = 12, 44) is now observed at low temperature. The detection of CO_2 can be the result of the reduction of CuO by some adventitious carbon at the surface of the catalyst, possibly derived from traces of remaining β-CD (this hypothesis will be further explored later when discussing XPS results).

In any case, the reducibility of the catalysts was determined from the temperature corresponding to the onset of NO production (T_{NO}) knowing the capacity of Cu(0) to reduce NO_3^- species into NO at low temperature. The most reducible solid being thus the one with the lowest value of T_{NO} (°C): 10 Cu-CD/Hap (110) < 10 Cu/Hap (150).

Hence, similar to what had been previously observed by Bai *et al.* [8], [10] in the case of zirconia supported-cobalt oxide catalysts, the use of β-CD promotes the production of active sites with an enhanced reducibility.

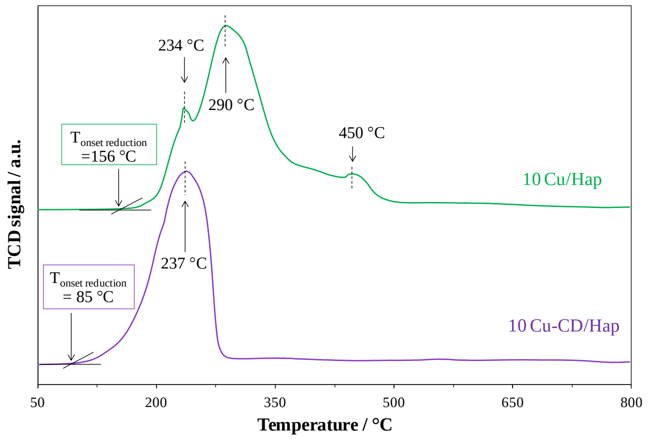

Figure 4.6. H_2-TPR profiles of 10 Cu/Hap and 10 Cu-CD/Hap solids calcined at 400 °C.

Table 4.2. H_2-TPR results.

Sample	$T_{onset\ reduction}$ [°C] [a]	T_{NO} [°C] [b]	$n(H_2)_{th}$ [c] [$mmol.g^{-1}$]	$n(H_2)_{ex}$ [d] [$mmol.g^{-1}$]
10 Cu/Hap	156	150	1.58	2.81
10 Cu-CD/Hap	85	110	1.58	1.99

[a] Temperature of onset reduction. [b] Temperature of NO appearance. [c] Theoretical amount of H_2 consumed. [d] Experimental amount of H_2 consumed.

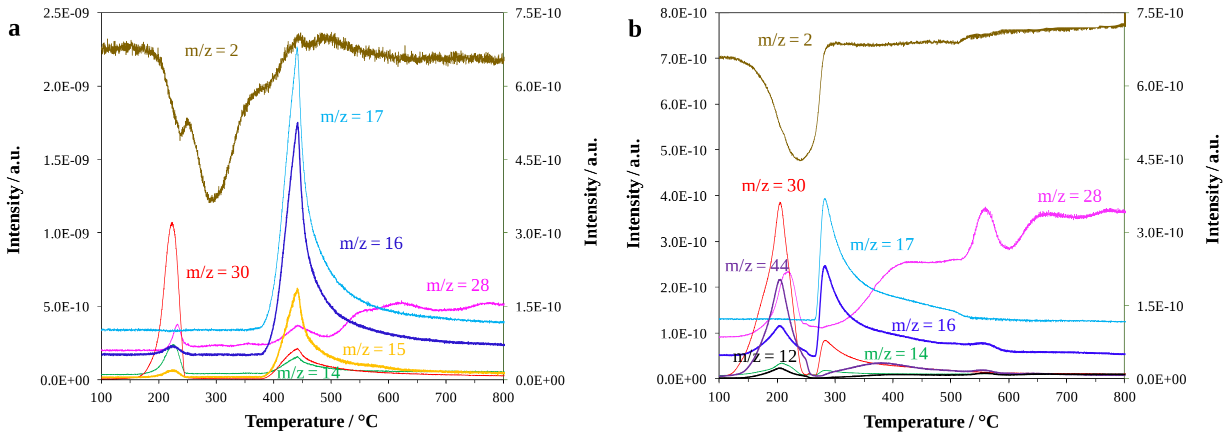

Figure 4.7. Evolution of the intensity of the signals corresponding to m/z = 2 (given by the y-axis on the right), 12, 14, 15, 16, 17, 28, 30, and 44 (given by the y-axis on the left) as a function of temperature for the solids: a) 10 Cu/Hap and b) 10 Cu-CD/Hap.

4.3.4. XPS

XPS analysis was conducted in order to examine the effect of β-CD addition on Cu dispersion and oxidation state, on the surface of the studied samples. The C1s core-level was also examined in order to investigate and quantify the carbonaceous based residues.

The binding energy of the Cu $2p_{3/2}$ photopeak was used to determine the chemical state of copper species present on the surface of prepared solids. All XPS based data are given in Table 4.3 and the Cu 2p core level XPS spectra are given in Figure 4.8. It can be seen that the Cu $2p_{3/2}$ binding energy (BE) values found for 10 Cu/Hap (933.6 eV) and 10 Cu-CD/Hap material (934.4 eV), agree with previously reported data on Cu $2p_{3/2}$ BE values of CuO compound [53]–[55]. The presence of Cu^{II} species is further confirmed by the detection of a “shake-up” structure characteristic of Cu (II) oxidation state in both of the acquired Cu 2p spectra. In addition, a calculation of the ratio of the satellite to that of the main Cu $2p_{3/2}$ peak (I_{sat}/I_{pp}) showed values of 0.50 and 0.55 for 10 Cu/Hap and 10 Cu-CD/Hap, respectively, which concord with literature data indicating that a 0.5 value for I_{sat}/I_{pp} is characteristic of Cu^{2+} species in octahedral coordination [56], [57].

The higher BE value (+0.8 eV) in the case of 10 Cu-CD/Hap can be explained by one of two factors: the dispersion degree of copper oxide species and metal–support interactions between the copper oxide moieties and the Hap support. Indeed, both those reasons have been invoked in the past to explain the shifts in BE value. Thus, on one hand, strong metal–support interactions (SMSI) can induce changes to the electronic properties of the supported metal clusters through electron transfer from the support to the supported particles, resulting in a negative shift of BE towards lower values [58], [59]. Therefore, based on the metal-support effect, it would seem that the use of β-CD leads towards weaker metal-support interactions ensuing higher Cu $2p_{3/2}$ BE value. On the other hand, the aggregation state (particle size and dispersion degree) of supported phases can have a paramount influence upon the energy position of the photoelectron signal due to a relaxation effect: the hole state produced by photoionization in a solid is shielded by the conduction electrons and the cores of neighboring atoms. This effect lowers the energy of the final state and results in a lower measured binding energy. Such an effect is clearly impossible for an isolated atom, and thus a shift to lower BE is expected in the transition from atom to bulk metal [55], [60]. Hence, based on the particle size effect it would appear that a promotion effect on the dispersion of Cu^{2+} species occurs by β-CD addition.

Moreover, a considerable increase in Cu dispersion can be noted when employing β-CD in the synthesis process. Indeed, as reported in Table 4.3, the XPS Cu/(Ca + P) ratio doubled for 10 Cu-CD/Hap, compared to its value in 10 Cu/Hap. In parallel, 10 Cu/Hap sample exhibits an about twice higher O/Cu ratio (36 *vs* 16 for 10 Cu-CD/Hap), all of which might be attributed to segregation of CuO phase [61]. This is also in line with what has been previously reported by Chlala *et al.* [1] who found that for their Cu10Hap (10 wt% load of Cu) sample, not all of Cu becomes apparent in XPS due to the formation of large CuO particles with a mean size > 10 nm, the latter corresponding to the analysis depth of the XPS technique.

Table 4.3. XPS based data for 10 Cu/Hap and 10 Cu-CD/Hap.

Sample	Cu $2p_{3/2}$ BE	FWHM[a] Cu $2p_{3/2}$	Cu $2p_{1/2}$ BE	FWHM[a] Cu $2p_{1/2}$	I_{sat}/I_{pp}[b]	C/Cu[d]	O/Cu[d]	Cu/P[d]	Cu/Ca[d]	Cu/(Ca+P)[d]
10 Cu/Hap	933.6 [932.8][e]	3.9 [2.7][e]	953.7	4.4	0.50 [0.47][c]	29.0	36.0	0.14	0.08	0.06
10 Cu-CD/Hap	934.4 [933.0][e]	3.8 [2.7][e]	954.5	4.4	0.55 [0.53][c]	19.0	16.0	0.29	0.22	0.13

[a] Full Width at Half Maximum. [b] Intensity ratio between Cu $2p_{3/2}$ and corresponding satellite peak. [c] Intensity ratio between Cu $2p_{1/2}$ and corresponding satellite peak. [d] XPS atomic ratio. [e] Data obtained for the 2nd recording.

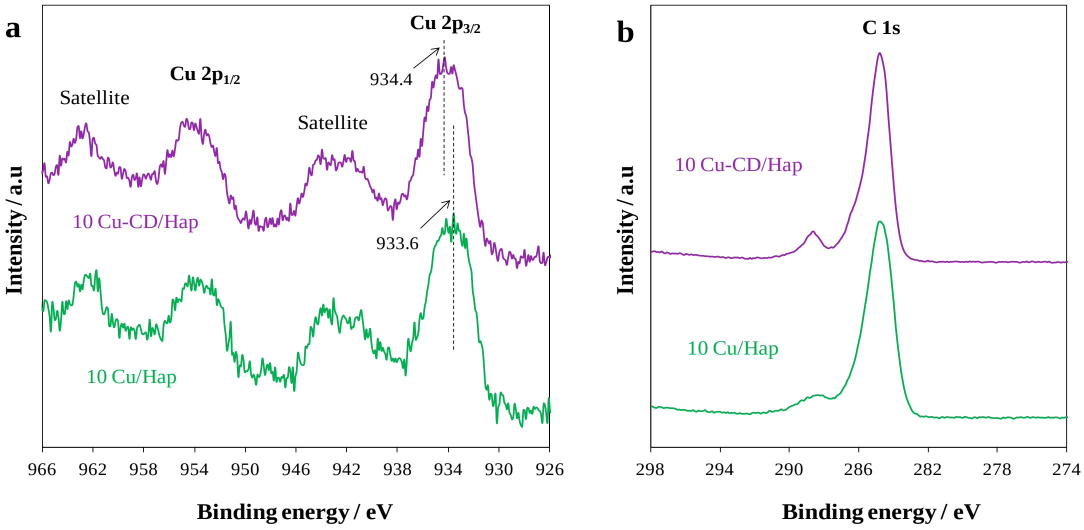

Figure 4.8. Cu 2p a) and C 1s b) XPS core levels for 10 Cu/Hap and 10 Cu-CD/Hap materials.

On another note, it should be signaled that while both Cu/P and Cu/Ca molar ratios increase when going from 10 Cu/Hap to 10 Cu-CD/Hap, Cu/P value is doubled for 10 Cu-CD/Hap (similarly to what is perceived for Cu/(Ca+P) ratio), whereas Cu/Ca value is almost tripled for 10 Cu-CD/Hap. This could be indicative of the role played by β-CD in preventing copper species migration deep inside the lattice of Hap by substitution of calcium ions which could lead towards surface enrichment in Ca and depletion of Cu.

It should nevertheless be noted that an XPS-induced reduction of copper particles, which has been previously reported to occur [62]–[70], did take place during data acquisition as demonstrated by the decrease in the Cu $2p_{3/2}$ BE (≈ 933 eV) and FWHM Cu $2p_{3/2}$ (2.7) values obtained for the 2nd recording, which were conducted at the end of XPS analysis (Table 4.3). Indeed, these values are indicative of a reduced state of copper entities (Cu^+/Cu^0) and so it does not seem that the use of β-CD is capable of improving the stability of Cu^{2+} species and lessening, thus, the in-situ reduction effect.

Finally, regarding the presence of any residual carbonaceous based entities in 10 Cu-CD/Hap, no additional feature or significant increase in the intensity of the peaks noted in C1s core level spectrum can be seen for 10 Cu-CD/Hap when compared to 10 Cu/Hap sample (Figure 4.8-b). Furthermore, an examination of the evolution of C/Cu ratio between 10 Cu/Hap and 10 Cu-CD/Hap offers no conclusive proof as to the presence of any carbonaceous based residues at the surface of 10 Cu-CD/Hap material.

Thus, XPS analysis evidences the effectiveness of using β-CD for enhancing copper dispersion as well as promoting the presence of Cu in its +II oxidation state at the catalyst surface.

4.4. Catalytic performances in the total oxidation of toluene

The effect of the initial concentration of toluene (C^0 = 200 ppmv, 400 ppmv, 800 ppmv) has been first investigated on the performances of 10 Cu/Hap and 10 Cu-CD/Hap catalysts in the total oxidation of this VOC throughout the determination of the toluene conversion as a function of time (24 h) at a temperature of 250 °C. The experiment has been carried out in a consecutive way by raising the concentration at each step. Between each step the catalyst is left in air for a duration needed to stabilize the new reactive flow rate. The time on stream curves are given in Figure 4.9 and the corresponding data are reported in Table 4.4. For both catalysts it should be noted that no deactivation occurs whatever the initial toluene concentration. Additionally for 10 Cu/Hap, an induction period of 8 h at 200 ppmv is observed, during which the conversion of toluene increases from 48% to 70%. A similar phenomenon is observed for C^0 = 400 ppmv but with a decreased duration (6 h instead of 8 h) and absent at C^0 = 800 ppmv. The activation step which does not occur for 10 Cu-CD/Hap can be the result of the reduction of residual nitrate species, shown to be present in 10 Cu/Hap catalyst by IR analysis. Indeed, the elimination of these remaining nitrates previously blocking the pores of the support would lead to an increase in the specific surface area value, inducing thus better catalytic performance [1].

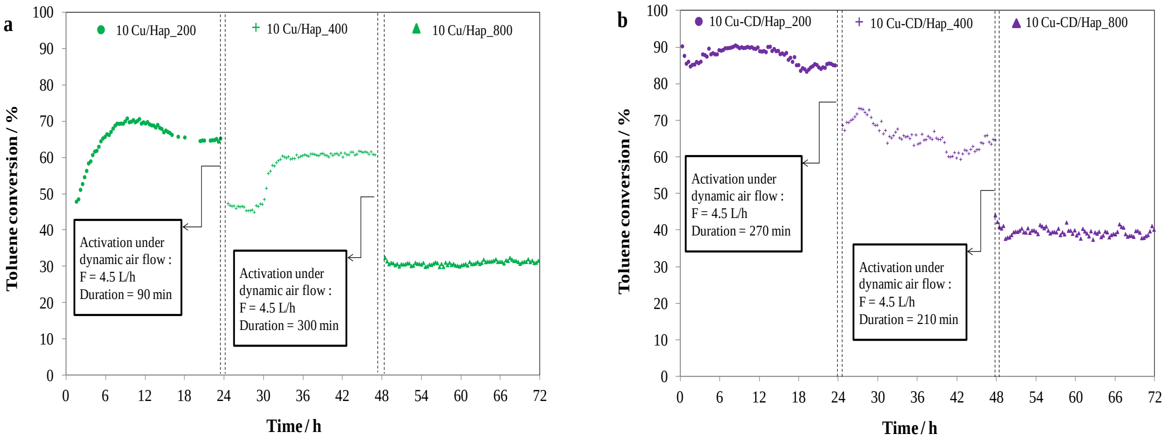

Figure 4.9. Time-on-stream plot of toluene conversion at 250 °C over 10 Cu/Hap and 10 Cu-CD/Hap catalysts for three different toluene concentration values: 200, 400, and 800 ppmv.

Regarding the influence of the toluene concentration on the standardized toluene conversion rate determined at 250 °C (r_{250}), expressed in mole of reacted toluene per hour and per mol of transition metal and determined according to:

$$r = \frac{\text{ppmv Tol} \times F_T \times C_t}{V_m \times n_{TM}} \qquad (4.4)$$

both catalysts reveal an initial increase in activity ($/10^{-2}$ h^{-1}) when the toluene concentration first increases within the feed composition (Figure 4.10).

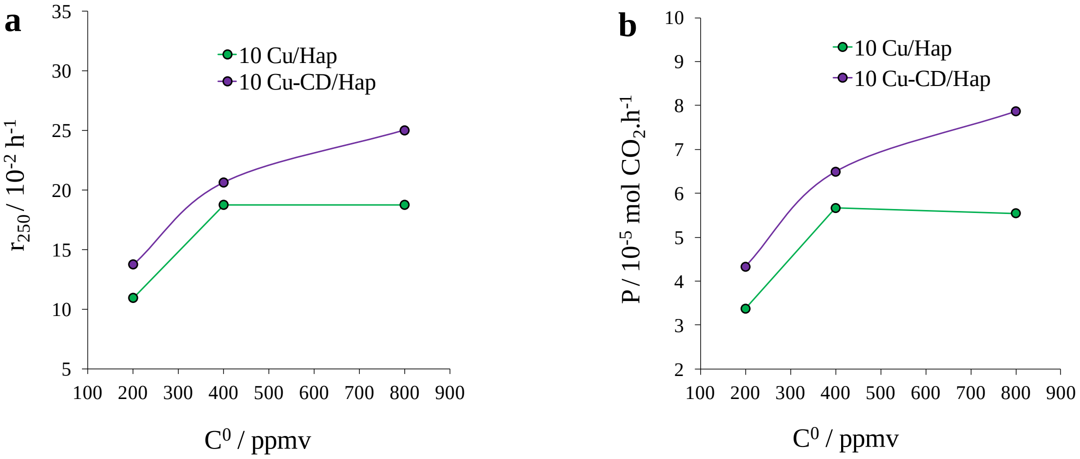

Figure 4.10. a) Rate of toluene conversion at 250 °C (r_{250}) and b) CO_2 Productivity (P) as a function of initial toluene concentration (C^0) for 10 Cu/Hap and 10 Cu-CD/Hap catalysts.

It can be noted that while 10 Cu-CD/Hap manifests a continuous increase in r_{250} with increasing toluene concentration, 10 Cu/Hap shows a rise in the initial value of r_{250} when going from 200 ppmv to 400 ppmv but then the catalyst's activity remains constant when the toluene concentration is further increased to 800 ppmv. When examining the time-on-stream plots represented in Figure 4.9, it is apparent that an inversely proportional relation exists between toluene conversion (C_t) and toluene concentration (C^0) for both catalysts. This is to be expected since the concentration of active sites remains unchanged while that of reactant increases [71]–[73]. Therefore, two reasons can be suggested as for why the catalytic activity ceases to increase above a toluene concentration of 400 ppmv in the case of 10 Cu/Hap whereas it continues on rising in the case of 10 Cu-CD/Hap: the first being that active sites saturation is reached sooner for 10 Cu/Hap when compared to 10 Cu-CD/Hap, due to the high dispersion of copper species in 10 Cu-CD/Hap catalyst which is likely to result in a higher number of copper active sites. The second reason could be that the use of β-CD leads to the formation of copper active sites with higher efficiency than those resulting from the conventional synthesis method (10 Cu/Hap).

Furthermore, by examining Figure 4.10-a, in which is represented the evolution of r_{250} as a function of toluene concentration for both 10 Cu/Hap and 10 Cu-CD/Hap solids, a higher position of the trace belonging to 10 Cu-CD/Hap catalyst can be noted. This observation implies an enhancement in toluene conversion efficiency due to the use of β-CD, which by improving copper dispersion gives rise to greater reducibility, the latter being a most determining parameter for a Mars-van Krevelen based oxidation mechanism. Therefore, both an increase in the number and quality of Cu active sites is achieved. The latter is further corroborated by the complete selectivity of 10 Cu-CD/Hap towards CO_2 (Table 4.4) resulting in higher productivity (Figure 4.10-b) compared to 10 Cu/Hap which produces some CO along with CO_2, but no other by-products.

To summarize, it appears that resorting to β-CD in the synthesis process is catalytically profitable: both toluene conversion rate and CO_2 productivity are positively affected by its use which allows for an increase in the number and quality of copper active sites.

Table 4.4. Stability tests data for 10 Cu/Hap and 10 Cu-CD/Hap.

Sample	C^0 [ppmv] [a]	C_t [%] [b]	r_{250} [h^{-1}] [c]	S_{CO2} [%] [d]	S_{CO} [%] [e]	P [/10^{-5} mol $CO_2.h^{-1}$] [f]
10 Cu/Hap_200	200	70	0.109	98	2	3.4
10 Cu/Hap_400	400	60	0.188	96	4	5.7
10 Cu/Hap_800	800	30	0.188	94	6	5.6
10 Cu-CD/Hap_200	200	88	0.138	100	0	4.3
10 Cu-CD/Hap_400	400	66	0.206	100	0	6.5
10 Cu-CD/Hap_800	800	40	0.250	100	0	7.9

[a] Concentration of toluene in the feed composition. [b] Toluene conversion. [c] Standardized conversion rate determined at 250 °C. [d] Selectivity towards CO_2. [e] Selectivity towards CO. [f] CO_2 productivity of the catalyst.

4.5. Characterization of the used catalysts

4.5.1. H_2-TPR/MS and XRD

The effect of stability tests on the reducibility of used 10 Cu/Hap U and 10 Cu-CD/Hap U was assessed by H_2-TPR coupled with MS. The H_2-TPR traces of the fresh and used 10 Cu/Hap and 10 Cu-CD/Hap are shown in Figure 4.11 and the related data given in Table 4.5. Regarding 10 Cu/Hap U, the H_2 consumption envelope is strongly modified. Four peaks are now observed at 240 °C, 280 °C, 330 °C and 360 °C in the 150-400 °C temperature range as well as a small peak at 618 °C. It is clear that the H_2 consumption peak at 240 °C attributed to the reduction of the dispersed small Cu(II) clusters on the surface decreases in 10 Cu/Hap U compared to what was observed in 10 Cu/Hap solid (peak at 234 °C). The additional high temperature peaks noted in the case of the used solid compared to fresh 10 Cu/Hap can be the result of the formation of bulk CuO at the surface with different particle sizes [21], [74], and a possible alteration in Cu speciation following catalytic oxidation of toluene, engendering Cu^+ species [75], [76]. Thus, it would seem that stability tests caused a decrease in the reducibility of copper species, which then resulted in a decline of the catalytic activity.

Concerning 10 Cu-CD/Hap U, the hydrogen consumption peak becomes narrower compared to that of the fresh sample, reflecting good homogeneity of the sample, with a shift to higher temperature. This suggests that while a good dispersion of small Cu(II) clusters is still maintained on the surface of the used catalyst, a sintering of the active copper species is starting to take place following stability test.

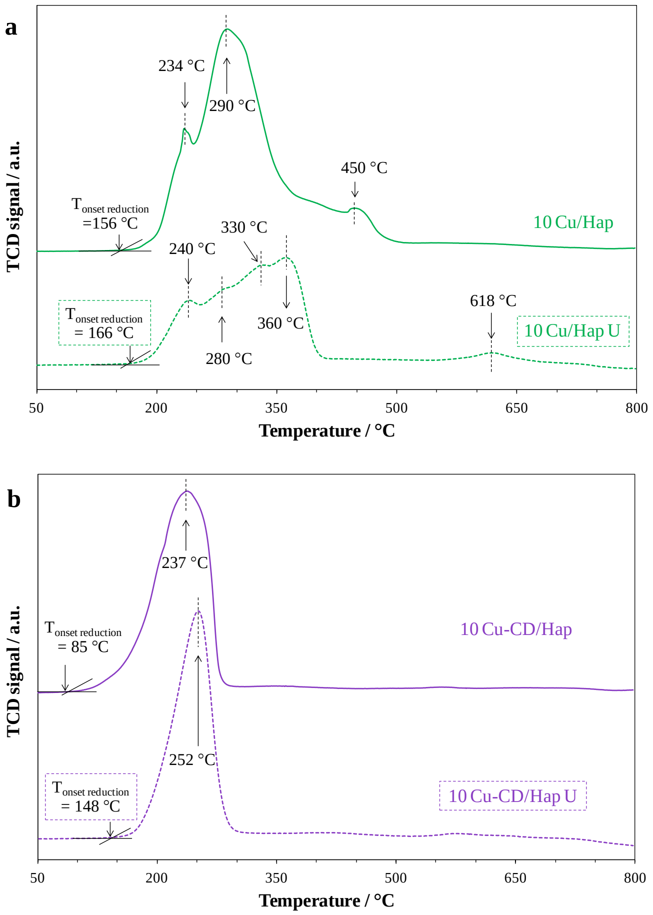

Figure 4.11. H_2-TPR profiles of fresh and used a) 10 Cu/Hap and b) 10 Cu-CD/Hap solids.

It should be noted that the onset of H_2 consumption is shifted to higher temperature for 10 Cu-CD/Hap U while this temperature is slightly affected for the cyclodextrin-free catalyst. In both cases the experimental H_2 consumption amount is close to the theoretical value meaning that the total amount of Cu(II) is reduced into Cu(0). This is consistent with the removal of the retained NO_3^- like species in the course of the reaction [77], as confirmed by the absence of m/z signals derived from the degradation of NO_3^- species (Figure 4.12-a).

The evolution of the intensity of m/z signals (12, 14, 15, 16, 28, 30, and 44) as a function of temperature is given in Figure 4.12-a. Taking into account the cracking patterns, a release of CO_2 is observed in the 200 °C-400 °C temperature range followed by the production of CH_4 and CO in the 500 °C-700 °C temperature range, indicating the occurrence of some fouling of the surface with coke and other carbon products following stability tests.

The XRD patterns of 10 Cu/Hap U and 10 Cu-CD/Hap U samples, illustrated in Figure 4.13, reveal no new crystalline phase, nor do they reveal any modification in the positions of the peaks previously observed in fresh samples relative to hydroxyapatite and copper oxide crystalline phases. They do show however some modification in the relative intensities of the peaks attributed to CuO. While an increase in the crystallite size (D_c) of CuO occurs in 10 Cu-CD/Hap U, as revealed by the appearance of the diffraction peak at $2\theta = 48.7$ ° attributed to CuO, previously masked in the fresh catalyst, and from which is calculated a mean CuO crystallite size of 16 nm (Table 4.5), an opposite effect is noted in the case of 10 Cu/Hap U. Indeed, a decrease in the size of CuO crystallites following the stability test can be remarked (45 nm for 10 Cu/Hap vs. 36 nm for 10 Cu/Hap U), suggesting a redispersion of the crystalline copper phases. Redispersion, the reverse phenomenon of crystal growth, is thought to be due to the fragmentation of copper oxide particles into small crystallites, following the reduction of these copper phases during the catalytic process [78].

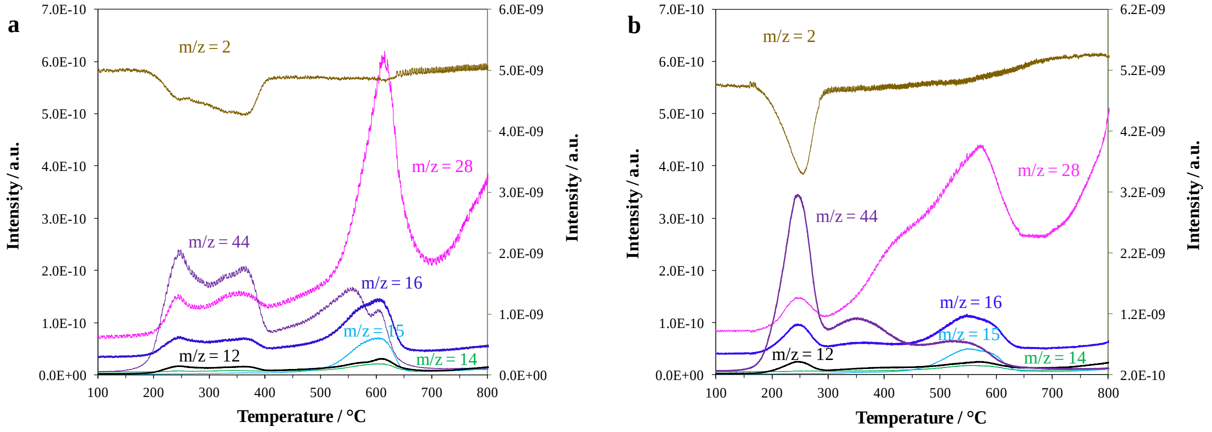

Figure 4.12. Evolution of the intensity of the signals corresponding to m/z = 2 (given by the y-axis on the right), 12, 14, 15, 16, 28, 30, and 44 (given by the y-axis on the left) as a function of temperature for the solids: a) 10 Cu/Hap U and b) 10 Cu-CD/Hap U.

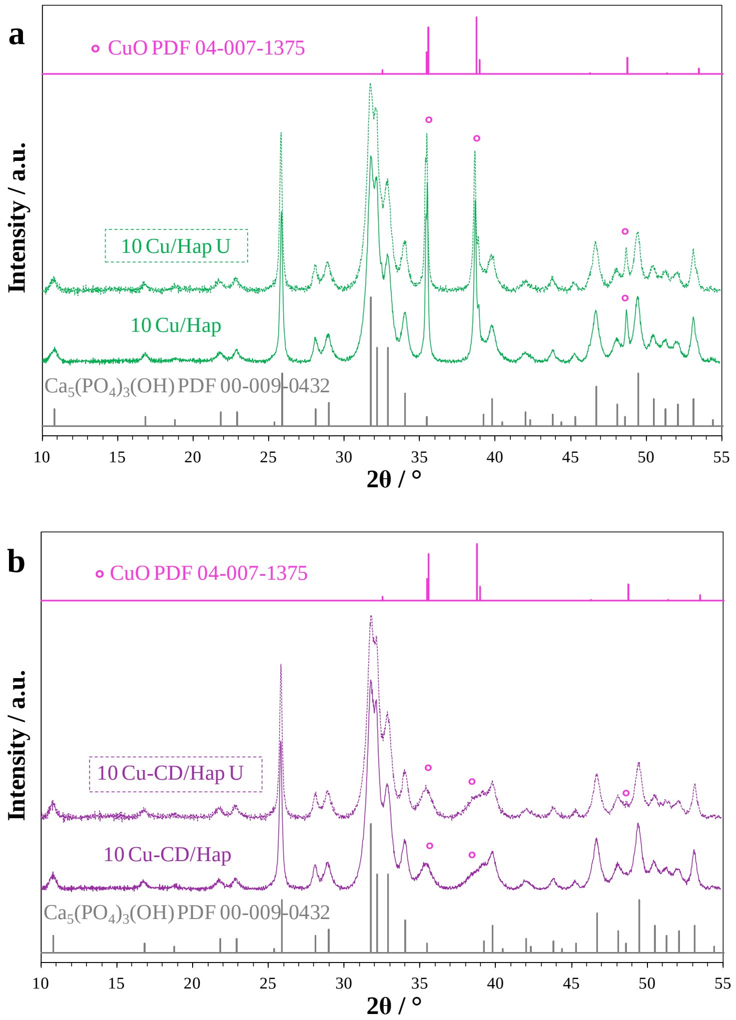

Figure 4.13. XRD patterns of fresh and used a) 10 Cu/Hap and b) 10 Cu-CD/Hap solids.

Based on both H_2-TPR and XRD results, it would seem that stability tests induce both a decrease in the reducibility of copper species and a change in the CuO crystallite size in both 10 Cu/Hap U and 10 Cu-CD/Hap U catalysts.

Table 4.5. H_2-TPR, XRD, and XPS results for fresh and used 10 Cu/Hap and 10 Cu-CD/Hap solids.

Sample	$T_{onset\ reduction}$[a] [°C]	$n(H_2)_{th}$[b] [mmol.g^{-1}]	Dc[d] CuO [nm]	Cu $2p_{3/2}$[e] [eV]	FWHM Cu $2p_{3/2}$ [f] [eV]	I_{sat}/I_{pp}[g]	C/Cu[h]	O/Cu[h]	Cu/P[h]	Cu/Ca[h]	Cu/(Ca+P) [h]
10 Cu/Hap	156	2.81 [1.58][c]	45	933.6	3.9	0.50	29.0	36.0	0.14	0.08	0.06
10 Cu/Hap U	166	1.55 [1.58][c]	36	932.5	3.0	0.20	26.8	54.2	0.08	0.05	0.03
10 Cu-CD/Hap	85	1.99 [1.58][c]	-	934.3	3.8	0.55	19.0	16.0	0.29	0.22	0.13
10 Cu-CD/Hap U	148	1.58 [1.58][c]	16	932.8	3.1	0.26	10.1	21.9	0.21	0.15	0.09

[a] Temperature of onset reduction. [b] Experimental amount of H_2 consumed. [c] Theoretical amount of H_2 consumed. [d] Mean CuO crystallite size. [e] Cu $2p_{3/2}$ binding energy. [f] Full width at half maximum of Cu $2p_{3/2}$ peak. [g] Intensity ratio between Cu $2p_{3/2}$ and corresponding satellite peak. [h] XPS atomic ratio.

4.5.2. XPS

For a better study of surface properties following stability experiments, XPS analysis was conducted on used catalysts and the results, summarized in Table 4.5, were compared with those noted for fresh materials. It is apparent that a decrease in the Cu $2p_{3/2}$ BE occurs when going from the fresh to the used catalysts (-1.1 eV for 10 Cu/Hap U and -1.5 eV for 10 Cu-CD/Hap U). In fact, the BE values of 932.5 and 932.8 eV found for the Cu $2p_{3/2}$ peak of 10 Cu/Hap U and 10 Cu-CD/Hap U, respectively, are in line with literature reported values for reduced copper states, be it Cu^{I} or Cu^{0} [54], [79]. In addition, the decrease in the FWHM values of the Cu $2p_{3/2}$ peak in the used samples suggests the occurrence of a reduction process succeeding stability tests. However, the presence of satellite peaks in the Cu 2p core level spectra of both used catalysts, shown in Figure 4.14-a, indicates the presence of remaining copper II species along with the reduced copper entities. In fact, the values found for I_{sat}/I_{pp} are 0.20 and 0.26 for 10 Cu/Hap U and 10 Cu-CD/Hap U, respectively, which are lower than 0.5, the characteristic value for Cu^{2+} species and higher than the one corresponding to Cu^{+} species, are representative of the presence of a mixture of copper oxidation states (+II; +I/0).

The Cu/(Ca+P) atomic ratio values decrease by half and by quarter compared with those on the fresh catalysts for 10 Cu/Hap U and 10 Cu-CD/Hap U, respectively. This can suggest some agglomeration of copper related species after test whose extent is minimized over the 10 Cu-CD/Hap showing again the beneficial effect of the cyclodextrin. Moreover, compared to what was obtained for fresh samples, the values of O/Cu increase by ca. 50% and 35% for 10 Cu/Hap U and 10 Cu-CD/Hap U, respectively. While this increase is partially caused by the agglomeration of copper entities following stability test, it is also the result of catalyst fouling by carbonaceous species. Indeed, despite the decrease of C/Cu ratio for used catalysts, a comparison of the normalized overlay of C 1s spectra for fresh and used 10 Cu/Hap and 10 Cu-CD/Hap materials, reported in Figure 4.14-b, reveals an increase in the intensity of the peak contribution at 288.6 eV assigned to O–C=O and the emergence of a shoulder at 286.9 eV attributed to C=O, all of which can be associated with the presence of adsorbed organic species on the surface of the used catalysts [80], [81]. The large particle size of these carbonaceous species might be at the origin of the low C/Cu ratio found in used samples.

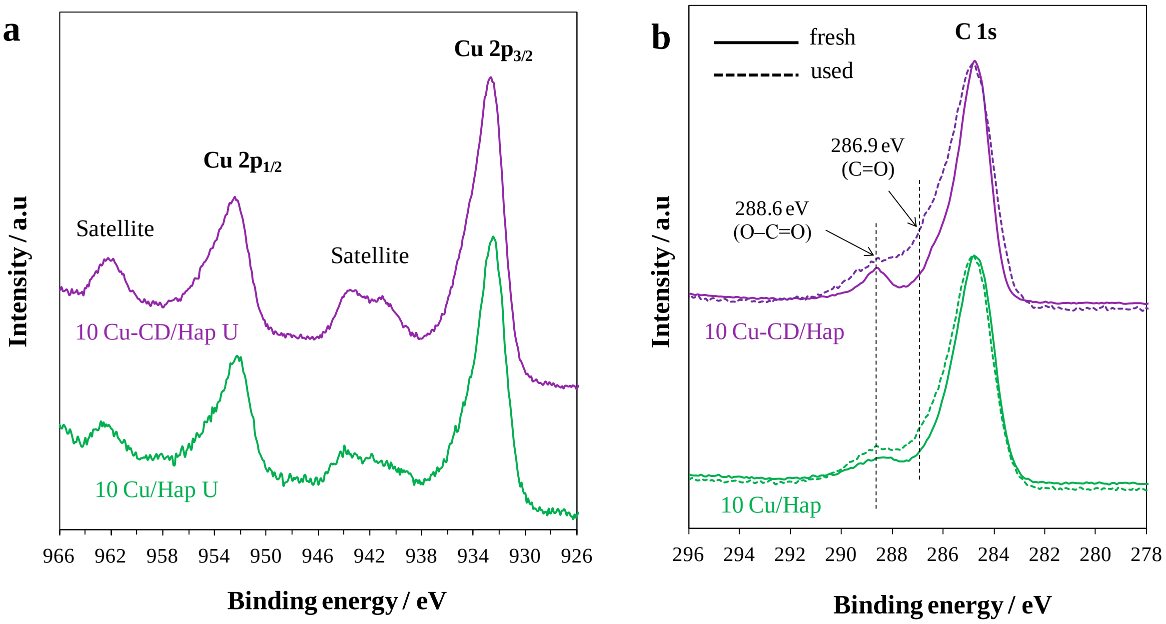

Figure 4.14. a) Cu 2p XPS core levels for used 10 Cu/Hap U and 10 Cu-CD/Hap U materials. b) Normalized overlay of C 1s XPS core levels for fresh and used 10 Cu/Hap and 10 Cu-CD/Hap materials.

Thus, it appears that stability tests resulted in a reduction of copper species and in a decrease of Cu dispersion in both catalysts. Nevertheless, the use of β-CD succeeded in lessening the extent of copper sintering by maintaining the bigger portion of copper entities in a highly dispersed state on the surface of 10 Cu-CD/Hap U, but it didn't manage to prevent the fouling of the surface by carbonaceous deposits. This finding agrees with the above H_2-TPR results.

4.6. Conclusion

The preceding examination of hydroxyaptite-supported copper materials has shown the efficiency of using β-CD in order to improve the catalytic performances of Cu/Hap catalysts in the total oxidation of toluene through an increase in both copper active species dispersion and reducibility. Indeed, it would appear that the modification of the surface composition of 10 Cu/Hap material by addition of β-CD to the synthesizing mixture allowed for better regulation of Cu location on the hydroxyapatite support. Thus, while difficultly reducible bulk CuO were predominant on the surface of 10 Cu/Hap material, as shown by XRD and H_2-TPR analysis, easily reducible highly dispersed small Cu(II) clusters were primarily formed in 10 Cu-CD/Hap solid, as indicated by XPS technique. Such a result is achieved through the occurrence of preferential interactions between β-CD and copper nitrate species, preventing the growth of the CuO particles during the calcination step while facilitating the total elimination of nitrate.

Owing to the promotion of copper species dispersion and reducibility through the use of β-CD, both the quality and number of active Cu sites increased resulting in a rise in toluene conversion rate and CO_2 productivity for 10 Cu-CD/Hap catalyst. Moreover, addition of β-CD to the impregnation solution proved to be advantageous in terms of reducing the sintering of copper species following stability tests, thus helping to retain better catalytic activity over time.

Even though the work presented in this chapter has given access to new prospects in the field of designing highly efficient copper supported catalysts, a clear understanding of the role played by β-cyclodextrin at each step of the synthesis, beginning from the interactions taking place between β-CD, the copper precursor, and hydroxyapatite support in the aqueous phase, up to the formation of active Cu species in the catalyst, remains out of reach. Thus, the upcoming chapter will be dedicated to carrying out an evaluation of the function occupied by β-cyclodextrin in Cu/Hap synthesis through Raman and ToF-SIMS monitoring.

References

[1] D. Chlala, J.-M. Giraudon, N. Nuns, M. Labaki, and J.-F. Lamonier, « Highly Active Noble-Metal-Free Copper Hydroxyapatite Catalysts for the Total Oxidation of Toluene », *ChemCatChem*, vol. 9, n^{o} 12, p. 2275–2283, 2017.

[2] E.-K. Lee, H.-S. Kim, K.-D. Jung, O.-S. Joo, and Y.-G. Shul, « Influence of copper precursors in the steam reforming of methanol over Cu/SnO_2/SiO_2 catalysts », *React. Kinet. Catal. Lett.*, vol. 81, n^{o} 1, p. 177–181, 2004.

[3] Y. Yin, W.-J. Jiang, X.-Q. Liu, Y.-H. Li, and L.-B. Sun, « Dispersion of copper species in a confined space and their application in thiophene capture », *J. Mater. Chem.*, vol. 22, n^{o} 35, p. 18514–18521, 2012.

[4] M. Schiavoni, S. Campisi, P. Carniti, A. Gervasini, and T. Delplanche, « Focus on the catalytic performances of Cu-functionalized hydroxyapatites in NH_3-SCR reaction », *Appl. Catal. A-Gen.*, vol. 563, p. 43–53, 2018.

[5] S. Karnjanakom, G. Guan, B. Asep, X. Hao, S. Kongparakul, C. Samart, and A. Abudula, « Catalytic upgrading of bio-oil over Cu/MCM-41 and Cu/KIT-6 prepared by β-cyclodextrin-assisted co-impregnation method », *J. Phys. Chem. C*, vol. 120, no. 6, p. 3396–3407, 2016.

[6] S. Tilloy, F. Bertoux, A. Mortreux, and E. Monflier, « Chemically modified β-cyclodextrins in biphasic catalysis: a fruitful contribution of the host–guest chemistry to the transition-metal catalyzed reactions », *Catal. Today*, vol. 48, n^{o} 1, p. 245–253, 1999.

[7] J. Liu, S. Mendoza, E. Román, M. J. Lynn, R. Xu, and A. E. Kaifer, « Cyclodextrin-Modified Gold Nanospheres. Host−Guest Interactions at Work to Control Colloidal Properties », *J. Am. Chem. Soc.*, vol. 121, n^{o} 17, p. 4304–4305, 1999.

[8] L. Bai, F. Wyrwalski, J.-F. Lamonier, A. Y. Khodakov, E. Monflier, and A. Ponchel, « Effects of β-cyclodextrin introduction to zirconia supported-cobalt oxide catalysts: From molecule-ion associations to complete oxidation of formaldehyde », *Appl. Catal. B Environ.*, vol. 138, p. 381–390, 2013.

[9] A. Tomer, F. Wyrwalski, C. Przybylski, J.-F. Paul, E. Monflier, M. Pera-Titus, and A. Ponchel, « Facile preparation of Ni/Al_2O_3 catalytic formulations with the aid of cyclodextrin complexes: Towards highly active and robust catalysts for the direct amination of alcohols », *J. Catal.*, vol. 356, p. 111–124, 2017.

[10] L. Bai, F. Wyrwalski, M. Safariamin, R. Bleta, J.-F. Lamonier, C. Przybylski, E. Monflier, and A. Ponchel, « Cyclodextrin-cobalt (II) molecule-ion pairs as precursors to active Co_3O_4/ZrO_2 catalysts for the complete oxidation of formaldehyde: Influence of the cobalt source », *J. Catal.*, vol. 341, p. 191–204, 2016.

[11] P. Blach, S. Fourmentin, D. Landy, F. Cazier, and G. Surpateanu, « Cyclodextrins: a new efficient absorbent to treat waste gas streams », *Chemosphere*, vol. 70, n^{o} 3, p. 374–380, 2008.

[12] J. Szejtli, « Utilization of cyclodextrins in industrial products and processes », *J. Mater. Chem.*, vol. 7, n^{o} 4, p. 575–587, 1997.

[13] Y. Matsui, « Complexes of copper (II) with cyclodextrins », *Bull. Chem. Soc. Jap.*, vol. 45, n° 10, p. 3229, 1972.

[14] Y. Matsui, T. Kurita, M. Yagi, T. Okayama, K. Mochida, and Y. Date, « The formation and structure of Copper (II) complexes with cyclodextrins in an alkaline solution », *Bull. Chem. Soc. Jpn.*, vol. 48, n° 7, p. 2187–2191, 1975.

[15] K. Mochida and Y. Matsui, « Kinetic study on the formation of a binuclear complex between copper (II) and cyclodextrin », *Chem. Lett.*, vol. 5, n° 9, p. 963–966, 1976.

[16] A. C. F. Ribeiro, M. A. Esteso, V. M. M. Lobo, A. J. M. Valente, S. M. N. Simões, A. J. F. N. Sobral, L. Ramos, H. D. Burrows, A. M. Amado, and A. M. Amorim da Costa *et al.*, « Interactions of Copper (II) Chloride with β-Cyclodextrin in Aqueous Solutions », *J. Carbohydr. Chem.*, vol. 25, n° 2‑3, p. 173–185, 2006.

[17] G. Kurokawa, M. Sekii, T. Ishida, and T. Nogami, « Crystal structure of a molecular complex from native β-cyclodextrin and copper (II) chloride », *Supramol. Chem.*, vol. 16, n° 5, p. 381–384, 2004.

[18] L. X. Song, J. Yang, L. Bai, F. Y. Du, J. Chen, and M. Wang, « Molecule-ion interaction and its effect on electrostatic interaction in the system of copper chloride and β-cyclodextrin », *Inorg. Chem.*, vol. 50, n° 5, p. 1682–1688, 2011.

[19] S. Campisi, C. Castellano, and A. Gervasini, « Tailoring the structural and morphological properties of hydroxyapatite materials to enhance the capture efficiency towards copper(II) and lead(II) ions », *New J. Chem.*, vol. 42, n° 6, p. 4520–4530, 2018.

[20] S. Campisi, M. G. Galloni, F. Bossola, and A. Gervasini, « Comparative performance of copper and iron functionalized hydroxyapatite catalysts in NH_3-SCR », *Catal. Commun.*, vol. 123, p. 79–85, 2019.

[21] Z. Qu, Y. Sun, D. Chen, and Y. Wang, « Possible sites of copper located on hydroxyapatite structure and the identification of active sites for formaldehyde oxidation », *J. Mol. Catal. Chem.*, vol. 393, p. 182–190, 2014.

[22] J. Jemal, H. Tounsi, S. Djemel, C. Pettito, and G. Delahay, « Characterization and $deNO_x$ activity of copper-hydroxyapatite catalysts prepared by wet impregnation », *React. Kinet. Mech. Catal.*, vol. 109, n° 1, p. 159–165, 2013.

[23] G. Cui, J. Wang, H. Fan, X. Sun, Y. Jiang, S. Wang, D. Liu, and J. Gui, « Towards understanding the microstructures and hydrocracking performance of sulfided Ni–W catalysts: Effect of metal loading », *Fuel Process. Technol.*, vol. 92, n° 12, p. 2320–2327, 2011.

[24] M. Akri, A. El Kasmi, C. Batiot-Dupeyrat, and B. Qiao, « Highly Active and Carbon-Resistant Nickel Single-Atom Catalysts for Methane Dry Reforming », *Catalysts*, vol. 10, n° 6, p. 630–650, 2020.

[25] Z. Boukha, M. Gil-Calvo, B. de Rivas, J. R. González-Velasco, J. I. Gutiérrez-Ortiz, and R. López-Fonseca, « Behaviour of Rh supported on hydroxyapatite catalysts in partial oxidation and steam reforming of methane: On the role of the speciation of the Rh particles », *Appl. Catal. A-Gen.*, vol. 556, p. 191–203, 2018.

[26] H. W. Richardson, « Copper Compounds », in *Kirk-Othmer Encyclopedia of Chemical Technology*, American Cancer Society, 2003.

[27] I. V. Morozov, K. O. Znamenkov, Y. M. Korenev, and O. A. Shlyakhtin, « Thermal decomposition of $Cu(NO_3)_2 \cdot 3H_2O$ at reduced pressures », *Thermochim. Acta*, vol. 403, n° 2, p. 173–179, 2003.

[28] M. Galera Martínez, D. Pham Minh, E. Weiss-Hortala, A. Nzihou, and P. Sharrock, « Synthesis, characterization, and thermo-mechanical properties of copper-loaded apatitic calcium phosphates », *Compos. Interfaces*, vol. 20, n° 8, p. 647–660, 2013.

[29] M. S. Zarif, A. R. Afidah, J. M. Abdullah, and A. R. Shariza, « Physicochemical characterization of vancomycin and its complexes with β-cyclodextrin », *Biomed. Res.-INDIA*, vol. 23, n° 4, p. 513–520, 2012.

[30] S. Khan and J. Boateng, « Effects of cyclodextrins (β and γ) and L-Arginine on stability and functional properties of mucoadhesive Buccal Films loaded with Omeprazole for pediatric Patients », *Polymers*, vol. 10, n° 2, p. 157–176, 2018.

[31] R.-P. Ye, L. Lin, C.-Q. Liu, C.-C. Chen, and Y.-G. Yao, « One-Pot Synthesis of Cyclodextrin-Doped Cu-SiO_2 Catalysts for Efficient Hydrogenation of Dimethyl Oxalate to Ethylene Glycol », *ChemCatChem*, vol. 9, n° 24, p. 4587–4597, 2017.

[32] J. M. Aguirre, A. Gutiérrez, and O. Giraldo, « Simple route for the synthesis of copper hydroxy salts », *J. Braz. Chem. Soc.*, vol. 22, n° 3, p. 546–551, 2011.

[33] W. M. Keely and H. W. Maynor, « Thermal Studies of Nickel, Cobalt, Iron and Copper Oxides and Nitrates. », *J. Chem. Eng. Data*, vol. 8, n° 3, p. 297–300, 1963.

[34] I. Schildermans, J. Mullens, B. J. Van der Veken, J. Yperman, D. Franco, and L. C. Van Poucke, « Preparation and thermal decomposition of $Cu_2(OH)_3NO_3$ », *Thermochim. Acta*, vol. 224, p. 227–232, 1993.

[35] R. A. Friedel, J. L. Shultz, and A. G. Sharkey, « Mass spectrum of nitric acid », *Anal. Chem.*, vol. 31, n° 6, p. 1128, 1959.

[36] D. Chlala, « Étude de l'ajout de métaux (Pt, Pd, Mn et Cu) sur hydroxyapatite: apport de la flexibilité du support dans l'oxydation catalytique totale du toluène », PhD Thesis, Lille, 2015.

[37] S. Kohata, K. Jyodoi, and A. Ohyoshi, « Thermal decomposition of cyclodextrins (α-, β-, γ-, and modified β-CyD) and of metal—(β-CyD) complexes in the solid phase », *Thermochim. Acta*, vol. 217, p. 187–198, 1993.

[38] K.-H. Frömming and J. Szejtli, *Cyclodextrins in Pharmacy*. Springer Science & Business Media, 2013.

[39] J. Wang, M. Wei, G. Rao, D. G. Evans, and X. Duan, « Structure and thermal decomposition of sulfated β-cyclodextrin intercalated in a layered double hydroxide », *J. Solid State Chem.*, vol. 177, n° 1, p. 366–371, 2004.

[40] V. Miskovic-Stankovic, S. Erakovic, A. Jankovic, M. Vukašinović-Sekulić, M. Mitrić, Y. C. Jung, S. J. Park, and K. Y. Rhee, « Electrochemical synthesis of nanosized hydroxyapatite/graphene composite powder », *Carbon Lett.*, vol. 16, n^o 4, p. 233–240, 2015.

[41] F. E. Tabaght, K. Azzaoui, A. Elidrissi, O. Hamed, E. Mejdoubi, S. Jodeh, N. Akartasse, M. Lakrat, and A. Lamhamdi, « New nanostructure based on hydroxyapatite modified cellulose for bone substitute, synthesis, and characterization », *Int. J. Polym. Mater. Polym. Biomater.*, p. 1–12, 2020.

[42] A. Jillavenkatesa and R. A. Condrate Sr, « The infrared and Raman spectra of tetracalcium phosphate ($Ca_4P_2O_9$) », *Spectrosc. Lett.*, vol. 30, n^o 8, p. 1561–1570, 1997.

[43] Y. Huang, H. Qiao, X. Nian, X. Zhang, X. Zhang, G. Song, Z. Xu, H. Zhang, and S. Han, « Improving the bioactivity and corrosion resistance properties of electrodeposited hydroxyapatite coating by dual doping of bivalent strontium and manganese ion », *Surf. Coat. Technol.*, vol. 291, p. 205–215, 2016.

[44] L. Berzina-Cimdina and N. Borodajenko, « Research of calcium phosphates using Fourier transform infrared spectroscopy », in *Infrared Spectroscopy-Materials Science, Engineering and Technology*, InTech, 2012.

[45] D. P. Minh, N. D. Tran, A. Nzihou, and P. Sharrock, « Carbonate-containing apatite (CAP) synthesis under moderate conditions starting from calcium carbonate and orthophosphoric acid », *Mater. Sci. Eng. C*, vol. 33, n^o 5, p. 2971–2980, 2013.

[46] J. C. Elliott, D. W. Holcomb, and R. A. Young, « Infrared determination of the degree of substitution of hydroxyl by carbonate ions in human dental enamel », *Calcif. Tissue Int.*, vol. 37, n^o 4, p. 372–375, 1985.

[47] J. R. Ferraro, « The nitrate symmetry in metallic nitrates », *J. Mol. Spectrosc.*, vol. 4, n^o 1‑6, p. 99–105, 1960.

[48] T. İnceboz, G. Erkan, G. C. Türkoğlu, A. M. Sarıışık, S. Bakırcı, S. Üner, and A. Üner, « In-vivo and in-vitro tick repellent properties of cotton fabric », *Text. Res. J.*, vol. 85, n^o 19, p. 2071–2082, 2015.

[49] A. R. Rojas-Mena, H. López-González, and A. Rojas-Hernández, « Preparation and characterization of holmium-beta-cyclodextrin complex », *Adv. Mater. Phys. Chem.*, vol. 5, n^o 03, p. 87–94, 2015.

[50] O. Egyed, « Spectroscopic studies on β-cyclodextrin », *Vib. Spectrosc.*, vol. 1, n^o 2, p. 225–227, 1990.

[51] W. Gao, N. Guan, J. Chen, X. Guan, R. Jin, H. Zeng, Z. Liu, and F. Zhang, « Titania supported Pd-Cu bimetallic catalyst for the reduction of nitrate in drinking water », *Appl. Catal. B Environ.*, vol. 46, n^o 2, p. 341–351, 2003.

[52] E. V. Filimonov and A. I. Shcherbakov, « Catalytic effect of copper ions on nitrate reduction », *Prot. Met.*, vol. 40, n^o 3, p. 280–285, 2004.

[53] J. Ghijsen, L. H. Tjeng, J. Van Elp, H. Eskes, J. Westerink, G. A. Sawatzky, and M. T. Czyzyk, « Electronic structure of Cu_2O and CuO », *Phys. Rev. B*, vol. 38, n^o 16, p. 11322–11330, 1988.

[54] M. C. Biesinger, L. W. Lau, A. R. Gerson, and R. S. C. Smart, « Resolving surface chemical states in XPS analysis of first row transition metals, oxides and hydroxides: Sc, Ti, V, Cu and Zn », *Appl. Surf. Sci.*, vol. 257, n° 3, p. 887–898, 2010.

[55] J. P. Espinós, J. Morales, A. Barranco, A. Caballero, J. P. Holgado, and A. R. González-Elipe, « Interface effects for Cu, CuO, and Cu_2O deposited on SiO_2 and ZrO_2. XPS determination of the valence state of copper in Cu/SiO_2 and Cu/ZrO_2 catalysts », *J. Phys. Chem. B*, vol. 106, n° 27, p. 6921–6929, 2002.

[56] E. S. Shpiro, W. Grünert, R. W. Joyner, and G. N. Baeva, « Nature, distribution and reactivity of copper species in over-exchanged Cu-ZSM-5 catalysts: an XPS/XAES study », *Catal. Lett.*, vol. 24, n° 1‑2, p. 159–169, 1994.

[57] D. Courcot, C. Pruvost, E. A. Zhilinskaya, and A. Aboukaïs, « Potential of Supported Copper and Potassium Oxide Catalysts in the Combustion of Carbonaceous Particles », *Kinet. Catal.*, vol. 45, n° 4, p. 580–588, 2004.

[58] B. A. Sexton, A. E. Hughes, and K. Foger, « XPS investigation of strong metal-support interactions on Group IIIa–Va oxides », *J. Catal.*, vol. 77, n° 1, p. 85–93, 1982.

[59] A. M. Venezia, A. Rossi, D. Duca, A. Martorana, and G. Deganello, « Particle size and metal-support interaction effects in pumice supported palladium catalysts », *Appl. Catal. A-Gen.*, vol. 125, n° 1, p. 113–128, 1995.

[60] M. G. Mason, « Electronic structure of supported small metal clusters », *Phys. Rev. B*, vol. 27, n° 2, p. 748–762, 1983.

[61] Z. Boukha, J. L. Ayastuy, M. Cortés-Reyes, L. J. Alemany, J. R. González-Velasco, and M. A. Gutiérrez-Ortiz, « Catalytic performance of Cu/hydroxyapatite catalysts in CO preferential oxidation in H2-rich stream », *Int. J. Hydrog. Energy*, vol. 44, n° 25, p. 12649–12660, 2019.

[62] M. Ibrahim, M. Labaki, N. Nuns, J.-M. Giraudon, and J.-F. Lamonier, « Cu- Mn Hydroxyapatite Materials for Toluene Total Oxidation », *ChemCatChem*, vol. 12, n° 2, p. 550–560, 2020.

[63] D. Chlala, J.-M. Giraudon, N. Nuns, M. Labaki, and J.-F. Lamonier, « Highly Active Noble-Metal-Free Copper Hydroxyapatite Catalysts for the Total Oxidation of Toluene », *ChemCatChem*, vol. 9, n° 12, p. 2275–2283, 2017.

[64] Y. Iijima, N. Niimura, and K. Hiraoka, « Prevention of the Reduction of CuO during X-ray Photoelectron Spectroscopy Analysis », *Surf. Interface Anal.*, vol. 24, n° 3, p. 193–197, 1996.

[65] C.-K. Wu, M. Yin, S. O'Brien, and J. T. Koberstein, « Quantitative analysis of copper oxide nanoparticle composition and structure by X-ray photoelectron spectroscopy », *Chem. Mater.*, vol. 18, n° 25, p. 6054–6058, 2006.

[66] D. C. Frost, A. Ishitani, and C. A. McDowell, « X-ray photoelectron spectroscopy of copper compounds », *Mol. Phys.*, vol. 24, n° 4, p. 861–877, 1972.

[67] J. C. Klein, C. P. Li, D. M. Hercules, and J. F. Black, « Decomposition of copper compounds in X-ray photoelectron spectrometers », *Appl. Spectrosc.*, vol. 38, n° 5, p. 729–734, 1984.

[68] W. M. Skinner, C. A. Prestidge, and R. S. C. Smart, « Irradiation effects during XPS studies of Cu (II) activation of zinc sulphide », *Surf. Interface Anal.*, vol. 24, n° 9, p. 620–626, 1996.

[69] J. P. Tobin, W. Hirschwald, and J. Cunningham, « XPS and XAES studies of transient enhancement of Cu^1 at CuO surfaces during vacuum outgassing », *Appl. Surf. Sci.*, vol. 16, n° 3‑4, p. 441–452, 1983.

[70] A. Losev, K. Rostov, and G. Tyuliev, « Electron beam induced reduction of CuO in the presence of a surface carbonaceous layer: an XPS/HREELS study », *Surf. Sci.*, vol. 213, n° 2‑3, p. 564–579, 1989.

[71] C.-H. Wang, S.-S. Lin, C.-L. Chen, and H.-S. Weng, « Performance of the supported copper oxide catalysts for the catalytic incineration of aromatic hydrocarbons », *Chemosphere*, vol. 64, n° 3, p. 503–509, 2006.

[72] E. Genty, S. Siffert, and R. Cousin, « Investigation of reaction mechanism and kinetic modelling for the toluene total oxidation in presence of CoAlCe catalyst », *Catal. Today*, vol. 333, p. 28–35, 2019.

[73] S. C. Kim, « The catalytic oxidation of aromatic hydrocarbons over supported metal oxide », *J. Hazard. Mater.*, vol. 91, n° 1, p. 285–299, 2002.

[74] L.-F. Chen, P.-J. Guo, L.-J. Zhu, M.-H. Qiao, W. Shen, H.-L. Xu, and K.-N. Fan, « Preparation of Cu/SBA-15 catalysts by different methods for the hydrogenolysis of dimethyl maleate to 1, 4-butanediol », *Appl. Catal. A-Gen.*, vol. 356, n° 2, p. 129–136, 2009.

[75] X. Wang, D. Liu, J. Li, J. Zhen, and H. Zhang, « Clean synthesis of Cu_2O@CeO_2 core@shell nanocubes with highly active interface », *NPG Asia Mater.*, vol. 7, n° 1, p. e158–e165, 2015.

[76] Q. Shi, N. Liu, and Y. Liang, « Preparation of MgO-Supported Cu_2O Catalyst and Its Catalytic Properties for Cyclohexanol Dehydrogenation », *Chin. J. Catal.*, vol. 28, n° 1, p. 57–61, 2007.

[77] D. Hleis, M. Labaki, H. Laversin, D. Courcot, and A. Aboukaïs, « Comparison of alkali-promoted ZrO_2 catalysts towards carbon black oxidation », *Colloids Surf. Physicochem. Eng. Asp.*, vol. 330, n° 2‑3, p. 193–200, 2008.

[78] M. Argyle and C. Bartholomew, « Heterogeneous catalyst deactivation and regeneration: a review », *Catalysts*, vol. 5, n° 1, p. 145–269, 2015.

[79] S. Poulston, P. M. Parlett, P. Stone, and M. Bowker, « Surface oxidation and reduction of CuO and Cu_2O studied using XPS and XAES », *Surf. Interface Anal.*, vol. 24, n° 12, p. 811–820, 1996.

[80] G. Arteaga, L. M. Rivera-Gavidia, S. J. Martínez, R. Rizo, E. Pastor, and G. García, « Methanol oxidation on graphenic-supported platinum catalysts », *Surfaces*, vol. 2, n° 1, p. 16–31, 2019.

[81] R. Muñoz, C. Sanchez-Sanchez, P. Merino, E. López-Elvira, C. Munuera, P. Gant, M. F. López, A. Castellanos-Gomez, J. A. Martín-Gago, and M. García-Hernández, « Tailored graphenic structures directly grown on titanium oxide boost the interfacial charge transfer », *Appl. Surf. Sci.*, vol. 504, p. 144439–144463, 2020.

Chapter V: Insight into the role of beta-cyclodextrin in Cu/Hap synthesis monitored by Raman and ToF-SIMS.

5.1. Introduction

Copper based particles tend to agglomerate during the preparation of Cu-supported catalysts, thereby minimizing their active surface areas which ultimately result in diminishing the material's performance. This effect can be minimized by stabilizing Cu particles through the use of β-CD complexing agent, a method which has been demonstrated to be effective in preventing copper species aggregation, leading thus to an improvement in the catalyst efficiency (refer to Chapter IV).

Immobilizing β-CD-complexed Cu ions on Hap support material may be contemplated to occur in one of three different ways, illustrated in Figure 5.1. Either the organic compound associated with metal entities becomes adsorbed to the support through chemical forces and so tethers the copper entities to the hydroxyapatite support, or the Cu particles themselves bind directly to the support and the oligosaccharide plays no role, or finally a combination of these two binding modes can take place.

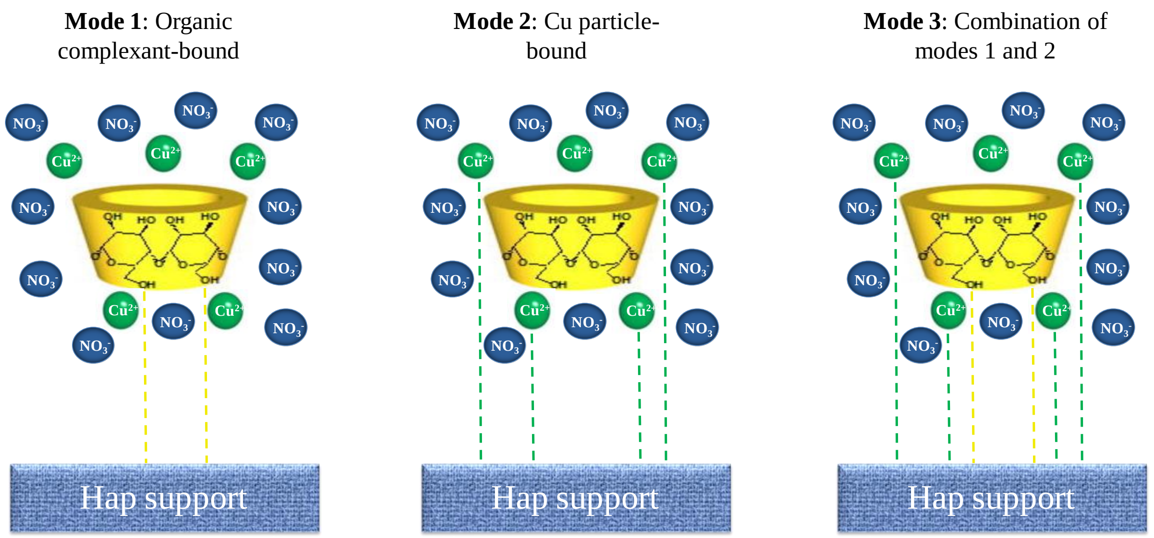

Mode 1: Organic complexant-bound

Mode 2: Cu particle-bound

Mode 3: Combination of modes 1 and 2

Figure 5.1. Schematic representation of three different ways β-CD-complexed Cu ions can bind to the surface of Hap support material.

Hence, knowing that β-CD can interact with both copper nitrate precursor and hydroxyapatite support makes the Cu-CD/Hap system even more complex. Indeed, in the synthesis process different interactions involving β-cyclodextrin could be taking place and depending on the force or predominance of these interactions, the properties of the resulting products would be determined.

For this reason, a comprehensive study into the role played by β-CD during the preparation of Cu/Hap catalysts will be presently performed. The eventual occurrence of any type of interaction between β-CD and the other participants involved in the formation of hydroxyapatite supported copper catalyst will be discussed on the basis of physicochemical data collected via Raman spectroscopy and ToF-SIMS analysis. While ToF-SIMS is very surface-sensitive and can thus give very useful information on the molecular chemistry of the first few monolayers of the examined samples, enabling the identification of the chemical moieties that may interact with β-CD, Raman can provide information on the extent of structural changes brought on by the use of the organic complexant. Hence, the knowledge gained from these two complementary techniques may yield very important chemical and structural data which are essential for understanding the β-CD-related interactions that impact the catalytic system and succeed in improving the efficiency of Cu/Hap materials. Besides the work of Song *et al.* [1], where only dried materials corresponding to the solid adduct of $CuCl_2$ and β-CD were investigated, no other paper has employed a combined Raman/ToF-SIMS approach for examining catalytic systems prepared via β-CD route, making this study all the more innovative and thorough. Regarding Raman investigation, which will be conducted first, products will be investigated at different points of the preparation (solution, dried state, and calcined state). At the solution level, an evaluation of the effect of increasing copper concentration as well as that of β-CD/Cu molar ratio on the evolution of the interactions taking place in the copper-bearing systems will be carried out. At the powder level, the structural effect of using β-CD on the obtained Cu-supported Hap systems will be probed by Raman, in both dried and calcined solids, seeing as the catalysts will undergo changes during both of drying and calcination stages. Concerning ToF-SIMS study, an inspection of pure β-CD and Hap compounds, in addition to a survey of dried Cu/β-CD D, β-CD/Hap D, 10 Cu/Hap D and 10 Cu-CD/Hap D compounds will be conducted, in order to give an insight into the manner in which β-CD might interact with both copper precursor and the Hap support.

The goal of this in-depth study is to produce a scheme highlighting the role of β-cyclodextrin throughout the genesis of the Cu/Hap catalyst by using the combined information obtained from Raman spectroscopy and ToF-SIMS experiments. Thus, the effect of β-CD on the final nature and environment of copper species will be determined, which will thereby reveal if a modulation of copper speciation at the end of the process, via the assistance of β-cyclodextrin, does in fact occur.

5.2. Raman

5.2.1. Solution

The use of Raman spectroscopy to study existing interactions in prepared aqueous solutions is required for a better understanding of the currently synthesized systems.

It was first necessary to determine the Raman signature of aqueous solutions of copper nitrate precursor, $Cu(NO_3)_2$, alone and of β-cyclodextrin alone, then compare these results with those reported in literature. Secondly, an evaluation of the effect of the Cu(II) precursor concentration on the coordination sphere of Cu(II) and NO_3^- was conducted. Thirdly, the interactions between Cu(II) precursor and β-CD were studied by comparison of the Raman signatures of aqueous mixtures of $Cu(NO_3)_2$ and β-CD with the Raman spectra of pure $Cu(NO_3)_2$ and β-CD aqueous solutions: both the impact of β-CD/Cu molar ratio and of Cu concentration (for a fixed β-CD/Cu ratio value) on the interaction forces between Cu(II) precursor and β-CD were rigorously examined. The results of these investigations are reported below.

It should be noted though, that a Raman analysis of water was first performed, with the resulting spectrum shown in Figure AC.1, in order to avoid any confusion by attributing some of H_2O related bands to another species. Therefore, it should be hereafter established that bands observed at 430, 485, 598, and 795 cm^{-1}, assigned to the ν_L libration mode arising from hydrogen bonding; and that noted at 1640 cm^{-1} attributed to the ν_2 bending mode, all derive from water vibrational modes [2], [3].

5.2.1.1. *Raman study of $Cu(NO_3)_2$*

In water, $Cu(NO_3)_2$ dissolves according to the following equation, yielding a blue solution composed of the octahedral complex ion $[Cu(OH_2)_6]^{2+}$ and nitrate anions:

$$Cu(NO_3)_2(s) \xrightarrow{H_2O} [Cu(OH_2)_6]^{2+}(aq) + 2\,NO_3^{-}(aq) \qquad (5.1)$$

Regarding the vibrational modes of $[Cu(OH_2)_6]^{2+}$ complex, low signal strength and the strong fluorescence background in the region 100-400 cm^{-1} obscured the fundamental modes of $[Cu(OH_2)_6]^{2+}$ which are at ν_1 (396 cm^{-1}), ν_2 (299 cm^{-1}), ν_3 (414 cm^{-1}), ν_4 (264 cm^{-1}), ν_5 (179 cm^{-1}), and ν_6 (119 cm^{-1}) [4]–[6].

The solvated NO_3^- ion has a D3h symmetry which results in four fundamental modes of vibration. However, only the totally symmetrical vibration ν_1, and the doubly degenerate vibrations ν_3 and ν_4 are Raman active. Thus, in their free state, when they are isotropically surrounded by water molecules from the aqueous solution, nitrate ions should manifest no more than three bands in the corresponding Raman spectra.

Yet, when examining the Raman spectrum of $Cu(NO_3)_2$ aqueous solution, with a concentration of 0.14 mol.L^{-1} (which corresponds to the Cu concentration used in the impregnation mixture to obtain 10 Cu/Hap catalyst), shown in Figure 5.2, it can be seen that in addition to the bands related to the Raman spectrum of water (430, 485, 598, 795, and 1640 cm^{-1}) [2], [3], four bands associated with copper nitrate can be detected. While the bands at 714 and 1045 cm^{-1} correspond to ν_4 and ν_1 vibrational modes respectively, the other two remaining bands at 1347 and 1405 cm^{-1} are the result of the splitting of the ν_3 degenerate vibrational mode. This splitting of the ν_3 band has been noted before by many authors and has been recognized as being the first effect of an increase in concentration of a very diluted copper nitrate solution [7], [8]. It has been explained by a lifting of the degeneracy of the fundamental ν_3 vibration due to an alteration of the electronic envelope of the ion by its changing surroundings. In other words, if a copper cation draws nearer to a nitrate anion it can create an inter-ionic association lowering thus its original symmetry.

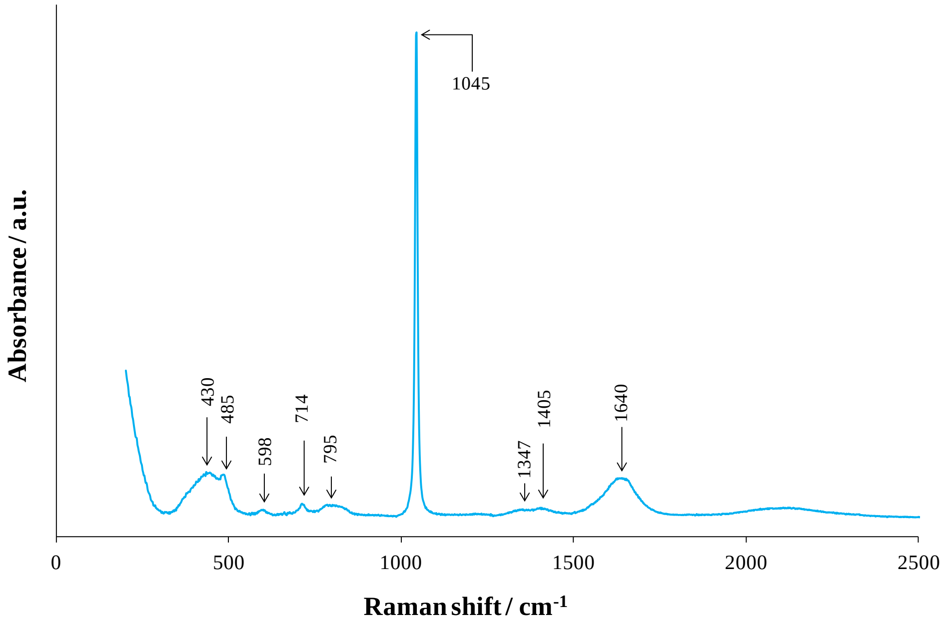

Figure 5.2. Raman spectrum of aqueous solution of $Cu(NO_3)_2$ with a concentration of 0.14 mol.L^{-1}.

5.2.1.2. *Raman study of β-CD*

β-cyclodextrin which is composed of seven glycosyl units, linked through α-(1,4)-glycosidic bonds, has 147 atoms and can produce 435 normal vibration modes [9]. The Raman spectrum of an aqueous β-CD solution with a concentration of 0.014 mol.L^{-1} (which corresponds to the β-CD concentration used in the impregnation mixture to obtain 10 Cu-CD/Hap catalyst) is displayed in Figure 5.3. Along with water associated bands, eight new bands emerge at 876, 945, 1042, 1080, 1127, 1258, 1335, and 1451 cm^{-1}, which can be ascribed to β-CD compound [10], [11]. Although, it should be noted that none of these β-CD-detected modes arise from a single type of molecular vibration.

Thus, the band noted at 876 cm^{-1} considered as an anomeric band [11], corresponds essentially to C-1-H deformation coupled with other motions among which figure the stretching mode of CO, CC, and bending mode of CCH. The band observed at 945 cm^{-1} may be ascribed to skeletal modes of β-CD involving α-1,4 linkage. C–O stretching vibration results in the bands occurring at 1080 and 1042 cm^{-1}. The band perceived at 1127 cm^{-1} can be assigned to pyranose ring vibrational mode superimposed with the asymmetric stretching vibration of the glycosidic C-O-C bonds. Moreover, the bands at 1335 and 1258 cm^{-1} may be attributed to complex modes of the CH_2OH group such as bending modes of CCH and COH along with other motions. Finally, the scissoring vibration of CH_2 and CH appears at 1451 cm^{-1}.

These presented results will constitute a good basis for future detection of complex formation with β-cyclodextrins, which could manifest by a Raman shift of any of these earlier mentioned bands, or also their disappearance.

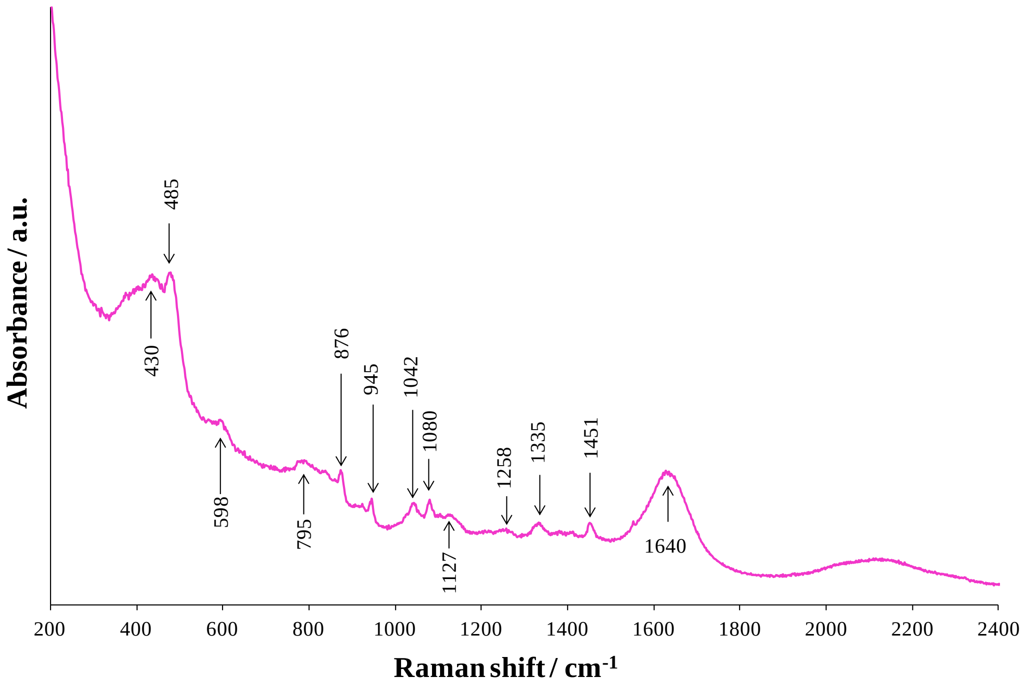

Figure 5.3. Raman spectrum of aqueous β-CD solution with a concentration of 0.014 mol.L^{-1}.

5.2.1.3. *Raman study of $Cu(NO_3)_2$: effect of Cu concentration*

It is important to pay particular attention to the modifications that take place inside the copper based systems during the synthesis process seeing as the microscopic structure and the eventual structural changes that occur in the solutions at high concentrations will most likely impact the resulting materials macroscopic properties.

Thus, we resolve to investigate the influence of copper(II) concentration on its environment from the study of Raman spectra given in Figure 5.4.

The Raman spectrum of the most diluted aqueous solution of copper nitrate investigated in this study (0.14 mol.L^{-1} – Figure 5.4-trace “A”) has already been discussed in detail in the section above (refer to “***5.2.1.1. Raman study of Cu(NO$_3$)$_2$***”). Basically, the spectrum shows four copper nitrate related bands: bands at 714 and 1045 cm^{-1} corresponding to ν_4 and ν_1 vibrational modes respectively, along with two other bands at 1347 and 1405 cm^{-1} resulting from the splitting of the ν_3 degenerate vibrational mode.

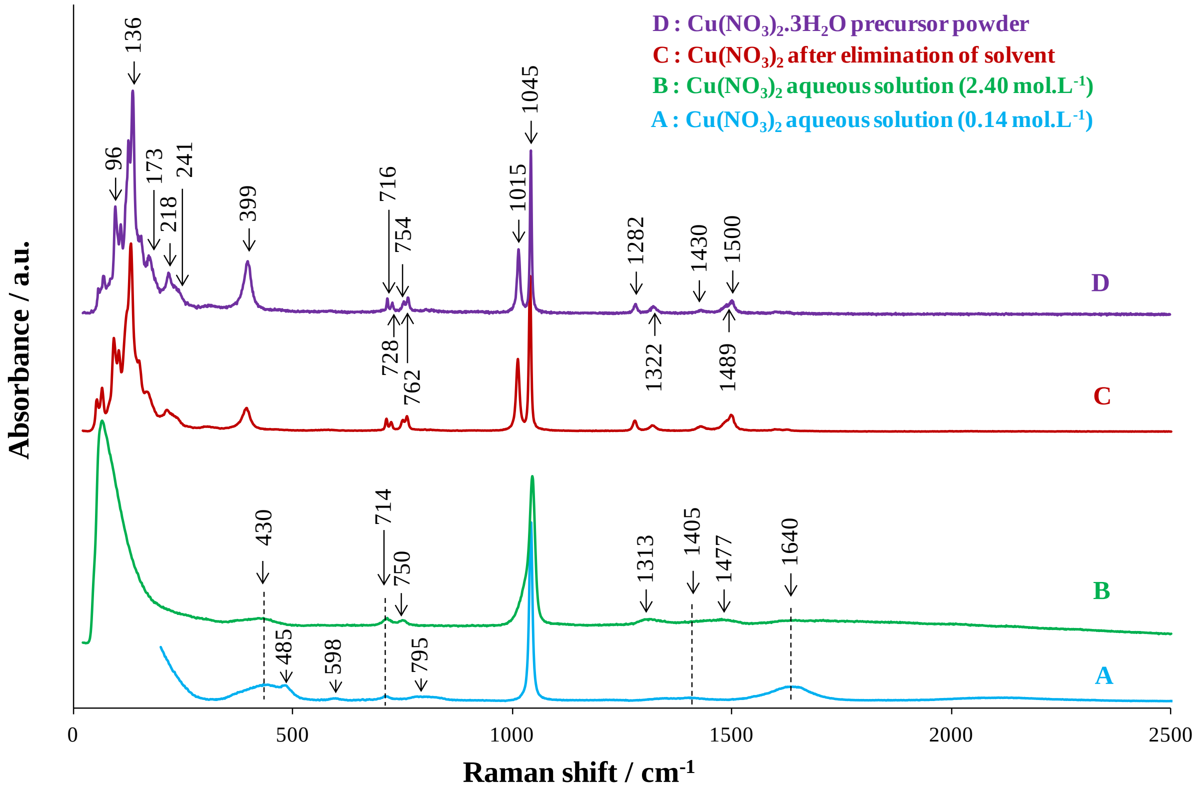

Figure 5.4. Raman spectra of aqueous solutions of Cu(NO$_3$)$_2$ with a concentration of 0.14 mol.L^{-1} and 2.33 mol.L^{-1}, along with the Raman spectra obtained after elimination of solvent and of Cu(NO$_3$)$_2$.3H$_2$O powder precursor.

When the concentration of the copper nitrate solution is increased to 2.33 mol.L^{-1} (Figure 5.4-trace “B”), two new bands appear at 750 and 1477 cm^{-1}. These bands have been assigned in several works with the formation of a nitrato-copper complex [12], [13], which becomes more and more favored with the increase in copper nitrate concentration. It can also be noticed that the ν_1 band (1045 cm^{-1}) becomes broader and asymmetric about its base (on its low frequency side) as the concentration grows from 0.14 to 2.33 mol.L^{-1}; this can be interpreted as the developing of a new band in this region, ascribed to the nitrato-copper complex. It should also be noted that the Raman shifts at 430 and 1640 cm^{-1} are in accordance with residual water.

Finally, a Raman analysis of the copper nitrate product after quasi elimination of the solvent, when all that is remaining is some droplets on the sides of the round-bottomed flask, was conducted (Figure 5.4-trace "C"). No Raman bands corresponding to water bonding modes could be detected in this spectrum confirming the departure of the quasi totality of water molecules. Therefore, a highly concentrated compound such as this one would be presumed to exhibit an analogous structure to that of the solid precursor. Indeed, the Raman spectrum obtained in trace "C" resembles that of the solid copper nitrate trihydrate precursor corresponding to trace "D" in Figure 5.4, which in turn agrees with literature reported data on Raman band positions of $Cu(NO_3)_2.3H_2O$ mineral [14] (Figure AC.2 and Table AC.1). Compared to its more diluted predecessor, the product in trace "C" exhibits in the low-frequency region (below 400 cm^{-1}) copper-nitrate and copper-oxygen bands. These bands, which are characteristic of copper nitrate crystal, had been absent in traces "A" and "B", due in all likeliness to the presence of higher amounts of water which by entering the coordination sphere of the metal displace the nitrate ions and thus cause the disappearance of the metal-to-nitrate bond [15]. Moreover, the shoulder which had been noted at the low frequency side of the ν_1 band in trace "B" becomes a well defined separate band at 1015 cm^{-1} in trace "C", and new bands appear in the 700-800 and 1250-1500 cm^{-1} frequency range, all of which could be attributed to copper-nitrate association.

5.2.1.4. Raman study of $CuCD_x$: effect of β-CD/Cu molar ratio

The focus will now be turned towards performing a thorough examination of the three $CuCD_x$ solutions with the aim of investigating the consequences of combining $Cu(NO_3)_2$ with β-CD on Raman spectrum, as well as that of varying the concentration of β-CD within the aqueous solution so as to obtain three different β-CD/Cu molar ratios equal to 0.05 ([β-CD] = 0.007 $mol.L^{-1}$), 0.1 ([β-CD] = 0.014 $mol.L^{-1}$) and 0.2 ([β-CD] = 0.028 $mol.L^{-1}$). The corresponding Raman spectra are given in Figure 5.5.

When it comes to aqueous solutions bearing β-CD with a concentration of 0.014 $mol.L^{-1}$, presented in Figure 5.5-a, the characteristic bands of β-cyclodextrin in water can be found at 876, 945, 1042, 1080, 1127, 1258, 1335, and 1451 cm^{-1}, as formerly stated in section "***5.2.1.2. Raman study of β-CD***". With the addition of copper nitrate to the β-CD aqueous solution (Cu/β-CD) new bands appear at 714 and 1045 cm^{-1}. These bands are related to the copper precursor as asserted by the Raman spectrum of aqueous solution of copper nitrate (refer to "***5.2.1.1. Raman study of $Cu(NO_3)_2$***").

Regarding the effect of β-CD/Cu molar ratio, it can be seen that an increase in this ratio's value leads to a rise in the intensity of all β-CD associated bands. Furthermore, a zoom made in the 650-1000 cm^{-1} range and represented in Figure 5.5-b, shows the occurrence of a 14 cm^{-1} red shift of the β-CD characteristic band at 876 cm^{-1} which emerges at 862 cm^{-1} in the Cu/β-CD solutions. This band which appears to be absent in the case of the Cu/β-CD solution with the lowest concentration of β-CD ([β-CD] = 0.007 $mol.L^{-1}$), and hence the lowest β-CD/Cu molar ratio value (0.05), becomes more and more defined when increasing the β-CD concentration from 0.014 to 0.028 $mol.L^{-1}$, or in other words when increasing the β-CD/Cu molar ratio from 0.1 to 0.2. The occurrence of a red shift in the position of this band compared with that of pure β-CD could be an indicator of the existence of an interaction between copper and β-CD species [16]. No additional bands or position shift could be otherwise detected.

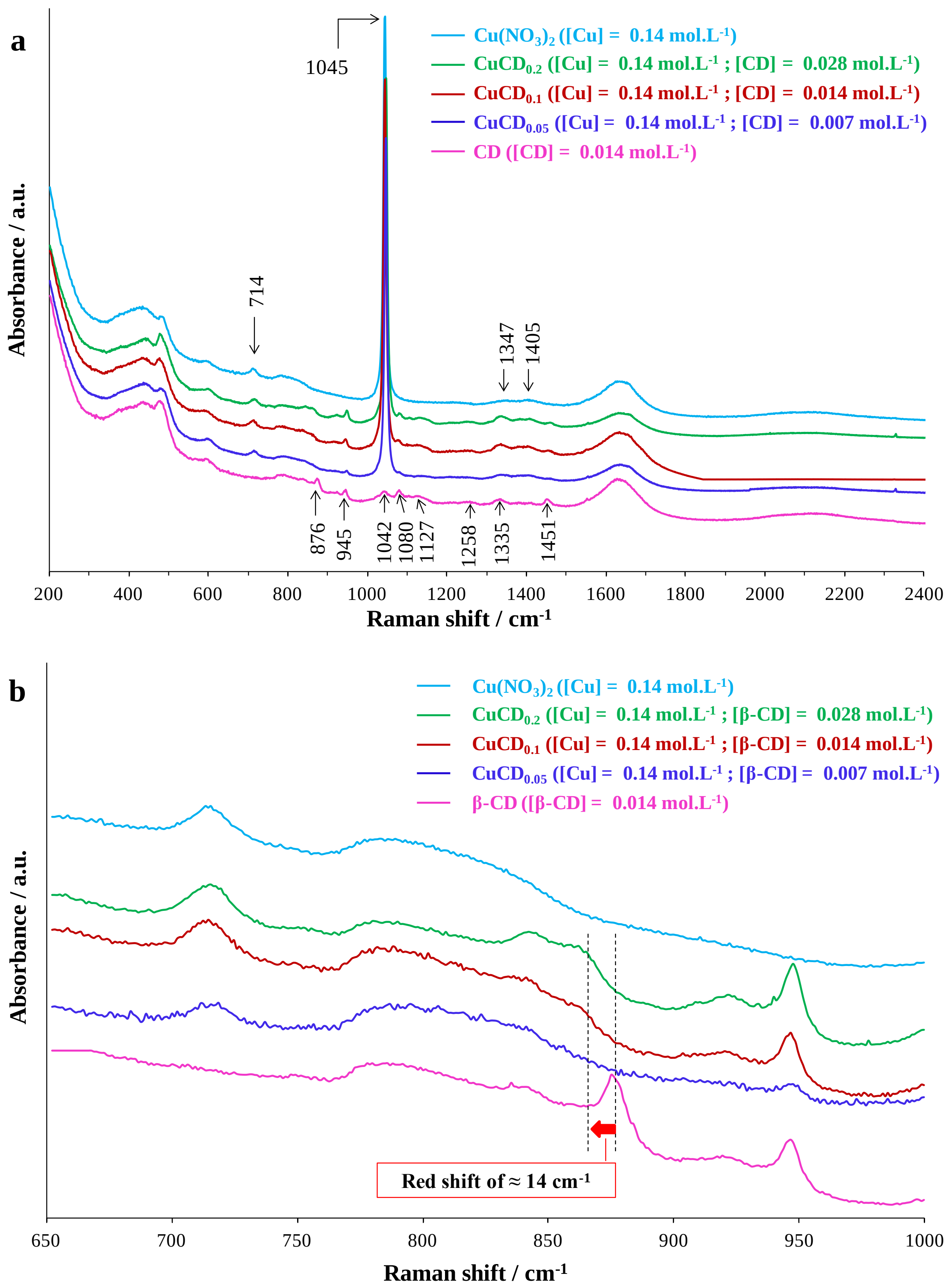

Figure 5.5. Raman spectra of aqueous solutions of β-CD; $Cu(NO_3)_2$; $CuCD_x$ with three different concentrations of β-CD a) recorded from 200 to 2400 cm^{-1} b) and a zoom in the range 650-1000 cm^{-1}.

5.2.1.5. Raman study of $CuCD_{0.1}$: effect of Cu concentration (β-CD/Cu ratio of 0.1)

A study of the effect of Cu concentration on the Raman spectra of aqueous solutions of $CuCD_{0.1}$, with a molar ratio of β-CD/Cu equal to 0.1, was carried out. The Raman spectra are represented in Figure 5.6.

The Raman spectrum of the most diluted solution ([Cu] = 0.14 mol.L^{-1}, trace “A”) shows characteristic bands related to β-CD, $Cu(NO_3)_2$, and water (a more detailed description has already been given above when discussing the results reported in Figure 5.5). When the concentration of $CuCD_{0.1}$ increases three times (trace “B”), additional bands appear at 440, 476, 573, and 1106 cm^{-1}, all of which are characteristic of β-CD which have been previously masked by excess water. However, what is noteworthy is the observation of a red shift regarding the β-CD-related band, formerly detected at 873 cm^{-1} in trace “A”, which in the case of trace “B” is shifted to a lower value, emerging thus at 861 cm^{-1}. Seeing as this anomeric band is usually considered as a marker of the CH_2OH position, a red shift in its position could signal a rotation of the CH_2OH group around the C-C axis [11], this latter being possibly caused by the occurrence of interactions between Cu^{2+} ions and β-CD molecules.

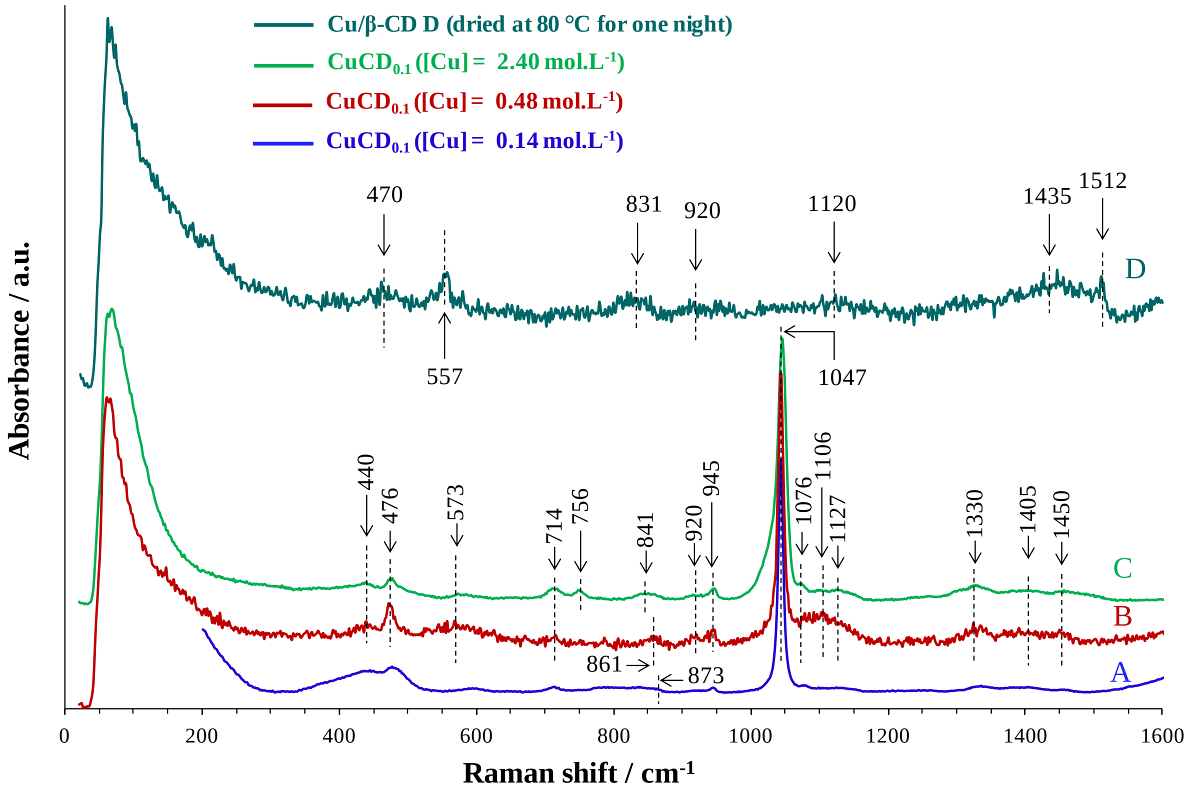

Figure 5.6. Raman spectra of aqueous $CuCD_{0.1}$ solutions with increasing concentrations of copper but constant β-CD/Cu = 0.1 molar ratio and dried Cu/β-CD D product.

When the concentration increases even further (trace “C”), β-CD and $Cu(NO_3)_2$ associated bands become better defined. In fact, a band at 756 cm^{-1}, ascribed to ν_4 in-plane bending vibration of nitrates [7], which had been previously absent in traces “A” and “B” appears in trace “C”. Moreover, an additional red shift in the band corresponding to C-1-H deformation is perceived, so that it now manifests at 841 cm^{-1}. This is suggestive of a strengthening in the interactions that are at the origin of the noted red shift.

Finally, when it comes to the Raman spectrum of the dried product, denoted Cu/β-CD D, it can be seen that only the most intense β-CD associated band emerges at 470 cm^{-1}, while all others are absent (trace “D” in Figure 5.6). Furthermore, unlike what was observed in section “***5.2.1.1. Raman study of $Cu(NO_3)_2$***”, where an increase in Cu concentration led towards the appearance of copper-nitrate bands and the intensification of nitrate related frequencies, in the case of the Raman spectrum of Cu/β-CD D, none of the bands characteristic of $Cu(NO_3)_2$ compound, or denoting a copper-nitrate association, are present.

However, new bands are detected at 557, 831, 920, 1120, 1435, and 1512 cm^{-1}. These six noted frequencies are actually distinctive of a hydrated copper oxalate mineral, $Cu(C_2O_4).nH_2O$, known by the name of moolooite, recognized for its green color and semitransparent property, qualities which are also found in Cu/β-CD D (refer to experimental section in Chapter II). This copper oxalate compound has a D2h symmetry and possesses eight optical modes among which four ($7\ A_g + 3\ B_{1g} + 3\ B_{2g} + 5\ B_{3g}$) are Raman-active. While the band at 557 cm^{-1} corresponds to stretching $\nu_{(Cu—O)}$ and $\nu_{(C—C)}$ vibrational modes, the bands at 831 and 920 cm^{-1} are attributed to symmetric stretching $\nu_{s(C—C)}$ and bending $\delta_{(O—C=O)}$ modes. Symmetric stretching $\nu_{s(C—O)}$ and bending $\delta_{(O—C=O)}$ modes also result in the bands noted at 1120 and 1435 cm^{-1}, whereas asymmetric stretching $\nu_{a(C=O)}$ can be ascribed to the band found at 1512 cm^{-1} [17]–[19].

Crystallographic studies of CuC_2O_4 structure indicate a square planar coordination of the Cu(II) cation with the oxalate anions acting as tetradentate ligands bridging two neighboring copper cations [20]. Thus, this mineral structure consisting of chains of Cu^{2+} bridged by oxygen, is clearly the result of Cu-β-CD interactions which likely started in the solution state (as suggested by the noted red shift of the anomeric band), and culminated into the creation of bonds involving the copper cations of the copper nitrate trihydrate precursor and the hydroxyl functions of β-CD.

Thus the existence of an interaction between cyclodextrin and copper species through the formation of molecule-ion adducts between β-CD and Cu^{2+} ions, an association which had been previously suggested by Song *et al.* [1], has been confirmed in the current analysis.

5.2.2. Dried precursors

Dried 10 Cu/Hap D and 10 Cu-CD/Hap D materials which have already been examined by XRD and TGA-DSC/MS analysis in the previous chapter (Chapter IV) will now be inspected by Raman spectroscopy. The use of this vibrational spectroscopy technique could enhance the comprehension of the structural effect of employing β-CD on the studied systems.

Before appraising each of these dried products separately, it should be first mentioned that heterogeneity could be perceived when analyzing different zones within these solids, especially for 10 Cu/Hap D. Consequently, six of the resulting Raman spectra for each sample are given in Figures 5.7 and 5.8, along with copper nitrate precursor, pure Hap, and β-CD Raman spectra.

Moreover, Raman spectra of pure $Cu(NO_3)_2.3H_2O$ and β-CD compounds are represented in Figure AC.2, with bands assignments for the noted frequencies in each of the $Cu(NO_3)_2.3H_2O$ and β-CD compounds summarized in Tables AC.1 and AC.2, respectively. A Raman spectrum of pure hydroxyapatite support is also illustrated in Figure AC.3.

5.2.2.1. Raman study of 10 Cu/Hap D

As can be seen in figure 5.7, the Raman spectra of 10 Cu/Hap D are complex showing characteristic bands of the Hap support together with other additional lines. Indeed, similarly to what can be seen when examining the calcined support Hap, an intense band derived from the non-degenerate ν_1 mode of the PO_4^{3-} tetrahedron (symmetric stretching of P-O) is noted at 961 cm^{-1}. Moreover, two peaks associated with the doubly degenerate ν_2 tetrahedron mode (bending modes of O-P-O) can be detected at 428 and 445 cm^{-1}. Three bands positioned at 578, 590, and 606 cm^{-1} arising from the triply degenerate ν_4 mode of PO_4^{3-} (bending modes of O-P-O) are observed. However, the three bands originating from the triply degenerate ν_3 tetrahedron modes (asymmetric stretching of P-O), which can be discerned at 1028, 1046, and 1074 cm^{-1} in the Raman spectrum of pure Hap material, cannot be distinguished in the spectra of 10 Cu/Hap D.

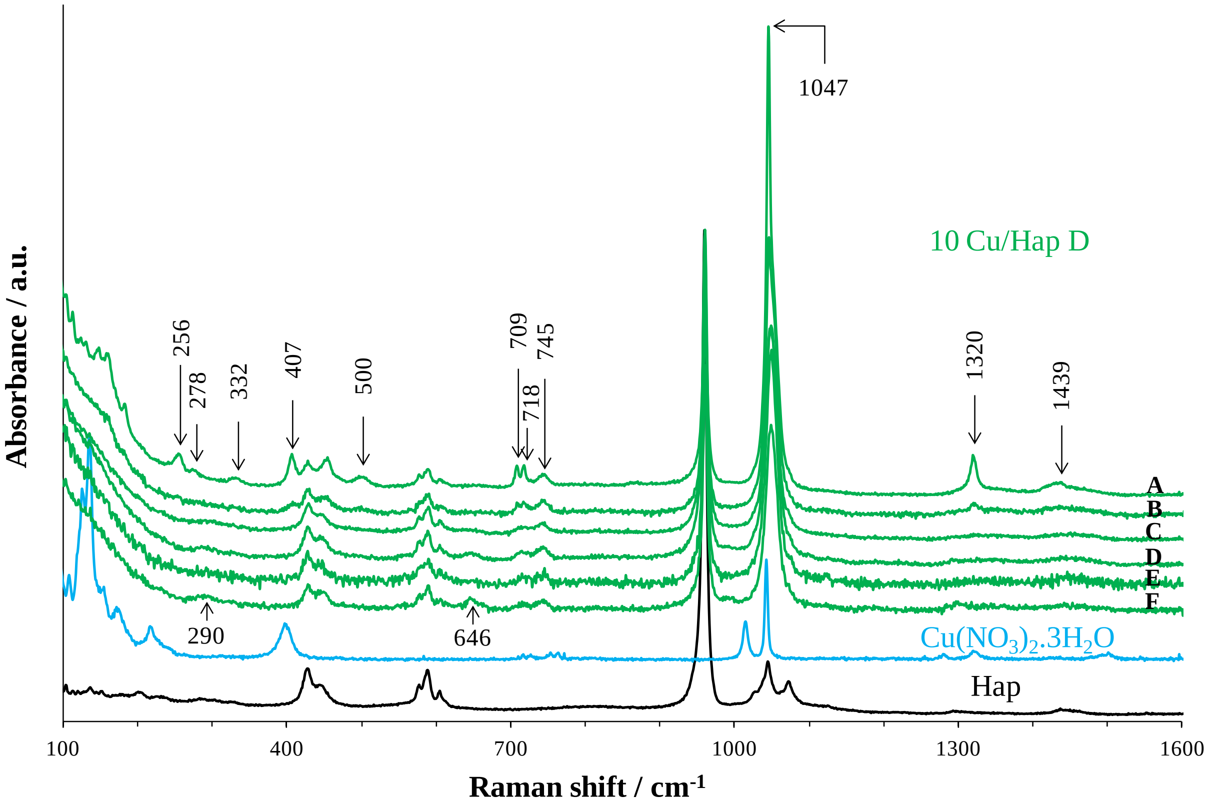

Figure 5.7. Raman spectra of Hap, $Cu(NO_3)_2.3H_2O$, and 10 Cu/Hap D.

Moreover, dissimilarities appear between the various spectra of 10 Cu/Hap D, both in terms of bands positions and intensity, signaling great surface heterogeneity. Besides Hap attributed frequencies, trace "A" of 10 Cu/Hap D reveals all the Raman band positions representative of gerhardtite phase, $Cu_2(OH)_3(NO_3)$, at 256, 278, 332, 407, 500, 709, 718, 745, 1047, 1320, and 1439 cm^{-1} [14], [21] (detected in XRD analysis in Chapter IV). In fact, it is the presence of gerhardtite's intense band at 1047 cm^{-1} that causes phosphates ν_3 bands to be hidden from all recorded 10 Cu/Hap D spectra. Indeed, all traces display some (trace "B", "C", "D", "E" and "F"), if not all (trace "A"), of gerhardtite characteristic bands, these latter becoming less defined and apparent when going from trace "A" to trace "F". Most interestingly though is the detection of bands at 290 and 646 cm^{-1} in traces "C" to "F", the intensity of these bands evolving in reverse mode to that of the gerhardtite related bands, meaning that it is in trace "F" where they are sharpest. It should be first noted that the band at 290 cm^{-1} cannot be ascribed to $Cu(OH)_2$ phase because of the absence of any band in the frequency range 485-488 cm^{-1} corresponding to the Cu-O-H deformation mode [22], [23] (refer to Table 5.1). Nor can the two newly detected bands be ascribed to libethenite phase ($Cu_2(PO_4)(OH)$), seeing as no bands in the frequency ranges 554-561, 815-818 and 1019-1022 cm^{-1} characteristic of out of plane P-O bending, Cu-OH bending and PO_4^{3-} symmetric stretching vibrational modes, respectively, can be perceived in any of the traces "C" to "F" (Table 5.1) [24]–[28]. These bands can be attributed to A_g and B_g^2 vibrational modes of copper oxide species, respectively, reported in Table 5.1 [24], [29]–[32]. Thus, this seems to suggest that small CuO particles start to form during the drying step of 10 Cu/Hap D through the decomposition of the already formed copper hydroxide nitrate which would explain the reverse evolution of the bands corresponding to CuO and $Cu_2(OH)_3(NO_3)$ respectively. Nevertheless, it should be remarked that an important blue shift in the position of the band corresponding to B_g^2 mode of CuO can be noted. This blue-shift could be perhaps explained by the start of copper oxide reduction due to a laser provoked local heating of the studied zone [33]. Furthermore, the band corresponding to B_g^1 mode of CuO, usually noted at ≈ 338-347 cm^{-1}, cannot be clearly distinguished in this case due to a probable band overlap with the gerhardtite characteristic band observed at 332 cm^{-1}.

Table 5.1. Raman band positions of CuO, $Cu(OH)_2$, $Cu_2(PO_4)(OH)$, and Cu_2O compounds based on literature results.

Wavenumber [cm^{-1}]			
CuO [a]	$Cu(OH)_2$ [b]	$Cu_2(PO_4)(OH)$ [c]	Cu_2O [d]
290-299	292	298-301	219
338-347	485-488	450-461	490-526
620-632		554-561	600-613
		621-627	645
		646-650	
		815-818	
		975-980	
		1019-1022	

[a] Based on references [24], [29]–[32]. [b] Based on references [22], [23]. [c] Based on references [24]–[28]. [d] Based on references [32], [34]–[36].

5.2.2.2. *Raman study of 10 Cu-CD/Hap D*

An inspection of 10 Cu-CD/Hap D Raman spectra showed no CuO related bands in any of the inspected traces (traces “A” to “F” in Figure 5.8). It did reveal, however, frequencies which were in line with β-CD compound (Table AC.2) at 475, 844, and 1128 cm^{-1}, in addition to some of gerhardtite characteristic bands at 712, 740, 1047, 1331, and 1455 cm^{-1}. Apart from β-CD and $Cu_2(OH)_3(NO_3)$ related bands, hydroxyapatite characteristic vibrational modes were also noted except for PO_4^{3-} ν_3 bands masked by the intense nitrate band at 1047 cm^{-1}. Interestingly, the only differences that can be observed between traces “A” to “F” are differences of intensity and broadness of the bands. Yet no differences in the position of bands (appearance of new bands or disappearance of previously noted ones) can be discerned, indicating a much less marked surface heterogeneity in the case of this sample.

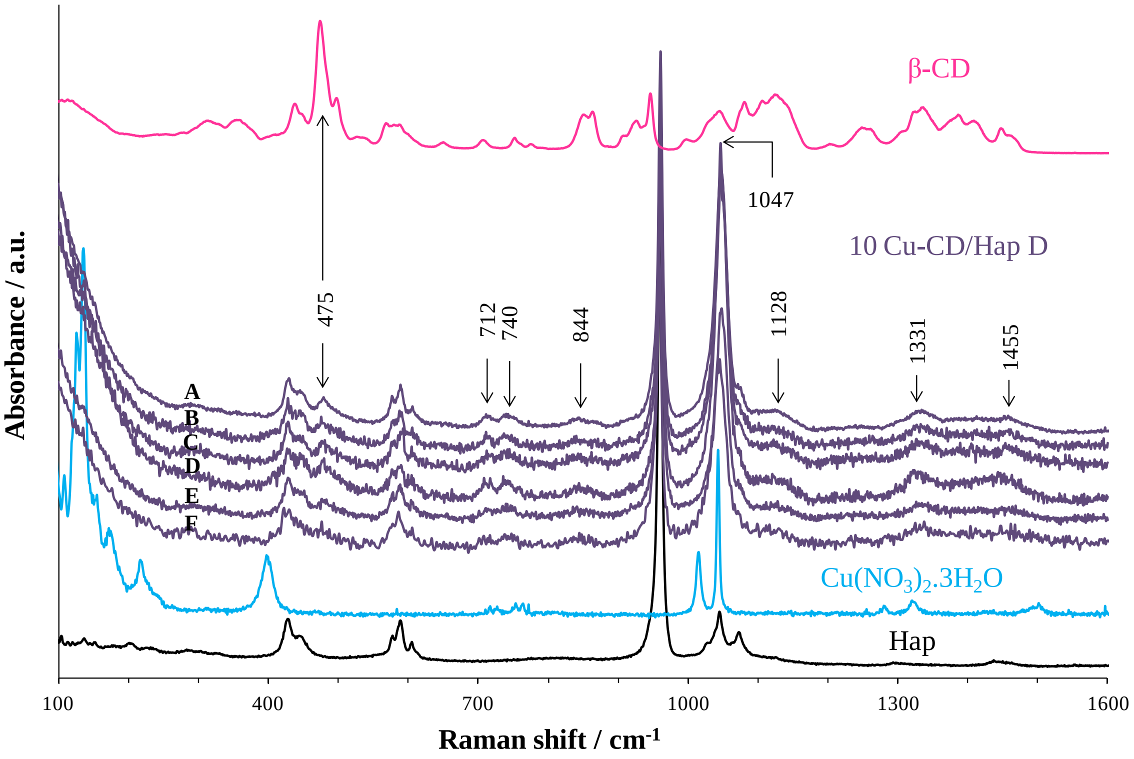

Figure 5.8. Raman spectra of Hap, $Cu(NO_3)_2.3H_2O$, β-CD, and 10 Cu-CD/Hap D materials.

Therefore, it appears that β-CD addition helps attain good surface homogeneity by delaying the production of copper oxide particles. This observation matches that of Bai *et al.* [37], who reported a similar retarding effect played by β-CD on the formation of the transition metal oxide phase during drying step.

5.2.3. Calcined catalysts

Before starting Raman analysis on the two calcined 10 Cu/Hap and 10 Cu-CD/Hap catalysts, an optical observation presented itself very clearly. When turning on the instrument's video camera to select a grain to be analyzed, an apparent distinction of color could be noticed when moving from one area to another. Indeed, bright zones could be seen along with dark ones. While the dark areas were black in the case of 10 Cu/Hap (Figure 5.9-a), the darkest areas found in 10 Cu-CD/Hap solid were brown (Figure 5.9-b).

It should be noted though, that while image contrast can indeed reveal chemical information, it can also be generated by some artifacts and have no chemical basis. Potential sources of artifacts include sample orientation, surface topography and laser-source induced photodegradation (in case of the white-light image being taken after spectra acquisition – see Figure AC.4) [38]. Still, image contrast is worth exploring for it can prove to be an indicator of chemical composition.

Thus, in the following section, a Raman investigation of both a bright and dark zone will be carried out for 10 Cu/Hap and 10 Cu-CD/Hap materials. Additionally, a Raman investigation of calcined CuDHap compound will be conducted too. However, unlike 10 Cu/Hap and 10 Cu-CD/Hap samples, CuDHap material displays no differences in color when moving from area to area when looking through the instrument's focusing camera. All the resulting Raman spectra are reported in Figure 5.10

and the values of the observed Raman shifts for the three considered compounds are tabulated in Table 5.2.

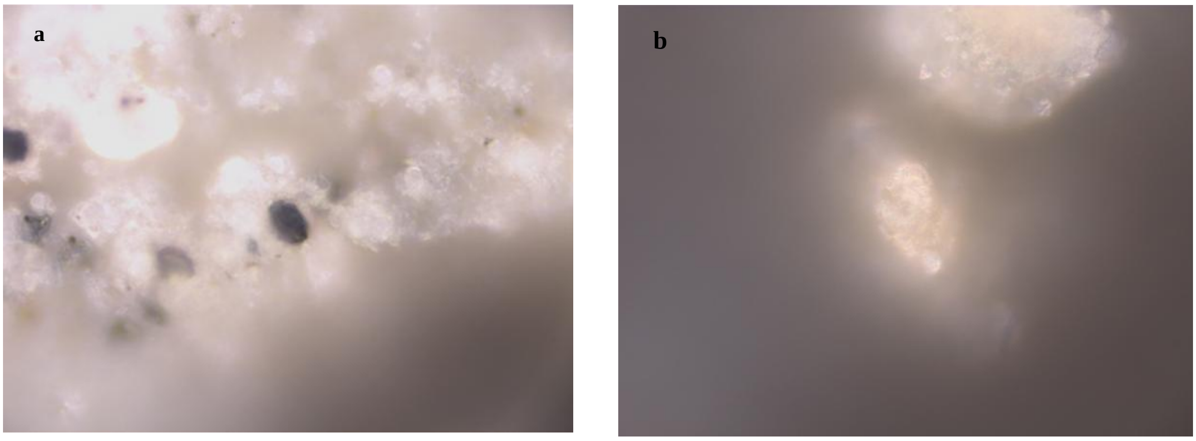

Figure 5.9. White-light images captured by the Raman apparatus video camera of a) 10 Cu/Hap and b) 10 Cu-CD/Hap.

5.2.3.1. Raman study of 10 Cu/Hap, 10 Cu-CD/Hap and CuDHap

Raman analysis of the bright areas of both 10 Cu/Hap and 10 Cu-CD/Hap result in similar spectra to that of pure Hap (Figure 5.10-a and b). Nonetheless, the bands perceived are less well defined than those of the support alone and more importantly, the main phosphate band corresponding to the ν_1 vibrational mode is broadened, especially in the case of 10 Cu/Hap. Indeed, the measured full width at half maximum (FWHM) of the intense peak at 961 cm^{-1} shows an increase when going from pure Hap to 10 Cu-CD/Hap, to finally 10 Cu/Hap, revealing values of 6.9, 7.5 and 8.9 cm^{-1}, respectively. This broadening of the ν_1 band can be connected with a decrease in the crystallinity of the hydroxyapatite material which appears to become more important when no β-CD is used. This decline in the crystallinity of Hap support can be induced by ionic substitution within Hap lattice. In fact, several studies which had investigated metal-ion-doped hydroxyapatite revealed that substitution of Ca^{2+} with other cations having different ionic radii led to changes in crystallographic parameters, ultimately resulting in some degree of crystallinity loss [39]–[41]. This in turn, caused a broadening and a decrease in the intensity of Hap's characteristic vibrational bands, observed in the Raman spectra of metal doped hydroxyapatite, when compared with those of undoped Hap [42]–[44]. Indeed, this was the case for the copper doped Hap compound prepared in the current study, and examined by Raman spectroscopy. When looking at the CuDHap spectrum reported in Figure 5.10-c, it can be clearly perceived that despite being nearly identical to the Raman spectrum of Hap support, the band associated with the PO_4^{3-} tetrahedron ν_1 frequency (960 cm^{-1}) is broader and less intense for CuDHap (FWHM = 8.5 cm^{-1}) than for Hap (FWHM = 6.9 cm^{-1}), same as for the bands corresponding to the doubly degenerate ν_2 tetrahedron mode. However, unlike the work of Unabia *et al.* [45] where insertion of copper within the hydroxyapatite lattice resulted in a marked red shift (7 cm^{-1}) of the ν_1 band, this was not so obvious in the present analysis where no significant wavenumber change could be discerned.

Thus, based on the variation of the crystallinity degree between 10 Cu/Hap and 10 Cu-CD/Hap (determined from FWHM values), it seems that the use of β-CD favors the formation of copper species situated on the surface of apatite crystals rather than inserted in its first subsurface layers.

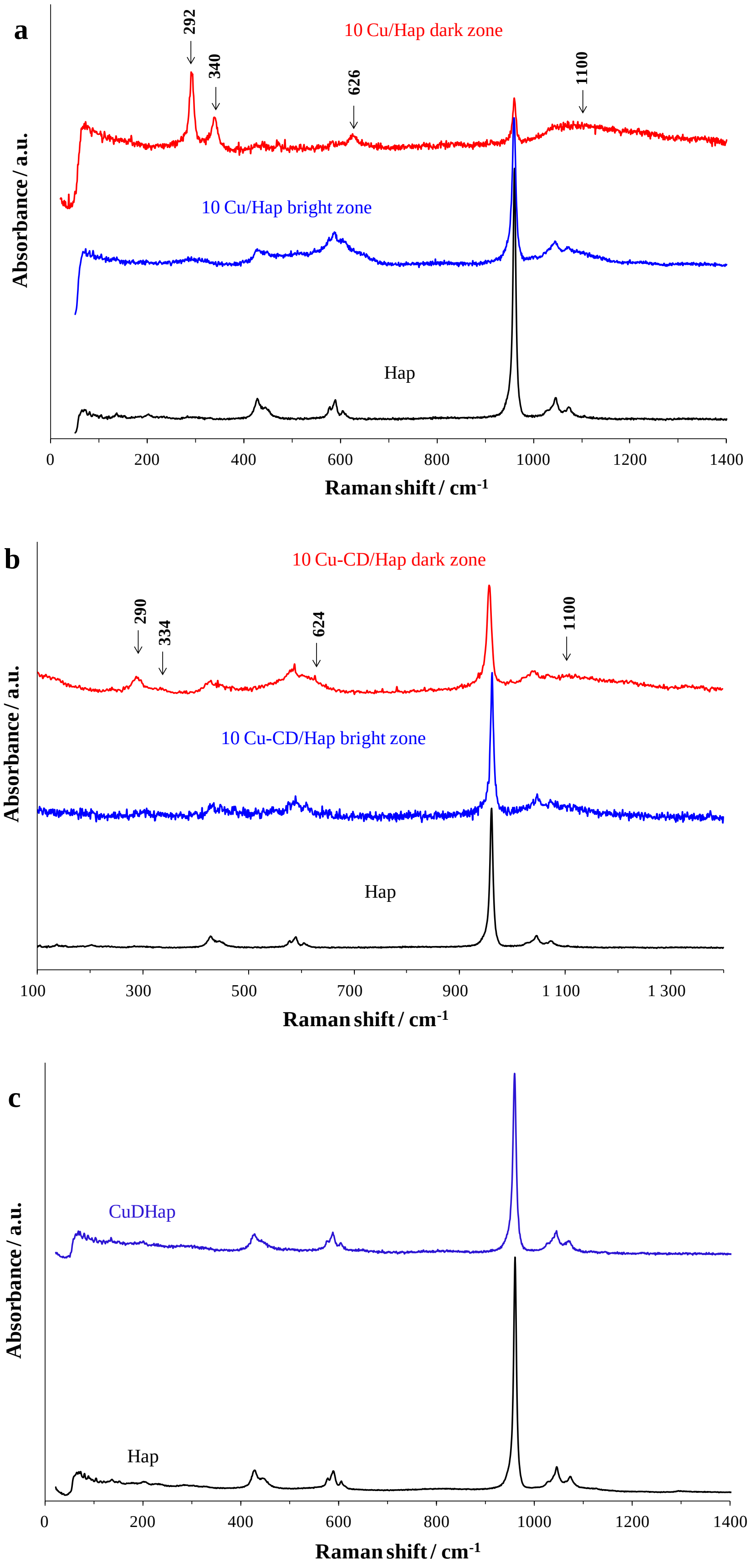

Figure 5.10. Raman spectrum of Hap support along with those of a) 10 Cu/Hap; b) 10 Cu-CD/Hap; and c) CuDHap compounds.

Furthermore, the bright area of 10 Cu/Hap sample manifests a broadening in the 620–650 cm^{-1} range. This broadening might be caused by the presence of another phase. Monoclinic CuO, which was previously shown to be present in 10 Cu/Hap material through XRD and infrared analysis, has three Raman active modes which are positioned at 290 (A_g), 338 (B_g^1) and 624 (B_g^2) cm^{-1} [29], [46]–[48]. When comparing these theoretical values with the current result, it can be supposed that the broadening of the 620–650 cm^{-1} range is the result of the presence of B_g^2 vibrations of tenorite (CuO) phase.

This supposition is confirmed when looking at the Raman spectra of the dark zone of 10 Cu/Hap (Figure 5.10-a), in which the CuO bands become much more emphasized, with bands clearly appearing at 292, 340, and 626 cm^{-1}. These frequencies are in line with the literature reported values cited above. In opposition, the bands associated with Hap support almost disappear with only the most intense phosphate band at 961 cm^{-1} remaining plainly visible, its FWHM having increased even further to become 9.5 cm^{-1}.

Regarding Raman analysis of a dark zone of 10 Cu-CD/Hap, the ensuing spectrum displays CuO characteristic frequencies at 290, 334, and 624 cm^{-1}. On the other hand, contrarily to what was noted in the case of Raman analysis of 10 Cu/Hap dark area, Hap characteristic bands are still apparent and the CuO related band are less sharp and more broad, suggesting thus the presence of smaller CuO particles [49]. This observation is in agreement with the results presented in the preceding chapter: XRD, XPS.

In conclusion, the analysis above seems to imply that color variation noted during optical visualization of the samples does have a chemical significance, with the bright zones corresponding to areas richer in hydroxyapatite whereas the dark zones would coincide with areas richer in copper oxide. Consequently, this indicates heterogeneity in the composition of the synthesized powders. However, it appears that these latter become more homogeneous with the use of β-CD as a Cu dispersing agent. Indeed, it is not without significance that the dark areas in 10 Cu-CD/Hap (brown zones) are lighter in color than those in 10 Cu/Hap (black zones), for it is yet another sign of better dispersion of copper species within the materials derived from β-CD assisted synthesis. Last but not least, employing β-CD in the synthesis process allows for better accessibility to the copper active sites, which by remaining at the surface rather than encapsulated between layers of hydroxyapatite become more available for catalytic activity.

Table 5.2. Raman line positions and assignment for calcined 10 Cu/Hap and 10 Cu-CD/Hap.

Sample	Wavenumber [cm^{-1}]	
	Hap	CuO
Hap	428; 445; 578; 590; 606; 961; 1028; 1046; 1074	-
10 Cu/Hap bright zone	428; 445; 577; 589; 605; 960; 1025; 1045; 1072	630
10 Cu/Hap dark zone	586; 960	292; 340; 626
10 Cu-CD/Hap bright zone	430; 447; 577; 590; 609; 962; 1030; 1047; 1072	-
10 Cu-CD/Hap dark zone	427; 444; 579; 588; 609; 957; 1030; 1040; 1067	290; 334; 624
CuDHap	428; 443; 577; 589; 604; 960; 1027; 1045; 1070	-

To summarize, compelling proofs of the existence of interactions between β-CD and copper cations have been supplied by Raman analysis. These interactions, which began at the solution state and continued evolving within the system upon drying, gave rise to homogeneously dispersed copper species more accessible and available for catalytic reactions, following the calcination step. Nonetheless, no information has been yet forthcoming regarding any type of interaction between β-CD and hydroxyapatite support.

Thus, an inspection of Cu and β-CD-bearing compounds, in their dried state, through ToF-SIMS monitoring could constitute an important first step towards filling the gaps in this domain and shedding some light into the interactions taking place between β-CD and Hap support.

5.3. ToF-SIMS

In order to better apprehend the role of β-CD which allows a better dispersion of the CuO phase over hydroxyapatite, dried samples 10 Cu-CD/Hap D and 10 Cu/Hap D have been investigated by ToF-SIMS as well as β-CD and Hap alone, in addition to dried Cu/β-CD D and β-CD/Hap D compounds.

5.3.1. ToF-SIMS of β-CD

Time-of-flight secondary ion mass spectrometry (ToF-SIMS) spectra in both polarities of β-CD ($C_{42}H_{70}O_{35}$) alone are presented in Figure 5.11, and its characteristic peaks are given in Table 5.3.

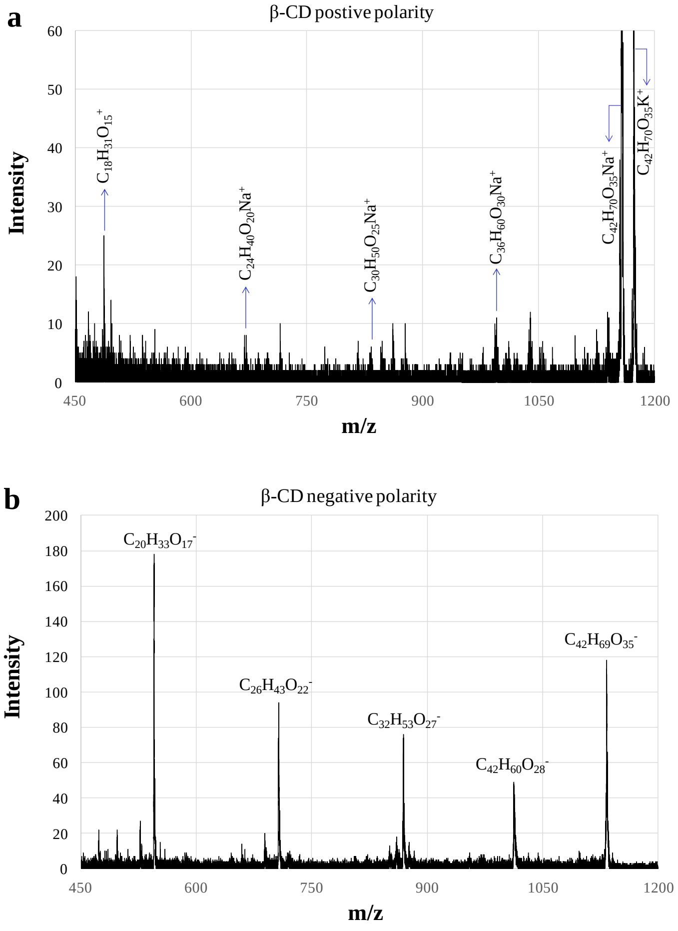

Figure 5.11. ToF-SIMS spectra of β-CD in the 450-1200 m/z range in a) positive polarity and b) negative polarity.

The fragmentation is characterized by a low signal-to-noise ratio. Because of the high affinity of β-CD (M) for Na^+ and K^+, secondary ions $[M\text{-}Na]^+$ and $[M\text{-}K]^+$ are detected in positive polarity, whereas intact β-CD is detected as $[M]^-$ in negative polarity [50].

The characteristic successive peaks detected in the positive ToF-SIMS spectrum decrease by consecutive losses of mass 162.14 starting from the sodiated entity $C_{42}H_{70}O_{35}Na^+$. The molecular mass of 162.14 can be ascribed to a dehydrated glucose molecule which constitutes the monomeric unit of β-CD. This observation is in accordance with the fragmentation pattern of β-CD from the sodiated entity $C_{42}H_{70}O_{35}Na^+$, which takes place at the acetal junction. In fact, it has been reported that this process can occur either according to the formation of Y- or Z-type ions, represented in Figure 5.12, with albeit the former being significantly more common than the latter ones [51]. Thus, it is assumed that the loss of mass 162 proceeds according to Y-type ion formation. Although, for the secondary ions having the lowest m/z values (m/z < 671), it can be noted that the Na^+ contribution disappears. Negative polarity ToF-SIMS spectrum showed few peaks, which are all ascribable to large fragment ions of β-CD in line with previous results [52], [53].

Table 5.3. Peak assignment of β-CD.

Peak	Secondary Ion	m/z	Intensity	Peak	Secondary Ion	m/z	Intensity
1	$C_6H_{11}O_5^+$	163.0593	130723	1	$C_{14}H_{23}O_{12}^-$	383.2	16977
2	$C_{12}H_{21}O_{10}^+$	325.1198	47908	2	$C_{20}H_{33}O_{17}^-$	545.1	5702
3	$C_{18}H_{31}O_{15}^+$	487.1409	821	3	$C_{26}H_{43}O_{22}^-$	707	2466
4	$C_{24}H_{40}O_{20}Na^+$	671.2516	113	4	$C_{32}H_{53}O_{27}^-$	869.2	1899
5	$C_{30}H_{50}O_{25}Na^+$	833.2350	113	5	$C_{42}H_{60}O_{28}^-$	1012.4	3156
6	$C_{36}H_{60}O_{30}Na^+$	995.2528	212	6	$C_{42}H_{69}O_{35}^-$	1133.2	4177
7	$C_{42}H_{70}O_{35}Na^+$	1157.2743	6295				
8	$C_{42}H_{70}O_{35}K^+$	1173.2876	2138				

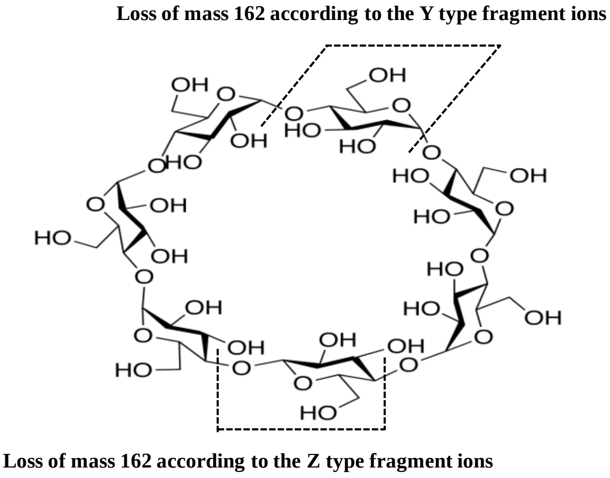

Figure 5.12. Decomposition process of $[M\text{-}Na]^+$ ion occurring according to the formation of Y- or Z-type ions. From reference [51].

5.3.2. ToF-SIMS of Hap

Both positive and negative ion TOF-SIMS spectra of calcined hydroxyapatite have been acquired and are reported in Figure 5.13. Ion fragments derived from the Hap support, detected in both positive and negative polarities are listed in Table 5.4. These noted secondary ions include all of the previously reported characteristic fragments of $Ca_5(PO_4)_3(OH)$ compound, namely $Ca_2PO_3^+$ (m/z = 159), $Ca_2PO_4^+$ (m/z = 175), $CaPO_3H^+$ (m/z = 120), $CaPO_4H_2^+$ (m/z = 137), $Ca_2PO_3H^+$ (m/z = 160), $Ca_3P_2O_3H^+$ (m/z = 231), $Ca_4P_2O_4H^+$ (m/z = 287), $Ca_5P_2O_5H^+$ (m/z = 343) and $Ca_5(PO_4)_3^+$ (m/z = 485) observed in positive spectrum, as well as $CaPO^-$ (m/z = 87), $CaPO_2^-$ (m/z = 103), $CaPO_3^-$ (m/z = 119) and $Ca_2PO_5^-$ (m/z = 191) observed in negative spectrum [54], [55]. However, some impurities were also found such as Na^+ (m/z = 23), Mg^+ (m/z = 24), K^+ (m/z = 39), along with some hydrocarbons noted in both polarities.

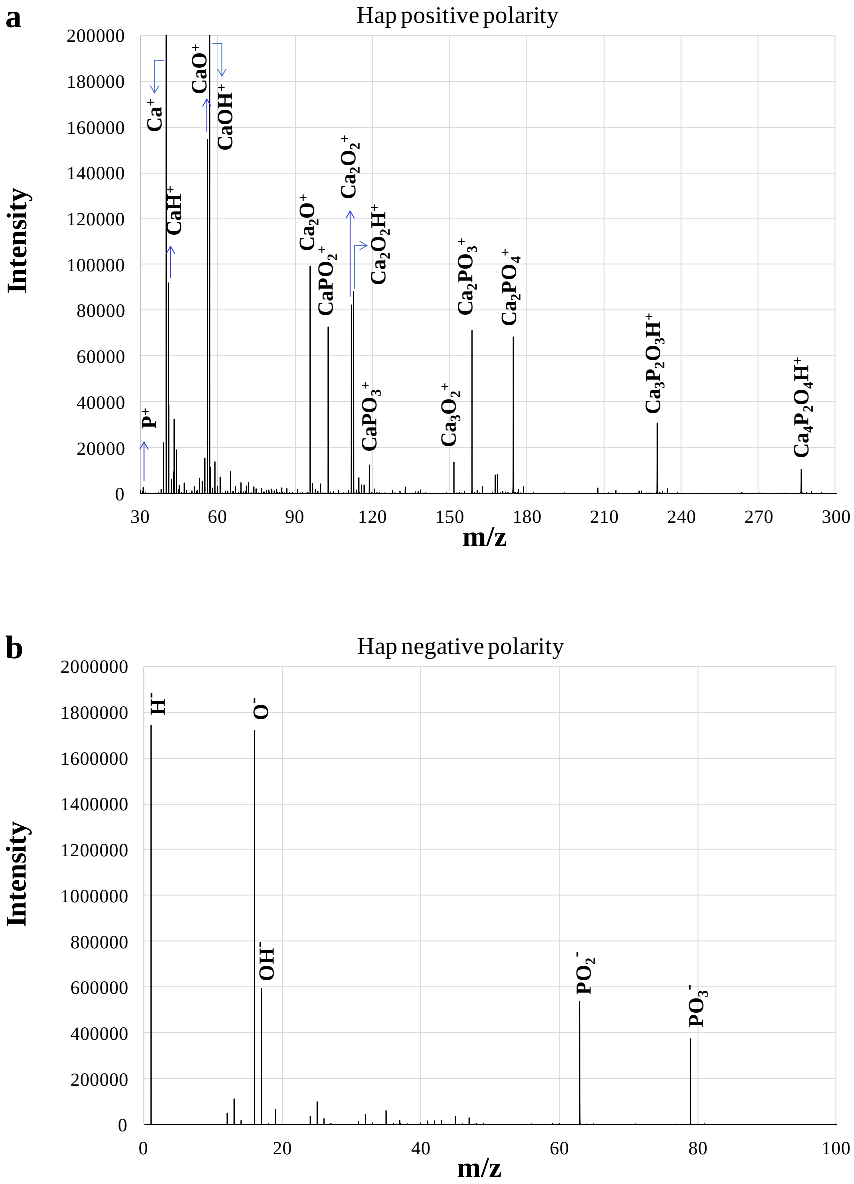

Figure 5.13. ToF-SIMS spectra of Hap a) in the 30-300 m/z range in positive polarity and b) in the 0-100 m/z range in negative polarity.

Table 5.4. List of ToF-SIMS positive and negative ion fragments related to the Hap support.

$Ca_vO_zH_w^+$	$P_tO_zH_w^+$	$Ca_vP_tO_zH_w^+$	$Ca_vO_z^-$	$P_tO_z^-$	$O_zH_w^-$	$Ca_vP_tO_z^-$
Ca^+	P^+	$CaPO^+$	CaO^-	P^-	O^-	$CaPO^-$
$^{44}Ca^+$	PO^+	$CaPO_2^+$	CaO_2^-	PO^-	O_2^-	$CaPO_2^-$
Ca_2^+	POH^+	$^{44}CaPO_2^+$		PO_2^-	OH^-	$CaPO_3^-$
CaO^+	PH^+	$CaPO_3^+$		PO_3^-	O_2H^-	$Ca_2PO_5^-$
$^{44}CaO^+$	PH_2^+	$^{44}CaPO_3^+$				
Ca_2O^+	$P_2H_3^+$	$Ca_2PO_3^+$				
$^{44}Ca_2O^+$		$Ca_2PO_4^+$				
$Ca_2O_2^+$		$^{44}Ca_2PO_4^+$				
$^{44}CaCaO_2^+$		$Ca_3PO_4^+$				
$Ca_3O_2^+$		$CaPO_3H^+$				
$^{44}CaCa_2O_2^+$		$CaPO_4H_2^+$				
$Ca_3O_3^+$		$Ca_2PO_3H^+$				
$^{44}CaCa_2O_3^+$		$Ca_3P_2O_3H^+$				
CaH^+		$Ca_4P_2O_4H^+$				
$^{44}CaH^+$		$Ca_5P_2O_5H^+$				
$CaOH^+$		$Ca_5P_3O_{12}^+$				
$^{44}CaOH^+$		$Ca_6P_3O_4H_2^+$				
Ca_2OH^+		$Ca_7P_3O_5H_2^+$				
$Ca_2O_2H^+$		$Ca_8P_4O_6H^+$				
$^{44}CaCaO_2H^+$		$Ca_9P_4O_7H^+$				
$Ca_3O_2H^+$		$Ca_{10}P_4O_8H^+$				
$Ca_3O_3H^+$		$Ca_{11}P_4O_9H^+$				
$^{44}CaCa_2O_3H^+$		$Ca_{12}P_4O_{10}H^+$				

5.3.3. ToF-SIMS of Cu/β-CD D (β-CD/Cu ratio of 0.1)

ToF-SIMS was used to obtain molecular information of the Cu/β-CD D surfaces ($n_{\beta\text{-CD}}/n_{Cu} = 0.1$). The positive ToF-SIMS spectrum for the dried Cu/β-CD D is shown in Figure 5.14-a, and the assignments for selected ions are shown in Table 5.5 with accurate mass determination. The presence of copper was confirmed by the 63 m/z peak ascribed to Cu^+. Additionally, $Cu_xO_yH_z^+$ (x = 1-5; y = 0-3; z = 0-3) secondary ions are clearly observed.

Table 5.5. Peak assignment of dried Cu/β-CD D sample.

Peak	Secondary Ion	m/z	Intensity	Peak	Secondary Ion	m/z	Intensity
1	$C_2H_2Cu^+$	88.9409	12373	1	CCu^-	75.0202	1443
2	$C_2H_2{}^{65}Cu^+$	90.9436	9186	2	$C^{65}Cu^-$	77.0045	579
3	$COCu^+$	90.9204	25502	3	$C_2H_2Cu^-$	88.9549	12388
4	$CO^{65}Cu^+$	92.9334	12719	4	$C_2H_2{}^{65}Cu^-$	90.9551	5519
5	$C_2H_2OCu^+$	104.9345	7927	5	$C_2H_2OCu^-$	104.9520	48988
6	$C_2H_2O^{65}Cu^+$	106.9389	4891	6	$C_2H_2O^{65}Cu^-$	106.9538	23705
7	$C_2H_3O_2Cu^+$	121.9370	3820	7	$C_2H_3OCu^-$	105.9505	47786
8	$C_2H_3O_2{}^{65}Cu^+$	123.9341	1535	8	$C_2H_3O^{65}Cu^-$	107.9492	20944
9	$C_2H_4O_2Cu^+$	122.9505	3470				
10	$C_2H_4O_2{}^{65}Cu^+$	124.9493	1771				
11	$C_3H_2O_2Cu^+$	132.9334	6429				
12	$C_3H_2O_2{}^{65}Cu^+$	134.9372	3568				
13	$C_2HCu_2{}^+$	150.8595	33394				
14	$C_2H^{65}CuCu^+$	152.8544	30164				
15	$C_2H^{65}Cu_2{}^+$	154.8547	8234				
16	$C_2HOCu_2{}^+$	166.8549	14202				
17	$C_2HO^{65}CuCu^+$	168.8537	12514				
18	$C_2HO^{65}Cu_2{}^+$	170.8563	3725				
19	$C_2H_2OCu_2{}^+$	167.8469	6342				
20	$C_2H_2O^{65}CuCu^+$	169.8436	4215				
21	$C_2H_2O^{65}Cu_2{}^+$	171.8482	2103				
22	$C_3HO_2Cu_2{}^+$	194.8442	2341				
23	$C_3HO_2{}^{65}CuCu^+$	196.8413	1520				
24	$C_3HO_2{}^{65}Cu_2{}^+$	198.8187	503				
25	$C_2H_2O_2Cu_3{}^+$	246.7753	2536				
26	$C_2H_2O_2{}^{65}CuCu_2{}^+$	248.7822	3199				
27	$C_2H_2O_2{}^{65}Cu_2Cu^+$	250.7780	2474				
28	$C_2H_2O_2{}^{65}Cu_3{}^+$	252.7721	1810				

Due to the excess of copper nitrate in the sample inducing high intensity secondary ions, the low intensity organic secondary ions relative to β-CD can be no longer observed unambiguously for m/z higher than 120 due to peak overlapping and matrix/concentration effects. The interaction between β-CD and copper species throughout a supramolecular interaction cannot be observed as a β-CD-Cu molecular ion is not observed. However, characteristic organic-copper secondary ions $C_xH_yO_zCu_w^+$ (Table 5.5) can be detected showing that copper interacts with cyclodextrin by means of covalent interaction.

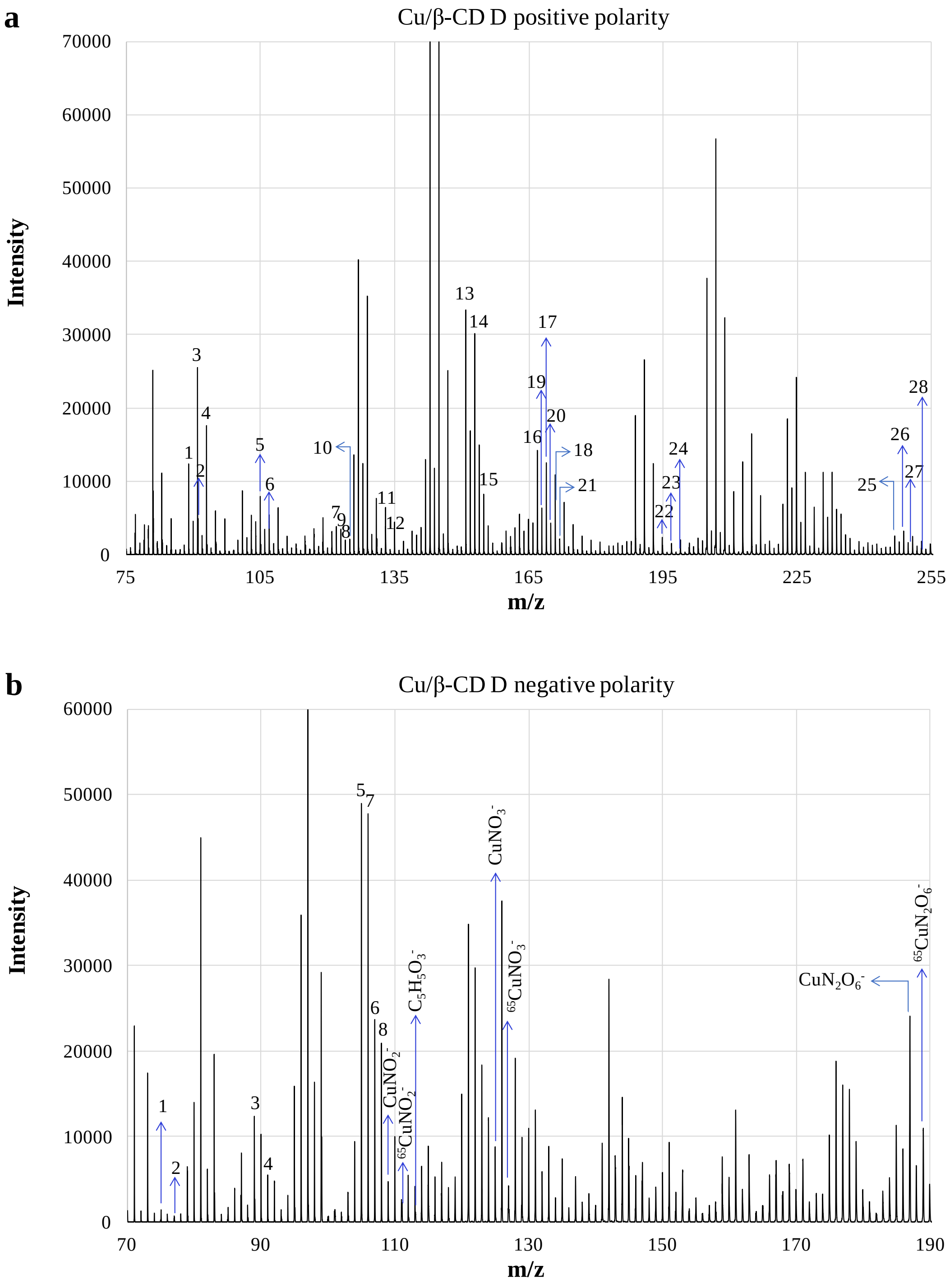

Figure 5.14. ToF-SIMS spectra of Cu/β-CD D a) in the 75-255 m/z range in positive polarity and b) in the 70-190 m/z range in negative polarity.

In negative polarity, the ToF-SIMS spectrum (Figure 5.14-b) shows alongside the $Cu_xO_yH_z^-$ peaks (x = 1-4; y = 1-4; z = 0-2) the m/z = 109, 125 and 186 peaks assigned to $CuNO_2^-$, $CuNO_3^-$ and $CuN_2O_6^-$, respectively, which indicate that copper is in close interaction with NO_3^-. The great abundance of NO^-, NO_2^-, NO_3^- secondary ions confirms the presence of such nitrate compounds at the surface of the sample. It is noteworthy that the detection of the 113 m/z peak attributed to $C_5H_5O_3^-$ has been previously detected in the fragmentation of glucose [56]. However, only four related organic-copper secondary ions, namely CCu^-, $C_2H_2Cu^-$, $C_2H_2OCu^-$ and $C_2H_3OCu^-$ can be unambiguously detected in negative polarity (cf. Table 5.5) confirming interaction between copper and organic species.

5.3.4. ToF-SIMS of β-CD/Hap D

ToF-SIMS of β-CD/Hap D sample was conducted in order to investigate the interactions likely to occur when mixing β-CD with the Hap support. Indeed, the existence of such interactions between β-CD and hydroxyapatite is made abundantly clear by the presence of a series of secondary ions involving organic fragments derived from β-CD associated with calcium cations derived from hydroxyapatite, noted in positive polarity and reported in Table 5.6. Moreover in negative polarity, one organic-P secondary ion highlighting a β-CD-Hap interaction can also be detected (Table 5.6). Based on these results, it can be assumed that β-CD preferentially interacts with Ca rather than P. In fact, a similar observation has been previously reported by Xiao *et al.* [57], who declared that interactions between β-CD and Hap would likely involve the OH groups of β-CD and Ca^{2+} cations of Hap.

Table 5.6. List of the organic ions detected in (+) and (−) polarity.

$C_xH_yO_zCa_w^+$	m/z	Intensity	$C_xH_yO_zP_t^-$	m/z	Intensity
$COCa^+$	67.9555	482	COP^-	58.9699	2503
$CHOCa^+$	68.9641	2904			
$C_2H_3O_2Ca^+$	98.9768	5656			
$C_3H_3O_2Ca^+$	110.9761	4617			
$C_4H_4O_2Ca^+$	123.9809	404			
$C_4H_5O_2Ca^+$	124.9906	1437			
$CO_3Ca_2^+$	139.9037	926			
$CHO_3Ca_2^+$	140.9117	1604			
$C_2H_3O_3Ca_2^+$	154.9303	597			

5.3.5. ToF-SIMS of 10 Cu/Hap D

ToF-SIMS analysis of 10 Cu/Hap D compound revealed in addition to the characteristic secondary ions of Hap, the presence of copper entities through the detection of $Cu_xO_yH_z^+$ (x = 1-6; y = 0-3; z = 0-1) and $Cu_xO_yH_z^-$ (x = 1-4; y = 0-4; z = 0-3) secondary ions in positive and negative spectrum, respectively.

The presence of nitrate ions derived from the copper precursor was established by the peaks noted at m/z = 30 and 46 in ToF-SIMS (+) spectrum, which can be ascribed to NO^+ and NO_2^+, respectively, as well as the peaks seen at m/z = 30, 46 and 62 in ToF-SIMS (-) spectrum, which can be attributed to NO^-, NO_2^- and NO_3^-, respectively. Moreover, we also observed ions correlated with nitrate precursors interacting not only with copper but with calcium ions too, as manifested by the appearance of several $Ca_vNO_z^+$, $Ca_vN_sO_zH_w^-$ and $Cu_xN_sO_zH_w^-$ secondary ions, displayed in Figure 5.15. Conversely, the detection of only one P-nitrate secondary ion, namely PON^- (m/z = 61) noted in negative polarity, is indicative of a clear affinity of nitrate entities towards calcium ions. This latter thus results in multiple calcium-nitrate interactions which are facilitated by the intimate contact between the copper nitrate precursor and hydroxyapatite support during the impregnation step.

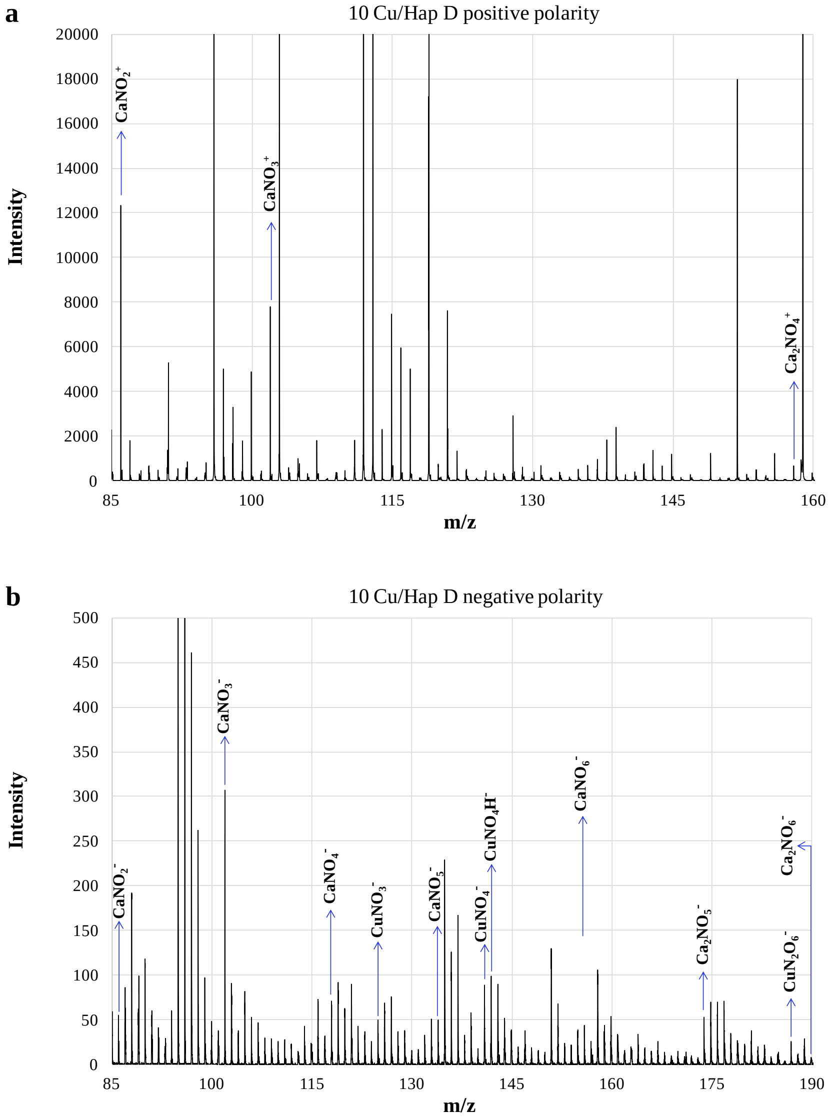

Figure 5.15. ToF-SIMS spectra of 10 Cu/Hap D a) in the 85-160 m/z range in positive polarity and b) in the 85-190 m/z range in negative polarity.

5.3.6. ToF-SIMS of 10 Cu-CD/Hap D

The main objective of the present ToF-SIMS analysis was to investigate the formation of a supramolecular adduct between β-CD and copper species, ideally with an intact β-CD molecular ion.

However, no signal above background levels could be observed for an ionized β-CD-Cu fragment. It might be that the interaction occurring between β-CD molecule and Cu ions are not sufficiently strong and thus cannot be easily preserved for mass spectrometric detection in the gas phase [58]. Furthermore, no intact β-CD can be noted, neither in positive or negative polarity. Nevertheless, a multitude of organic ion fragments were detected in both polarities. The ions and the peak assignments are listed in Table 5.7.

Among these ions, $C_xO_zCu_w^+$ and $C_xH_yO_zCu_w^-$ secondary ions can be observed denoting the occurrence of interactions between organic fragments derived from β-cyclodextrin and copper cations. It should be noted that while no sodiated β-CD ion fragment was detected in either (+) or (-) ToF-SIMS spectra, one sodiated copper-organic ion fragment could be discerned in negative polarity, namely $C_2H_2Cu_3Na^-$ (m/z = 238). More importantly Ca_xCu_y-organic secondary ions were also perceived signaling the interaction of β-CD derived organic fragments with both copper species and hydroxyapatite support through its calcium cations: $C_2CaCu_6^+$ (m/z = 442), $C_3H_3OCaCu_2^-$ (m/z = 221), $CH_3OCa_2Cu_3^-$ (m/z = 300).

Table 5.7. List of the organic ions detected in (+) and (−) polarity.

Secondary ion	m/z	Intensity	Secondary ion	m/z	Intensity
CCu^+	74.9297	1789	$CCaP^-$	82.9363	484
$C^{65}Cu^+$	76.9285	584	$C_4H_5O_2^-$	85.0289	358
$COCu^+$	90.9217	833	C_2Cu^-	86.9293	222
$CO^{65}Cu^+$	92.9264	423	$COCu^-$	90,9275	167
$C_{10}H_{16}O_6^+$	232.0950	181	$CO^{65}Cu^-$	90.9295	57
$C_{18}H_{31}O_6^+$	343.2204	100	C_2HOCu^-	103,9326	139
$C_2CaCu_6^+$	441.5429	12	$C_2HCa_3^-$	144.8930	270
$C_2Ca^{65}CuCu_5^+$	443.5403	22	$C_3H_3OCaCu_2^-$	220.8405	299
$C_2Ca^{65}Cu_2Cu_4^+$	445.5397	25	$C_3H_3OCa^{65}CuCu^-$	222.8395	178
$C_2Ca^{65}Cu_3Cu_3^+$	447.5393	16	$C_3H_3OCa^{65}Cu_2Cu^-$	224.8308	66
$C_2Ca^{65}Cu_4Cu_2^+$	449.5398	7	$C_2H_2Cu_3Na^-$	237.7911	88
			$C_2H_2{}^{65}CuCu_2Na^-$	239.7901	107
			$C_2H_2{}^{65}Cu_2CuNa^-$	241.7882	48
			$CH_3OCa_2Cu_3^-$	299.7318	49
			$CH_3OCa_2{}^{65}CuCu_2^-$	301.7307	58
			$CH_3OCa_2{}^{65}Cu_2Cu^-$	303.7241	35

Besides organic ion fragments, secondary ions characteristic of hydroxyapatite support were detected. Additionally, the presence of copper is also manifested by the observation of $Cu_xO_yH_z$ entities in the ToF-SIMS spectra of 10 Cu-CD/Hap D. In order to investigate the potential effect of β-CD use on copper species dispersion, an evaluation of the relative surface density of these $Cu_xO_yH_z$ entities was performed by calculating the ToF-SIMS intensity ratios of $Cu_xO_yH_z^+/Ca_2PO_4^+$ secondary ions for 10 Cu/Hap D and 10 Cu-CD/Hap D solids. The corresponding results are reported in Table 5.8. By examining the evolution of $Cu_xO_yH_z^+/Ca_2PO_4^+$ ratio value when going from 10 Cu/Hap D to 10 Cu-CD/Hap D, it became apparent that a higher ratio value was always obtained for 10 Cu-CD/Hap D compound which clearly highlights an increase in the surface density of $Cu_xO_yH_z$ entities in the case of the 10 Cu-CD/Hap D material. Thus, it would seem that resorting to β-CD as a copper dispersing agent is very effective for obtaining copper entities highly dispersed at the topmost surface of the solid rather than encapsulated in deeper layers of the material. Moreover, the higher surface density of $Cu_xO_yH_z$ entities in the case of 10 Cu-CD/Hap D compound was further proven by the detection in negative polarity of some $Cu_xO_yH_z^-$ secondary ions, namely $Cu_2O_3^-$ (m/z = 174), $HCu_2O_3^-$ (m/z = 175) and $Cu_3O_3^-$ (m/z = 237), which were absent from the ToF-SIMS (-) spectrum of 10 Cu/Hap D sample.

Table 5.8. Secondary ions $Cu_xO_yH_z^+/Ca_2PO_4^+$ and $Ca_wN_tO_y^+/Ca_2PO_4^+$ intensity ratios in 10 Cu/Hap D and 10 Cu-CD/Hap D samples.

$Cu_xO_yH_z^+/Ca_2PO_4^+$ intensity ratios	Sample		$Ca_vNO_z^+/Ca_2PO_4^+$ intensity ratios	Sample	
	10 Cu/Hap D	10 Cu-CD/Hap D		10 Cu/Hap D	10 Cu-CD/Hap D
$Cu^+/Ca_2PO_4^+$	2.72E-01	9.14E-01	$CaNO_2^+/Ca_2PO_4^+$	1.30E-01	0.58E-01
$Cu_2^+/Ca_2PO_4^+$	0.35E-02	1.36E-02	$CaNO_3^+/Ca_2PO_4^+$	8.23E-02	3.67E-02
$Cu_2H^+/Ca_2PO_4^+$	3.15E-03	8.59E-03	$Ca_2NO_3^+/Ca_2PO_4^+$	7.98E-03	*
$Cu_3^+/Ca_2PO_4^+$	0.76E-03	3.25E-03	$Ca_2NO_4^+/Ca_2PO_4^+$	7.01E-03	*
$Cu_2O^+/Ca_2PO_4^+$	0.76E-02	2.64E-02			
$Cu_3O^+/Ca_2PO_4^+$	0.77E-02	3.02E-02			
$Cu_3O_2^+/Ca_2PO_4^+$	0.47E-03	1.73E-03			
$Cu_4O_2^+/Ca_2PO_4^+$	1.09E-03	4.26E-03			
$Cu_5O_2^+/Ca_2PO_4^+$	0.75E-03	2.18E-03			
$Cu_5O_3^+/Ca_2PO_4^+$	2.43E-04	6.77E-04			
$Cu_6O_3^+/Ca_2PO_4^+$	1.48E-04	5.04E-04			
$Cu_2OH^+/Ca_2PO_4^+$	1.43E-02	3.80E-02			
$Cu_3O_2H^+/Ca_2PO_4^+$	0.56E-03	1.82E-03			

*: $Ca_wN_tO_y^+$ fragment ion not present

On another note, when discussing the ToF-SIMS results of the 10 Cu/Hap D compound in the previous section, an observation was made regarding the occurrence of calcium-nitrate interactions. These latter were also present in 10 Cu-CD/Hap D solid, as revealed by its ToF-SIMS (+) spectrum in which $Ca_vNO_z^+$ secondary ions are detected. However, as can be perceived from the results reported in Table 5.8, the intensity ratios of $Ca_vNO_z^+/Ca_2PO_4^+$ secondary ions peaks are higher in the case of 10 Cu/Hap D compound when compared to those of 10 Cu-CD/Hap D, with even certain $Ca_vNO_z^+$ secondary ions being absent from the ToF-SIMS (+) spectrum of 10 Cu-CD/Hap D sample. This evidently indicates a higher tendency for calcium-nitrate interactions to take place within 10 Cu/Hap D solid. Such a tendency could be explained by β-CD acting as a chemical spacer between copper nitrate precursor and hydroxyapatite support, preventing thus close interaction between nitrate entities and calcium cations which would subsequently account for the lesser amount of residual nitrates present in calcined 10 Cu-CD/Hap compared to calcined 10 Cu/Hap material (refer to chapter IV).

Finally, a semi-quantitative study was conducted by using TOF-SIMS technique in order to investigate the evolution of the Ca^+/P^+ ratio when going from pure hydroxyapatite support, i.e. Hap sample, to copper impregnated on Hap, i.e. 10 Cu/Hap D, to finally a copper-cyclodextrin mixture impregnated on Hap support, i.e. 10 Cu-CD/Hap D. The results of this study are represented in Figure 5.16. A Ca^+/P^+ ratio of 18 was found for pure Hap support. In the case of 10 Cu/Hap D sample, this ratio manifests a remarkable increase, reaching a value of 31. A previous work examining hydroxyapatite material, carried out by Silvester *et al.* [59], indicated a higher exposure of Ca^{2+} ions to the surface. Therefore, when copper is added to the Hap support (10 Cu/Hap D) such a calcium surface enrichment would facilitate a copper-calcium cation exchange causing a further enrichment of the topmost surface with calcium ions and hence leading towards the noted increase of the Ca^+/P^+ ratio value when going from pure Hap support to 10 Cu/Hap D compound. On the contrary, when it comes to 10 Cu-CD/Hap D, the Ca^+/P^+ ratio displays a pronounced decrease compared to pure Hap, with a value of 10. A combination of two factors could account for this decline in the value of the Ca^+/P^+ ratio. The first being that the presence of β-CD acts as a separating agent between copper entities and hydroxyapatite support which would hinder the ion exchange process between copper and calcium cations and thus prevent a calcium surface enrichment. The second factor likely to be responsible for the decrease in the Ca^+/P^+ ratio is the formation of bonds involving calcium ions and β-cyclodextrin molecules as signaled by the detection of Ca-organic secondary ions (Table 5.7).

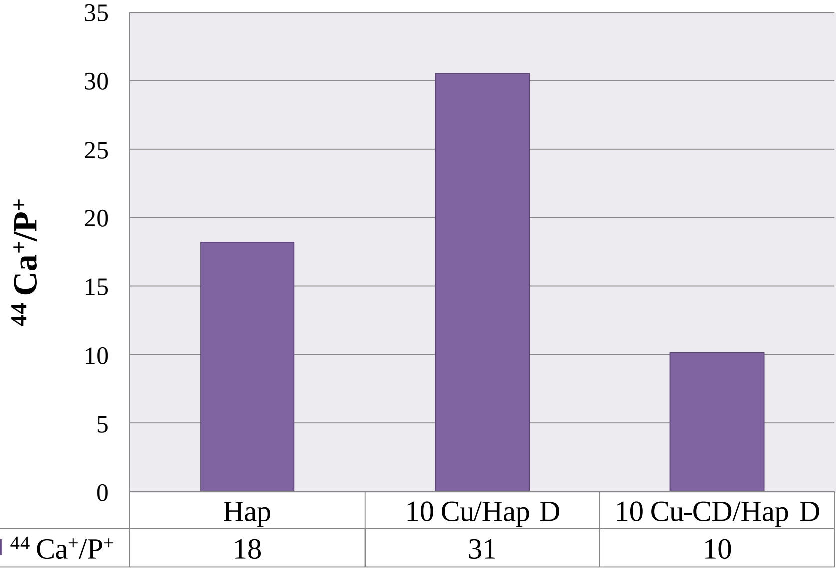

Figure 5.16. Ca^+/P^+ ratio for Hap, 10 Cu/Hap D and 10 Cu-CD/Hap D samples.

5.4. Discussion

Based on all the above acquired data, schemes of the evolution of both Cu-CD/Hap and Cu/Hap systems during the synthesis process from beginning (where the starting materials are mixed) to end (where the desired catalyst is obtained) are proposed in Figure 5.17. Scheme (a) shows the formation of Cu-CD supramolecular adducts, in which complexes between copper ions and β-CD molecules occur, via electrostatic interactions involving the hydroxyl functions of β-CD.

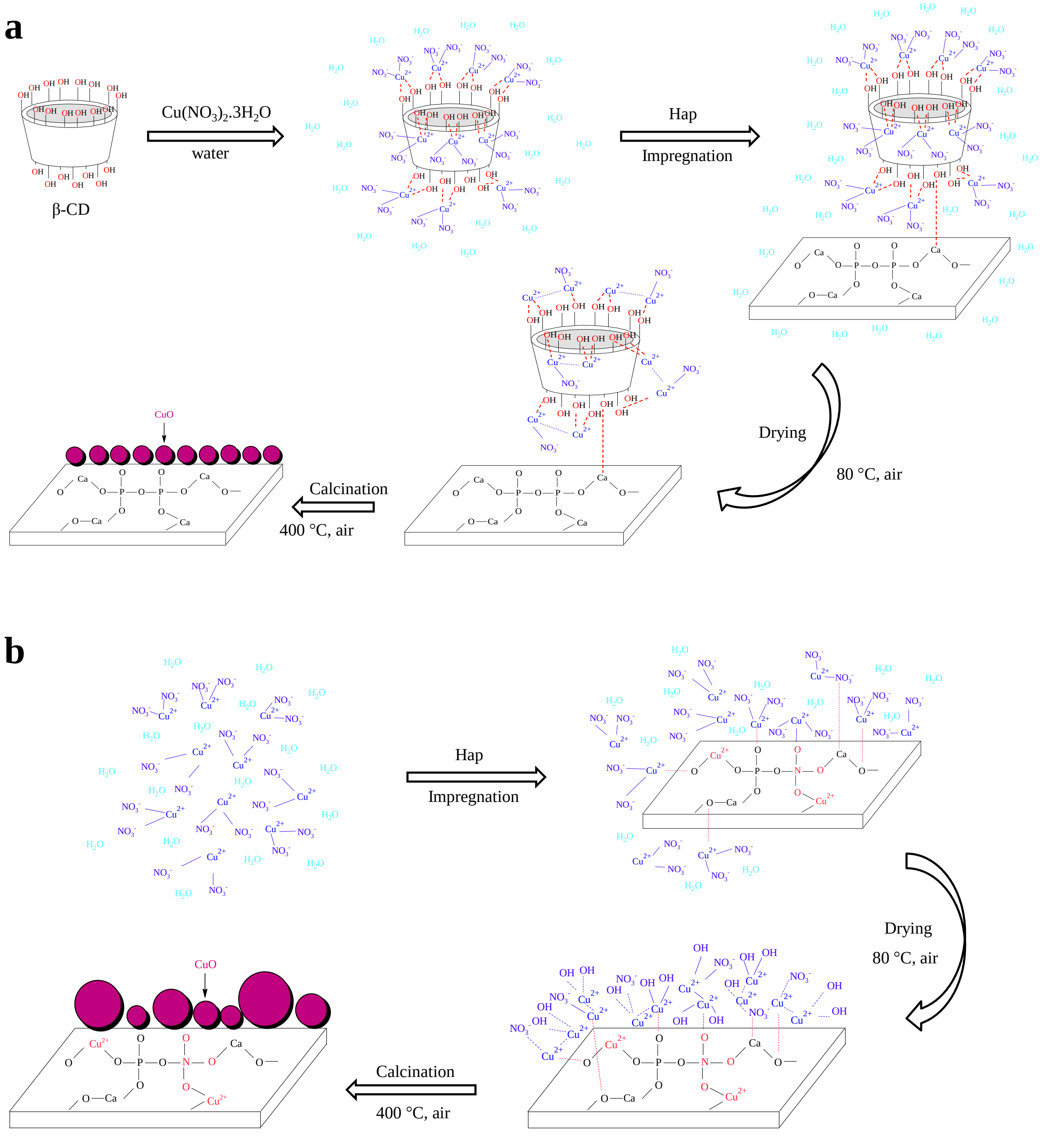

Figure 5.17. Schematic illustration of the creation of copper oxide particles with a) and without b) the assistance of β-CD.

These molecule-ion associations noted when β-CD aqueous solution and copper nitrate trihydrate precursor are brought into contact, remain in place when the hydroxyapatite support is added to the Cu-CD mixture. Nonetheless, additional interactions, involving this time hydroxyapatite's Ca^{2+} cations and β-CD's hydroxyl functions, arise. Through these double interactions taking place between β-cyclodextrin and copper entities on the one hand, and between the oligosaccharide and Hap support on the other, not only does the risk of particle aggregation decrease by preventing the interactions of copper ions together, but the direct interaction between copper precursors and hydroxyapatite support is reduced as well. The latter both diminishes the strong retention of nitrate anions within the lattice of Hap support and hinders the occurrence of surface copper-calcium cation exchange process, promoting thus a higher surface density of copper entities.

Following the calcinations step, the oligosaccharides are eliminated. However, the stable complexes they had created with copper ions result in a deceleration in the copper oxide nucleation rate, leading towards higher dispersion, availability, and reducibility of the formed CuO species compared to the catalyst obtained without the assistance of β-CD (Figure 5.17-b).

5.5. Conclusion

The main objective of this chapter was to achieve a better understanding of the role of β-CD in the Cu-CD/Hap system. With this purpose in mind, Raman and ToF-SIMS analyses were conducted at various stages of the catalyst preparation. A Raman study of the effect of Cu concentration and of β-CD/Cu molar ratio value evidenced the occurrence of interactions involving β-CD molecules and Cu^{2+} ions, which resulted, after the thermal decomposition of the complexing agent during the calcination step, in an enhanced copper dispersion on the surface of hydroxyapatite support. On the other hand, ToF-SIMS analysis indicated the formation of Ca-organic ion-fragments within dried 10 Cu-CD/Hap system, signaling interactions taking place between β-cyclodextrin molecules and calcium ions of hydroxyapatite. Such interactions obstructed both calcium ions substitution with Cu^{2+} and strong nitrate species retention within the Hap supported material. Thus, the data collected from both Raman and ToF-SIMS monitoring, allowed for a first outline of the gradual progression of the Cu-CD/Hap system during the catalyst synthesis procedure to be put forward in this work.

References

[1] L. X. Song, J. Yang, L. Bai, F. Y. Du, J. Chen, and M. Wang, « Molecule-ion interaction and its effect on electrostatic interaction in the system of copper chloride and β-cyclodextrin », *Inorg. Chem.*, vol. 50, n° 5, p. 1682–1688, 2011.

[2] M. Moskovits and K. H. Michaelian, « A reinvestigation of the Raman spectrum of water », *J. Chem. Phys.*, vol. 69, n° 6, p. 2306–2311, 1978.

[3] D. M. Carey and G. M. Korenowski, « Measurement of the Raman spectrum of liquid water », *J. Chem. Phys.*, vol. 108, n° 7, p. 2669–2675, 1998.

[4] R. G. Brown and S. D. Ross, « Forbidden transitions in the infra-red spectra of tetrahedral aniona—VI: Tutton's salts and other double sulphates and selenates », *Spectrochim. Acta Part Mol. Spectrosc.*, vol. 26, n° 4, p. 945–953, 1970.

[5] M. J. Bushiri and V. U. Nayar, « Raman and FTIR spectra of $[Cu(H_2O)_6](BrO_3)_2$ and $[Al(H_2O)_6](BrO_3)_3·3H_2O$ », *Spectrochim. Acta. A. Mol. Biomol. Spectrosc.*, vol. 58, n° 5, p. 899–909, 2002.

[6] P. Rajagopal and G. Aruldhas, « Vibrational spectra of $M_2Cu(SO_4)_2·6H_2OD_2O$ (M= NH_4 or K) », *J. Solid State Chem.*, vol. 80, n° 2, p. 303–307, 1989.

[7] J.-P. Mathieu and M. Lounsbury, « The Raman spectra of metallic nitrates and the structure of concentrated solutions of electrolytes », *Discuss. Faraday Soc.*, vol. 9, p. 196–207, 1950.

[8] D. E. Irish and A. R. Davis, « Interactions in aqueous alkali metal nitrate solutions », *Can. J. Chem.*, vol. 46, n° 6, p. 943–951, 1968.

[9] W. Li, B. Lu, A. Sheng, F. Yang, and Z. Wang, « Spectroscopic and theoretical study on inclusion complexation of beta-cyclodextrin with permethrin », *J. Mol. Struct.*, vol. 981, n° 1‑3, p. 194–203, 2010.

[10] L. D. Barron, A. R. Gargaro, Z. Q. Wen, D. D. MacNicol, and C. Butters, « Vibrational Raman optical activity of cyclodextrins », *Tetrahedron Asymmetry*, vol. 1, n° 8, p. 513–516, 1990.

[11] O. Egyed, « Spectroscopic studies on β-cyclodextrin », *Vib. Spectrosc.*, vol. 1, n° 2, p. 225–227, 1990.

[12] A. R. Davis and C. Chong, « Laser Raman study of aqueous copper nitrate solutions », *Inorg. Chem.*, vol. 11, n° 8, p. 1891–1895, 1972.

[13] P. M. Castro and P. W. Jagodzinski, « FTIR and Raman spectra and structure of $Cu(NO_3)^+$ in aqueous solution and acetone », *Spectrochim. Acta Part Mol. Spectrosc.*, vol. 47, n° 12, p. 1707–1720, 1991.

[14] V. Hayez, V. Costa, J. Guillaume, H. Terryn, and A. Hubin, « Micro Raman spectroscopy used for the study of corrosion products on copper alloys: study of the chemical composition of artificial patinas used for restoration purposes », *Analyst*, vol. 130, n° 4, p. 550–556, 2005.

[15] J. R. Ferraro and A. Walker, « Far-Infrared Spectra of Anhydrous Metallic Nitrates », *J. Chem. Phys.*, vol. 42, n° 4, p. 1273–1277, 1965.

[16] C. S. Mangolim, C. Moriwaki, A. C. Nogueira, F. Sato, M. L. Baesso, A. M. Neto, and G. Matioli, « Curcumin–β-cyclodextrin inclusion complex: stability, solubility, characterisation by FT-IR, FT-Raman, X-ray diffraction and photoacoustic spectroscopy, and food application », *Food Chem.*, vol. 153, p. 361–370, 2014.

[17] R. L. Frost, J. Yang, and Z. Ding, « Raman and FTIR spectroscopy of natural oxalates: Implications for the evidence of life on Mars », *Chin. Sci. Bull.*, vol. 48, n° 17, p. 1844–1852, 2003.

[18] R. L. Frost, « Raman spectroscopy of natural oxalates », *Anal. Chim. Acta*, vol. 517, n° 1‑2, p. 207–214, 2004.

[19] M. C. D'Antonio, D. Palacios, L. Coggiola, and E. J. Baran, « Vibrational and electronic spectra of synthetic moolooite », *Spectrochim. Acta. A. Mol. Biomol. Spectrosc.*, vol. 68, n° 3, p. 424–426, 2007.

[20] A. N. Christensen, B. Lebech, N. H. Andersen, and J.-C. Grivel, « The crystal structure of paramagnetic copper (ii) oxalate (CuC_2O_4): formation and thermal decomposition of randomly stacked anisotropic nano-sized crystallites », *Dalton Trans.*, vol. 43, n° 44, p. 16754–16768, 2014.

[21] D. C. Pereira, D. L. A. de Faria, and V. R. Constantino, « Cu^{II} hydroxy salts: characterization of layered compounds by vibrational spectroscopy », *J. Braz. Chem. Soc.*, vol. 17, n° 8, p. 1651–1657, 2006.

[22] J. J. Pagano, S. Thouvenel-Romans, and O. Steinbock, « Compositional analysis of copper–silica precipitation tubes », *Phys. Chem. Chem. Phys.*, vol. 9, n° 1, p. 110–116, 2007.

[23] A. Chaudhary and H. C. Barshilia, « Nanometric multiscale rough $CuO/Cu(OH)_2$ superhydrophobic surfaces prepared by a facile one-step solution-immersion process: transition to superhydrophilicity with oxygen plasma treatment », *J. Phys. Chem. C*, vol. 115, n° 37, p. 18213–18220, 2011.

[24] D. Chlala, J.-M. Giraudon, N. Nuns, M. Labaki, and J.-F. Lamonier, « Highly Active Noble-Metal-Free Copper Hydroxyapatite Catalysts for the Total Oxidation of Toluene », *ChemCatChem*, vol. 9, n° 12, p. 2275–2283, 2017.

[25] R. L. Frost, P. A. Williams, W. Martens, J. T. Kloprogge, and P. Leverett, « Raman spectroscopy of the basic copper phosphate minerals cornetite, libethenite, pseudomalachite, reichenbachite and ludjibaite », *J. Raman Spectrosc.*, vol. 33, n° 4, p. 260–263, 2002.

[26] S. Kharbish, P. Andráš, J. Luptáková, and S. Milovská, « Raman spectra of oriented and non-oriented Cu hydroxy-phosphate minerals: libethenite, cornetite, pseudomalachite, reichenbachite and ludjibaite », *Spectrochim. Acta. A. Mol. Biomol. Spectrosc.*, vol. 130, p. 152–163, 2014.

[27] I.-S. Cho, D. W. Kim, S. Lee, C. H. Kwak, S.-T. Bae, J. H. Noh, S. H. Yoon, H. S. Jung, D.-W. Kim, and K. S. Hong, « Synthesis of Cu_2PO_4OH hierarchical superstructures with photocatalytic activity in visible light », *Adv. Funct. Mater.*, vol. 18, n° 15, p. 2154–2162, 2008.

[28] P. S. Malavi, S. Karmakar, D. Karmakar, A. K. Mishra, H. Bhatt, N. N. Patel, and S. M. Sharma, « High pressure structural and vibrational properties of the spin-gap system $Cu_2PO_4(OH)$ », *J. Phys. Condens. Matter*, vol. 25, n° 4, 10 pages, 2012.

[29] J. Chrzanowski and J. C. Irwin, « Raman scattering from cupric oxide », *Solid State Commun.*, vol. 70, n^o 1, p. 11–14, 1989.

[30] Y. S. Gong, C. Lee, and C. K. Yang, « Atomic force microscopy and Raman spectroscopy studies on the oxidation of Cu thin films », *J. Appl. Phys.*, vol. 77, n^o 10, p. 5422–5425, 1995.

[31] M.-F. Luo, P. Fang, M. He, and Y.-L. Xie, « In situ XRD, Raman, and TPR studies of CuO/Al_2O_3 catalysts for CO oxidation », *J. Mol. Catal. Chem.*, vol. 239, n^o 1‑2, p. 243–248, 2005.

[32] L. Sinatra, A. P. LaGrow, W. Peng, A. R. Kirmani, A. Amassian, H. Idriss, and O. M. Bakr, « A Au/Cu_2O–TiO_2 system for photo-catalytic hydrogen production. A pn-junction effect or a simple case of in situ reduction? », *J. Catal.*, vol. 322, p. 109–117, 2015.

[33] H. Ferreira, G. Poma, D. R. Acosta, J. Barzola-Quiquia, M. Quintana, L. Barreto, and A. Champi, « Laser power influence on Raman spectra of multilayer graphene, multilayer graphene oxide and reduced multilayer graphene oxide », in *J. Phys. Conf. Ser.*, vol. 1143, 8 pages, 2018.

[34] A. Kudelski and B. Pettinger, « Raman study on methanol partial oxidation and oxidative steam reforming over copper », *Surf. Sci.*, vol. 566, p. 1007–1011, 2004.

[35] F. F. M. De Mul, M. H. J. Hottenhuis, P. Bouter, J. Greve, J. Arends, and J. J. Ten Bosch, « Micro-Raman line broadening in synthetic carbonated hydroxyapatite », *J. Dent. Res.*, vol. 65, n^o 3, p. 437–440, 1986.

[36] B. L. Hurley, S. Qiu, and R. G. Buchheit, « Raman spectroscopy characterization of aqueous vanadate species interaction with aluminum alloy 2024-T3 surfaces », *J. Electrochem. Soc.*, vol. 158, n^o 5, p. C125–C131, 2011.

[37] L. Bai, F. Wyrwalski, J.-F. Lamonier, A. Y. Khodakov, E. Monflier, and A. Ponchel, « Effects of β-cyclodextrin introduction to zirconia supported-cobalt oxide catalysts: From molecule-ion associations to complete oxidation of formaldehyde », *Appl. Catal. B Environ.*, vol. 138, p. 381–390, 2013.

[38] I. R. Lewis and H. Edwards, *Handbook of Raman Spectroscopy: From the Research Laboratory to the Process Line*. CRC Press, 2001.

[39] N. C. Andrés, N. L. D'Elía, J. M. Ruso, A. E. Campelo, V. L. Massheimer, and P. V. Messina, « Manipulation of Mg^{2+}–Ca^{2+} switch on the development of bone mimetic hydroxyapatite », *ACS Appl. Mater. Interfaces*, vol. 9, n^o 18, p. 15698–15710, 2017.

[40] D. Predoi, S. L. Iconaru, A. Deniaud, M. Chevallet, I. Michaud-Soret, N. Buton, and A. M. Prodan, « Textural, structural and biological evaluation of hydroxyapatite doped with zinc at low concentrations », *Materials*, vol. 10, n^o 3, p. 229–245, 2017.

[41] S. Dasgupta, S. S. Banerjee, A. Bandyopadhyay, and S. Bose, « Zn-and Mg-doped hydroxyapatite nanoparticles for controlled release of protein », *Langmuir*, vol. 26, n^o 7, p. 4958–4964, 2010.

[42] C. S. Ciobanu, F. Massuyeau, L. V. Constantin, and D. Predoi, « Structural and physical properties of antibacterial Ag-doped nano-hydroxyapatite synthesized at 100 °C », *Nanoscale Res. Lett.*, vol. 6, n^o 1, p. 1–8, 2011.

[43] C. S. Ciobanu, C. L. Popa, and D. Predoi, « Cerium-doped hydroxyapatite nanoparticles synthesized by the co-precipitation method », *J. Serb. Chem. Soc.*, vol. 81, n^{o} 4, p. 433–446, 2016.

[44] C. S. Ciobanu, S. L. Iconaru, F. Massuyeau, L. V. Constantin, A. Costescu, and D. Predoi, « Synthesis, structure, and luminescent properties of europium-doped hydroxyapatite nanocrystalline powders », *J. Nanomater.*, vol. 2012, 9 pages, 2012.

[45] R. B. Unabia, S. Bonebeau, R. T. Candidato Jr, J. Jouin, O. Noguera, and L. Pawłowski, « Investigation on the structural and microstructural properties of copper-doped hydroxyapatite coatings deposited using solution precursor plasma spraying », *J. Eur. Ceram. Soc.*, vol. 39, n^{o} 14, p. 4255–4263, 2019.

[46] L. Debbichi, M. C. Marco de Lucas, J. F. Pierson, and P. Kruger, « Vibrational properties of CuO and Cu_4O_3 from first-principles calculations, and Raman and infrared spectroscopy », *J. Phys. Chem. C*, vol. 116, n^{o} 18, p. 10232–10237, 2012.

[47] A. P. Litvinchuk, A. Möller, L. Debbichi, P. Krüger, M. N. Iliev, and M. M. Gospodinov, « Second-order Raman scattering in CuO », *J. Phys. Condens. Matter*, vol. 25, n^{o} 10, p. 105402–105406, 2013.

[48] H. F. Goldstein, D. Kim, Y. Y. Peter, L. C. Bourne, J. P. Chaminade, and L. Nganga, « Raman study of CuO single crystals », *Phys. Rev. B*, vol. 41, n^{o} 10, p. 7192–7194, 1990.

[49] J. F. Xu, W. Ji, Z. X. Shen, W. S. Li, S. H. Tang, X. R. Ye, D. Z. Jia, and X. Q. Xin, « Raman spectra of CuO nanocrystals », *J. Raman Spectrosc.*, vol. 30, n^{o} 5, p. 413–415, 1999.

[50] T. Uyar, R. Havelund, J. Hacaloglu, X. Zhou, F. Besenbacher, and P. Kingshott, « The formation and characterization of cyclodextrin functionalized polystyrene nanofibers produced by electrospinning », *Nanotechnology*, vol. 20, n^{o} 12, p. 125605–125618, 2009.

[51] R. Frański, B. Gierczyk, G. Schroeder, S. Beck, A. Springer, and M. Linscheid, « Mass spectrometric decompositions of cationized β-cyclodextrin », *Carbohydr. Res.*, vol. 340, n^{o} 8, p. 1567–1572, 2005.

[52] L. Rabara, M. Aranyosiova, and D. Velic, « Supramolecular host–guest complexes based on cyclodextrin–diphenylhexatriene », *Appl. Surf. Sci.*, vol. 252, n^{o} 19, p. 7000–7002, 2006.

[53] T. Uyar, R. Havelund, Y. Nur, A. Balan, J. Hacaloglu, L. Toppare, F. Besenbacher, and P. Kingshott, « Cyclodextrin functionalized poly(methyl methacrylate) (PMMA) electrospun nanofibers for organic vapors waste treatment », *J. Membr. Sci.*, vol. 365, n^{o} 1‑2, p. 409–417, 2010.

[54] M. Ibrahim, M. Labaki, N. Nuns, J.-M. Giraudon, and J.-F. Lamonier, « Cu-Mn Hydroxyapatite Materials for Toluene Total Oxidation », *ChemCatChem*, vol. 12, n^{o} 2, p. 550–560, 2020.

[55] D. Chlala, A. Griboval-Constant, N. Nuns, J.-M. Giraudon, M. Labaki, and J.-F. Lamonier, « Effect of Mn loading onto hydroxyapatite supported Mn catalysts for toluene removal: Contribution of PCA assisted ToF-SIMS », *Catal. Today*, vol. 307, p. 41–47, 2018.

[56] V. F. Taylor, R. E. March, H. P. Longerich, and C. J. Stadey, « A mass spectrometric study of glucose, sucrose, and fructose using an inductively coupled plasma and electrospray ionization », *Int. J. Mass Spectrom.*, vol. 243, n^{o} 1, p. 71–84, 2005.

[57] X. Xiao, R. Liu, C. Qiu, D. Zhu, and F. Liu, « Biomimetic synthesis of micrometer spherical hydroxyapatite with β-cyclodextrin as template », *Mater. Sci. Eng. C*, vol. 29, n° 3, p. 785–790, 2009.

[58] Y. Cai, M. A. Tarr, G. Xu, T. Yalcin, and R. B. Cole, « Dication induced stabilization of gas-phase ternary beta-cyclodextrin inclusion complexes observed by electrospray mass spectrometry », *J. Am. Soc. Mass Spectrom.*, vol. 14, n° 5, p. 449–459, 2003.

[59] L. Silvester, J.-F. Lamonier, R.-N. Vannier, C. Lamonier, M. Capron, A.-S. Mamede, F. Pourpoint, A. Gervasini, and F. Dumeignil, "Structural, textural and acid–base properties of carbonate-containing hydroxyapatites," *J. Mater. Chem. A*, vol. 2, no. 29, p. 11073–11090, 2014.

Chapter VI: Hydroxyapatite-supported manganese oxide catalysts: Mn speciation study.

6.1. Introduction

The term 'speciation' has been frequently employed to designate the analytical activity of distinguishing chemical species and evaluating their distribution in a specific sample or matrix [1]. Chemical speciation can also be described as a method of establishing and identifying particular chemical species or binding forms which would permit to determine the mobility and reactivity of metals, so as to understand their chemical conduct in the course of a studied reaction.

Mn speciation study in the case of the manganese-based catalysts is very important. Indeed, knowledge of the distribution of each speciation form of a chemical element is often more essential than the determination of its total amount. This is especially true in the case of supported catalysts where the final location and speciation of the metal species can have a very powerful impact on the overall catalytic performances.

When it comes to hydroxyapatite-supported manganese oxide catalysts, the task of discerning the valence state and location of the Mn species becomes much more difficult due to the extreme compositional flexibility of Hap support: as has been explained in the literature survey chapter, the hydroxyapatite crystal lattice is susceptible to undergoing ion exchange mechanisms, during which metal ions can be incorporated into Hap structure by substituting Ca^{2+} ions, for example. Thus, the determination of manganese speciation under these conditions grows more complex. Nonetheless, identification of the nature of active sites, with emphasis on the valence state of Mn species, remains fundamental, seeing as it could constitute a means of overcoming the drawbacks which currently limit the effective use of Mn/Hap materials (e.g. poor durability conduct).

Consequently, the speciation of Mn species in Mn/Hap samples was investigated. More precisely, this study will deal with the effects of manganese loading in manganese oxide supported on hydroxyapatite materials, on the manganese speciation in the resulting sample: 2.5; 5; 10; and 20 wt% Mn/Hap. However, in order to have a set of reference data on the basis of which it would become possible to interpret the results obtained from the analysis of the Mn/Hap catalyst compounds, a series of manganese oxide standards, characterized by different Mn oxidation states, were prepared and analyzed as well. These manganese oxide reference solids were: ε-MnO_2, β-MnO_2, Mn_5O_8, Mn_2O_3, γ-MnOOH, Mn_3O_4, and MnO. The techniques that were used to provide information on the chemical speciation of manganese-bearing compounds were XRD, Raman, XAS, H_2-TPR, and XPS.

6.2. XRD analysis

6.2.1. XRD analysis of reference compounds

XRD patterns of manganese oxide reference compounds are given in Figure 6.1. The X-ray diffractogram represented in Figure 6.1-a indicates that no pure phase of hexagonal ε-MnO_2 (PDF n ° 89-5171, P63/mmc) was obtained in the case of the synthesized ε-MnO_2 sample. In fact, small fractions of Mn_3O_4 and La_2MnO_4 can be detected in the obtained product, with the akhtenskite manganese dioxide (ε-MnO_2) phase forming, nonetheless, the majority of the reference compound as shown by a calculation based on the Reference Intensity Ratio (RIR) quantitative analysis method, using the I/Icor ratio values provided in the PDF cards of the crystalline phases. It should be noted that the La_2MnO_4 phase, discerned presently, is derived from the perovskite $LaMnO_3$ precursor used in the synthesis procedure, which following an acid treatment yielded the desired ε-MnO_2 phase.

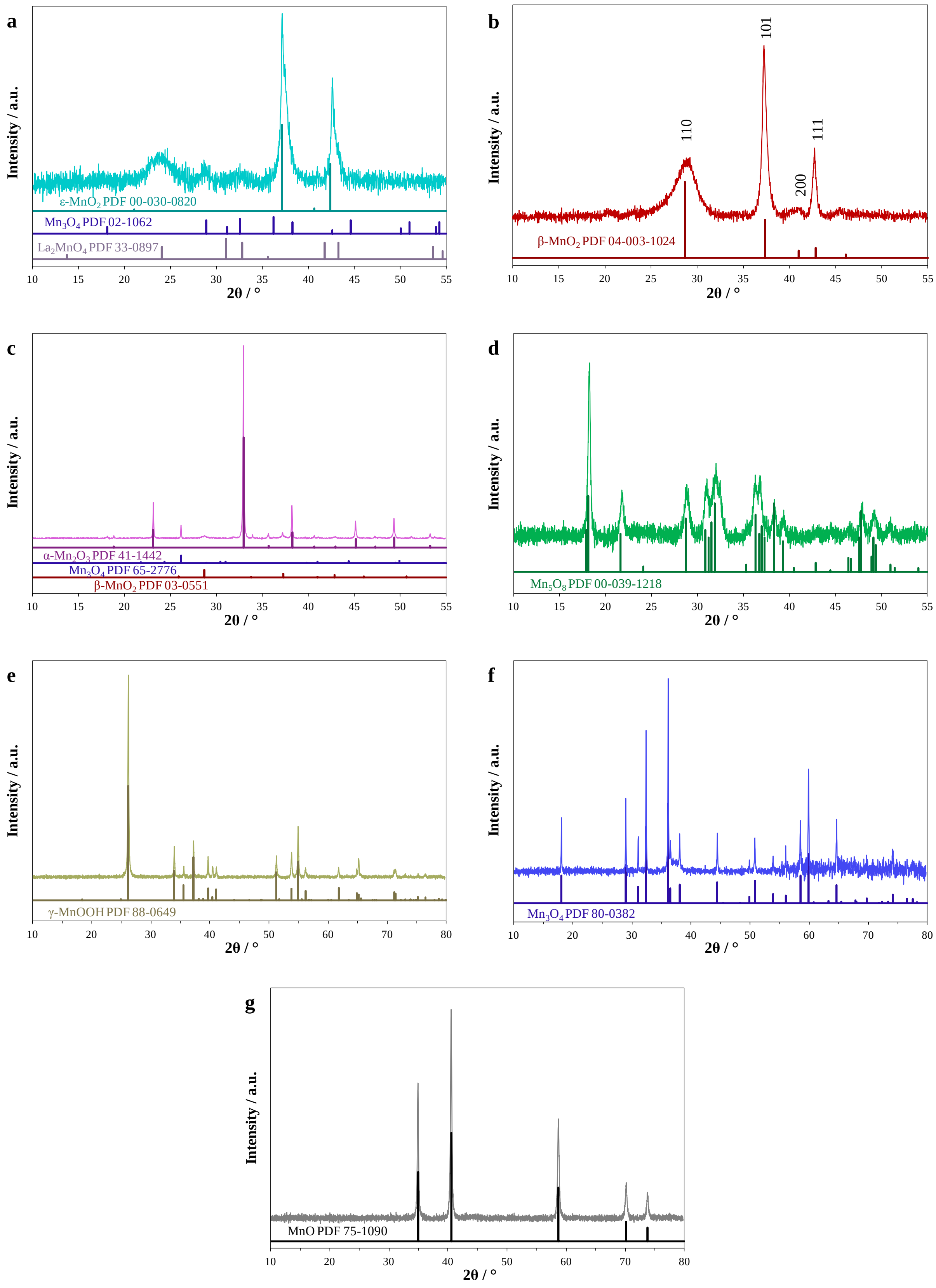

Figure 6.1. XRD patterns of a) ε-MnO_2, b) β-MnO_2, c) Mn_2O_3, d) Mn_5O_8, e) γ-MnOOH, f) Mn_3O_4 and g) MnO reference compounds.

Figure 6.1-b shows the XRD patterns of the prepared β-MnO_2 material. It clearly demonstrates the presence of pure pyrolusite β-MnO_2 (PDF n ° 04-003-1024) phase in this material. However, it should be noted, that the relative intensity of the peak at 2θ = 37.4 °, corresponding to the (101) plane, is much stronger than that of the standard PDF card, whereas in the case of the peak at 2θ = 28.7 °, corresponding to the (110) plane, it is the opposite. Seeing as the relative intensities of the other diffraction peaks are basically comparable to those of the standard PDF card, the previous observation seems to suggest that the prepared β-MnO_2 sample has a preferred crystal orientation along the (101) plane [2].

Commercially obtained Mn_2O_3 reference compound (Figure 6.1-c) reveals traces of Mn_3O_4 and β-MnO_2 along with the predominant phase bixbyite, α-Mn_2O_3 (PDF n ° 41-1442).

On the contrary, regarding Mn_5O_8, γ-MnOOH, Mn_3O_4 and MnO compounds, all peaks present in their XRD patterns can be indexed to pure Mn_5O_8 (Figure 6.1-d), γ-MnOOH (Figure 6.1-e), Mn_3O_4 (Figure 6.1-f) and MnO (Figure 6.1-g) phases, respectively.

Accordingly, it appears that each manganese oxide reference compound is in full accord with its corresponding manganese oxide crystalline phase, indicating thus the successful synthesis of the desired reference products.

6.2.2. XRD analysis of Mn/Hap catalysts

The powder X-ray diffraction patterns of x Mn/Hap catalysts (with x = 2.5; 5; 10; and 20%) are given in Figure 6.2.

The diffractograms of the supported manganese catalysts exhibit differences related with the manganese loading within the catalyst. Indeed, for an amount of manganese lower than 10 wt%, the only crystalline phase which can be detected is that of the hydroxyapatite support, $Ca_5(PO_4)_3(OH)$ (PDF n ° 00-009-0432). However, when the Mn loading reaches 10 wt%, an additional peak appears on the X-ray diffractogram of the 10 Mn/Hap samples at 2θ = 37.1 °. This peak can be attributed to either ε-MnO_2 or β-MnO_2 crystalline phase. At this point it is difficult to ascertain which, seeing as the most intense peak of the pyrolusite (β-MnO_2) phase appears at 2θ = 28.7 ° and might thus be difficult to distinguish in the midst of the two overlapping peaks attributed to the hydroxyapatite phase observed at 2θ = 28.1 ° and 2θ = 29.0 °. When the Mn amount increases to 20 wt%, not only can an increase in the intensity of the peak positioned at 2θ = 37.1 ° be noted, but also the Hap characteristic peak located at 2θ = 42.1 ° presents a well defined shoulder at 2θ = 42.6 °. This latter can be once again ascribed to either ε-MnO_2 or β-MnO_2. While no distinct shoulder characteristic of the pyrolusite phase can be detected at 2θ = 28.7 °, the presence of β-MnO_2 cannot be excluded. Indeed, similarly to what was indicated when examining the XRD pattern of pure β-MnO_2 (Figure 6.1-b), the formed pyrolusite phase in the case of the Mn/Hap catalysts might also have a preferred crystal orientation along the (101) plane which could result in the peak corresponding to the (110) plane, at 2θ = 28.7 °, being less intense and broader than what can be expected, thus more easily concealed by the Hap two overlapping peaks at 2θ = 28.1 ° and 2θ = 29.0 °. This precludes discriminating ε-MnO_2 from β-MnO_2 phase at this stage. However, it can be established that an increase in the crystallinity of the MnO_2 phase, previously detected when examining the XRD pattern of 10 Mn/Hap, occurs in 20 Mn/Hap sample.

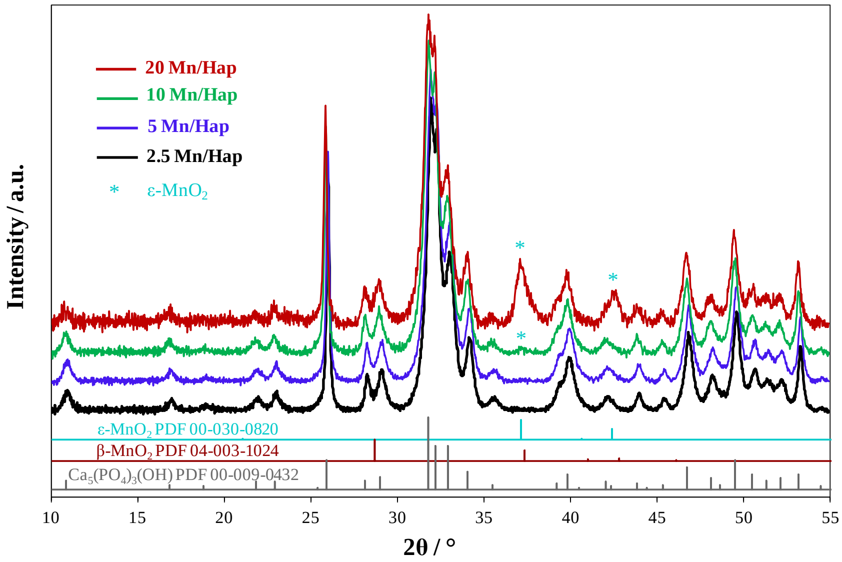

Figure 6.2. XRD patterns of x Mn/Hap catalysts (with x = 2.5; 5; 10; and 20 wt%).

6.3. Raman analysis

To verify the XRD results, Raman analysis was also carried out for both reference compounds and Mn/Hap catalysts, with the resulting Raman spectra given in Figures 6.3 and 6.4, respectively.

6.3.1. Raman analysis of reference compounds

Figure 6.3-a shows a peak at 632 cm^{-1} for the ε-MnO_2 synthesized material, corresponding to the Mn-O stretching mode characteristic of this manganese dioxide polymorph [3], [4]. The Raman spectra displayed in Figure 6.3-b, obtained for the prepared β-MnO_2 sample, reveals three discernible bands peaks at 527, 570, and 657 cm^{-1}, along with weaker bands centered at 273, 366, 391, 479, and 756 cm^{-1}. These results are not consistent with the characteristic Raman shifts of the pyrolusite (β-MnO_2) phase, but are rather in line with those of another MnO_2 polymorph which is nsutite, γ-MnO_2 [5]–[7]. The structure of γ-MnO_2 has been described as a disordered intergrowth of ramsdellite (R-MnO_2) and pyrolusite (β-MnO_2) structures, with the spectrum of γ-MnO_2 being in fact formed by a superposition of the contributions of the two different crystal forms of MnO_2 [8], [9]. This phase evolution of the manganese dioxide from the original β-MnO_2 phase might be caused by the Raman laser beam. Indeed, manganese compounds have been reported as being particularly unstable during Raman analysis due to a noted tendency for degradation following laser impact [10], [11]. Therefore, even the adopted precaution of using the lowest laser power during the analysis, might not be enough to prevent some structure modification within the sample.

In the case of Mn_5O_8 solid, the Raman spectrum observed in Figure 6.3-c manifests 10 Raman bands at 169, 261, 299, 393, 431, 477, 533, 577, 617, and 645 cm^{-1}, in good agreement with literature data for Mn_5O_8 powders [12], [13]. Moreover, in these 10 Raman bands detected in the spectrum of metastable Mn_5O_8 compound, none could be attributed to Mn_3O_4 phase whose main peaks are positioned at 290, 320, 380, and 660 cm^{-1} [14], [15], which precludes any potential presence of this impurity in the Mn_5O_8 solid, in accordance with the previously exposed XRD results.

Regarding the trivalent manganese compounds, on one hand the Raman spectrum of Mn_2O_3 solid shows three main peaks at 170, 261, and 651 cm^{-1} (Figure 6.3-d), in agreement with literature reference values for bulk Mn_2O_3 [16], [17]. On the other hand, for hydrothermally synthesized γ-

MnOOH, nine Raman-active modes are identified at 140, 213, 251, 277, 352, 381, 523, 551, and 617 cm^{-1}, which coincide well with former studies carried out on monoclinic γ-MnOOH products [18], [19].

Concerning the Raman spectrum of multivalent Mn_3O_4 compound, the peaks noted at 303, 370, 506, 572, and 645 cm^{-1} do no concord with the Raman band positions typical of Mn_3O_4 crystal phase, usually observed at 290, 320, 380, and 660 cm^{-1} [14], [15]. In fact, the currently detected peaks are more in line with a birnessite-type MnO_2 (δ-MnO_2): the peak positioned at 506 cm^{-1} could be ascribed to the stretching vibration of Mn–O–Mn, while the Raman band located at 572 cm^{-1} could be the result of the ν_3 (Mn–O) stretching vibration generated primarily by Mn^{4+} in the basal plane of the [MnO_6] sheet; and the Raman shift around 645 cm^{-1} can be attributed to the [MnO_6] symmetric ν_2 (Mn–O) stretching vibrations [20], [21]. It is important to mention that birnessite consists of sheets of edge-sharing [MnO_6] octahedra with vacancies, whose resulting negative layer charge is compensated by interlayer cations such as K^+ [22]. Therefore, in order to offer an explanation for the formation of this phase, a quick reminder of the synthesis procedure of Mn_3O_4 ought to be done: Mn_3O_4 was obtained through the heat treatment of a mixture of glycerol and $KMnO_4$; and though a subsequent washing was conducted, it might not have been sufficient to remove all remaining trace of the alkali metal ions (K^+). Yet, if traces of this alkali metal persist, they could, under the impact of the laser beam, be brought to induce a structural change within the sample, modifying the original arrangement of the atoms and leading towards the genesis of this new phase. Besides, the noted results seem to corroborate the hypothesis of remaining K^+ species in the analyzed product seeing as a considerable weakening in the intensity of the peak at 572 cm^{-1} is detected when compared to the intensity of the peak corresponding to the ν_2 stretching vibration, which is suggestive of the presence of a significant amount of K^+ (detected later on during XPS analysis) in the material according to a previous study conducted by Rong *et al.* [22].

It ought to be pointed out that while different hypotheses have been given as to the nature of the compounds perceived in each of β-MnO_2 and Mn_3O_4 solids' Raman spectrum, a great resemblance can be noted between the two individual spectra (Figure 6.3-b and f). In fact, it would seem that despite starting from two different MnO_x materials (β-MnO_2 and Mn_3O_4 were shown to be pure by XRD), β-MnO_2 and Mn_3O_4 samples evolve in a similar way under laser beam exposure. It should be signaled that both Raman spectra of nsutite (γ-MnO_2) and birnessite (δ-MnO_2) display their two most intense lines at ~570 and ~640 cm^{-1}, ascribed to Mn–O stretching vibrations along octahedra chains and Mn–O stretching vibrations along a perpendicular direction to the double chains of [MnO_6] octahedra, respectively, [23] and their Raman signatures have been previously described as presenting much similarities [24]. Nevertheless, the structural differences between the two MnO_2 polymorphs, in which different distortion of [MnO_6] octahedra occur, results in differences in the relative intensity and position of the peaks perceived in nsutite and birnessite. Based on these latter, attributions were proposed for each of β-MnO_2 and Mn_3O_4 solids' Raman spectrum. However, they would require further characterization to be either validated or refuted.

Finally, in the case of divalent MnO compound, the Raman spectrum presented in Figure 6.3-g reveals a single large peak at 645 cm^{-1}, characteristic of the fundamental Mn–O Raman scattering peak of manganosite phase [25]–[27].

To summarize, apart from β-MnO_2 and Mn_3O_4 solids, in which a laser induced transformation is likely to have occurred, the Raman spectra obtained for the other manganese oxide reference compounds reassert what had been previously validated by XRD analysis, which is the successful synthesis of the desired Mn-based standards.

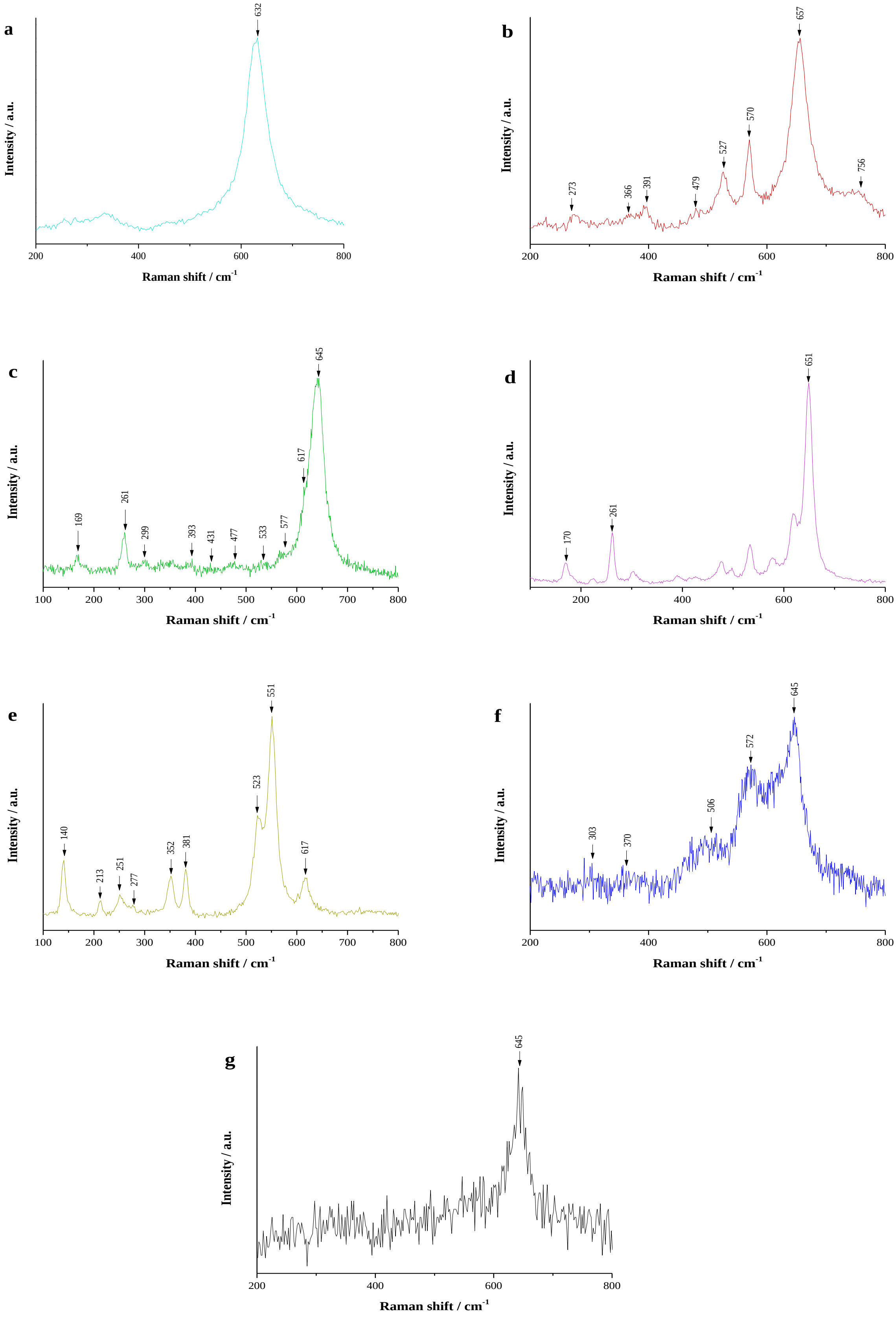

Figure 6.3. Raman spectra of a) ε-MnO_2, b) β-MnO_2, c) Mn_5O_8, d) Mn_2O_3, e) γ-MnOOH, f) Mn_3O_4 and g) MnO reference compounds.

6.3.2. Raman analysis of Mn/Hap catalysts

Similarly to what was optically discerned in the previous chapter regarding the Raman analysis of hydroxyapatite supported copper compounds (10 Cu/Hap and 10 Cu-CD/Hap), an apparent distinction of color can be noted when moving from one area to another (bright and dark zones) but only in the case of 2.5 and 5 Mn/Hap. The results obtained from the analysis of each of these zones for both these compounds are reported in Figure 6.4-a and b.

For 2.5 and 5 Mn/Hap, analysis of the bright zone revealed the characteristic hydroxyapatite-related bands, albeit less well-defined. However, it should be pointed out that the position of the peak ascribed to ν_1 mode of the PO_4^{3-} tetrahedron, usually found at 961 cm^{-1}, has been considerably red shifted by 7 cm^{-1}. This red shift, as has been previously explained, is indicative of lattice expansion and structure distortion within the Hap system. In the current case, it could be the result of ion substitution between the Ca^{2+} cations of Hap support and Mn^{2+} entities, an occurrence reported in several papers [28]–[31]. Furthermore, two additional peaks appear around 650 ± 3 cm^{-1} and 812 ± 2 cm^{-1}, the former can be associated with Mn–O stretching mode of β-MnO_2 [6], [32], while the latter can be attributed to the ν_1 vibrations of MnO_4^{3-} groups [33], [34]. The presence of manganese in the anionic form of $(MnO_4)^{3-}$ could signify a partial substitution of $(PO_4)^{3-}$ groups in the hydroxyapatite matrix. Such an anionic exchange involving MnO_4^{3-} species has been previously observed in a study conducted over Mn-doped hydroxyapatite [31]. Nevertheless, Chadefaux *et al.* [35] report that the formation of Mn^{5+} entities in apatites is very likely to be a heat-induced phenomenon. Hence, it could be that this detected phase is the result of a laser-engendered transformation within the sample, the latter having poor heat dispersion ability.

In the dark zones of 2.5 and 5 Mn/Hap, the bands corresponding to the hydroxyapatite phase become less visible, with mainly the ν_1 phosphate band still clearly defined, yet again red shifted from its expected value (961 cm^{-1}). New peaks appear around 499, 564, and 645 cm^{-1}. It can be remarked that these newly emerged peaks present a similar Raman signature to those noted earlier in the case of both β-MnO_2 and Mn_3O_4 solids, which were believed to have undergone a laser-induced transformation during Raman analysis and evolved into nsutite (γ-MnO_2) and birnessite (δ-MnO_2), respectively. It can also be seen that due to the fact that the manganese oxide species being examined is of a supported rather than bulk nature the detected peaks in the Raman spectra are rather broad and not well defined which makes discrimination between γ- and δ-MnO_2 very difficult. Therefore, it appears that the catalysts may initially contain β-MnO_2 and/or Mn_3O_4. In order to determine which, additional characterization techniques will be subsequently employed.

When the Mn content increases from 5 wt%, no more bright zones can be discerned through visual observation and all collected Raman data for the same sample reveal similar spectra. Thus, only one spectrum is presented for each of 10 Mn/Hap and 20 Mn/Hap catalysts. Both of the illustrated spectra (Figure 6.4-c and d) are comparable with the spectra obtained in the dark zone of the Mn/Hap catalysts with lower Mn loading (2.5 and 5 Mn/Hap), with, however, the peaks associated with manganese oxide phase becoming sharper and better defined, indicating therefore an increase in the crystallinity and particle size of the Mn_xO_y phase (β-MnO_2 and/or Mn_3O_4) [36].

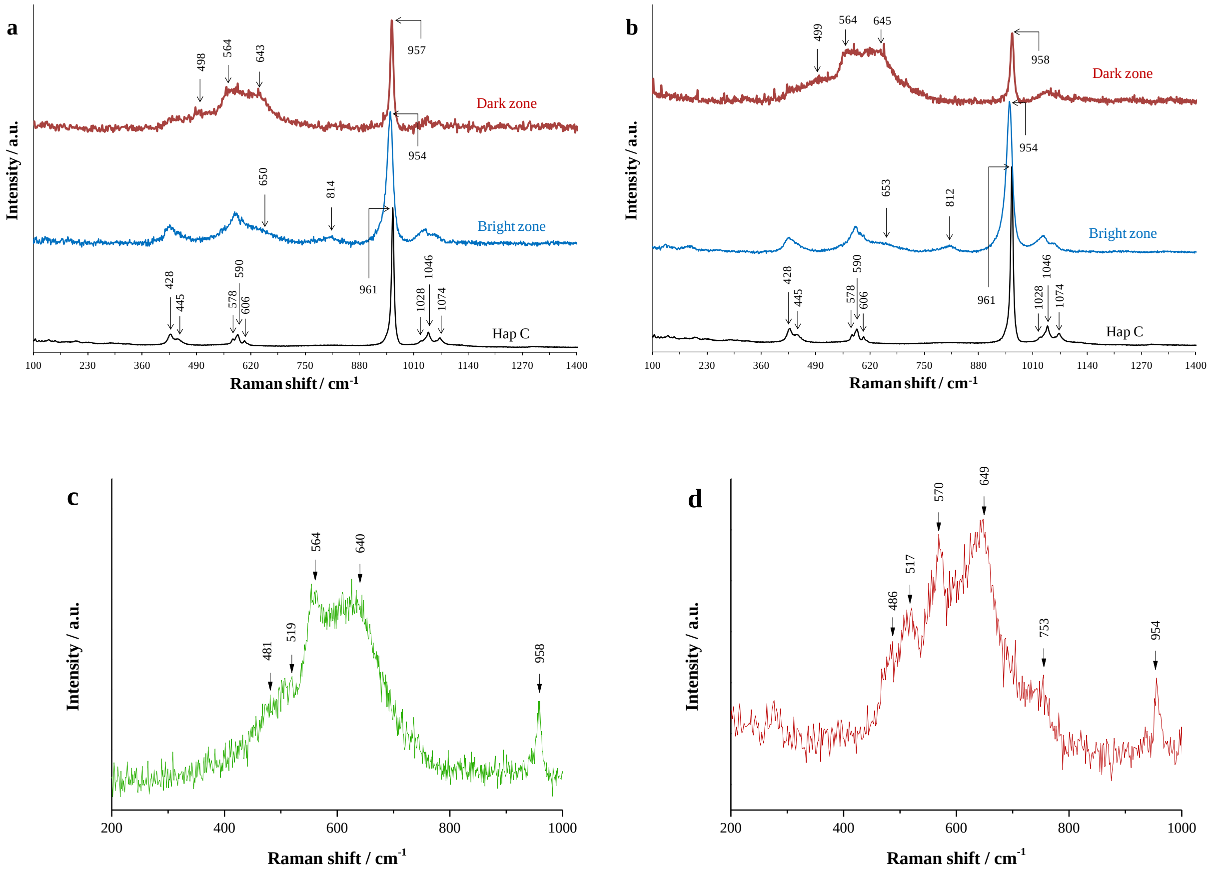

Figure 6.4. Raman spectra of x Mn/Hap catalysts, with x = 2.5 (a); 5 (b); 10 (c) and 20 wt% (d).

6.4. XANES at the Mn-K edge of manganese-bearing samples

6.4.1. Ex situ analysis

X-Ray Absorption Spectroscopy using synchrotron radiation sources is an important tool for investigating the local structures of different materials. Moreover, X-ray Absorption Near Edge Structures (XANES) analysis, covering the range from 0 to roughly 50-100 eV above the absorption edge [37], can provide electronic and structural information on molecules present in crystalline or non-crystalline phases, even at diluted conditions, information which cannot be accessed by other well known structural characterization methods such as XRD.

It is known that Mn oxidation states can vary from 0 to +7. However, among this range of values, the divalent (+2), trivalent (+3) and tetravalent (+4) states are the most commonly encountered valences in chemical compounds. It should be noted though that in a number of Mn bearing phases (such as Mn_3O_4 and Mn_5O_8), several valences of manganese can coexist (+2 and +3 in the case of Mn_3O_4, +2 and +4 in the case of Mn_5O_8).

In the following study, several manganese oxide reference compounds will be examined, with valences going from +2 to +4: β-MnO_2 (Mn^{4+}); Mn_5O_8 (2 Mn^{2+} + 3 Mn^{4+}); γ-MnOOH (Mn^{3+}); Mn_2O_3 (Mn^{3+}); Mn_3O_4 (Mn^{2+} + 2 Mn^{3+}) and MnO (Mn^{2+}).

The Mn K-edge XANES spectra of the references compounds are presented in Figure 6.5. They will be used for subsequent analyses of the average oxidation state of Mn in each examined manganese-based catalyst.

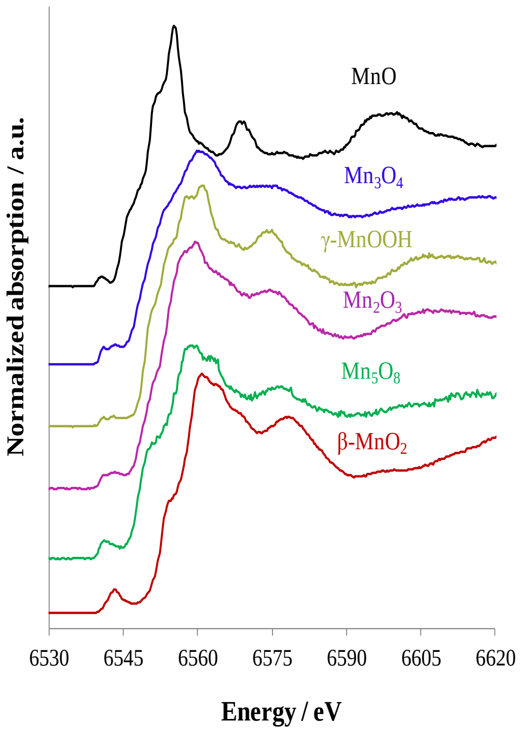

Figure 6.5. Mn-K edge XANES experimental spectra of Mn_xO_y reference compounds measured at a fluorescence detection energy of 6491.5 eV.

Analysis of XANES spectra reported in Figure 6.5 reveals for all studied compounds a weak absorption feature (pre-edge) at ~ 6540-6543 eV, immediately prior to a strong absorption peak (main edge) at ~ 6555-6561 eV. The pre-edge is caused by the dipolar 1s→4p transition, similar to the main edge [38], [39]. This peak is a typical signature of noncentrosymmetric sites. Indeed the absence of center of symmetry (distorted MnO_6 octahedral, Mn tetrahedral symmetry…) makes the odd-even hybridization between the 4p and 3d orbitals possible. This leads to a relatively strong density of p-states at this energy. However some contribution due to quadrupolar transition (1s → 3d) could also occur for the compounds.

Moreover, Figure 6.5 shows clearly an energy shift of the absorption edge which is directly related with the average oxidation state of the absorber atom. Indeed, the more the latter is oxidized, the higher the energy of the absorption edge is, giving thus a direct indication of the absorber atom’s degree of oxidation. It should be noted that the XANES spectra obtained for the reference samples agree with those reported in literature for each of the Mn_xO_y material prepared in this study (Figures AD.1-2-3-4-5). Furthermore, it can be seen that the XANES signature of the reference compounds are quite different from one another. Therefore, these manganese oxide reference compounds can serve as a basis for the identification of the MnO_x phase(s) present in the synthesized x Mn/Hap catalysts (with x = 2.5; 5; 10; and 20 wt%).

However, it should be very well noted that the above analysis has also been a very clear indicator that manganese oxides may have different XANES features even for the same oxidation state and coordination number of Mn, such as Mn_2O_3 and γ-MnOOH (see Figure 6.5), or the different polymorphs of MnO_2 (see Figure AD.5-b and c) for example. Therefore, it might prove difficult to be conclusive about the speciation of Mn in the prepared Mn/Hap samples. Nevertheless, that does not negate the fact that the above XANES spectra will be able to provide qualitative and quasi-quantitative information by which the change in oxidation state when moving from one sample to another can be estimated.

In Figure 6.6 are presented the Mn-K edge XANES spectra of the x Mn/Hap catalysts (with x = 2.5; 5; 10; and 20 wt%). It is apparent that the edge position shifted towards a higher energy value when the weight load of manganese within the sample increased, indicating thus an increase in the oxidation state when going from 2.5 Mn/Hap to 20 Mn/Hap.

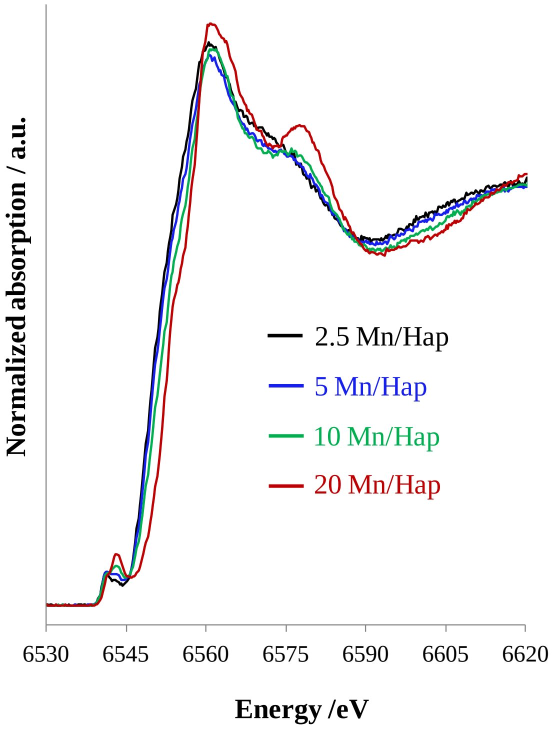

Figure 6.6. Mn-K edge XANES experimental spectra of x Mn/Hap prepared catalysts (with x = 2.5; 5; 10 and 20 wt%) measured at a fluorescence detection energy of 6491.5 eV.

It ought to be stressed out that the XANES spectra of both the Mn/Hap catalysts and Mn_xO_y reference compounds were measured at the same fluorescence detection energy (6491.5 eV) which makes all upcoming comparisons between the two viable.

Starting with the sample with the lowest weight load of Mn (i.e. 2.5 Mn/Hap), a visual comparison of this catalyst XANES spectrum with each of those of the reference compounds (whose spectra were thoroughly discussed above), was first performed (Figure 6.7-a and b). It can be perceived that the spectrum of 2.5 Mn/Hap is very similar to that of Mn_3O_4, as revealed by Figure 6.7-c, showing comparable oscillations at the same energy positions. Hence, a first visual approach seems to indicate the presence of a Mn_3O_4 phase in the 2.5 Mn/Hap sample, which implies a Mn oxidation state of ~ + 2.6 for 2.5 Mn/Hap material.

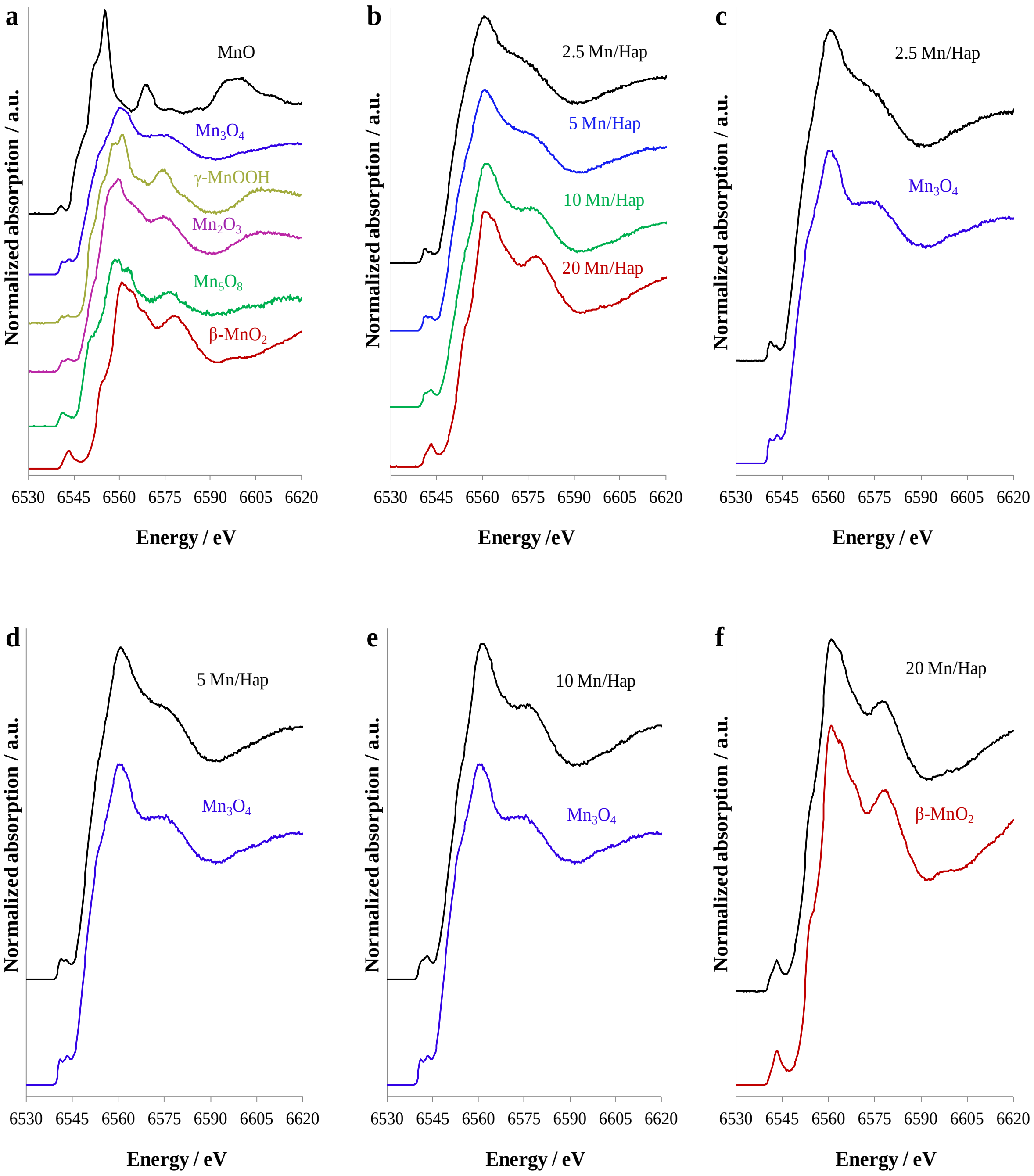

Figure 6.7. Mn-K edge XANES experimental spectra, measured at a fluorescence detection energy of 6491.5 eV, of a) Mn_xO_y reference compounds; b) x Mn/Hap catalysts; c) 2.5 Mn/Hap and Mn_3O_4 compound; d) 5 Mn/Hap and Mn_3O_4 compound; e) 10 Mn/Hap and Mn_3O_4 compound ; f) 20 Mn/Hap and β-MnO_2 compound.

Analogous comparisons were carried out for the remaining Mn/Hap catalysts (Figure 6.7). These comparisons revealed that 5 Mn/Hap and 10 Mn/Hap, just like 2.5 Mn/Hap, present very similar spectra to that of Mn_3O_4, suggesting the presence of this manganese oxide phase within these catalysts and as consequence of an Mn average oxidation state (AOS) of ~ + 2.6. Whereas, in the case of 20 Mn/Hap, its spectrum resembles that of β-MnO_2, manifesting the same oscillations at the same energy positions as those of the tetravalent manganese oxide compound, which hints at the presence of β-MnO_2 phase in the sample with the highest manganese weight load (i.e. 20 Mn/Hap); the latter presenting an average manganese oxidation state of ∼ + 4.

Thus, a first visual inspection of the catalysts XANES spectra indicated that for an Mn weight load ranging between 2.5 and 10%, Mn_3O_4 was the predominant phase, whereas for 20 wt% of Mn, it was β-MnO_2 that was majorily present. In order to refine this initial interpretation, an attempt at a more quantitative approach was performed through the Athena program by the means of a linear XANES combination fitting. Indeed, for these x Mn/Hap catalysts, valence fractions can be derived by conducting linear combination fitting (LCF) analysis in which the spectra of the previously examined manganese oxide reference compounds are used.

The aim of LCF will be to determine if other minority Mn_xO_y species are also present in the prepared catalysts. One possible method for achieving this is to measure all plausible reference compounds and to try fitting a large number of different combinations of the standards to the data. In the following study, the components' weights were constrained to be between 0 and 1; the sum of all components weight fractions was constrained to be equal to 1; and the number of standards used in each fit was limited to four. The quality of the fit is given by the R-factor which is a measure of mean square sum of the misfit at each data point.

For each x Mn/Hap catalyst, the best quality fit along with the experimental spectrum, as well as a plot of the difference between the fit and the data, are given in Figure 6.8 and the values are reported in Table 6.1.

It should be noted that regarding the results of LCF, component fractions less than 10% were determined to be statistically insignificant and were not included in the chosen fit.

In the case of 2.5 Mn/Hap whose spectral signature resembles that of Mn_3O_4, the LCF plot shown in Figure 6.8-a indicates that Mn_2O_3 can be added as a second component to achieve the best fit. No significant gain could be obtained by adding more than these two components (Mn_3O_4 and Mn_2O_3) to the fit (Figure AD.6; Table AD.1), suggesting thus the presence of Mn_3O_4 and Mn_2O_3 phases in the relative weight fractions of 66 and 34%, respectively. However, it is also apparent that this chosen fit fails to reproduce completely all the experimental XANES features of the catalyst (in the pre-edge as well as the post-edge region). Therefore, different hypotheses are possible: a) the presence of an additional Mn_xO_y phase whose XANES spectrum hasn't been collected when examining bulk manganese oxide reference samples; b) the insertion of the added Mn into the Hap structure. Indeed, seeing as the hydroxyapatite support has the ability to substitute its calcium cations with other transition metals by an ion exchange mechanism, an incorporation of manganese into Hap, in the form of Mn^{2+}, can occur at the apatite surface [28], [40]. However, it should be reminded that there are two nonequivalent types of calcium sites: columnar Ca_I ions which are nine-fold coordinated and triangular Ca_{II} ions which are seven-fold coordinated. DFT calculations reported in previous works indicated that the Ca_{II} site is the most energetically favorable site for Mn^{2+} substitutions [28], [41]. Moreover, in a very recent publication, Oliveira *et al.* [42] demonstrated by using X-ray difference Fourier maps that the insertion of Mn into the hydroxyapatite structure occurs preferentially in Ca_{II} sites, In any case, the incorporation of Mn^{2+} leads to appreciable structural deformations associated with the shortening of Mn-O distances compared to Ca-O bonds, resulting in Mn^{2+} ions having distorted octahedral site symmetry [43], [44]. Raman results which were discussed above seem to indicate the occurrence of such cation exchange between Mn^{2+} and Ca^{2+}. Therefore, it can be assumed that the divergence between the fit and the experimental data in certain parts of the spectrum might be due to the presence of Mn inserted within the hydroxyapatite structure. However, it should be noted that the main edge position of 2.5 Mn/Hap is similar to that of Mn_3O_4 (Mn AOS of ~ + 2.6), but is at a higher energy than MnO (Mn AOS of ~ + 2). Furthermore, the spectral features of the XANES spectrum of 2.5 Mn/Hap are more in accordance with those of Mn_3O_4 (Mn^{2+} in tetrahedral sites and Mn^{3+} in octahedral positions [45]) rather than MnO (Mn^{2+} in octahedral symmetry) compound. Given that the energy position of the main edge and shape of the XANES spectrum are function of Mn oxidation state and its coordinating environment, the concomitant presence of Mn_3O_4 and Mn inserted in Hap structure is highly probable.

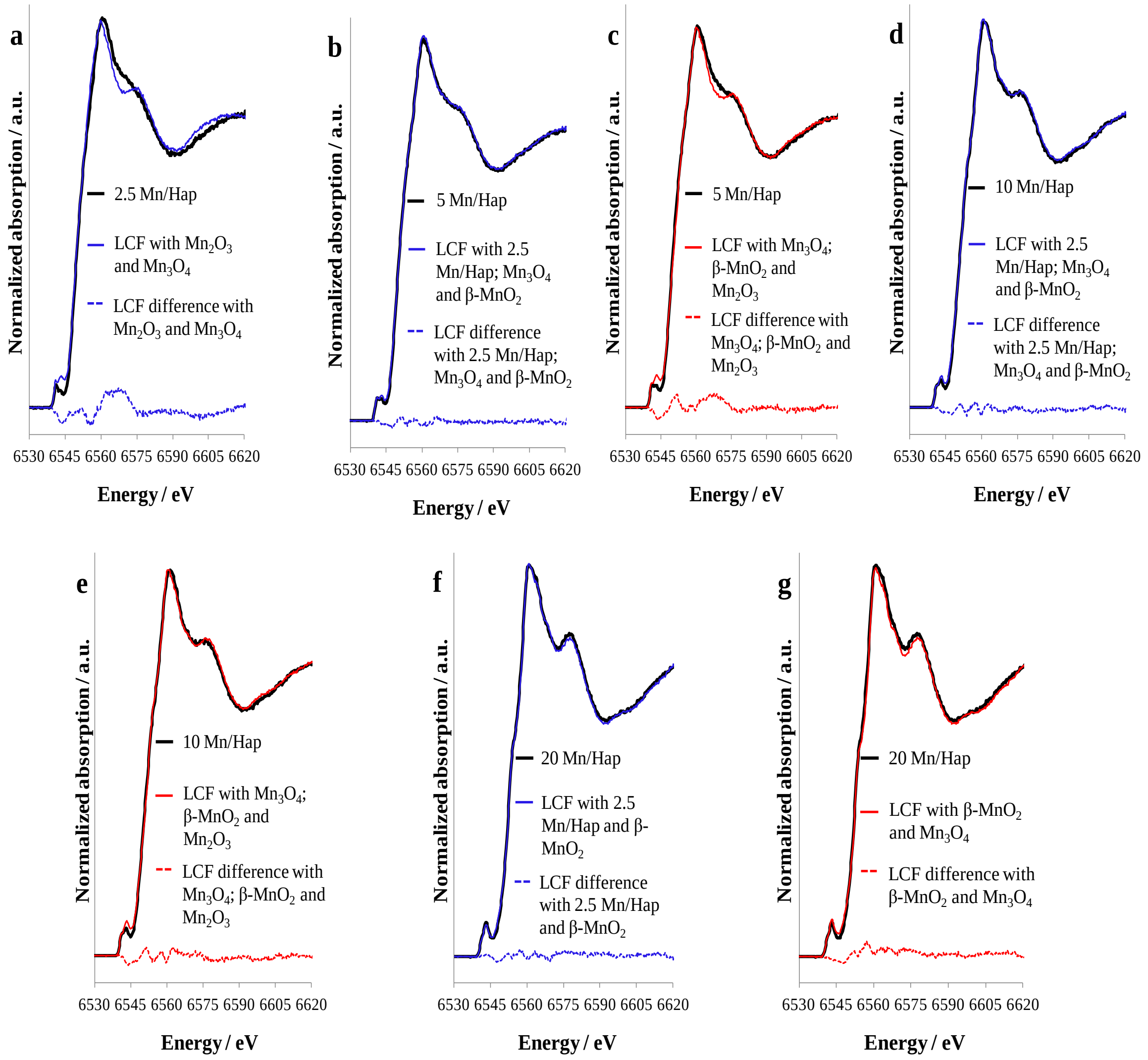

Figure 6.8. Best quality LCF along with the LCF difference from data points and Mn-K edge XANES experimental spectra, measured at a fluorescence detection energy of 6491.5 eV, of 2.5 Mn/Hap a); 5 Mn/Hap b-c); 10 Mn/Hap d-e) and 20 Mn/Hap f-g): with b-d-f) and without c-e-g) 2.5 Mn/Hap as a component.

In a previous study conducted by Chlala *et al.* [30], the authors had stated that part of the total manganese weight load used in the Mn/Hap sample would be trapped as Mn^{2+} in the Hap structure, before the dispersion of the rest on the Hap surface. Hence, if we consider the 2.5 Mn/Hap catalyst as being representative of the Mn inserted into Hap phase, employing it as a standard compound in the combination fit analysis carried out over the rest of the Mn/Hap materials appears to be highly appropriate. In that way, the presence of this type of Mn species (Mn-doped Hap) would be taken into account when realizing the LCF analysis. However, in order to validate this approach, LCF analysis will be first performed without taking into consideration 2.5 Mn/Hap and then while using 2.5 Mn/Hap as a standard compound, revealing thus if the quality of the fit improves by employing this method. Therefore, an illustration of the fit with and without 2.5 Mn/Hap will indicate if Mn inserted in the Hap structure does indeed exist in a significant amount in the three remaining Mn/Hap catalysts.

Table 6.1. The linear combination fitting results for x Mn/Hap samples.

Sample	Standard sample	Weight fraction	R factor [a]
2.5 Mn/Hap	Mn_3O_4	0.660	0.00112
	Mn_2O_3	0.340	
5 Mn/Hap (with 2.5 Mn/Hap as a component)	2.5 Mn/Hap	0.548	0.00008
	Mn_3O_4	0.326	
	β-MnO_2	0.126	
5 Mn/Hap (without 2.5 Mn/Hap as a component)	Mn_3O_4	0.601	0.00043
	Mn_2O_3	0.231	
	β-MnO_2	0.167	
10 Mn/Hap (with 2.5 Mn/Hap as a component)	2.5 Mn/Hap	0.257	0.00015
	Mn_3O_4	0.385	
	β-MnO_2	0.357	
10 Mn/Hap (without 2.5 Mn/Hap as a component)	Mn_3O_4	0.503	0.00021
	β-MnO_2	0.375	
	Mn_2O_3	0.122	
20 Mn/Hap (with 2.5 Mn/Hap as a component)	2.5 Mn/Hap	0.291	0.00012
	β-MnO_2	0.709	
20 Mn/Hap (without 2.5 Mn/Hap as a component)	Mn_3O_4	0.250	0.00036
	β-MnO_2	0.750	

[a] R-factor is defined as follows: R= sum((data-fit)^2)/sum(data^2).

It can be seen that by including the 2.5 Mn/Hap spectrum among the standards used for the LCF, a good fit could be achieved in the entirety of the spectrum for 5 Mn/Hap sample. Whereas, if 2.5 Mn/Hap is disregarded as a component, a misfit can be detected in both the pre-edge and post-edge regions (Figure 6.8-c). Regarding 10 Mn/Hap and 20 Mn/Hap, a good fit can be attained despite the exclusion of 2.5 Mn/Hap as component (Figure 6.8-e and g), indicating that its use as a standard would be superfluous in both these catalysts cases. Indeed, even though the R-factor reported in Table 6.1

shows a decrease in its value when 2.5 Mn/Hap is used as a reference compound for 10 Mn/Hap and 20 Mn/Hap, it is not significant enough to be considered pertinent. Consequently, in the following discussion, the LCFs including 2.5 Mn/Hap in the case of 5 Mn/Hap and excluding 2.5 Mn/Hap in the cases of 10 Mn/Hap and 20 Mn/Hap will be considered as representing the best quality fit and their results will constitute the basis for the subsequent interpretation. Thus, it seems that three phases of Mn are present in the 5 Mn/Hap sample in the following order of decreasing quantity: 2.5 Mn/Hap (54.8%) > Mn_3O_4 (32.6%) > β-MnO_2 (12.6%). Three phases are also found in 10 Mn/Hap: Mn_3O_4, β-MnO_2 and Mn_2O_3 instead of 2.5 Mn/Hap, with Mn_3O_4 (50.3%) being predominant followed by β-MnO_2 (37.5%) and lastly by Mn_2O_3 (12.2%). It can be noted that the weight fraction of β-MnO_2 becomes much more significant in 10 Mn/Hap leading to an increase in the average oxidation state of Mn in this sample compared to 5 Mn/Hap. Finally, in the case of 20 Mn/Hap, 2 types of Mn species are co-present: β-MnO_2 and Mn_3O_4 in the proportions of 75% and 25%, respectively.

It can be clearly perceived that when the amount of Mn increases within the Mn/Hap material, the weight fraction of β-MnO_2 (Mn^{4+}) increases. This observation agrees with the previously noted shift of the edge position towards higher energy values when going from 2.5 Mn/Hap to 20 Mn/Hap, which indicated a parallel evolution between the Mn oxidation state and the Mn loading in the sample. Thus, the sample with the highest Mn weight load, *i.e.* 20 Mn/Hap, consists mainly of β-MnO_2; the additional presence of other Mn species, type 2.5 Mn/Hap or Mn_3O_4 or even ε-MnO_2 (which was revealed to be possibly present by XRD analysis but for which no XANES reference spectrum is presently available) cannot be excluded at this stage. On the opposite end, the sample with the lowest Mn weight load, *i.e.* 2.5 Mn/Hap, is comprised of Mn species with lower AOS (between +2 and +3) and hypotheses have been proposed as to the nature of Mn species potentially present in 2.5 Mn/Hap (Mn inserted in Hap structure in the form of Mn^{2+} in addition to Mn_3O_4). Finally, regarding the catalysts with an intermediate content of Mn, *i.e.* 5 Mn/Hap and 10 Mn/Hap, it can be seen that the amount of Mn_3O_4 increases with that of the Mn weight load, possibly signaling a change of the Mn AOS from a ratio of +2/+3 in favor of +3, on the way towards a ratio of +3/+4, which is becoming more important when the Mn content increases from 5 to 10 wt%.

6.4.2. In situ analysis

In situ XANES of the temperature-programmed reduction of 10 Mn/Hap catalyst and the reference samples β-MnO_2, Mn_2O_3 and Mn_3O_4 was conducted. The resulting absorption spectra were recorded and given in Figure 6.9.

For all samples, we observe a very rapid decrease in the intensity of the white line and a shift of the absorption edge towards lower energies, showing that the samples have undergone major changes in their geometric and electronic structures.

What is more, the overall shape of the spectra obtained at the end of the ramp (Figure 6.9) is similar for all samples, testifying to the presence of same type of Mn species at the end of all *in situ* experiments, regardless of the nature of the sample being examined. It can be noted that the shape of the spectrum obtained towards the end of the analysis corresponds to none other than that of the MnO reference compound, indicating that at the conclusion of the temperature-programmed reduction experiments all manganese oxide species present in the samples have been reduced to the maximum degree possible (Mn^{2+}) under the analysis conditions (MnO does not reduce to metallic Mn before 1000 ° C for thermodynamic reasons [46]).

Concerning the transformation of the 10 Mn/Hap sample during the temperature-programmed reduction, it can be seen that, compared to the other reference compounds (β-MnO_2; Mn_2O_3; Mn_3O_4), its XANES spectrum shows an evolution that is most similar to that of Mn_3O_4, which seems to imply a predominant presence of this manganese oxide phase in 10 Mn/Hap compared to the other reference compounds with higher Mn AOS (β-MnO_2 and Mn_2O_3). This corroborates the results of the LCF carried above for 10 Mn/Hap catalyst, which showed that the latter consists predominantly of Mn_3O_4. Therefore, it does seem that for an Mn weight load ≤ 10 wt%, the Mn AOS leans towards rather low values comprised between +2 and +3. Furthermore, seeing as LCF results showed 5 Mn/Hap to be comprised mainly of 2.5 Mn/Hap (54.8%) and Mn_3O_4 (32.6%); and having formerly proposed a concomitant presence of Mn_3O_4 and Mn^{2+} inserted in Hap within 2.5 Mn/Hap, it is possible to push the interpretation further and suggest that for an Mn weight load ≤ 10 wt%, Mn_3O_4 is the majorly present MnO_x phase in Mn/Hap catalyst.

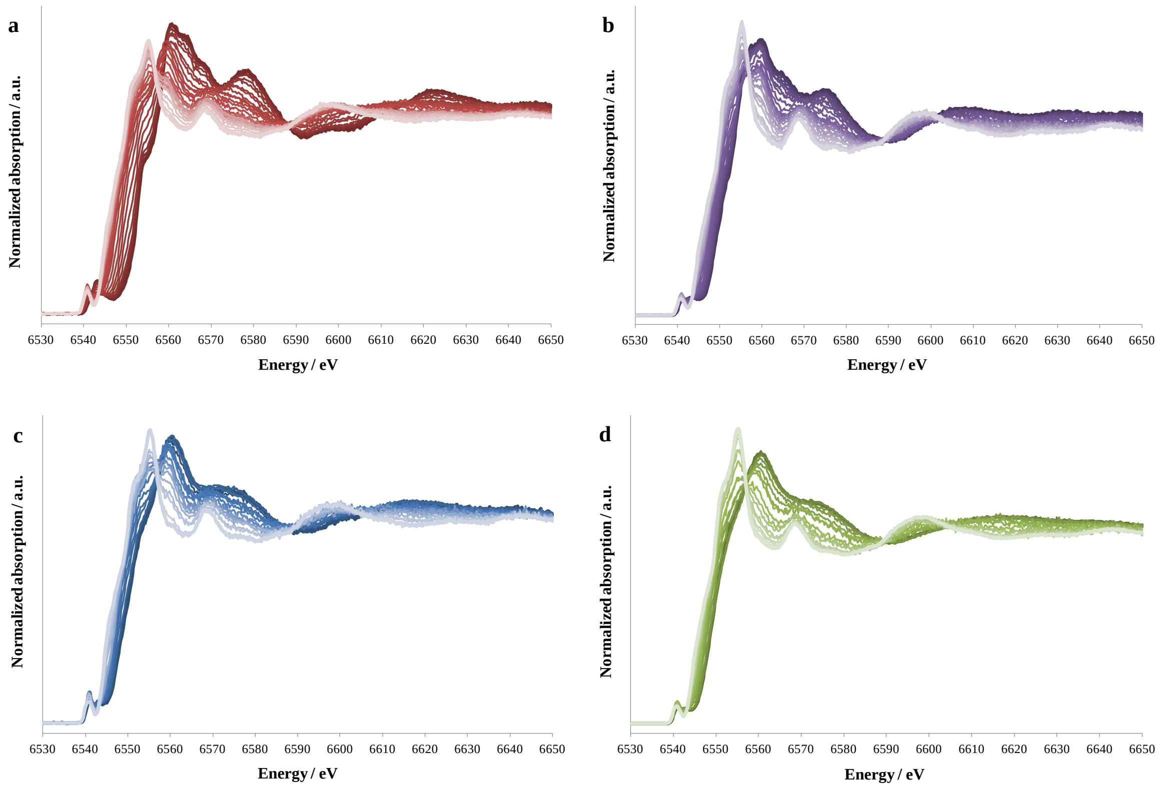

Figure 6.9. *In situ* Mn-K edge XANES experimental spectra, recorded during the temperature-programmed reduction of a) β-MnO_2; b) Mn_2O_3; c) Mn_3O_4 and d) 10 Mn/Hap compounds. In each series of recorded spectra, every subsequent spectrum is a shade darker than the previous one, so that the one corresponding to the first acquired spectrum (at the beginning of the experiment) is the darkest in color and the one corresponding to the last acquired spectrum (at the end of the experiment) is the lightest in color. All XANES spectra were measured at a fluorescence detection energy of 6491.5 eV.

6.5. H_2-TPR analysis

The H_2-TPR analyses were conducted in order to examine the reducibility of the manganese oxide reference compounds (except for MnO which will not exhibit any reduction behavior before 1000 °C [46]), as well as that of x Mn/Hap series of catalysts (x = 2.5; 5; 10 and 20 wt%). The resulting reduction profiles are shown in Figure 6.10 and the related data reported in Table 6.2.

6.5.1. H_2-TPR analysis of reference compounds

It could be first remarked that the Mn_{calc} AOS, calculated from the total amount of hydrogen consumption during the TPR experiments for each of the reference compounds by assuming that MnO is the final state, are in good accordance with the theoretical Mn_{th} AOS (Table 6.2). This serves in validating the presence of the indicated stoichiometry in each manganese oxide reference sample.

Regarding the reduction of manganese oxides materials, the process can be described as follows [47]–[49]:

$$\mathrm{MnO_2} \rightarrow \mathrm{Mn_2O_3} \rightarrow \mathrm{Mn_3O_4} \rightarrow \mathrm{MnO}. \qquad (6.1)$$

However, no distinct reduction peak for an intermediate transformation of MnO_2 into Mn_2O_3 can always be noted during the reduction of MnO_2 solids [50]–[52] and this is clearly the case in the current reduction analysis of the synthesized β-MnO_2 material. Indeed, the H_2-TPR pattern of β-MnO_2 (Figure 6.10-a) reveals two reduction peaks: the first intense and narrow centered at 345 °C; and the second weaker and broader centered at 449 °C, in line with literature data concerning the reduction of this manganese dioxide polymorph [52], [53]. The ratio between the areas of the first to second hydrogen consumption peak, which is in the order of 2:1, is consistent with the successive reduction of MnO_2 into Mn_3O_4, followed by a final reduction to MnO. The H_2-TPR profile of ε-MnO_2 was comparable to that of β-MnO_2, but the two reduction peaks both shifted slightly to lower temperatures at 327 and 444 °C. Moreover, ε-MnO_2 manifests a clear shoulder on the first reduction peak at 362 °C, implying that an intermediate transformation into Mn_2O_3 occurs, readily followed by an additional reduction to Mn_3O_4.

In the case of Mn_5O_8, the reduction pattern observed in Figure 6.10-a indicates that a two-step reduction process takes place within this sample [47], with a first reduction peak centered at 311 °C and a second one at 446 °C. However, the ratio between the H_2 consumption during the first reduction step and the second one is 1:1, which suggests a slightly different reduction route than what has been seen so far: meaning that instead of having Mn_3O_4 being the distinguishable intermediate between MnO_2 and MnO, it is this time Mn_2O_3 which will be the intermediate compound between the initial and the final manganese oxide state.

γ-MnOOH showed two peaks centered at 316 and 437 °C, with an area ratio of the lower temperature peak to the higher one of about 1:1, indicating a reduction process of purely trivalent Mn in γ-MnOOH to first multivalent Mn (II and III) in Mn_3O_4, then to divalent Mn in MnO.

Compared to the H_2-TPR profile of γ-MnOOH, that of Mn_2O_3 showed only a single reduction peak centered at 627 °C. Thus, it would seem that no clear boundaries between the consecutive reduction steps ($Mn_2O_3 \rightarrow Mn_3O_4 \rightarrow MnO$) can be defined in this compound. A similar reduction profile has been noted before for Mn_2O_3 in another work [50].

As for the last examined reference compound, i.e. Mn_3O_4, its H_2-TPR profile reveals, surprisingly, two reduction peaks centered at 323 °C and 378 °C, despite the absence of any possible reduction intermediate product between Mn_3O_4 and MnO. This unexpected two-step reduction process has been explained by Yongnian *et al.* [54] (and later reasserted by Kim *et al.* [55]) as being due to the particular structure of the Mn_3O_4 compound in which Mn^{2+} ions occupy tetrahedral sites while Mn^{3+} ions are located in tetragonally distorted octahedral sites. The distortion caused by the Jahn-Teller

effect on the octahedron of oxygen ions around Mn^{3+} ions in high-spin configuration results in the occurrence of four short Mn^{III}—O bonds and two long Mn^{III}—O bonds. Thus, become present two different types of Mn^{III}—O which lead towards the detection of two reduction peaks.
This first unexpected finding in the H_2-TPR profile of Mn_3O_4 having been clarified, there remains another perplexing observation which is the better reducibility manifested by this compound (lowest value of $T_{onset\ reduction}$) compared to all other examined reference compounds. What makes this latter result rather puzzling is the fact that authors have announced in the past the existence of a correlation between the Mn oxidation states and the reducibility of the material: a higher Mn AOS resulting in a higher reducibility [48]. Yet, in the current study, Mn_3O_4 which is characterized by the lowest Mn AOS is also the one presenting the highest reducibility. This can perhaps be accounted for by enhanced oxygen mobility for this product. Indeed, this same reason was proposed by Kim *et al.* [55] to justify the better reducibility of their Mn_3O_4 compound when compared to both MnO_2 and Mn_2O_3.

Therefore, on the basis of the obtained $T_{onset\ reduction}$ values, summarized in Table 6.2, the reducibility of the manganese oxide reference compounds decreases in the following order:

$Mn_3O_4 \approx \varepsilon$-$MnO_2 > Mn_5O_8 > \beta$-$MnO_2 > \gamma$-MnOOH $> Mn_2O_3$.

Table 6.2. H_2-TPR results.

Sample	$T_{onset\ reduction}$ [°C] [a]	$n(H_2)$ [b] [$mmol.g^{-1}$]	Mn_{calc} AOS [c]	Mn_{th} AOS [d]
β-MnO_2	150	11.82	4.1	4.0
ε-MnO_2	135	11.13	3.9	4.0
Mn_5O_8	145	7.58	3.2	3.2
γ-MnOOH	235	5.75	3.0	3.0
Mn_2O_3	285	7.13	3.1	3.0
Mn_3O_4	135	6.07	2.9	2.7
2.5 Mn/Hap	190	0.44	3.6	-
5 Mn/Hap	160	0.75	3.4	-
10 Mn/Hap	150	1.27	3.3	-
20 Mn/Hap	190	3.18	3.7	-

[a] Temperature of onset reduction. [b] Experimental amount of H_2 consumed. [c] Calculated manganese average oxidation state based on H_2-TPR results. [d] Theoretical manganese average oxidation state.

6.5.2. H_2-TPR analysis of Mn/Hap catalysts

Regarding the reduction pattern of the x Mn/Hap series of catalysts, shown in Figure 6.10-b, it is clear that for low Mn contents (≤ 10 wt%), the curve of the TCD signal is characterized by a large asymmetrical peak, with a shoulder located at 433 °C and 380 °C for Mn loadings of 10 and 2.5 wt%, respectively. In the case of 5 Mn/Hap catalyst, a broad peak appears at 360 °C with no apparent shoulder, which does not negate however the possibility of the presence of more than contribution within it.

By opposition, for higher Mn content, *i.e.* 20 Mn/Hap, the H_2-TPR profile is characterized by two overlapping peaks located at high temperatures, at around 360 and 470 °C.

In fact, it is this catalyst with the highest amount of manganese (20 Mn/Hap) that manifested by XRD analysis the existence of large MnO_2 crystallites (ε- and/or β-MnO_2) and whose XANES spectrum was very similar to that of manganese dioxide (β-MnO_2) reference product. Thus, it is expected that its reduction profile would resemble that of MnO_2 compound (Figure 6.10-a). Indeed, it is very similar to that of β-MnO_2, therefore confirming XANES results and reinforcing the predominant presence of the β- polymorph of MnO_2 in 20 Mn/Hap.

In parallel, 2.5, 5, and 10 Mn/Hap samples, which were previously shown through XANES analysis to mainly consist of Mn_3O_4, demonstrate in the present H_2-TPR analysis reduction profiles that are in line with that of Mn_3O_4 reference compound.

On a different note, the effect of potentially reducible NO_3^- species, which were shown to persist in Hap supported manganese bearing catalysts (despite the calcination step at 400 °C) and to participate in the overall consumption of hydrogen in Chapter III, has also been studied presently by coupling the H_2-TPR analysis with mass spectrometry (MS) and monitoring the evolution of selected m/z signals at the outlet of the reactor. The results indicate the appearance of m/z signals at 30, 14, 15, and 16 in agreement with the NO fragmentation spectrum, for all of the examined Mn/Hap catalysts in the temperature range 250 to 450 °C with a maximum temperature between 300 and 380 °C. From this observation, it was deduced that the reduction of nitrate occurs for these materials in the form of NO.

In terms of calculated Mn AOS, the values obtained vary in the range of 3.3-3.7. However, seeing as these samples contain remaining traces of reducible nitrate species, the Mn AOS calculated for the Mn/Hap solids could prove to be an overestimation of the actual Mn AOS value. It would actually depend on the nitrate species' percentage of contribution in the overall H_2 consumption process, within each of the examined Mn/Hap catalysts. Thus, no pertinent interpretation of the calculated Mn AOS could be proposed at this stage.

Nonetheless, it can be noted that the production of NO (signal m/z = 30) starts while the consumption of hydrogen (signal m/z = 2) has already well begun (Figure AD.7). Therefore, it is safe to assume that the beginning of the reduction process is related to the reduction of manganese-based species.

By comparing the onset reduction temperature values ($T_{onset\ reduction}$) between the four Mn/Hap catalysts, it can be observed that $T_{onset\ reduction}$ decreases with the addition of manganese up to an Mn weight load of 10% for which the lowest $T_{onset\ reduction}$, equal to 150 °C, is achieved. After that, $T_{onset\ reduction}$ increases significantly to attain 190 °C for 20 Mn/Hap (Table 6.2). To summarize, the reducibility of the dispersed M_xO_y species decreases according to the following sequence: 10 Mn/Hap > 5 Mn/Hap > 2.5 Mn/Hap ≈ 20 Mn/Hap. It can be noted that this trend follows that of decreasing Mn_3O_4 amount in the Mn/Hap catalysts, as revealed by prior XANES results. Therefore, this explains the obtained reducibility sequence in the Mn/Hap catalysts, since according to a previous H_2-TPR finding (section 6.5.1), Mn_3O_4 presents the highest reducibility among all examined Mn_xO_y reference compounds.

In conclusion, as has been demonstrated by the results discussed above, the H_2-TPR patterns strongly depend both on the oxidation state of the Mn species, as well as on the structure and geometry in which these Mn entities are present within the sample. Moreover, it seems that an increase in Mn content up to 10 wt% load enhances the reducibility of Mn/Hap catalyst, seeing as it favors the presence of Mn_3O_4, the most reducible Mn species. While, conversely, a further increase in Mn amount is detrimental for the reducibility conduct of the solid seeing as it promotes the formation of β-MnO_2 which is a less reducible Mn species.

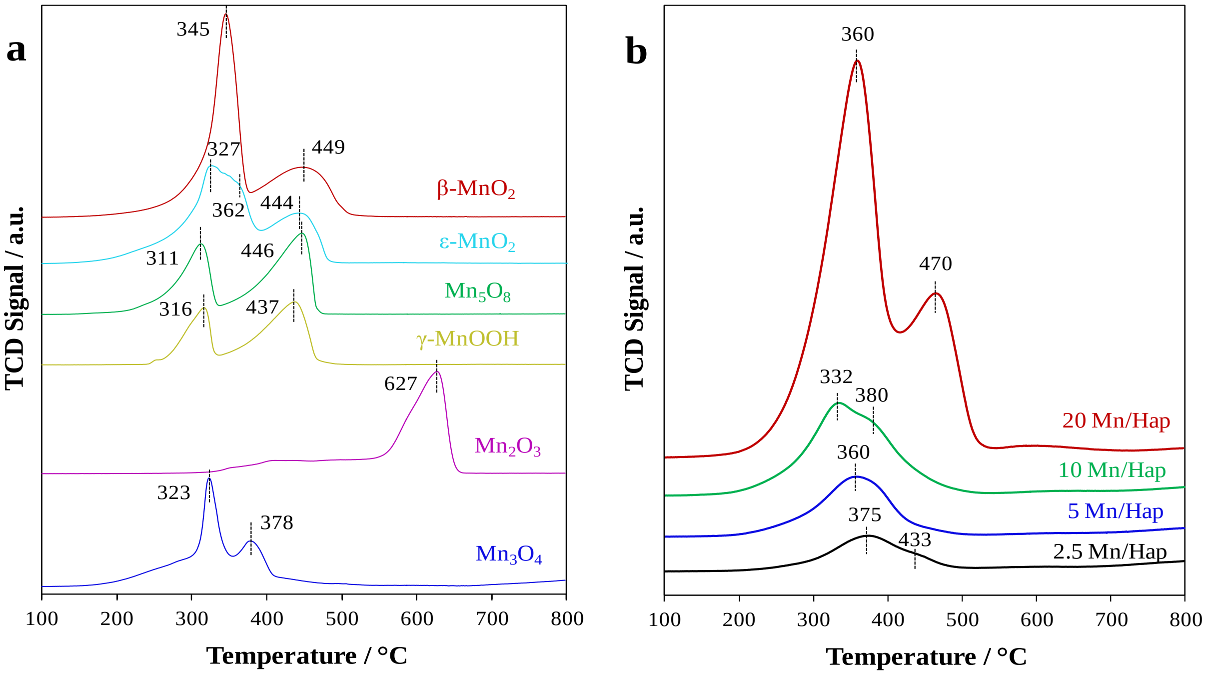

Figure 6.10. H_2-TPR reduction profiles for a) Mn_xO_y reference compounds and b) x Mn/Hap catalysts.

6.6. XPS analysis

XPS is a powerful tool to study surface properties, delivering both elemental (determination of the surface's chemical composition) and chemical state information (evaluation of metal oxidation state and investigation of the nature of oxygen species present in solid surfaces). Moreover, by being a quantitative spectroscopic technique, information about the enrichment or depletion of elements on the surface can be attained. In this study, XPS was used for all of these purposes.

6.6.1. XPS analysis of fresh Mn-based compounds

6.6.1.1. Survey spectra

The survey XPS spectra recorded for β-MnO_2; Mn_5O_8; γ-MnOOH; Mn_2O_3; and MnO reveal no significant presence of impurities, except for the contaminant carbon. However, the survey spectra of ε-MnO_2 and Mn_3O_4 manifest, in addition to contaminant carbon, photoelectron emissions characteristic of lanthanum (in the case of ε-MnO_2) and potassium (in the case of Mn_3O_4) elements. Therefore, it would appear that a certain amount of La and K species remain in ε-MnO_2 and Mn_3O_4, respectively, despite the acid treatment conducted in the case of the former and the washing step carried out in the case of the latter, in the course of the synthesis process.

In the case of the catalysts x Mn/Hap (x = 2.5; 5; 10; and 20 wt%), besides Mn, O, Ca, P and adventitious carbon, another element could be discerned by analysis of their survey spectra, which was none other than nitrogen "N", reaffirming once more the presence of residual nitrates in these hydroxyapatite supported manganese samples.

6.6.1.2. *Manganese spectra*

The XPS spectra of Mn 2p and Mn 3s energy levels were recorded for all reference compounds. All XPS related data are reported in Table 6.3.

Regarding the determination of the Mn oxidation state in the analyzed samples, studies have shown that this task could be accomplished either by examining the binding energy values of the Mn $2p_{3/2}$ main peak or by measuring the Mn 3s multiplet splitting: the higher the oxidation state, the higher the Mn $2p_{3/2}$ binding energy (BE) value and the lower the Mn 3s splitting [56]–[58].

However, it should be pointed out that contrary to Mn(II) species for which the attribution may not prove to be too difficult, trivalent Mn cannot be clearly distinguished from tetravalent Mn by relying only on Mn $2p_{3/2}$ BE [59]. Indeed, the small influence induced by the change in Mn oxidation state on the BE shifts of the Mn $2p_{3/2}$ peak, added to the usual broadness of this peak, renders the determination of Mn oxidation state based solely on Mn $2p_{3/2}$ BE value very complicated, even more so when two or more species of Mn are present simultaneously (i.e. Mn_5O_8 and Mn_3O_4).

Table 6.3. XPS results for Mn-bearing compounds.

Sample	O 1s							Mn $2p_{3/2}$	Mn 3s					Mn AOS
	O_I		O_{II}		O_{III}				Mn $3s_1$		Mn $3s_2$			
	BE (eV)	At. (%) [a]	BE (eV)	At. (%) [a]	BE (eV)	At. (%) [a]	O_{II}/ O_I	BE (eV)	BE (eV)	FWHM (eV)	BE (eV)	FWHM (eV)	ΔE (eV)	
MnO	530.0	66	531.4	20	532.0	14	0.30	641.1	89.3	3.3	83.3	3.1	6.0	1.9
Mn_3O_4	529.5	64	530.9	26	532.1	11	0.40	641.9 [640.6] [b]	88.9	3.4	83.8	3.3	5.1 [6.1] [b]	3.1 [1.8] [b]
Mn_2O_3	529.9	72	531.4	23	533.0	5	0.32	641.9 [640.7] [b]	89.1	3.3	84.0	3.2	5.1 [6.0] [b]	3.1 [1.9] [b]
γ-MnOOH	529.7	30	530.9	40	532.3	30	1.32	641.8	89.2	3.4	84.0	3.0	5.2	3.0
Mn_5O_8	529.6	68	531.1	23	532.7	9	0.34	641.5	88.7	3.8	83.7	4.1	5.0	3.2
β-MnO_2	529.6	72	531.1	23	532.8	4	0.33	642.0 [640.8] [b]	89.0	3.2	84.5	2.9	4.4 [6.1] [b]	4.0 [1.8] [b]
ε-MnO_2	529.5	60	531.0	20	532.6	20	0.34	642.0	89.1	3.4	84.5	3.1	4.5	3.9
2.5 Mn/Hap	-	-	-	-	-	-	-	641.8	90.1	4.0	84.1	3.6	6.0	1.9
5 Mn/Hap	-	-	-	-	-	-	-	642.5	89.6	3.9	84.1	3.7	5.5	2.6
10 Mn/Hap	-	-	-	-	-	-	-	642.7 [641.1] [b]	89.2	3.7	84.0	3.3	5.2 [6.1] [b]	3.0 [1.8] [b]
20 Mn/Hap	-	-	-	-	-	-	-	642.7	89.4	4.0	84.5	3.3	4.9	3.4

[a] XPS atomic concentration. [b] Data obtained after H_2 reduction test.

In the present work, in order to evaluate the oxidation state of Mn on the samples surface, we will use several methods complementarily, namely curve fitting of Mn $2p_{3/2}$ peak, but only in the case of monovalent Mn-bearing compounds; and Mn 3s multiplet splitting for all prepared reference compounds and catalysts.

The Mn $2p_{3/2}$ peak is broad due to multiplet splitting. By using curve fitting of Mn $2p_{3/2}$ spectra for single-valence compounds, based on the fitting parameters proposed by Biesinger *et al.* [60] for MnO_2, γ-MnOOH, Mn_2O_3, and MnO, a further validation of the successful synthesis of these manganese reference compounds could be attained. Fitting parameters for the Mn $2p_{3/2}$ peak of ε-MnO_2, β-MnO_2, γ-MnOOH, Mn_2O_3, and MnO are presented in Table 6.4 with spectra for these references given in Figure 6.11: ε-MnO_2 is fitted with 6 peaks of equal Full Width at Half Maximum (FWHM), similarly to β-MnO_2, while γ-MnOOH and Mn_2O_3 are fitted with 5 peaks of equal FWHM. It can be seen that a good fitting is obtained for these products by following the same curve fitting procedure as the one reported in the paper of Biesinger *et al.* [60], signaling the formation of the desired phase in the above-mentioned compounds. However, in the case of MnO material, Figure 6.11-e shows a minor misfit due to a problem with the satellite peak component area (Peak 6). The latter could be the result of a slight oxidation of the MnO layer at the surface.

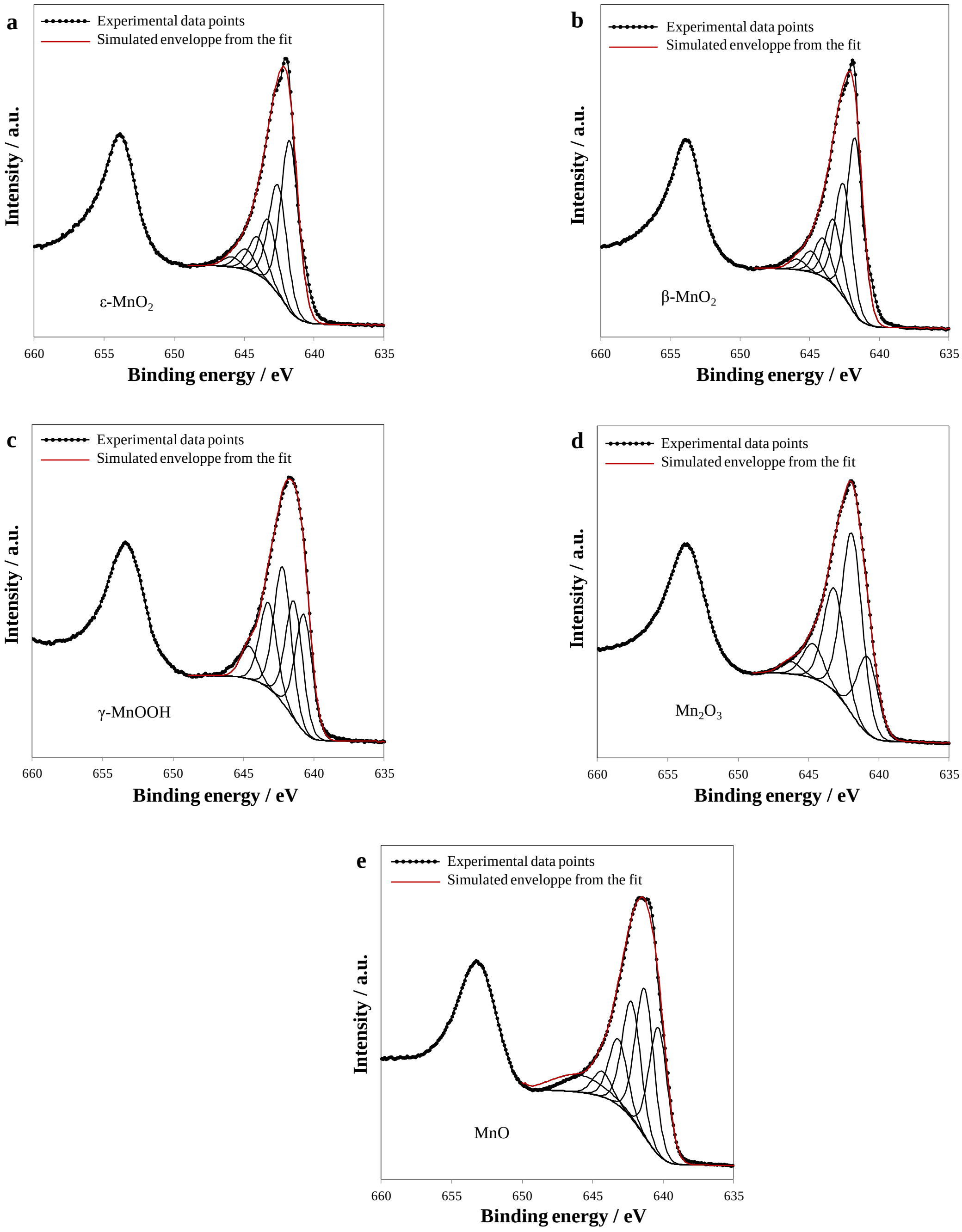

Figure 6.11. Mn $2p_{3/2}$ spectrum of a) ε-MnO_2; b) β-MnO_2; c) γ-MnOOH; d) Mn_2O_3; and e) MnO fitted with parameters from Table 6.4.

A visual inspection of the Mn 2p core level spectra of Mn/Hap catalysts illustrated in Figure 6.12 reveals first an increase in the binding energy values of the Mn $2p_{3/2}$ main peak with that of Mn content within the sample (Table 6.3). This could be indicative of Mn species becoming more oxidized at the surface when the Mn loading increases. Secondly, a satellite feature which is characteristic of an Mn^{2+} oxidation state appears clearly in the Mn 2p spectrum of 2.5 Mn/Hap, becoming less marked when Mn content rises to 5 wt% and even less so when the Mn weight load reaches 10 wt%, to the point of being indiscernable in 20 Mn/Hap. This supports the proposition of an increasing Mn oxidation with that of Mn content.

An attempt at curve fitting of Mn 2p spectra of Mn/Hap catalysts with the envelope of an Mn_xO_y reference compound was conducted (the experimental details of this procedure is described in Chapter II). This approach revealed that the best fitting could be obtained by using an asymetrical lineshape representative of Mn_3O_4 compound in the case of 2.5 Mn/Hap, 5 Mn/Hap, and 10 Mn/Hap (Figure 6.12-b, c, and d). A noticeable misfit can be nevertheless seen for 2.5 Mn/Hap and 5 Mn/Hap in the region where the satellite feature of Mn^{2+} appears, signaling the additional presence of an Mn phase with an Mn AOS of +2, which has been previously suggested to correspond to Mn^{2+} inserted in Hap structure (refer to XANES analysis). However, in the case of 20 Mn/Hap, the best fitting was achieved by using an asymetrical lineshape representative of β-MnO_2 reference compound (Figure 6.12-e). This would suggest that, just as stated in the XANES results section, 2.5, 5, and 10 Mn/Hap samples are predomianatly composed of Mn_3O_4, with 10 Mn/Hap presenting the highest amount of Mn_3O_4 among these three catalysts (no notable misfit in Figure 6.12-d), while 20 Mn/Hap majorly consists of β- MnO_2. This proposition will be further examined when looking into the multiplet splitting of Mn 3s peaks which was subsequently employed for determining the oxidation state of Mn.

Table 6.4. Mn $2p_{3/2}$ spectral fitting parameters: binding energy (eV), percentage of total area, spectral component separation (eV), and FWHM value (eV).

Sample	Peak 1 (eV)	%	Peak 2 (eV)	ΔPeak 2 - Peak 1 (eV)	%	Peak 3 (eV)	ΔPeak 3 - Peak 2 (eV)	%	Peak 4 (eV)	ΔPeak 4 - Peak 3 (eV)	%	Peak 5 (eV)	ΔPeak 5 - Peak 4 (eV)	%	Peak 6 (eV)	ΔPeak 6 - Peak 5 (eV)	%	FWHM
Mn(II) MnO [a]	640.3	24	641.3	0.97	27.8	642.2	0.93	22.1	643.2	0.95	12.5	644.3	1.14	4.7	646.1	1.75	9.1	1.57
Mn(III) Mn_2O_3	640.8	18.9	641.9	1.10	44.5	643.2	1.27	25.3	644.7	1.50	8.5	646.3	1.62	3.1				1.74
Mn(III) γ-MnOOH	640.8	24	641.5	0.70	24.0	642.3	0.81	27.8	643.3	1.02	17.5	644.7	1.37	6.7				1.42
Mn(IV) β-MnO_2	641.7	41.7	642.6	0.86	26.5	643.3	0.70	15.5	644.0	0.75	9.1	644.9	0.85	4.9	645.9	1.00	2.5	1.40
Mn(IV) ε-MnO_2	641.7	41.7	642.6	0.86	26.5	643.3	0.70	15.5	644.0	0.75	9.1	644.9	0.85	4.9	645.9	1.00	2.5	1.50

[a] Peak 6 is a satellite peak with FWHM of 4.4 eV.

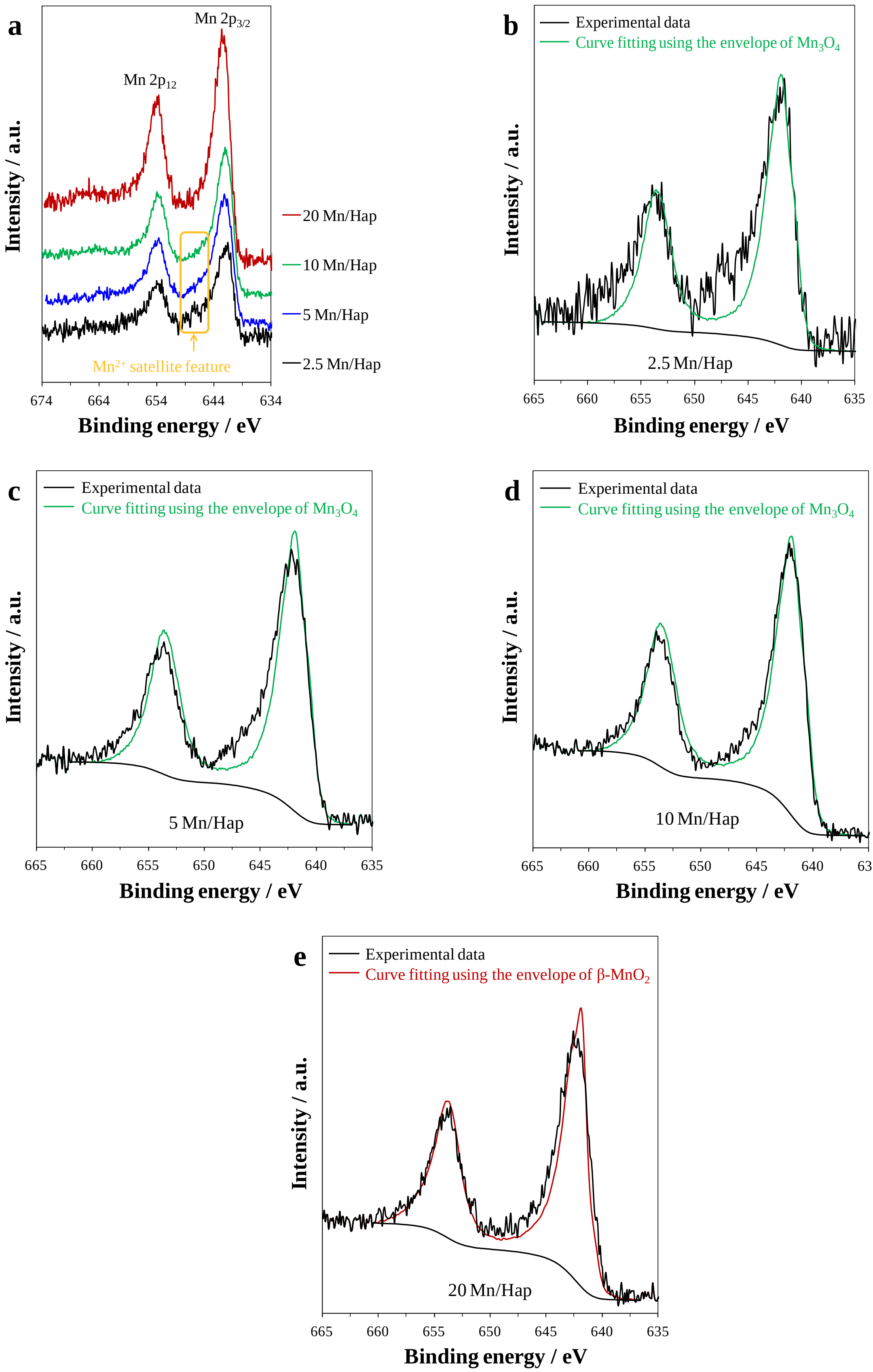

Figure 6.12. a) Mn 2p core level spectra of Mn/Hap catalysts. Curve fitting of the Mn 2p spectrum of b) 2.5 Mn/Hap; c) 5 Mn/Hap; d) 10 Mn/Hap and e) 20 Mn/Hap catalyst with the asymmetrical lineshape of Mn_3O_4 (b-c-d) and β-MnO_2 (e) reference compounds.

Indeed, the spectral splitting of the Mn 3s photoelectron peak, which is due to the exchange interaction between 3s core hole and 3d electrons, can be correlated with the Mn AOS (average oxidation state) [58]. Thus, the Mn 3s region of Mn bearing compounds was firstly investigated, as illustrated in Figure 6.13, with the derived values reported in Table 6.3.

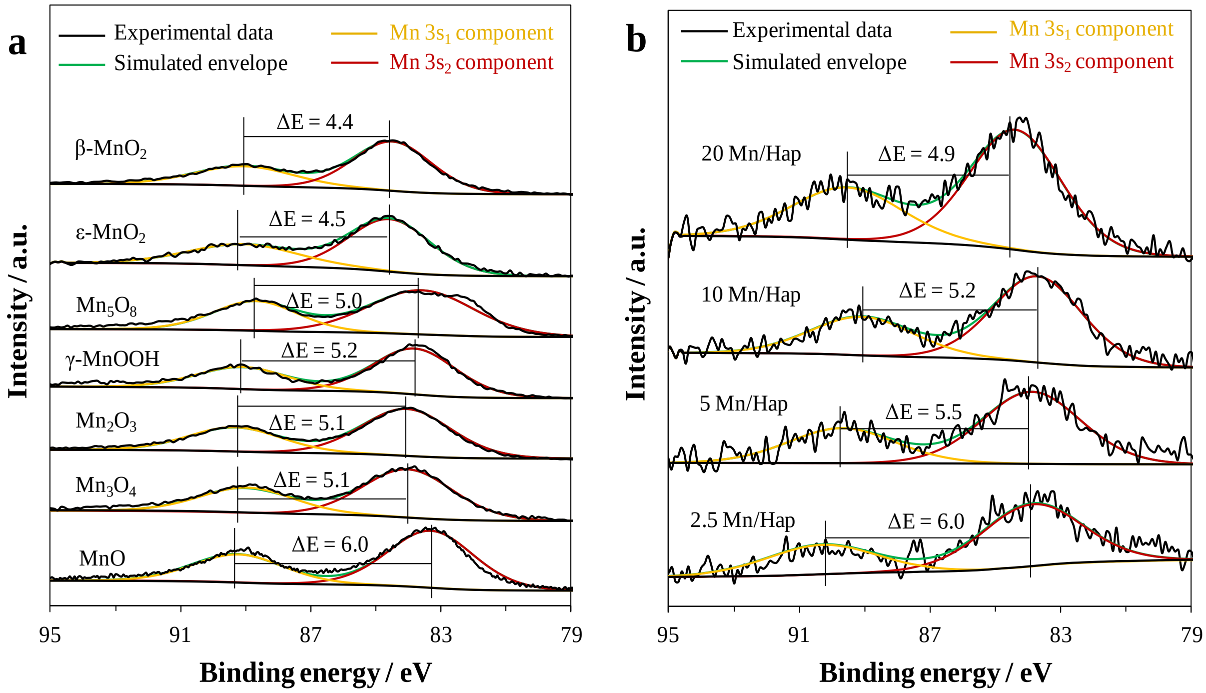

Figure 6.13. Mn 3s XPS spectra of a) Mn_xO_y reference compounds and b) x Mn/Hap catalysts, fitted with two components.

Secondly, Mn 3s splitting of the examined Mn_xO_y reference compounds was plotted as a function of the formal valence of the Mn ions, as shown in Figure 6.14.

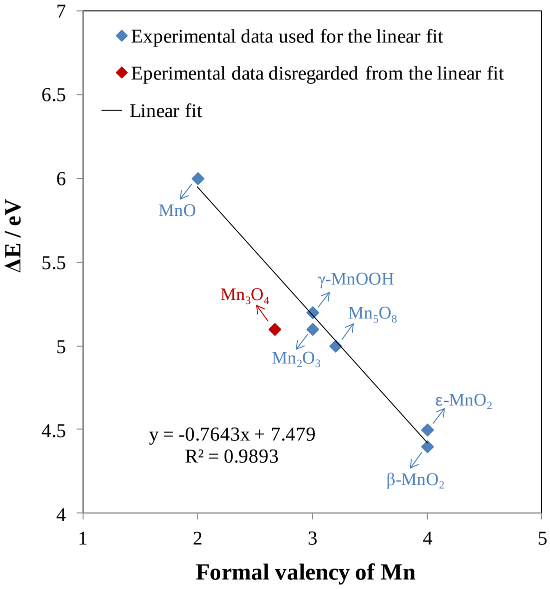

Figure 6.14. Mn 3s splitting of the examined Mn_xO_y reference compounds as function of the formal valence of Mn ions.

It can be seen that the relationship between Mn 3s splitting and the formal valency of Mn ions seem to be following a linear tendency, with the magnitude of the Mn 3s splitting decreasing monotonically with the increase of the formal valency of the manganese ions, except in the case of Mn_3O_4 material. Seeing as the prior inspection of Mn $2p_{3/2}$ peak for ε-MnO_2, β-MnO_2, γ-MnOOH, Mn_2O_3, and MnO revealed results in line with previous literature data in respect to those reference compounds, thus confirming the presence of the expected Mn_xO_y phases these former will used to conduct the linear fit. Regarding the mixed valence compound Mn_5O_8, besides the Mn 3s multiplet splitting being in line with the linear trend connecting it to the formal valency of Mn, characteristic features in the Mn 2p and Mn 3s spectra of the Mn_5O_8 solid, reported in Figure 6.15, attest more conclusively to the presence of this phase. Indeed, comparably to what was observed in the work of Gao *et al.* [12], in the Mn 2p XPS core level spectrum, the Mn $2p_{3/2}$ peak presents a distinct shoulder at 639.7 eV, while the Mn $2p_{1/2}$ peak reveals a less defined one at 651.3 eV. A shoulder also appears in the Mn $3s_2$ peak at 82.4 eV. These additional Mn 2p and Mn 3s components, emerging at lower binding energy values than those of the main peak contributions, are likely to correspond to the divalent manganese ions (Mn^{2+}) present in this multivalent material. Besides, it should be noted that the great values of the FWHM of the Mn 3s components (Table 6.3) are consistent with the presence of a mixture of oxidation states and are in line with those reported previously in the literature for Mn_5O_8 solid [59]. Therefore, the experimental data for this compound can also be used to conduct the linear fit.

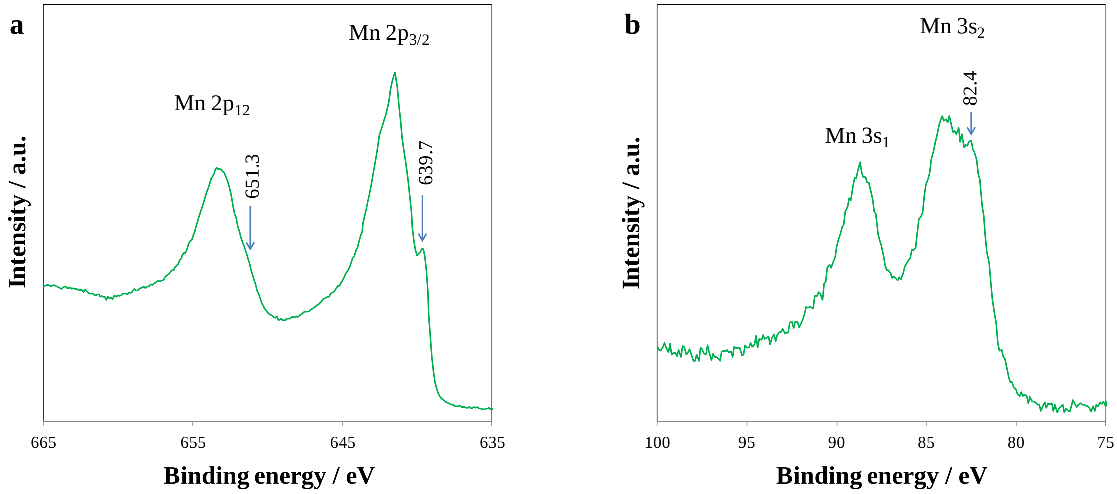

Figure 6.15. a) Mn 2p and b) Mn 3s XPS core level spectra of Mn_5O_8 compound.

By conducting a linear fit from the considered experimental data, the following equation is obtained:

$$\text{Mn AOS} = 9.785 - 1.31\ \Delta\text{E (eV)} \quad (6.2)$$

where ΔE is the Mn 3s multiplet splitting energy.

Concerning the multivalent reference compound Mn_3O_4 (whose experimental data was disregarded when conducting the linear fit), the calculation of Mn AOS based on equation (1) revealed a value of 3.1 for this sample. This number which exceeds significantly the theoretical value of 2.7, in addition to FWHM values of the Mn 3s peaks (Table 6.3) which are incongruent with the presence multivalent Mn species [59], suggest that the surface is characteristic of a single manganese oxidation state which is most likely Mn^{3+}, at least for the upper 10 nm of the sample. This occurrence might be explained by several theories. A first viable explanation would be a possible oxidation of Mn species occurring at the surface of the sample. A second plausible option would be that Mn_3O_4 exposes at the outer surface, layers consisting principally of Mn^{3+} ions, which would lead to an increase in the Mn AOS. A third postulate would be that the potassium entities remaining in the material (as shown by the survey spectrum of Mn_3O_4) could be at the origin of a structural modification leading towards an increase of Mn oxidation state at the surface. In fact, XPS quantification study revealed an atomic concentration of 11.3% for K element, which is not a negligible amount; and seeing as K^+ ions are known to be very mobile in oxide layers [61], X-ray irradiation exposure might drive the migration of these mobile species [62], being thus responsible for instigating a change in the structural arrangement of the atoms constituting the Mn_3O_4 sample. This could result for example in a birnessite-type MnO_2 structure (as seen by Raman spectroscopy analysis) in which interlayer cations, such as K^+, balance charge [22], which would account for the higher than expected Mn AOS value calculated for this compound.

Finally, when it comes to Mn/Hap catalysts (Figure 6.13-b), it can be noted that the Mn AOS increases from 1.9 to 3.4 when the Mn loading increases from 2.5 wt% to 20 wt% (Table 6.3). This is in agreement with XANES results which also indicated an increase of Mn AOS associated with that of Mn content in the Mn/Hap catalyst.

Hence, the increase in surface Mn species' oxidation state with that of Mn content within the sample, which was formerly suggested by the evolution of BE Mn $2p_{3/2}$ values, has been confirmed by the study of the Mn 3s splitting in Mn/Hap catalysts.

6.6.1.3. Oxygen spectra

The O 1s spectrum is often employed to distinguish the types of surface oxygen species present in a certain sample. Depending on the peak positions, three types of oxygen species can be recognized: lattice oxygen (O_2^{2-}) corresponding to the low binding energy peak (O_I: 529.5–530.0 eV), the surface adsorbed oxygen (O^{2-} or O^-), OH groups and oxygen vacancies associated with the medium binding energy peak (O_{II}: 530.9–531.4 eV), and at last adsorbed molecular water linked with the high binding energy peak (O_{III}: 532.0–533.0 eV) [49], [63]–[65].

The O 1s spectra were fitted using the three peaks referred to above. However, it should be pointed out that no curve-fitting of the O1s spectrum of Mn/Hap catalysts was attempted due to the fact that in the case of the presently examined Mn loadings (≤ 20 wt%), the manganese-bound oxygen species will be hidden by the oxygen associated with the calcium phosphate phase (Hap support), making any deconvolution operation very delicate. Therefore, curve-fitting of the O1s spectrum was only carried out in the case of Mn reference compounds. The corresponding spectra are presented in Figure 6.16 and the curve-fitting data reported in Table 6.3.

As revealed by the results noted in Figure 6.16 and Table 6.3, the O 1s spectrum could be successfully deconvoluted into three components related to various oxygen-involving chemical bonds. The relative percentage of each of these surface oxygen species could have a powerful impact on the catalytic properties of the studied material. Indeed, former studies have advanced that O_{II} species present higher mobility than lattice oxygen and that a higher amount of HO^- groups and oxygen vacancies might lead towards an increase in the oxidation activity [48], [66].

In the present work, apart from γ-MnOOH, Mn_3O_4 catalyst contained the highest percentage of O_{II} species compared to the other reference compounds. Moreover, as has been noticed in H_2-TPR analysis, Mn_3O_4 material presents the highest reducibility (lowest $T_{\text{onset reduction}}$) among the examined manganese reference compounds (β-MnO_2; ε-MnO_2; Mn_5O_8; γ-MnOOH; Mn_2O_3; and Mn_3O_4) even while having the lowest Mn average oxidation state. Accordingly, an increase in the atomic ratio of O_{II}/O_I does in fact seem to be correlated with an increase in the sample's reducibility in the current study. The fact that γ-MnOOH which possesses the highest ratio of O_{II}/O_I among the investigated reference compounds did not exhibit the highest reducibility among said solids does not negate the previous postulate, for it should also be remarked that this trivalent compound also has the highest relative percentage of adsorbed water species (O_{III}) among the examined samples. The latter could result in an adverse effect on the reducibility behavior of the sample, hence explaining its slightly higher $T_{onset\ reduction}$ value compared to that of Mn_3O_4 material.

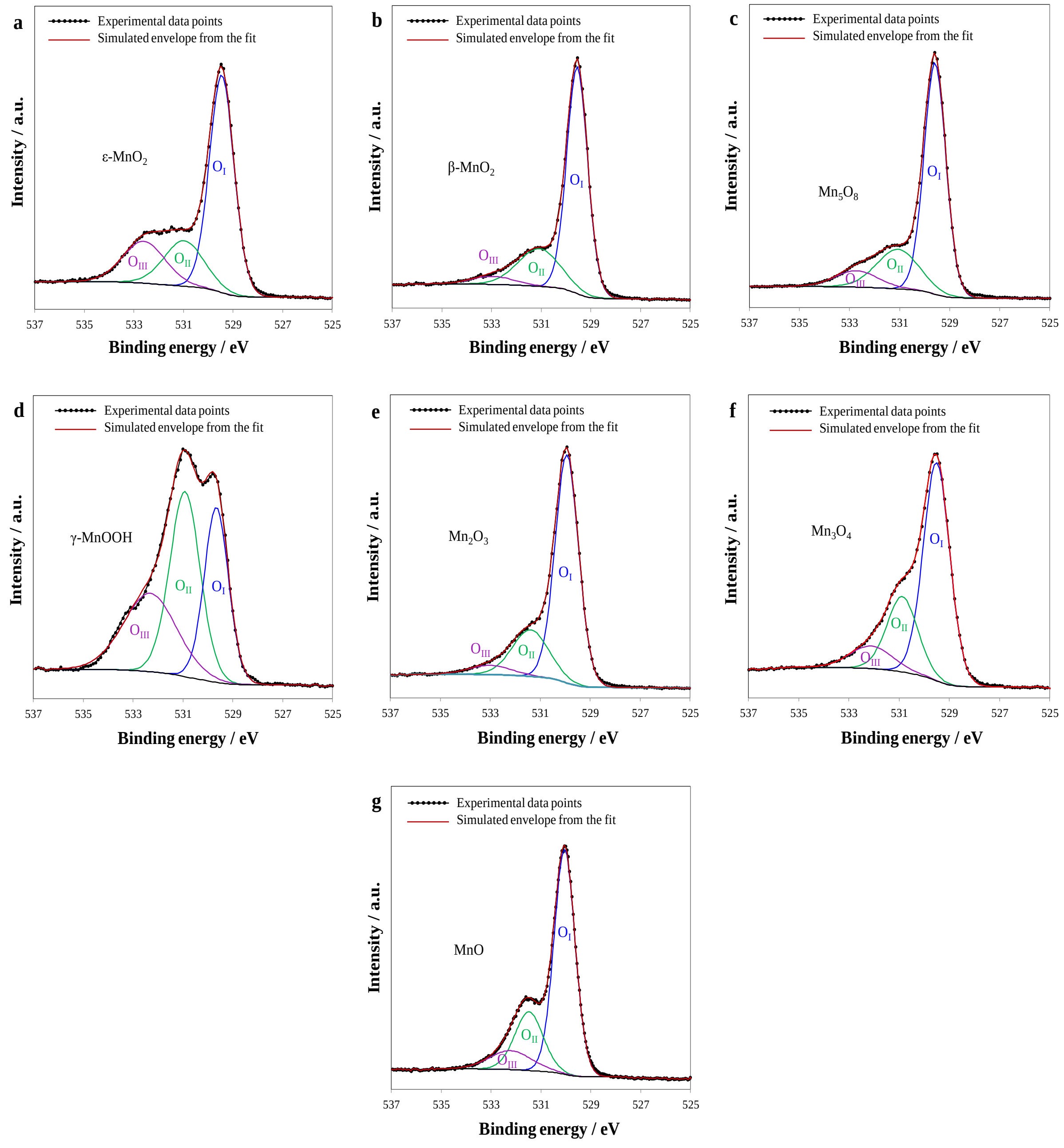

Figure 6.16. O 1s spectrum of a) ε-MnO_2; b) β-MnO_2; c) Mn_5O_8; d) γ-MnOOH; e) Mn_2O_3 f) Mn_3O_4 and g) MnO fitted with 3 components.

Finally, a quantitative evaluation of surface Mn/O atomic ratio was performed for all Mn_xO_y reference compounds. The results reported in Table 6.5 indicate a surface enrichment in oxygen for all Mn_xO_y materials except for β-MnO_2 for which a slight surface depletion in oxygen can be noted. Furthermore, what is even more interesting is that Mn_3O_4 shows the greatest deviation from the theoretical stoichiometric Mn/O ratio, with its experimental value being significantly lower than what can be expected (Deviation ≈ + 41%), thus representating the compound with the most pronounced oxygen surface enrichment. This finding could thus be at the origin of the previous constation concerning the Mn AOS value of 3.1 found for Mn_3O_4, exceeding the theoretical value of ≈ 2.7. It could also be a possible cause behind the enhanced reducibility of Mn_3O_4 compared to β-MnO_2. In fact, it has been previously reported that metal oxide structures with superstoichiometric surface oxygen, can be highly beneficial in terms of reducibility due to the fact that the excess oxygen is considered to be weakly bound to the cationic center and can thereby readily pass into the gas phase when the temperature is increased [67].

Table 6.5. Surface Mn/O ratios for Mn_xO_y reference compounds based on XPS results.

Sample	Mn/O [a]	Mn/O [b]	Deviation (%) [c]
MnO	1.00	0.69	+ 31
Mn_3O_4	0.75	0.44	+ 41
Mn_2O_3	0.67	0.61	+ 10
Mn_5O_8	0.63	0.58	+ 8
γ-MnOOH	0.50	0.33	+ 34
β-MnO_2	0.50	0.54	- 8
ε-MnO_2	0.50	0.38	+ 25

[a] Theoretical atomic ratio. [b] Experimental atomic ratio derived from XPS results. [b] Calculated deviation between theoretical and experimental data based on the following equation: $\text{Deviation}\ (\%) = \frac{\text{Mn/O}^{\text{th}} - \text{Mn/O}^{\text{ex}}}{\text{Mn/O}^{\text{th}}} \times 100$. A positive deviation corresponds to an experimental value of the ratio lower than the experimental one and is thus representative of a surface enrichment in O and depletion in Mn atoms, whereas a negative deviation would correspond to an experimental value of the ratio higher than the experimental one and is thus representative of a surface enrichment in Mn and depletion in O atoms.

6.6.2. XPS analysis of Mn-based compounds after H_2-reduction test

β-MnO_2, Mn_2O_3, Mn_3O_4, and 10 Mn/Hap compounds were submitted to an H_2-reduction reaction, at the end of which an XPS analysis of the resulting materials was conducted. Reduction of Mn in the samples obtained following H_2-reduction test was confirmed by several means and the presence of manganese species in a divalent oxidation state was also indisputably proven.

First as noted in Table 6.3, the binding energy of Mn $2p_{3/2}$ found in all four of the samples having undergone the H_2-reduction reaction was in the range of 640.6- 641.1 eV, in line with the literature reported values for MnO compound (Mn^{2+}) [56], [57], [68]. Furthermore, the presence of the typical Mn 2p satellite features produced by Mn (II) species is clearly discernable in all the examined Mn 2p spectra, which are displayed in Figure 6.17.

Finally, multiplet splitting of Mn 3s peaks is also consistent with a Mn oxidation state of +2 (Figure 6.17 and Table 6.3), all of which validates the in-situ XANES analysis results.

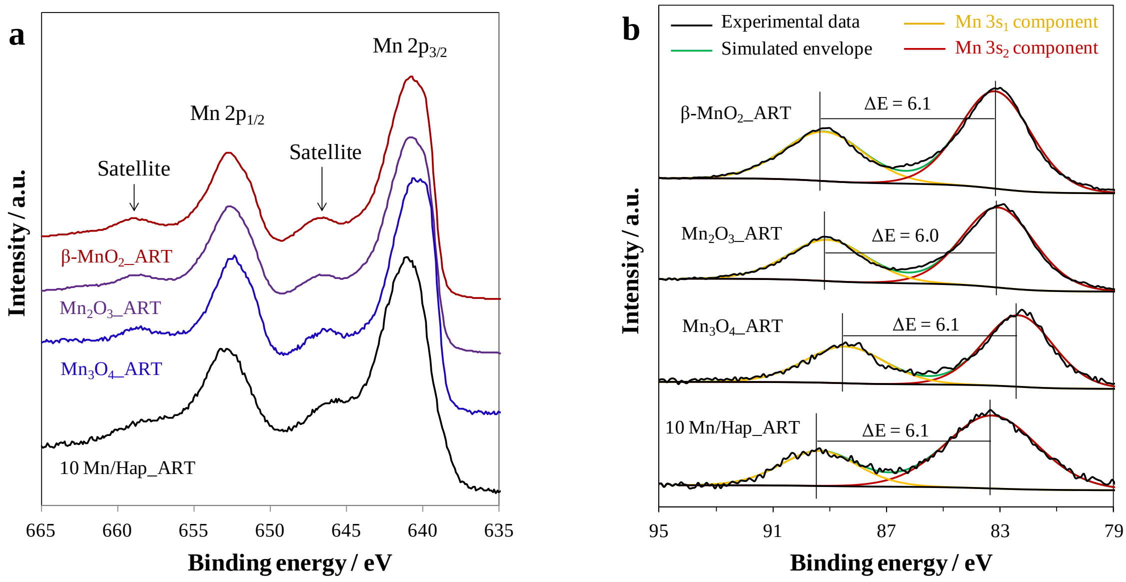

Figure 6.17. a) Mn 2p and b) Mn 3s XPS core level spectra of β-MnO_2_ATR, Mn_2O_3_ATR, Mn_3O_4_ATR, and 10 Mn/Hap_ATR compounds obtained after H_2-reduction test.

6.7. Conclusion

In this work, we have employed several characterization techniques, among which some (in situ XAS, H_2-TPR) allowed to monitor the H_2-reduction process in manganese-bearing samples: Mn_xO_y reference compounds and Mn/Hap catalysts; all in the aim of clarifying the influence of Mn loading in Mn/Hap catalysts on the Mn speciation in the obtained product.

The various methods yield a substantially comparable result in terms of Mn-speciation both in the fresh samples and in the materials obtained following the H_2-reduction reaction. Indeed, all of the above discussed data describe a similar trend regarding the evolution of Mn-speciation versus Mn amount: for low Mn loadings, the Mn oxidation state leans towards lower values (2-3) as revealed by Raman, XAS and XPS analysis; the majority of Mn oxide species being in the form of Mn_3O_4 phase. Furthermore, when the Mn loading increases, a higher Mn AOS becomes predominant (≈ 4) and manganese dioxide (MnO_2) turns into the main Mn oxide phase present on the surface of the Mn/Hap catalyst. While XRD revealed for the two catalysts with the highest Mn weight load (10 Mn/Hap and 20 Mn/Hap) the presence of an MnO_2 phase whose crystallinity increases when going from 10 Mn/Hap to 20 Mn/Hap, no conclusive discrimination between ε- or β-MnO_2 phases was possible at that stage. Yet, through subsequent analysis methods (Raman, XANES and H_2-TPR) a distinction became possible and β-MnO_2 phase was found to be the majorly formed Mn species with increasing Mn content within the catalysts.

However, what is perhaps even more interesting to note is the fact that a lower Mn AOS appears to be conductive to an enhanced reducibility, as shown by H_2-TPR experiments. This enhanced reducibility seems to be correlated with the increase of Mn_3O_4 amount in Mn/Hap catalysts. Thus, the following sequence of catalysts with decreasing reducibility was obtained: 10 Mn/Hap > 5 Mn/Hap > 2.5 Mn/Hap ≈ 20 Mn/Hap. It was postulated that enhanced oxygen mobility could account for the better reducibility of Mn_3O_4 compared to other Mn species with higher Mn AOS, among which figures β-MnO_2. In order to gain further clarity regarding this matter, XPS analysis was conducted over the Mn-bearing materials. Results from the fitting of the O 1s spectrum of Mn_xO_y reference compounds indicated that Mn_3O_4 contained a higher percentage of O_{II} species compared to other Mn_xO_y materials, such as β-MnO_2. Since these O_{II} species have been shown in previous works to promote oxygen mobility, the hypothesis of a higher reducibility engendered by higher oxygen mobility appears to uphold thus far. Moreover, quantitative evaluation of surface Mn/O atomic ratio revealed that among all examined Mn_xO_y reference compounds, Mn_3O_4 presented the greatest proportion of surface excess oxygen; this latter having been formerly shown to promote a metal oxide's reducibility.

Seeing as it has been agreed that an oxidation process occurs through a Mars-van-Krevelen mechanism in the case of transition metal oxide based-catalysts, the reducibility of the catalyst will be decidedly closely related to the catalytic activity. Therefore, Mn_3O_4 should result in a better catalytic performance in the oxidation of toluene than β-MnO_2. This was indeed the case in the study conducted by Kim *et al.* [55], as well as in another performed by Piumetti *et al.* [69].

Hence, it follows that Mn_3O_4-rich samples would be more catalytically efficient than β-MnO_2-rich materials. The validity of this notion will be further investigated in future work focusing on the catalytic performances of these Mn-bearing solids.

References

[1] D. Templeton, F. Ariese, R. Cornelis, L.-G. Danielsson, H. Muntau, H. P. V. Leeuwen, and R. Lobinski, « Guidelines for Terms Related to Chemical Speciation and Fractionation of Elements. Definitions, Structural Aspects, and Methodological Approaches (IUPAC Recommendations 2000) », *Pure Appl. Chem.*, vol. 72, p. 1453–1470, 2000.

[2] S. Islam, M. Alfaruqi, V. Mathew, J. Song, S. Kim, S. Kim, J. Jo, J. P. Baboo, D. T. Pham, and D. Y. Putro, « Facile synthesis and the exploration of the zinc storage mechanism of β-MnO_2 nanorods with exposed (101) planes as a novel cathode material for high performance eco-friendly zinc-ion batteries », *J. Mater. Chem. A*, vol. 5, n° 44, p. 23299–23309, 2017.

[3] D. Vernardou, A. Kazas, M. Apostolopoulou, N. Katsarakis, and E. Koudoumas, « Hydrothermal Growth of MnO_2 at 95 °C as an anode material », *Int. J. Thin. Films Sci. Technol.*, vol. 5, p. 121–127, 2016.

[4] D. Vernardou, A. Kazas, M. Apostolopoulou, N. Katsarakis, and E. Koudoumas, « Cationic effect on the electrochemical characteristics of the hydrothermally grown manganese dioxide », *J. Electron. Mater.*, vol. 46, n° 4, p. 2232–2240, 2017.

[5] Y. Xiong, Y. Xie, Z. Li, and C. Wu, « Growth of Well-Aligned γ-MnO_2 Monocrystalline Nanowires through a Coordination-Polymer-Precursor Route », *Chem. Eur. J.*, vol. 9, n° 7, p. 1645–1651, 2003.

[6] H. Chen, Y. Wang, and Y.-K. Lv, « Catalytic oxidation of NO over MnO_2 with different crystal structures », *Rsc Adv.*, vol. 6, n° 59, p. 54032–54040, 2016.

[7] C. M. Julien and M. Massot, « Local structure of manganese oxides and lithium intercalates », *Ionics*, vol. 11, n° 3–4, p. 226–235, 2005.

[8] C. M. Julien, M. Massot, and C. Poinsignon, « Lattice vibrations of manganese oxides: Part I. Periodic structures », *Spectrochim. Acta. A. Mol. Biomol. Spectrosc.*, vol. 60, n° 3, p. 689–700, 2004.

[9] C. Julien, M. Massot, S. Rangan, M. Lemal, and D. Guyomard, « Study of structural defects in γ-MnO_2 by Raman spectroscopy », *J. Raman Spectrosc.*, vol. 33, n° 4, p. 223–228, 2002.

[10] M.-C. Bernard, A. Hugot-Le Goff, B. V. Thi, and S. C. de Torresi, « Electrochromic reactions in manganese oxides I. Raman analysis », *J. Electrochem. Soc.*, vol. 140, n° 11, p. 3065–3070, 1993.

[11] R. Baddour-Hadjean and J.-P. Pereira-Ramos, « Raman microspectrometry applied to the study of electrode materials for lithium batteries », *Chem. Rev.*, vol. 110, n° 3, p. 1278–1319, 2009.

[12] T. Gao, P. Norby, F. Krumeich, H. Okamoto, R. Nesper, and H. Fjellvåg, « Synthesis and properties of layered-structured Mn_5O_8 nanorods », *J. Phys. Chem. C*, vol. 114, n° 2, p. 922–928, 2009.

[13] C. B. Azzoni, M. C. Mozzati, P. Galinetto, A. Paleari, V. Massarotti, D. Capsoni, and M. Bini, « Thermal stability and structural transition of metastable Mn_5O_8: in situ micro-Raman study », *Solid State Commun.*, vol. 112, n° 7, p. 375–378, 1999.

[14] G. C. Silva, F. S. Almeida, M. S. S. Dantas, A. M. Ferreira, and V. S. Ciminelli, « Raman and IR spectroscopic investigation of As adsorbed on Mn_3O_4 magnetic composites », *Spectrochim. Acta. A. Mol. Biomol. Spectrosc.*, vol. 100, p. 161–165, 2013.

[15] T. Larbi, K. Doll, and T. Manoubi, « Density functional theory study of ferromagnetically and ferrimagnetically ordered spinel oxide Mn_3O_4. A quantum mechanical simulation of their IR and Raman spectra », *J. Alloys Compd.*, vol. 688, p. 692–698, 2016.

[16] Z. W. Chen, J. K. L. Lai, and C. H. Shek, « Influence of grain size on the vibrational properties in Mn_2O_3 nanocrystals », *J. Non-Cryst. Solids*, vol. 352, n^o 30–31, p. 3285–3289, 2006.

[17] Z. Chen, S. Tan, S. Zhang, J. Wang, S. Jin, Y. Zhang, and H. Sekine, « Size dependence of phonon raman spectra in Mn_2O_3 nanocrystals », *Jpn. J. Appl. Phys.*, vol. 39, n^o 11R, p. 6293–6295, 2000.

[18] M. Sun, B. Lan, T. Lin, G. Cheng, F. Ye, L. Yu, X. Cheng, and X Zheng, « Controlled synthesis of nanostructured manganese oxide: crystalline evolution and catalytic activities », *CrystEngComm*, vol. 15, n^o 35, p. 7010–7018, 2013.

[19] L. Lan, Q. Li, G. Gu, H. Zhang, and B. Liu, « Hydrothermal synthesis of γ-MnOOH nanorods and their conversion to MnO_2, Mn_2O_3, and Mn_3O_4 nanorods », *J. Alloys Compd.*, vol. 644, p. 430–437, 2015.

[20] C. Julien, M. Massot, R. Baddour-Hadjean, S. Franger, S. Bach, and J. P. Pereira-Ramos, « Raman spectra of birnessite manganese dioxides », *Solid State Ion.*, vol. 159, n^o 3–4, p. 345–356, 2003.

[21] R. M. Freitas, T. A. Perilli, and A. C. Q. Ladeira, « Oxidative precipitation of manganese from acid mine drainage by potassium permanganate », *J. Chem.*, vol. 2013, p. 287257–287265, 2013.

[22] S. Rong, K. Li, P. Zhang, F. Liu, and J. Zhang, « Potassium associated manganese vacancy in birnessite-type manganese dioxide for airborne formaldehyde oxidation », *Catal. Sci. Technol.*, vol. 8, n^o 7, p. 1799–1812, 2018.

[23] O. S. Ivanova, M. A. Teplonogova, A. D. Yapryntsev, A. E. Baranchikov, and V. K. Ivanov, « Hydrothermal Microwave Synthesis of MnO_2 in the Presence of Melamine: The Role of Temperature and pH », *Russ. J. Inorg. Chem.*, vol. 63, n^o 6, p. 708–713, 2018.

[24] R. E. Ruther, H. Dixit, A. M. Pezeshki, R. L. Sacci, V. R. Cooper, J. Nanda, and G. M. Veith, « Correlating local structure with electrochemical activity in Li_2MnO_3 », *J. Phys. Chem. C*, vol. 119, n^o 32, p. 18022–18029, 2015.

[25] Y. Xiao, X. Wang, W. Wang, D. Zhao, and M. Cao, « Engineering hybrid between MnO and N-doped carbon to achieve exceptionally high capacity for lithium-ion battery anode », *ACS Appl. Mater. Interfaces*, vol. 6, n^o 3, p. 2051–2058, 2014.

[26] X. Gu, J. Yue, L. Chen, S. Liu, H. Xu, J. Yang, Y. Qian, and X. Zhao, « Coaxial MnO/N-doped carbon nanorods for advanced lithium-ion battery anodes », *J. Mater. Chem. A*, vol. 3, n^o 3, p. 1037–1041, 2015.

[27] B. Liu, X. Hu, H. Xu, W. Luo, Y. Sun, and Y. Huang, « Encapsulation of MnO nanocrystals in electrospun carbon nanofibers as high-performance anode materials for lithium-ion batteries », *Sci. Rep.*, vol. 4, p. 4229–4235, 2014.

[28] M. E. Zilm, L. Chen, V. Sharma, A. McDannald, M. Jain, R. Ramprasad, and M. Wei, « Hydroxyapatite substituted by transition metals: experiment and theory », *Phys. Chem. Chem. Phys.*, vol. 18, n^o 24, p. 16457–16465, 2016.

[29] I. Mayer, G. Pető, A. Karacs, G. Molnár, and I. Popov, « Divalent Mn in calcium hydroxyapatite by pulse laser deposition », *J. Inorg. Biochem.*, vol. 104, n^o 10, p. 1107–1111, 2010.

[30] D. Chlala, J.-M. Giraudon, N. Nuns, C. Lancelot, Rose-Noëlle Vannier, M. Labaki, and J.-F. Lamonier, « Active Mn species well dispersed on Ca^{2+} enriched apatite for total oxidation of toluene », *Appl. Catal. B Environ.*, vol. 184, p. 87–95, 2016.

[31] C. Paluszkiewicz, A. Ślósarczyk, D. Pijocha, M. Sitarz, M. Bućko, A. Zima, A. Chróścicka, and M. Lewandowska-Szumiel, « Synthesis, structural properties and thermal stability of Mn-doped hydroxyapatite », *J. Mol. Struct.*, vol. 976, n^o 1, p. 301–309, 2010.

[32] B. Yin, S. Zhang, H. Jiang, F. Qu, and X. Wu, « Phase-controlled synthesis of polymorphic MnO_2 structures for electrochemical energy storage », *J. Mater. Chem. A*, vol. 3, n^o 10, p. 5722–5729, 2015.

[33] L. K. Noda, M. C. C. Ribeiro, N. S. Gonçalves, A. H. Jubert, and O. Sala, « Electronic transitions of the manganate (V) ion in aqueous solution: a resonance Raman study », *J. Raman Spectrosc.*, vol. 30, n^o 8, p. 697–704, 1999.

[34] R. J. Smith, Y. Shen, and K. L. Bray, « The effect of pressure on vibrational modes in Li_3PO_4 », *J. Phys. Condens. Matter*, vol. 14, n^o 3, p. 461–469, 2001.

[35] C. Chadefaux, C. Vignaud, E. Chalmin, J. Robles-Camacho, J. Arroyo-Cabrales, E. Johnson, and I. Reiche, « Color origin and heat evidence of paleontological bones: Case study of blue and gray bones from San Josecito Cave, Mexico », *Am. Mineral.*, vol. 94, n^o 1, p. 27–33, 2009.

[36] M. Che and J. C. Védrine, *Characterization of solid materials and heterogeneous catalysts: From structure to surface reactivity*. John Wiley & Sons, 2012.

[37] P. J. Durham, J. B. Pendry, and C. H. Hodges, « Calculation of X-ray absorption near-edge structure, XANES », *Comput. Phys. Commun.*, vol. 25, n^o 2, p. 193–205, 1982.

[38] R. A. Scott and C. M. Lukehart, *Applications of Physical Methods to Inorganic and Bioinorganic Chemistry*. John Wiley & Sons, 2013.

[39] V. Briois, C. C. D. Moulin, and M. Verdaguer, « Seuils d'absorption des rayons X: un outil de caractérisation indispensable en chimie de coordination. », *Actual. Chim.*, vol. 3, p.31–40, 2000.

[40] M. Pereira Moreira, V. Teixeira da Silva Aragão, G. D. de Almeida Soares, and E. Araujo dos Santos, « Simultaneous insertion of Mg^{2+}, Sr^{2+} and Mn^{2+} ions into hydroxyapatite structure », *Key Eng. Mater.*, vol. 493, p. 20–26, 2012.

[41] M. Gafurova, Marat, T. Biktagirova, G. Mamina, E. Klimashinab, V. Putlayevb, L. Kuznetsovac, and S. Orlinskiia, « Case Study of the Interplay of Manganese and Nitrate in

Hydroxyapatite Nanoparticles: Association of Oppositely Charged Impurities as Revealed by Pulsed EPR and DFT », *Phys. Chem. Chem. Phys.*, vol. 17, 7 pages, 2015.

[42] P. H. Oliveira Jr, L. A. B. Santana, N. S. Ferreira, S. Sharifi-Asl, T. Shokuhfar, R. Shahbazian-Yassar, G. M. L. Dalmônico, J. Werckmann, M. Farina, and E. A. dos Santos, « Manganese behavior in hydroxyapatite crystals revealed by X-ray difference Fourier maps », *Ceram. Int.*, vol. 46, n^o 8, p. 10585–10597, 2020.

[43] J. C. Elliott, *Structure and Chemistry of the Apatites and Other Calcium Orthophosphates*. Elsevier, 2013.

[44] K. Ravindranadh, B. Babu, V. P. Manjari, G. T. Rao, M. C. Rao, and R. Ravikumar, « Optical and structural properties of undoped and Mn^{2+} doped Ca–Li hydroxyapatite nanopowders using mechanochemical synthesis », *J. Lumin.*, vol. 159, p. 119–127, 2015.

[45] O. Y. Gorbenko, I. E. Graboy, V. Amelichev, A. Bosak, A. R. Kaul, B. Güttler, V. L. Svetchnikov, and H. Zandbergen, « The structure and properties of Mn_3O_4 thin films grown by MOCVD », *Solid State Commun.*, vol. 124, p. 15–20, 2002.

[46] S. PalDey, S. Gedevanishvili, W. Zhang, and F. Rasouli, « Evaluation of a spinel based pigment system as a CO oxidation catalyst », *Appl. Catal. B Environ.*, vol. 56, n^o 3, p. 241–250, 2005.

[47] F. Kapteijn, L. Singoredjo, A. Andreini, and J. A. Moulijn, « Activity and selectivity of pure manganese oxides in the selective catalytic reduction of nitric oxide with ammonia », *Appl. Catal. B Environ.*, vol. 3, n^o 2‑3, p. 173–189, 1994.

[48] J. Wang, H. Zhao, J. Song, T. Zhu, and W. Xu, « Structure-Activity Relationship of Manganese Oxide Catalysts for the Catalytic Oxidation of (chloro)-VOCs », *Catalysts*, vol. 9, n^o 9, p. 726–743, 2019.

[49] V. P. Santos, M. F. R. Pereira, J. J. M. Órfão, and J. L. Figueiredo, « The role of lattice oxygen on the activity of manganese oxides towards the oxidation of volatile organic compounds », *Appl. Catal. B Environ.*, vol. 99, n^o 1‑2, p. 353–363, 2010.

[50] K. Ramesh, L. Chen, F. Chen, Y. Liu, Z. Wang, and Y.-F. Han, « Re-investigating the CO oxidation mechanism over unsupported MnO, Mn_2O_3 and MnO_2 catalysts », *Catal. Today*, vol. 131, n^o 1‑4, p. 477–482, 2008.

[51] X. Tang, J. Li, L. Sun, and J. Hao, « Origination of N_2O from NO reduction by NH_3 over β-MnO_2 and α-Mn_2O_3 », *Appl. Catal. B Environ.*, vol. 99, n^o 1‑2, p. 156–162, 2010.

[52] S. Liang, F. Teng, G. Bulgan, R. Zong, and Y. Zhu, « Effect of phase structure of MnO_2 nanorod catalyst on the activity for CO oxidation », *J. Phys. Chem. C*, vol. 112, n^o 14, p. 5307–5315, 2008.

[53] Y. Peng, H. Chang, Y. Dai, and J. Li, « Structural and surface effect of MnO_2 for low temperature selective catalytic reduction of NO with NH_3 », *Procedia Environ. Sci.*, vol. 18, p. 384–390, 2013.

[54] Y. Yongnian, H. Ruili, C. Lin, and Z. Jiayu, « Redox behavior of trimanganese tetroxide catalysts », *Appl. Catal. A-Gen.*, vol. 101, n^o 2, p. 233–252, 1993.

[55] S. C. Kim and W. G. Shim, « Catalytic combustion of VOCs over a series of manganese oxide catalysts », *Appl. Catal. B Environ.*, vol. 98, n° 3‑4, p. 180–185, 2010.

[56] M. Oku, K. Hirokawa, and S. Ikeda, « X-ray photoelectron spectroscopy of manganese—oxygen systems », *J. Electron Spectrosc. Relat. Phenom.*, vol. 7, n° 5, p. 465–473, 1975.

[57] M. Chigane and M. Ishikawa, « Manganese oxide thin film preparation by potentiostatic electrolyses and electrochromism », *J. Electrochem. Soc.*, vol. 147, n° 6, p. 2246–2251, 2000.

[58] V. R. Galakhov, M. Demeter, S. Bartkowski, M. Neumann, N.A. Ovechkina, E. Z. Kurmaev, N. I. Lobachevskaya, Y. M. Mukovskii, J. Mitchell, and D. L. Ederer, « Mn 3 s exchange splitting in mixed-valence manganites », *Phys. Rev. B*, vol. 65, n° 11, p. 113102–113105, 2002.

[59] J. W. Murray, J. G. Dillard, R. Giovanoli, H. Moers, and W. Stumm, « Oxidation of Mn (II): Initial mineralogy, oxidation state and ageing », *Geochim. Cosmochim. Acta*, vol. 49, n° 2, p. 463–470, 1985.

[60] M. C. Biesinger, B. P. Payne, A. P. Grosvenor, L. W. Lau, A. R. Gerson, and R. S. C. Smart, « Resolving surface chemical states in XPS analysis of first row transition metals, oxides and hydroxides: Cr, Mn, Fe, Co and Ni », *Appl. Surf. Sci.*, vol. 257, n° 7, p. 2717–2730, 2011.

[61] T. Z. Hossain and J. K. Lowell, « Method and apparatus for the detection of light elements on the surface of a semiconductor substrate using x-ray fluorescence (XRF) », US5778039A, 1998.

[62] J. Cazaux, « A physical approach to the radiation damage mechanisms induced by X-rays in X-ray microscopy and related techniques », *J. Microsc.*, vol. 188, n° 2, p. 106–124, 1997.

[63] A. Ramírez, P. Hillebrand, D. Stellmach, M. M. May, P. Bogdanoff, and S. Fiechter, « Evaluation of MnO_x, Mn_2O_3, and Mn_3O_4 electrodeposited films for the oxygen evolution reaction of water », *J. Phys. Chem. C*, vol. 118, n° 26, p. 14073–14081, 2014.

[64] C. Revathi and R. R. Kumar, « Electro Catalytic Properties of α, β, γ, ε-MnO_2 and γ-MnOOH Nanoparticles: Role of Polymorphs on Enzyme Free H_2O_2 Sensing », *Electroanalysis*, vol. 29, n° 5, p. 1481–1489, 2017.

[65] D. P. Dubal and R. Holze, « Self-assembly of stacked layers of Mn_3O_4 nanosheets using a scalable chemical strategy for enhanced, flexible, electrochemical energy storage », *J. Power Sources*, vol. 238, p. 274–282, 2013.

[66] H. Chen, A. Sayari, A. Adnot, and F. Larachi, « Composition–activity effects of Mn–Ce–O composites on phenol catalytic wet oxidation », *Appl. Catal. B Environ.*, vol. 32, n° 3, p. 195–204, 2001.

[67] O. A. Bulavchenko, O. S. Venediktova, T. N. Afonasenko, P. G. Tsyrul'Nikov, A. A. Saraev, V. V. Kaichev, and S. V. Tsybulya, « Nonstoichiometric oxygen in Mn–Ga–O spinels: reduction features of the oxides and their catalytic activity », *RSC Adv.*, vol. 8, n° 21, p. 11598–11607, 2018.

[68] A. J. Nelson, J. G. Reynolds, and J. W. Roos, « Core-level satellites and outer core-level multiplet splitting in Mn model compounds », *J. Vac. Sci. Technol. Vac. Surf. Films*, vol. 18, n° 4, p. 1072–1076, 2000.

[69] M. Piumetti, D. Fino, and N. Russo, « Mesoporous manganese oxides prepared by solution combustion synthesis as catalysts for the total oxidation of VOCs », *Appl. Catal. B Environ.*, vol. 163, p. 277–287, 2015.

[70] C.-H. Kuo, I. M. Mosa, S. Thanneeru, V. Sharma, L. Zhang, S. Biswas, M. Aindow, S. P. Alpay, J. F. Rusling, and S. L. Suib, « Facet-dependent catalytic activity of MnO electrocatalysts for oxygen reduction and oxygen evolution reactions », *Chem. Commun.*, vol. 51, n^o 27, p. 5951–5954, 2015.

[71] Y. An, S. Wang, L. Duan, J. Liu, and Z. Wu, « Local Mn structure and room temperature ferromagnetism in Mn-doped In_2O_3 films », *Appl. Phys. Lett.*, vol. 102, p. 212411–212415, 2013.

[72] T. Ye, S. Li, X. Wu, M. Xu, X. Wei, K. Wang, H. Bao, J. Wang, and J. Chen, « Sol–gel preparation of efficient red phosphor Mg_2TiO_4: Mn^{4+} and XAFS investigation on the substitution of Mn^{4+} for Ti^{4+} », *J. Mater. Chem. C*, vol. 1, n^o 28, p. 4327–4333, 2013.

[73] A. J. Gibson, B. Johannessen, Y. Beyad, J. Allen, and S. W. Donne, « Dynamic electrodeposition of manganese dioxide: temporal variation in the electrodeposition mechanism », *J. Electrochem. Soc.*, vol. 163, n^o 5, p. H305–H312, 2016.

[74] D. A. McKeown, W. K. Kot, H. Gan, and I. L. Pegg, « X-ray absorption studies of manganese valence and local environment in borosilicate waste glasses », *J. Non-Cryst. Solids*, vol. 328, n^o 1‑3, p. 71–89, 2003.

[75] Z. Yang, D. C. Ford, J. S. Park, Y. Ren, S. Kim, H. Kim, T. T. Fister, M. K. Y. Chan, and M. M. Thackeray, « Probing the Release and Uptake of Water in α-$MnO_2\cdot$ x H_2O », *Chem. Mater.*, vol. 29, n^o 4, p. 1507–1517, 2017.

[76] A. Leven, D. Vlassopoulos, M. Kanematsu, J. Goin, and P. A. O'Day, « Characterization of manganese oxide amendments for in situ remediation of mercury-contaminated sediments », *Environ. Sci. Process. Impacts*, vol. 20, n^o 12, p. 1761–1773, 2018.

[77] F. Jiao, A. Harrison, A. H. Hill, and P. G. Bruce, « Mesoporous Mn_2O_3 and Mn_3O_4 with crystalline walls », *Adv. Mater.*, vol. 19, n^o 22, p. 4063–4066, 2007.

General conclusions and outlook

Catalytic systems composed of transition metal oxides (TMO), Cu and/or Mn oxides, supported on stoichiometric hydroxyapatite (Hap) were studied in the total oxidation reaction of toluene, a widely encountered Volatile Organic Compound (VOC). Different strategies for enhancing the catalytic performances of these Hap supported TMO were methodically examined. The synthesized materials, prepared via wet impregnation route, were characterized by different physicochemical techniques, namely X-Ray Diffraction (XRD), Thermal Analysis coupled with Mass Spectrometry (TGA/DSC-MS), Infrared spectroscopy (IR), Temperature Programmed Reduction coupled with Mass Spectrometry (H_2-TPR/MS), X-Ray Photoelectron Spectroscopy (XPS), Raman spectroscopy, Time of Flight Secondary Ion Mass Spectrometry (ToF-SIMS), X-ray Absorption Spectroscopy (XAS), etc ..., in order to better understand the obtained compounds' catalytic reactivity towards the complete oxidation of toluene.

First, binary Cu-Mn oxides supported on Hap, with a total metal loading of 10 wt%, were investigated in the total oxidation of toluene. Different molar Cu/Mn compositions (2; 1; 0.5) were examined and compared with the corresponding supported single transition metal oxide catalysts (Cu/Hap and Mn/Hap). The catalytic performances of the supported Cu-Mn oxide catalysts revealed the existence of a synergetic effect in terms of activity and selectivity towards CO_2 through the formation of Cu-Mn mixed oxides. The strongest synergetic effect was observed for a Cu/Mn molar ratio of 2 as confirmed by the standardized conversion rate values determined at 190 °C (r_{190}) which followed the decreasing sequence ($/10^{-2}$ h^{-1}): Cu_2Mn/Hap (2.57) > CuMn/Hap (2.04) > $CuMn_2$/Hap (1.59) > Mn/Hap (1.13) >> Cu/Hap (0.13). The highest activity of Cu_2Mn/Hap was explained by a better reducibility of the active phase in line with a high density of Cu-O-Mn interactions at the outermost layers as shown by ToF-SIMS results. Nonetheless, a poor stability conduct was noted for these Hap supported $CuMnO_x$ catalysts which was correlated with a decomposition of the mixed entities, the latter being likely induced by a slow rate in the Mn reoxidation step.

A second catalytic performances optimization scheme consisted in using an organic complexant, β-cyclodextrin (β-CD), as a Cu species dispersing agent in the synthesis procedure of copper oxides dispersed on hydroxyapatite support. The catalyst prepared via a β-CD assisted route, noted 10 Cu-CD/Hap was compared to a conventionally synthesized Hap supported copper oxide material, noted 10 Cu/Hap. TGA/DSC-MS results showed that the use of β-CD accelerated the thermal decomposition of nitrates, due most probably to optimized interactions between β-CD and copper precursors which helped reduce the direct interaction of Cu^{2+} and NO_3^- species with the support, thus preventing a strong retention of nitrates and resulting in a better elimination efficiency of residual nitrate species, as revealed through infrared spectroscopy. Most importantly, it turned out that the addition of β-cyclodextrin altered copper location on the hydroxyapatite support. Indeed, XRD, XPS, and H_2-TPR/MS analyses indicated that highly dispersed small Cu(II) clusters were primarily formed in 10 Cu-CD/Hap solid, which resulted in enhanced copper particles dispersion and reducibility compared to 10 Cu/Hap material, where bulk CuO were predominant on the surface. It followed that the catalytic performances of 10 Cu-CD/Hap were better than those manifested by 10 Cu/Hap. Both toluene conversion rate and CO_2 productivity were improved by the use of β-CD during the catalyst preparation due to a rise in the quality and number of Cu active sites. In fact, the catalyst derived from a β-CD-assisted synthesis (10 Cu-CD/Hap) displayed less sintering of copper species following stability tests, which ultimately led to it retaining better catalytic conduct over time.

By demonstrating the effectiveness of using β-CD oligosaccharides in order to prevent copper species aggregation and enhance their reducibility, thus succeeding in improving the catalytic performances of

Hap supported copper oxide catalyst, it became imperative to gain a better grasp of the role of β-CD in the Cu-CD/Hap system. Therefore, a thorough study of the evolution of this Cu-CD/Hap system starting from the interactions taking place between β-CD, the copper precursor, and hydroxyapatite support in the aqueous phase, up to the formation of active Cu species in the catalyst was carried out. Based on the data obtained through Raman and ToF-SIMS monitoring, it appeared that molecule-ion associations between β-CD and Cu^{2+} ions derived from the copper nitrate precursor were generated. Indeed, solutions Raman analysis revealed the occurrence of a 14 cm^{-1} red shift of the β-CD characteristic band at 876 cm^{-1} which emerged at 862 cm^{-1} in the Cu/β-CD solutions, indicating the existence of an interaction between copper and β-CD species. The occurrence of such interactions between Cu entities and β-CD molecules was further proven by the detection of Cu-organic fragments in the ToF-SIMS spectra of dried 10 Cu-CD/Hap D. Furthermore, the formation of Ca-organic ion-fragments within dried 10 Cu-CD/Hap D system evidenced interactions taking place between β-cyclodextrin molecules and calcium ions of hydroxyapatite. Hence, by acting as a chemical spacer between copper species and hydroxyaptite support, β-cyclodextrin succeeded not only in preventing copper species agglomeration but also their close interaction with the support. Indeed, the high surface density of $Cu_xO_yH_z$ entities detected by ToF-SIMS analysis of 10 Cu-CD/Hap D compared to those noted for 10 Cu/Hap D, in addition to the higher cristallinity degree of Hap support obtained in the case of 10 Cu-CD/Hap compared to 10 Cu/Hap highlighted the role of β-CD in favoring the formation of homogeneously dispersed copper species situated on the surface of hydroxyapatite support rather than inserted in its subsurface layers, thus making the copper active sites more accessible and available for catalytic reactions.

Regarding manganese oxides supported on Hap (Mn/Hap) catalysts, in the aim of achieving effective future optimization of this catalytic system, a deeper inspection of the nature of active Mn species responsible for the material's high activity in the total oxidation of toluene was of essence. Thus, an extensive study of the speciation of Mn entities in Mn/Hap samples was performed. Mn/Hap solids with various manganese loadings: 2.5; 5; 10; and 20 wt% of Mn were prepared in order to examine the effect of Mn content on the manganese speciation in the resulting sample. Moreover, a series of synthesized manganese oxide bulk solids (ε-MnO_2, β-MnO_2, Mn_5O_8, Mn_2O_3, γ-MnOOH, Mn_3O_4, and MnO) served as a set of reference data for the various physicochemical characterizations carried out. Raman, XAS, and XPS analysis revealed that for low Mn loadings the Mn average oxidation state (AOS) tended towards lower values (2-3), with the majority of Mn oxide species present in Mn/Hap sample being in the form of Mn_3O_4 phase. However, when the Mn content increased, a higher Mn AOS became predominant (≈ 4) and manganese dioxide (MnO_2) turned into the main Mn oxide phase present in Mn/Hap catalyst. This agreed with the results of XRD analysis indicating that for both 10 Mn/Hap and 20 Mn/Hap an MnO_2 crystalline phase was formed, whose crystallinity grew with that of Mn loading within the sample, without being able to ascertain nonetheless the type of MnO_2 polymorph it represented (ε- and/or β-MnO_2). Moreover, what was perhaps a most significant revelation was the fact that H_2-TPR analysis demonstrated that a lower Mn AOS promoted a higher reducibility of the Mn/Hap sample: a higher amount of Mn_3O_4 being conductive to a higher reducibility. Indeed, the reducibility of Mn-bearing samples increased when going from β-MnO_2 to Mn_3O_4 reference compound. It ensued that it was the Mn/Hap catalysts with lower Mn content (≤ 10 wt%), rich in Mn_3O_4, which presented the greater reducibility when compared to the Mn/Hap catalyst with the highest Mn loading (20 Mn/Hap), rich in β-MnO_2. It was suggested that an increase in oxygen mobility might be at the origin of the enhanced reducibility of Mn_3O_4 bearing materials. This hypothesis was supported by XPS results which indicated that Mn_3O_4 contained a higher percentage of O_{II} species, which were shown in previous works to promote oxygen mobility, compared to other Mn_xO_y materials, such as β-MnO_2. Moreover, Mn_3O_4 presented the greatest proportion of superstoichiometric surface oxygen, previously reported to be highly beneficial in terms of reducibility owing to their weakly bound state to the cationic center.

Having now presented the main findings of this research, it should be noted that based on the catalytic performances limitations encountered when examining binary CuMn oxides supported on Hap materials, some modifications of the catalytic system can be envisaged in the intent of overcoming the poor stability conduct of Hap supported $CuMnO_x$ catalysts. One of them being metal doping, with noble or transition metal, of the supported $CuMnO_x$ solids. Indeed, previous works have shown that gold doping of copper manganese oxides modified the catalyst surface so that it could store much more oxygen, promoting thus the Mars van Krevelen mechanism and enhancing the redox efficiency of the catalyst [1]. Moreover, another investigation on cobalt doping of $CuMnO_x$ catalysts revealed that the addition of cobalt creates a higher amount of oxygen vacancies which would most likely facilitate the exchange of oxygen between lattice and surface oxygen, i.e. the reoxidation step of the catalyst [2]. Therefore, a prospective study of the impact of metal doping of binary Cu-Mn oxides supported on Hap, with either gold or cobalt, on the durability behavior of the catalyst tested in the total oxidation of toluene might prove to be highly rewarding. It has the potential of increasing the reoxidation rate of manganese species which would allow averting the decomposition of the highly active mixed $CuMnO_x$ entities.

Last but not least, it would also be interesting to examine the effect of using β-CD in the synthesis of Hap supported binary Cu-Mn oxides on the physicochemical properties and catalytic performances of the resulting material. For it might not only lead to an enhancement in the catalytic oxidation activity of Cu_xMn_y/Hap as a result of an increase in active species dispersion, but even more importantly to an improvement in this catalyst's previously noted poor stability conduct.

[1] K. Morgan, K. J. Cole, A. Goguet, C. Hardacre, G. Hutchings, N. Maguire, S. O. Shekhtman, and S. H. Taylor, « TAP studies of CO oxidation over $CuMnO_X$ and Au/$CuMnO_X$ catalysts », *J. Catal.*, vol. 276, n° 1, p. 38–48, 2010.

[2] S. Dey, G. C. Dhal, D. Mohan, R. Prasad, and R. N. Gupta, « Cobalt doped $CuMnO_x$ catalysts for the preferential oxidation of carbon monoxide », *Appl. Surf. Sci.*, vol. 441, p. 303–316, 2018.

Appendix A

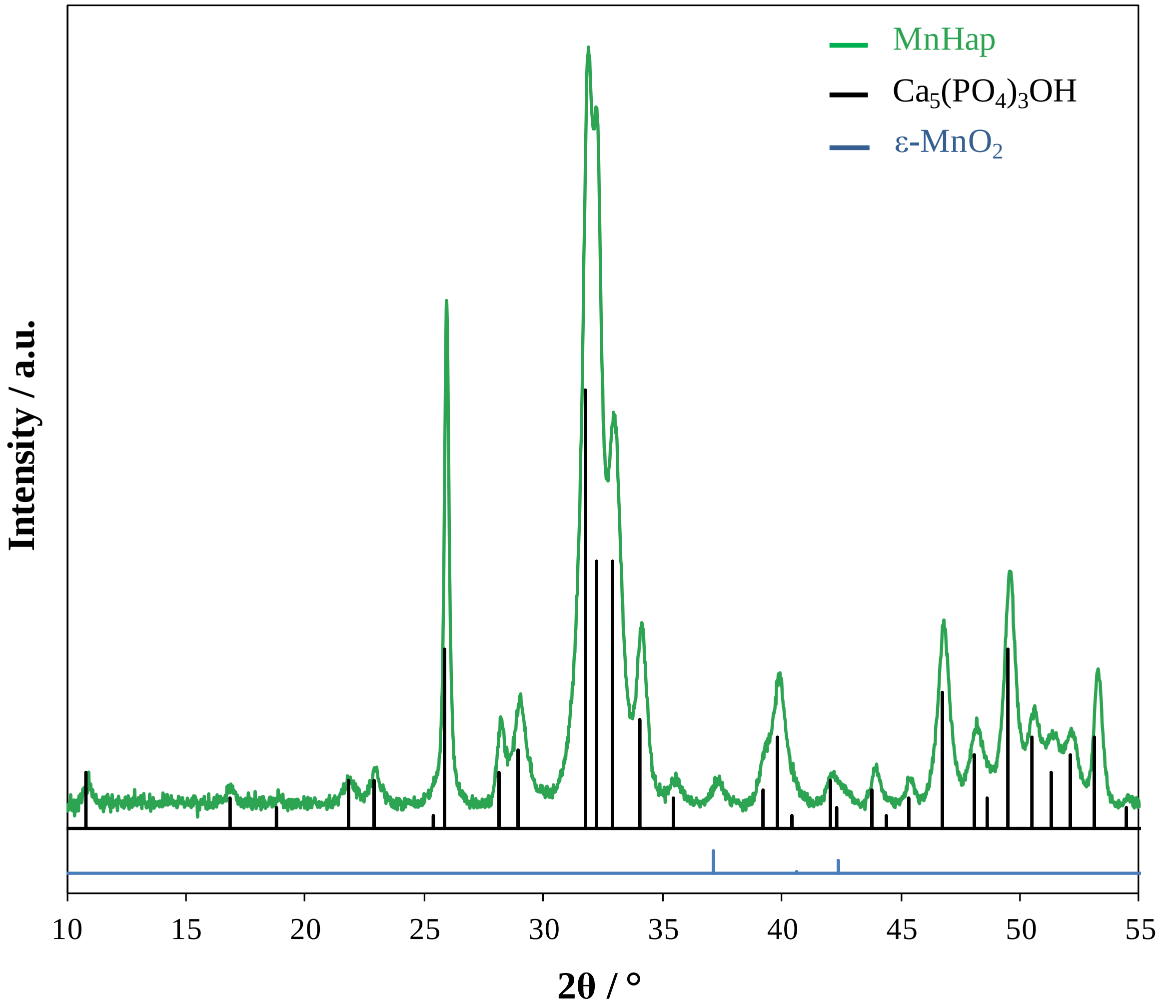

Figure AA.1. X-ray diffractogram of MnHap solid.

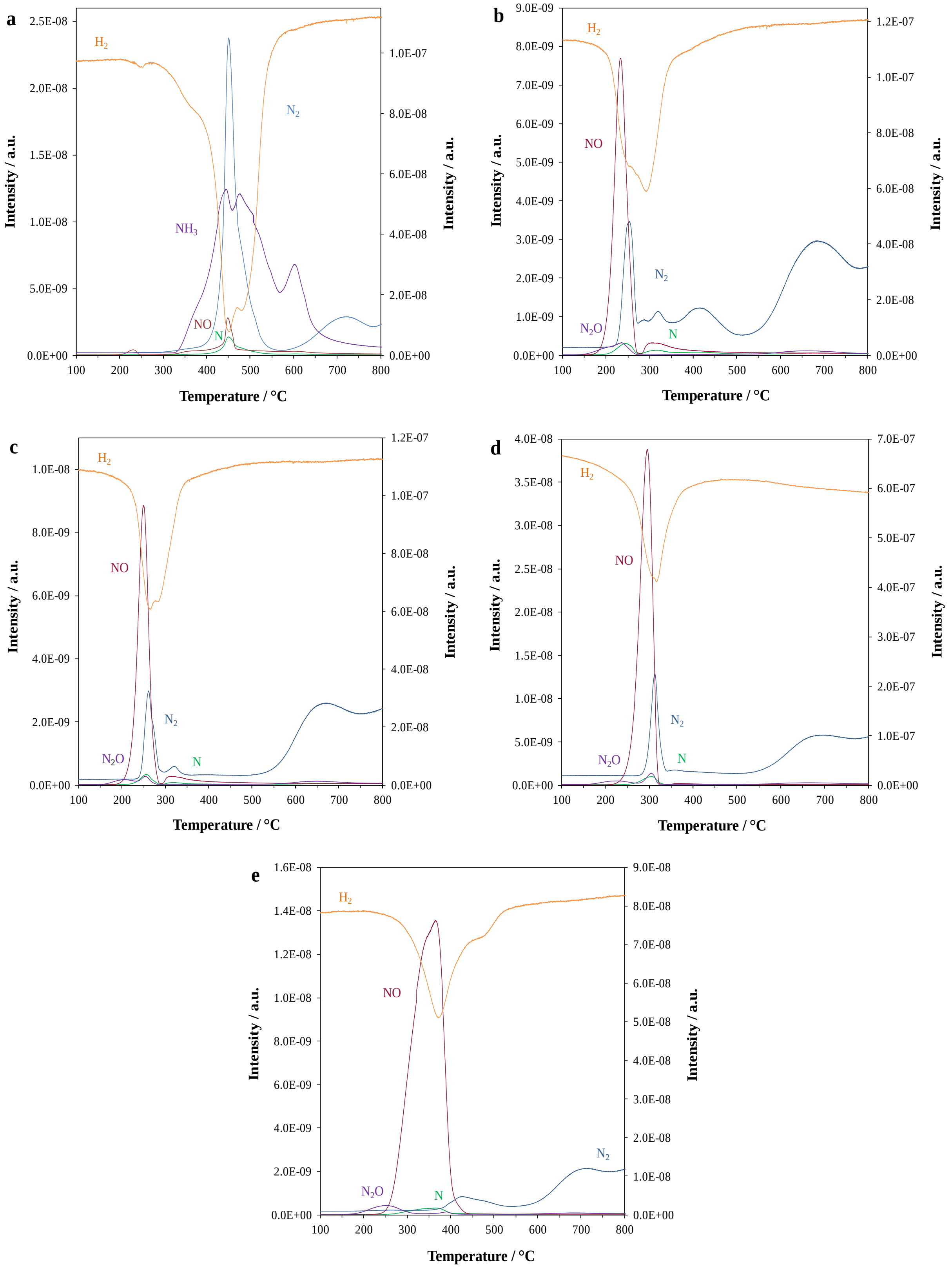

Figure AA.2. Evolution of the intensity of the signals corresponding to m/z = 2, 14, 17, 28, 30, and 44 as a function of temperature for the solids: a-CuHap; b-Cu_2MnHap; c-CuMnHap; d-$CuMn_2Hap$; e-MnHap. The y-axis on the left gives the intensities of the signals m/z = 14, 17, 28, 30 and 44. The y-axis on the right gives the intensity of the peak m/z = 2.

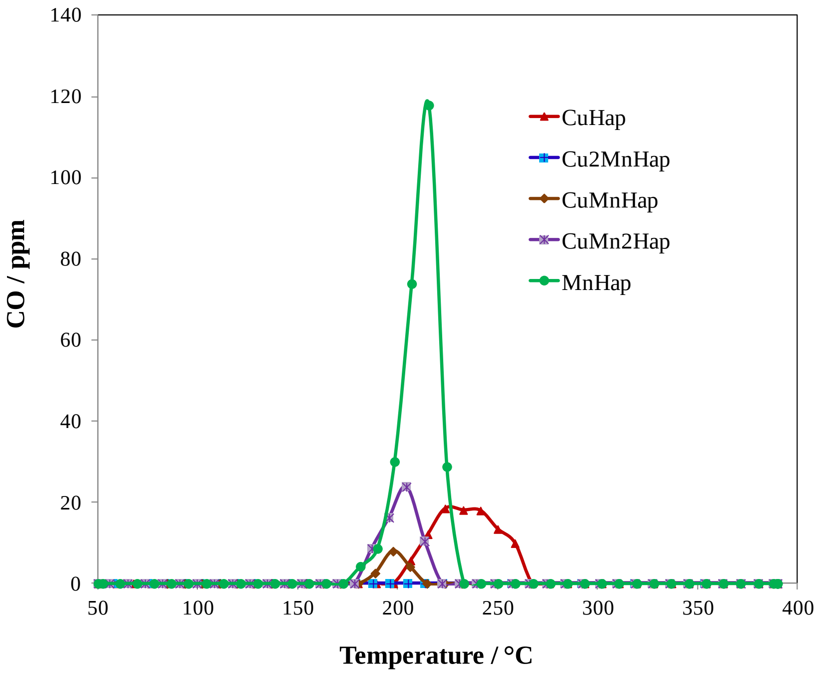

Figure AA.3. CO production as a function of temperature over Cu_xMn_yHap catalysts.

Table AA.1. TGA based data obtained for dried CuHap D, Cu_2MnHap D, and MnHap D samples.

Sample	Global weight loss	Experimental weight loss (%)			Theoretical weight loss (%)
		1st step	2nd step	3rd step	Nitrates
CuHapD	17.5	4.0 (20 - 180 °C)	11.2 (180 - 400 °C)	2.3 (400 - 600 °C)	13.7
$Cu_2MnHapD$	19.4	5.1 (20 - 140 °C)	12.0 (140 - 400 °C)	2.3 (400 - 600 °C)	13.6
MnHapD	20.4	6.4 (20 - 130 °C)	12.5 (130 - 400 °C)	1.5 (400 - 600 °C)	13.2

Table AA.2. T_{10}, T_{50}, and T_{90} (CO_2) obtained in toluene oxidation for Hap and Cu_xMn_yHap catalysts.

Sample	T_{10} (CO_2) [°C]	T_{50} (CO_2) [°C]	T_{90} (CO_2) [°C]
Hap	297	-	-
CuHap	223	255	302
Cu_2MnHap	180	196	213
CuMnHap	180	202	216
$CuMn_2Hap$	185	205	218
MnHap	192	210	224

Appendix B

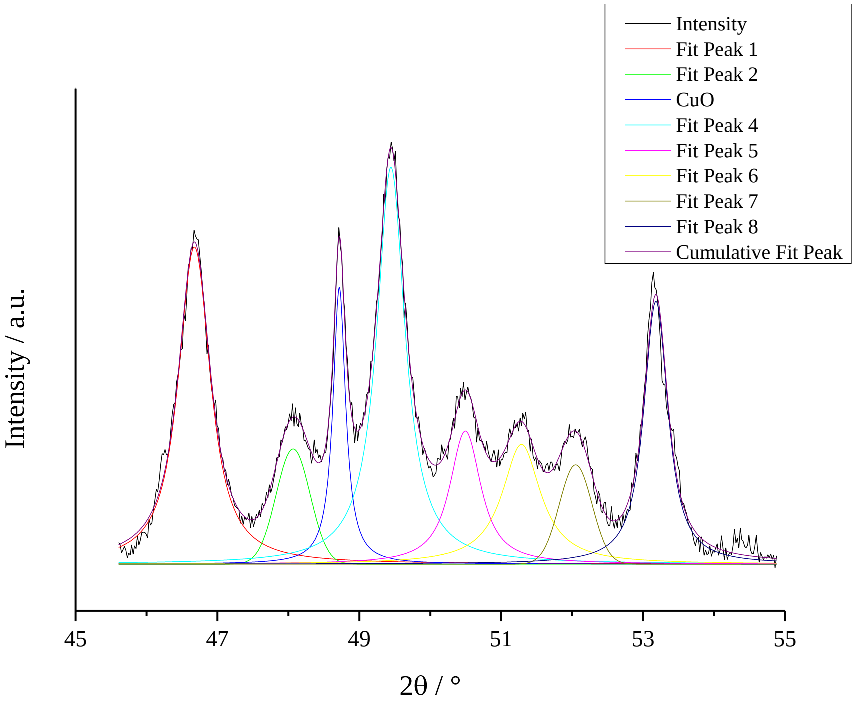

Figure AB.1. Deconvolution of the XRD peaks obtained in the 2θ range 45.5 ° < 2θ < 54 ° for 10 Cu/Hap.

Table AB.1. Cracking Patterns of various fragments

Gas	MM	m/z	R. A. [a]/ %
NO_2	46	(NO) 30	100
		(NO_2) 46	32
		(O) 16	24
		(N) 14	10
N_2O	44	(N_2O) 44	100
		(NO) 30	30.5
		(N) 14	12.5
		(N_2) 28	10
		(O) 16	5
NO	30	(NO) 30	100
		(N) 14	8
		(NH) 15	2
		(O) 16	1
N_2	28	(N_2) 28	100
		(N) 14	14
		(N_2H) 29	2

Table AB.1. Cracking Patterns of various fragments (continued)

Gas	MM	m/z	R. A. [a]/ %
CO_2	44	(CO_2) 44	100
		(CO) 28	11.5
		(O) 16	11
		(C) 12	10
CO	28	(CO) 28	100
		(C) 12	5
		(O) 16	2
CH_4	16	(CH_4) 16	100
		(CH_3) 15	90
		(CH_2) 14	21
		(CH) 13	17
		(C) 12	5
		(CH_5) 17	2
NH_3	17	(NH_3) 17	100
		(NH_2) 16	80
		(NH) 15	7
		(N) 14	2.5
		(NH_4) 18	0.5
H_2O	18	(H_2O) 18	100
		(HO) 17	21
		(O) 16	1
HCHO	30	(HCHO) 30	58
		(HCO) 29	100
		(CO) 28	24
HNO_3	63	(HNO_3) 63	2
		(NO_2) 46	100
		(O_2) 32	4
		(NO) 30	86
		(N_2) 28	20
		(H_2O) 18	49
		(OH) 17	24
		(O) 16	22
		(N) 14	10

[a] Relative abundance.

Appendix C

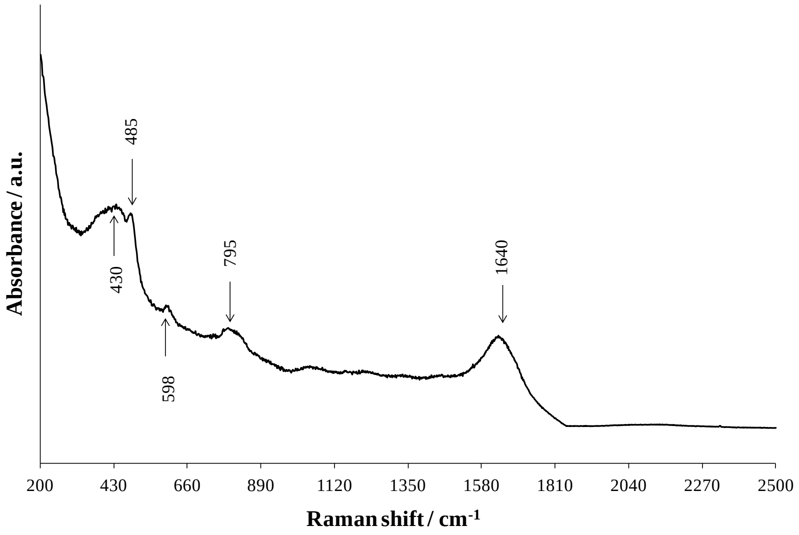

Figure AC.1. Raman spectrum of water.

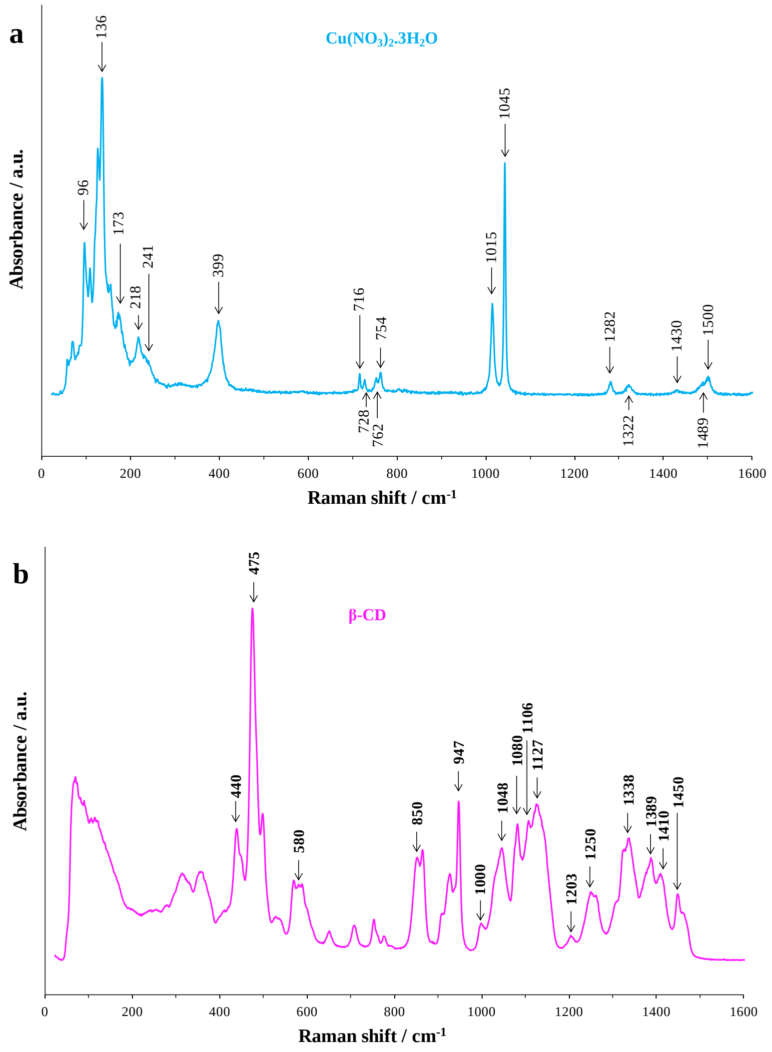

Figure AC.2. Raman spectra of pure a) copper nitrate trihydrate precursor and b) β-CD compound with band indexation.

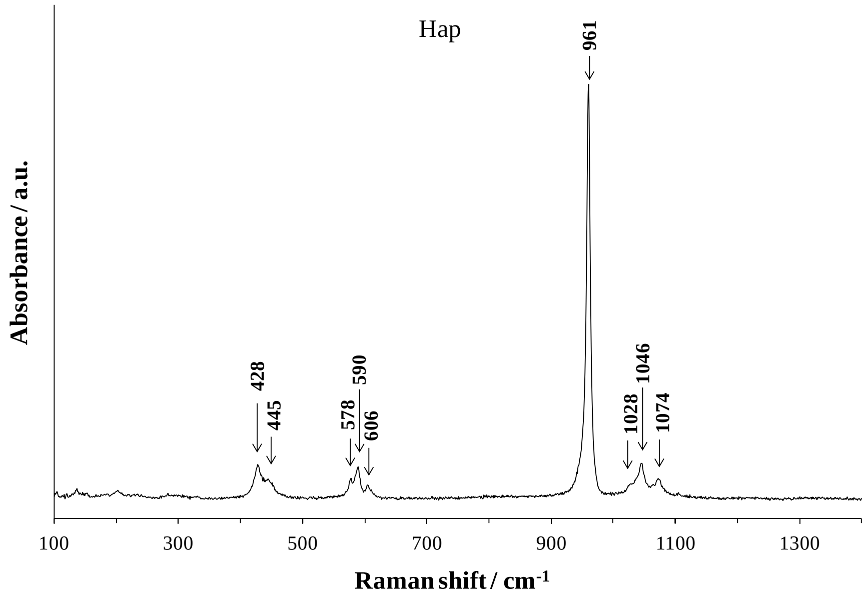

Figure AC.3. Raman spectrum of calcined support Hap.

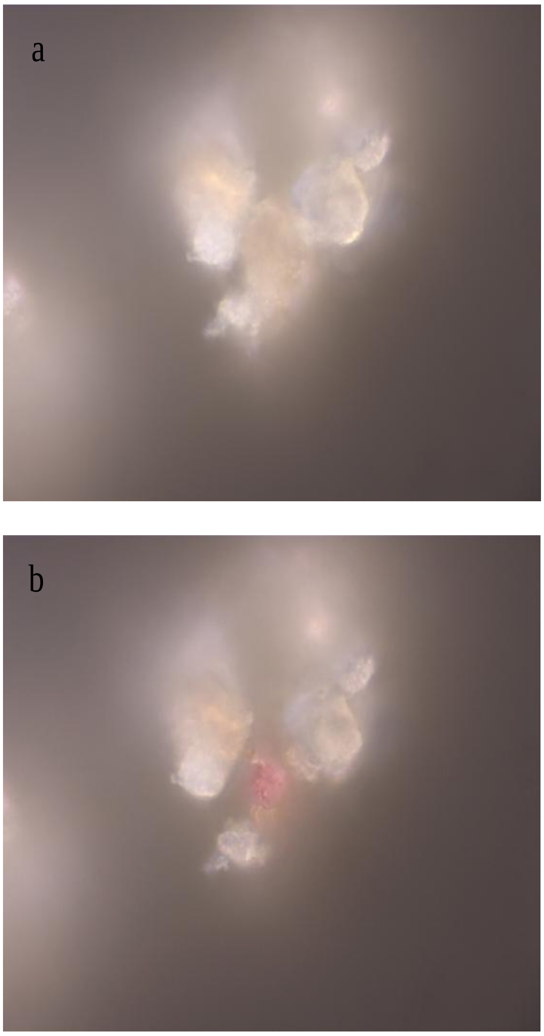

Figure AC.4. White-light images captured by the Raman apparatus video camera of sample a) before and b) after laser-induced photodegradation.

Table AC.1. Raman spectroscopic data of $Cu(NO_3)_2.3H_2O$.

Raman	Assignment
96	Lattice vibrations
136	
173	—NO_2 restricted rotations
218	Coordinated nitrate (Cu—O_{st})
241	
399	
716	ν_3—ONO_2
728	
754	
762	
1015	ν_2—ONO_2
1045	
1282	ν_1—ONO_2
1322	
1430	ν_4—ONO_2
1489	
1500	

Table AC.2. Raman spectroscopic data of β-CD (r = Stretching mode; ϕ = Bending mode).

Raman	Assignment
440	Skeletal vibrations
475	
580	
850	ϕ CCH, r CO, r CC [a]
947	skeletal vibration involving α-1,4 linkage
1000	r CC, ϕ OCH, ϕ CCH, ϕ CCO
1048	r CO, r CC
1106	r CO, ϕ COH, r CC
1081	r CO, ϕ COH, r CC
1127	r CO [b]
1203	r CO, ϕ CCH, ϕ COH
1250	ϕ OCH, ϕ COH, ϕ CCH [c]

Table AC.2. Raman spectroscopic data of β-CD (r = Stretching mode; ϕ = Bending mode)_(continued).

Raman	Assignment
1338	ϕ CCH, ϕ COH, ϕ HCH [c]
1389	ϕ CCH, ϕ OCH, ϕ COH
1410	ϕ OCH, ϕ CCH
1450	ϕ OCH, ϕ HCH

[a] anomeric vibration. [b] pyranose ring vibration. [c] Complex CH_2OH vibration.

Appendix D

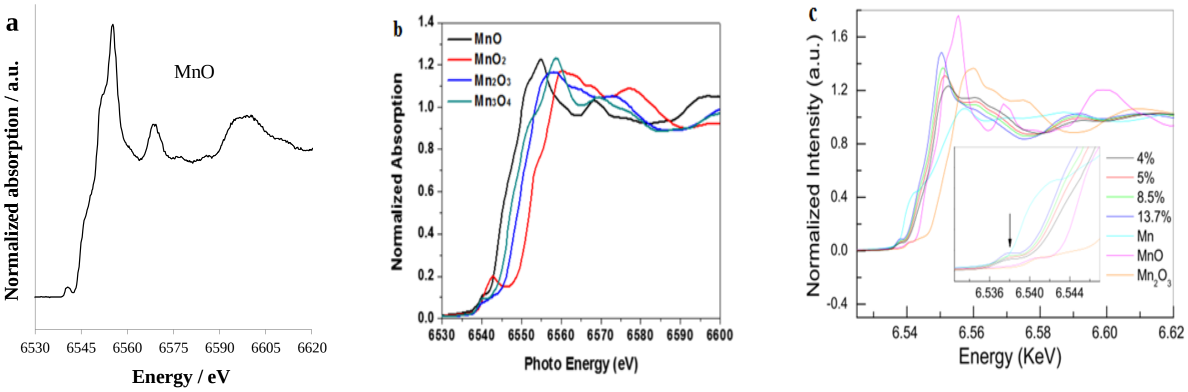

Figure AD.1. Mn-K edge XANES spectrum of MnO a) obtained from the current study, b) taken from the work of Kuo *et al.* [70] (in black) and c) taken from the work of An *et al.* [71] (in pink).

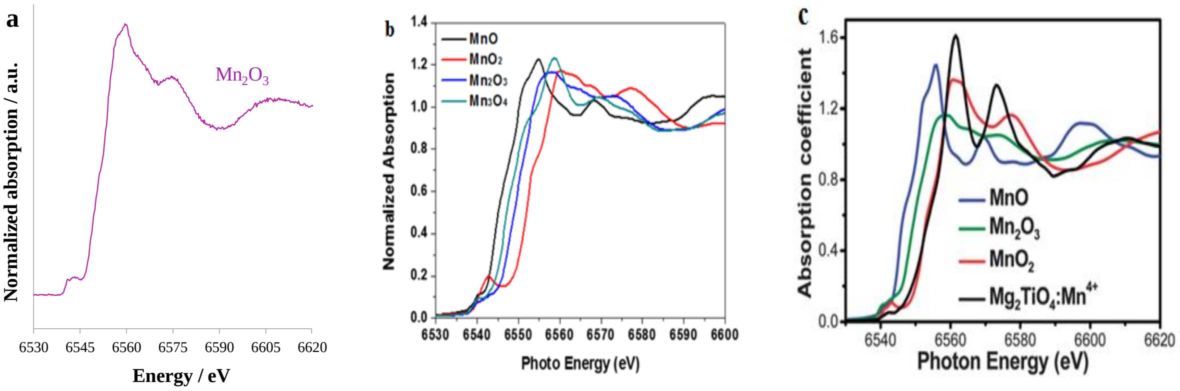

Figure AD.2. Mn-K edge XANES spectrum of Mn_2O_3 a) obtained from the current study, b) taken from the work of Kuo *et al.* [70] (in blue) and c) taken from the work of Ye *et al.* [72] (in green).

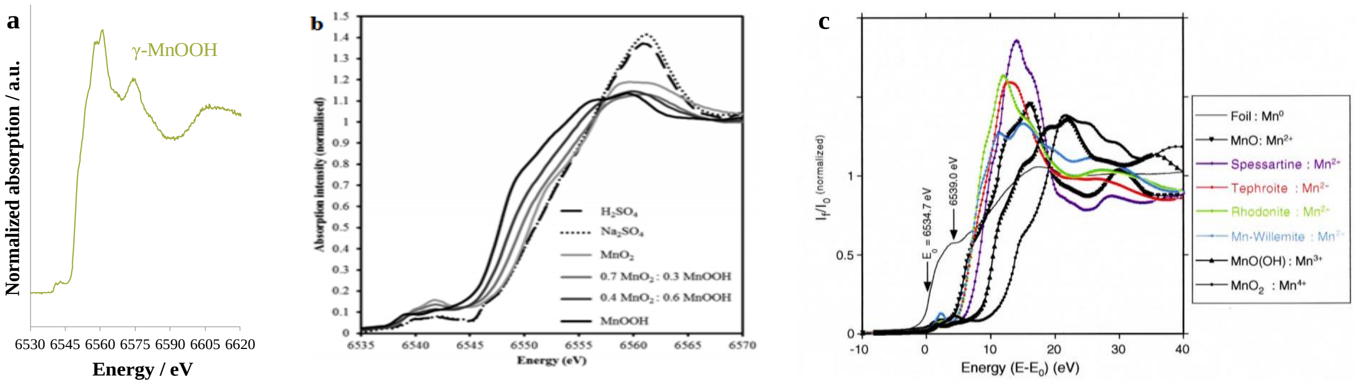

Figure AD.3. Mn-K edge XANES spectrum of γ-MnOOH a) obtained from the current study, b) taken from the work Gibson *et al.* [73] (full black line) and c) taken from the work of McKeown *et al.* [74] (in black with an upward facing arrow).

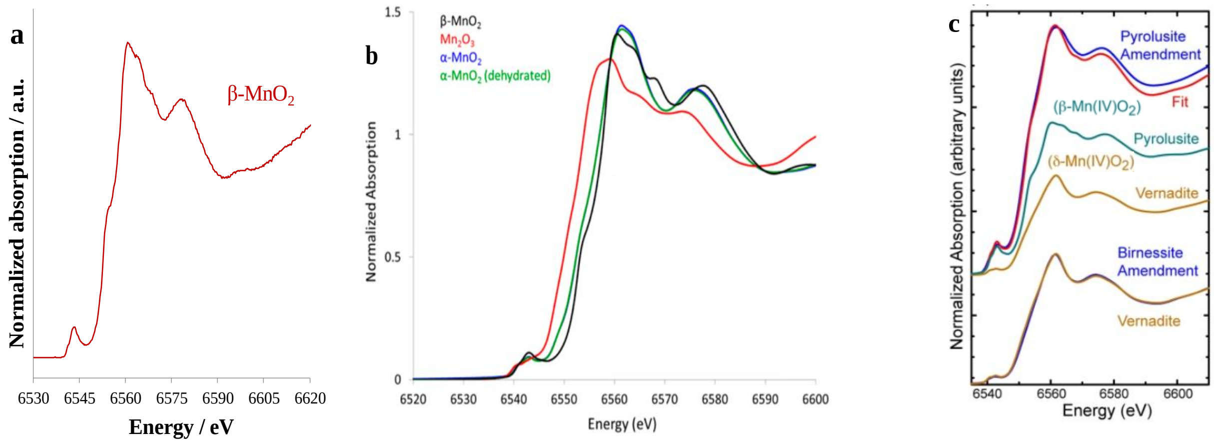

Figure AD.4. Mn-K edge XANES spectrum of β-MnO$_2$ a) obtained from the current study, b) taken from the work of Yang *et al.* [75] (in black) and c) taken from the work of Leven *et al.* [76] (in black).

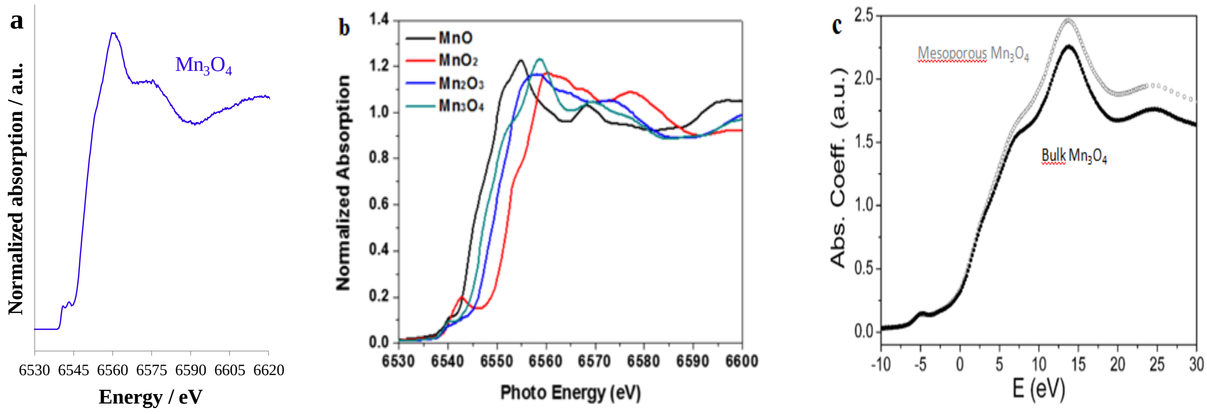

Figure AD.5. Mn-K edge XANES spectrum of Mn$_3$O$_4$ a) obtained from the current study, b) taken from the work of Kuo *et al.* [70] (in green) and c) taken from the work of Jiao *et al.* [77].

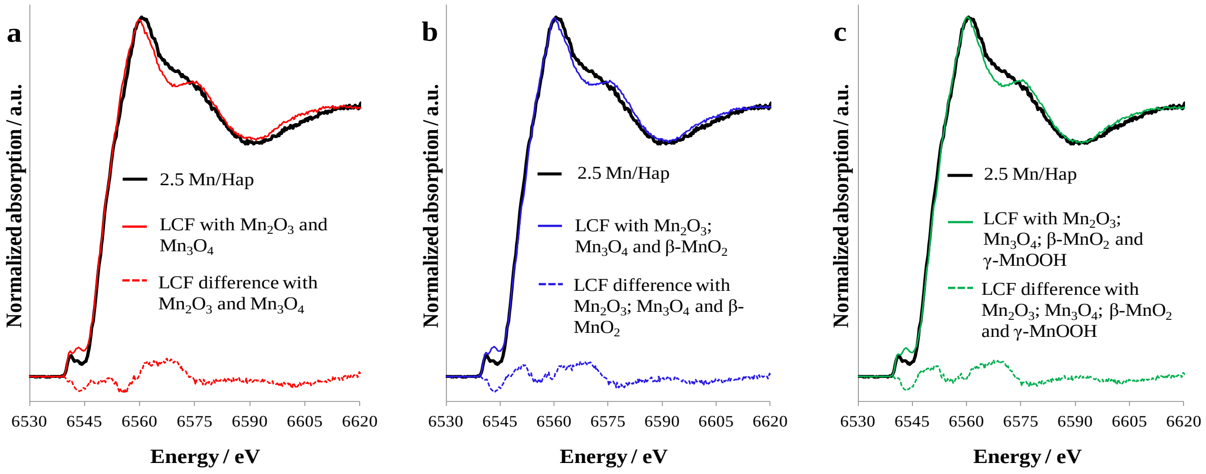

Figure AD.6. LCF with 2 a), 3 b), and 4 c) components along with the LCF difference from data points and Mn-K edge XANES experimental spectrum of 2.5 Mn/Hap measured at a fluorescence detection energy of 6491.5 eV.

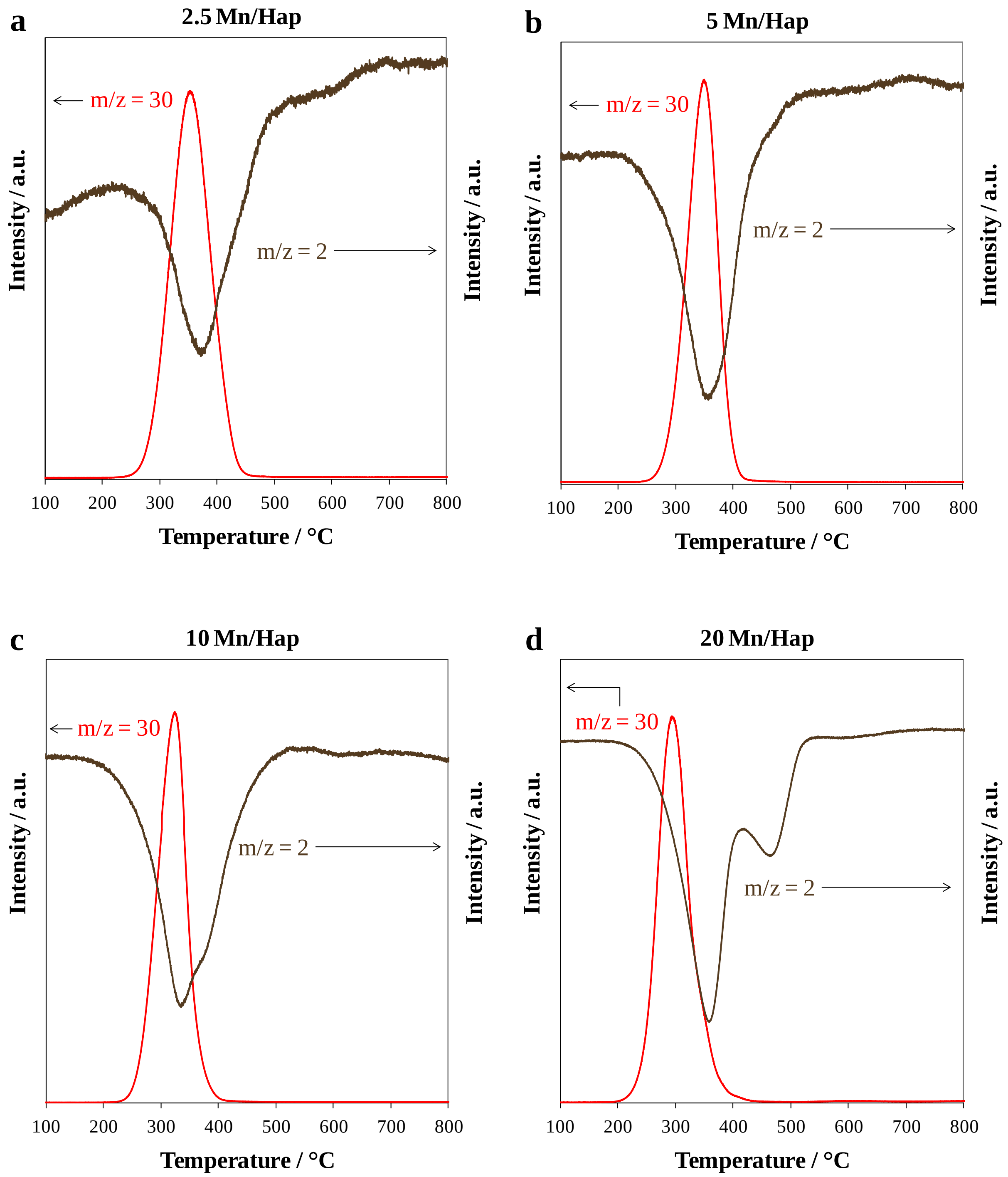

Figure AD.7. Evolution of the intensity of the signals corresponding to m/z = 2 and 30 as a function of temperature for the solids: a) 2.5 Mn/Hap, b) 5 Mn/Hap, c) 10 Mn/Hap and d) 20 Mn/Hap. The y-axis on the left gives the intensities of the signals m/z = 30. The y-axis on the right gives the intensity of the peak m/z = 2.

Table AD.1. The linear combination fitting results for 2.5 Mn/Hap sample with 2, 3, and 4 components.

Sample	Number of components	Standard sample	Weight fraction	R factor [a]
2.5 Mn/Hap	2	Mn_3O_4	0.66	0.00112
		Mn_2O_3	0.34	
2.5 Mn/Hap	3	Mn_3O_4	0.587	0.00079
		Mn_2O_3	0.314	
		β-MnO_2	0.099	
2.5 Mn/Hap	4	Mn_3O_4	0.535	0.00075
		Mn_2O_3	0.256	
		β-MnO_2	0.101	
		γ-MnOOH	0.108	

[a] R-factor is defined as follows: $R = \mathrm{sum}((\mathrm{data}-\mathrm{fit})^2)/\mathrm{sum}(\mathrm{data}^2)$.

Scientific contributions

1. List of publications

[1] M. Ibrahim, M. Labaki, J.-M. Giraudon, and J.-F. Lamonier, « Hydroxyapatite, a multifunctional material for air, water and soil pollution control: A review », *J. Hazard. Mater.*, vol. 383, p. 121–139, 2020.

[2] M. Ibrahim, M. Labaki, N. Nuns, J.-M. Giraudon, and J.-F. Lamonier, « Cu-Mn Hydroxyapatite Materials for Toluene Total Oxidation », *ChemCatChem*, vol. 12, n° 2, p. 550–560, 2020.

2. Conference, Forum and workshop participations

Doctoral Forum Doctoral School of Science and Technology (DSST)- Hadath, Lebanon
Oral Presentation ***September 2017***
Title: « Toluene total oxidation over $Cu_xMn_yO_z$ *dispersed on hydroxyapatite »*

LAAS Conference Lebanese University - Faculty of Sciences – Fanar, Lebanon
Oral Presentation ***April 2017***
Title: « Toluene total oxidation over $Cu_xMn_yO_z$ *dispersed on hydroxyapatite »*

NWIMA-2 Workshop Lebanese University - Faculty of Sciences – Fanar, Lebanon
Oral Presentation ***April 2019***
Title: « Catalytic oxidation of toluene over copper-manganese mixed oxides supported on hydroxyapatite: durability tests »

FCCAT 2 Conference Fréjus, France
Poster presentation ***June 2019***
Title: « Bioinspired Cu-Mn hydroxyapatite materials for toluene total oxidation »
Prize: Best Poster Presentation